

OPTIMAL INPUT DESIGN AND SYSTEM IDENTIFICATION FOR AN
AGILE AIRCRAFT

A THESIS SUBMITTED TO
THE GRADUATE SCHOOL OF NATURAL AND APPLIED SCIENCES
OF
MIDDLE EAST TECHNICAL UNIVERSITY

BY
MURAT MİLLİDERE

IN PARTIAL FULFILLMENT OF THE REQUIREMENTS
FOR
THE DEGREE OF DOCTOR OF PHILOSOPHY
IN
ENGINEERING SCIENCES

SEPTEMBER 2021

Approval of the thesis:

**OPTIMAL INPUT DESIGN AND SYSTEM IDENTIFICATION FOR AN
AGILE AIRCRAFT**

submitted by **MURAT MİLLİDERE** in partial fulfillment of the requirements for
the degree of **Doctor of Philosophy in Engineering Sciences, Middle East
Technical University** by,

Prof. Dr. Halil Kalıpçılar
Dean, Graduate School of **Natural and Applied Sciences**

Prof. Dr. Murat Dicleli
Head of the Department, **Engineering Sciences**

Assoc. Prof. Dr. Ferhat Akgül
Supervisor, **Engineering Sciences, METU**

Prof. Dr. Kemal Leblebicioğlu
Co-Supervisor, **Electrical and Electronic Engineering,
METU**

Examining Committee Members:

Prof. Dr. Ozan Tekinalp
Aerospace Engineering, METU

Assoc. Prof. Dr. Ferhat Akgül
Engineering Sciences, METU

Assoc. Prof. Dr. Senih Gürses
Engineering Sciences, METU

Prof. Dr. Coşku Kasnakoğlu
Electrical and Electronics Engineering, TOBB University of
Economics and Technology

Prof. Dr. Mehmet Önder Efe
Computer Engineering., Hacettepe University

Date: 07.09.2021

I hereby declare that all information in this document has been obtained and presented in accordance with academic rules and ethical conduct. I also declare that, as required by these rules and conduct, I have fully cited and referenced all material and results that are not original to this work.

Name Last name: Murat Millidere

Signature :

ABSTRACT

OPTIMAL INPUT DESIGN AND SYSTEM IDENTIFICATION FOR AN AGILE AIRCRAFT

Millidere, Murat

Doctor of Philosophy, Engineering Sciences

Supervisor: Assoc. Prof. Dr. Ferhat Akgül

Co-Supervisor: Prof. Dr. Kemal Leblebicioğlu

September 2021, 216 pages

This doctorate study aims to provide a methodology for developing aerodynamic and engine thrust models using simulated flight test data for the F16 fighter aircraft. An accurate and comprehensive representation of an aircraft's aerodynamic characteristics is required to design a flight control system or develop a high-fidelity flight simulator. Modern computational methods and wind tunnel testing can provide the aerodynamic database, but flight test data is required to obtain a more accurate and realistic aerodynamic database. As a result, system identification methods can characterize applied forces and moments acting on the aircraft. The F-16 nonlinear model also includes sensor models to simulate the actual flight data. The flight tests are carried out in the F16 simulation model using different excitations on the control surfaces. Simulation data is collected in predefined trim points. The equation error and output error methods are employed to analyze simulated data to estimate aerodynamic parameters in the time domain. The equation-error method is used firstly to identify aerodynamic parameters, and the results are then utilized as a starting point in the output-error process for fine-tuning. In general, thrust forces and moments are obtained from ground tests. The contribution of this doctoral study is to implement an iterative aerodynamic and thrust estimation approach in the absence

of engine manufacturer data. The validation of resulting models is accomplished by comparing the measured flight data to the model's predictions for identical control inputs, as specified by the Federal Aviation Administration (FAA).

Keywords: Parameter Estimation, Sensitivity Analysis, Equation Error Method, Output Error Method, Aerodynamic Database

ÖZ

ÇEVİK UÇAKLARIN OPTİMAL GİRDİ TASARIMI VE SİSTEM TANIMLAMASI

Millidere, Murat
Doktora, Mühendislik Bilimleri
Tez Yöneticisi: Doç. Dr. Ferhat Akgül
Ortak Tez Yöneticisi: Prof. Dr. Kemal Leblebicioğlu

Eylül 2021, 216 sayfa

Bu doktora çalışmasının amacı, F16 savaş uçağının simule test verileri kullanılarak aerodinamik ve itki modellerinin belirlenmesinde kullanılacak yöntemi geliştirmektir. Uçuş control sistemi tasarlarken veya yüksek sadakat seviyeli uçuş simulatörleri geliştirirken, hava aracının tutarlı ve kapsamlı aerodinamik modeli gerekmektedir. Aerodinamik veritabanı, hesaplamalı yöntemler ve rüzgar tüneli ile çıkarılmasına rağmen daha doğru ve gerçekçi aerodinamik veritabanı için uçuş testlerine ihtiyaç duyulmaktadır. Bu sebeple, sistem belirleme yöntemleri ile uçağa etki eden kuvvet ve momentler karakterize edilmektedir. Daha gerçekçi uçuş test verisi benzetmek için, 6DOF model içerisinde sensor modelleri mevcuttur. Simulasyon modeli içerisinde, kontrol yüzeyleri farklı türde girdilerle aktif duruma getirilerek uçuş testleri gerçekleştirilmiştir. Simulasyon datası önceden belirlenen denge noktalarında toplanmıştır. Aerodinamik modellerin tahmininde zaman bölgesinde denklem hatası ve sonuç hatası yöntemleri kullanılmaktadır. İlk olarak denklem hatası yöntemi kullanılmakta olup, çıkan sonuçlar sonuç hatası yöntemine ilk değer olarak verilip, modelin ince ayarı yapılmaktadır. Genelde itki kuvvet ve momenti üretici firmadan hazır alınır. Bu doktora çalışmasının literatüre katkısı,

retici firmadan itki verisi alınamaması durumunda, tekrarlayan aerodinamik ve itki tahmin yntemi geliřtirmektir. Elde edilen modelere sisteme verilen girdilerin aynısı verilerek, Federal Havacılık Dairesi kılavuzu standartlarına gre sonuları karřılařtırılıp, modeller doęrulanır.

Anahtar Kelimeler: Parametre Kestirimi, Duyarlılık Analizi, Denklem Hatası Yntemi, Sonu Hatası Yntemi, Aerodinamik Veritabanı

To My Family.

ACKNOWLEDGMENTS

This study was carried out during my time as a modeling and simulation engineer at Turkish Aerospace company. Many people have contributed to making this work successful in a variety of ways.

First and foremost, I want to express my gratitude to my research supervisor, Assoc. Prof. Ferhat Akgul, for allowing me to pursue my goals with great freedom. His excellent guidance, continuous support, patience, and understanding over the past three years were constructive for me throughout this study.

Prof. Dr. Kemal Leblebicioğlu, my co-supervisor, deserves special thanks for his motivation, sharing expertise, and insightful discussion about the system identification methodology.

I would also like to thank my committee, including Prof. Dr. Ozan Tekinalp and Assoc. Prof. Senih Gurses, for raising several precious topics in our discussion, and I believe I have managed to address several of them here.

Prof. Dr. Dilek Keskin has also assisted me with several administrative matters.

Several discussions with Dr. Ravindra Jategaonkar have strongly influenced the guidelines of my work. I appreciate him sharing his expertise in the area of aircraft identification with me.

The acquisition of flight data was not as simple as one might think. I appreciate the efforts of Samet Uslu and Uğur Çakın, who contributed significantly to providing the experimental data applicable for analysis.

I want to extend my thanks to all current and former colleagues, in particular Tolga Yigit, Fazıl Selcuk Gomec, Assoc. Prof. Tayfun Cimen, Huseyin Burak Kurt, Ugur Karaman, Hakan Ballı, Mehmet Yıldız, and Hakan Sargın, for their support, many technical debates and a friendly working atmosphere.

I want to thank my parents and family members, whose unconditional love and everlasting support have enabled me to complete this study.

TABLE OF CONTENTS

ABSTRACT	v
ÖZ	vii
ACKNOWLEDGMENTS	x
TABLE OF CONTENTS	xii
LIST OF TABLES	xvi
LIST OF FIGURES	xix
LIST OF ABBREVIATIONS	xxvi
LIST OF SYMBOLS	xxvii
CHAPTERS	
1 INTRODUCTION	1
1.1 System Identification	1
1.2 Modern Methods of Aircraft Parameter Estimation	3
1.3 The Motivation for System Identification	3
1.4 Literature Review	6
2 AIRCRAFT MODELING AND TRIM	9
2.1 Air Vehicle Flight Simulation Model	9
2.1.1 Definition of Reference Systems	10
2.1.2 Nonlinear Equations of Motion	11
2.1.3 Auxiliary Equations	18
2.1.4 Off-Nominal Calculations	19
2.2 Forces and Moments	21
2.2.1 Aerodynamic Forces and Moments	22

2.2.2	Propulsion Forces and Moments	24
2.2.3	Gravity Force.....	29
2.3	Sensor Models.....	30
2.4	Aircraft Trim and Linearization.....	31
2.4.1	Dynamic Model Representation for Aircraft Trim	31
2.4.2	Numerical Methods for Aircraft Trim.....	34
2.4.3	Steady-State Flight Conditions (Trim Conditions)	39
3	FLIGHT DATA GATHERING AND ANALYSIS	41
3.1	Flight Data Gathering	41
3.1.1	Optimized Maneuvers	42
3.1.2	Optimal Input Design	44
3.1.3	Flight Test Instrumentation and Measurement.....	47
3.2	Flight Data Analysis	48
3.2.1	Flight Data Prefiltering.....	49
3.2.2	Flight Path Reconstruction	49
4	METHODOLOGY	55
4.1	Model Description	55
4.2	Integration of State Equations.....	56
4.3	Parameter Estimation Methods	57
4.3.1	Gauss-Newton Algorithm	59
4.3.2	Equation Error Method.....	62
4.3.3	Output Error Method	68
4.4	Model Structure Determination and Validation.....	78
4.4.1	The Correlation Based Particle Swarm Optimization	78

4.4.2	Statistical Accuracy	88
4.4.3	Qualitative Graphical Results	89
4.4.4	Resampling Methods	89
4.4.5	Proof-of-Match (POM)	93
4.4.6	Theil's Inequality Coefficient	96
4.4.7	Range of Model Applicability in Frequency Domain	97
4.5	Thrust Calculation from Steady State Flight Tests.....	98
4.5.1	Introduction to Flight Performance.....	98
4.5.2	Steady State Flight	99
4.5.3	Gliding Flight.....	100
4.5.4	Calculating Thrust Using Newton-Raphson Algorithm	102
4.6	Iterative Equation Error Method	102
5	RESULTS AND DISCUSSION.....	105
5.1	Case 1: Availability of Engine Database from Manufacturer	105
5.1.1	Phase 1.1: Model Structure Determination.....	105
5.1.2	Phase 1.2: Equation Error Method.....	117
5.1.3	Phase 1.3: Sensitivity Analysis	139
5.1.4	Phase 2: Output Error Method	148
5.1.5	Phase 3: Model Validation.....	155
5.2	Case 2: Non-Availability of Engine Database from Manufacturer	185
5.2.1	Calculating Thrust from Steady State Flights.....	185
5.2.2	Turbofan Engine Thrust Model	188
5.2.3	Iterative Equation Error Method.....	191
6	CONCLUSION	201

6.1	Iterative Equation Error Estimation Approach	201
6.2	Feature Selection Using Correlation-Based Binary Particle Swarm Optimization Approach.....	201
	REFERENCES	203
	CURRICULUM VITAE	215

LIST OF TABLES

TABLES

Table 2.1 Characteristics of the Sensor Models	31
Table 3.1 F-16 Aircraft Geometry and Mass Properties	42
Table 3.2 Aircraft Inertia Tensor in kg-m ²	42
Table 3.3 Flight Test Instrumentation Accuracy and Resolution.....	48
Table 3.4 Input, State, Observation, and Unknown Variables Vectors for Data Compatibility.....	51
Table 3.5 Maneuvers and Primary Unknown Variables for Data Compatibility....	52
Table 4.1 Input, State Variable, and Output Vectors and Unknown Variables for the Equation Error Method.....	63
Table 4.2 Input, State Variable, and Output Vectors and Unknown Variables in the Reduced Longitudinal Motion for the Output Error Method	70
Table 4.3 Input, State Variable, and Output Vectors and Unknown Variables in the Full Longitudinal Motion for the Output Error Method.....	72
Table 4.4 Input, State Variable, and Output Vectors and Unknown Variables in the Lateral Motion for the Output Error Method	75
Table 4.5 S-Shaped Family of Transfer Functions.....	85
Table 4.6 V-Shaped Family of Transfer Functions	86
Table 4.7 Different Transfer Functions	86
Table 4.8 Different Inertia Weight Update Strategies.....	87
Table 4.9 Different Acceleration Update Strategies.....	88
Table 4.10 Effective Aerodynamic Parameters in Proof-of-Match Maneuvers.....	94
Table 4.11 FAA Validation Tests and Tolerance Values	95
Table 4.12 Input, State Variable, and Output Vectors and Unknown Variables for the Iterative Equation Error Method.	103
Table 5.1 The Dropped Variables of <i>CY</i> model after Correlation Analysis.....	106
Table 5.2 The Remaining Variables of <i>CY</i> Model after Correlation Analysis.....	106
Table 5.3 The Optimized Variables of <i>CY</i> Model	107

Table 5.4 The Results of the Best 10 BPSO Configurations for <i>CY</i> Model	107
Table 5.5 The Optimal Subset of the Best 10 BPSO Configuration for <i>CY</i> Model	108
Table 5.6 The Number of Instances the Model Variables are Selected Using All BPSO Configurations for <i>CY</i> Model.....	109
Table 5.7 The Dropped Variables of <i>Cl</i> model after Correlation Analysis	109
Table 5.8 The Remaining Variables of <i>Cl</i> Model after Correlation Analysis	110
Table 5.9 The Optimized Variables of <i>Cl</i> Model.....	110
Table 5.10 The Results of the Best 10 BPSO Configurations for <i>Cl</i> Model	111
Table 5.11 The Optimal Subset of the Best 10 BPSO Configuration for <i>Cl</i> Model	111
Table 5.12 The Number of Instances the Model Variables are Selected Using All BPSO Configurations for <i>Cl</i> Coefficient	112
Table 5.13 The Dropped Variables of <i>Cn</i> model after Correlation Analysis	112
Table 5.14 The Remaining Variables of <i>Cn</i> Model after Correlation Analysis ...	113
Table 5.15 The Optimized Variables of <i>Cn</i> Model.....	113
Table 5.16 The Results of the Best 10 BPSO Configurations for <i>Cn</i> Model	114
Table 5.17 The Optimal Subset of the Best 10 BPSO Configuration for <i>Cn</i> Model	114
Table 5.18 The Number of Instances the Model Variables are Selected Using All BPSO Configurations for <i>Cn</i> Coefficient	115
Table 5.19 The Results of the Best 10 BPSO Configurations with respect to Fitness Scaling Sum (FSS) for Lateral/Directional Coefficients	116
Table 5.20 Correlation Analysis of BPSO Hyperparameters with respect to Fitness Scaling Sum for Lateral/Directional Coefficients.....	116
Table 5.21 Normalized Fitness Scaling Sum for Each Hyperparameter Selections	117
Table 5.22 The Estimates, Standard Deviations, and Relative Standard Deviations of the <i>CD</i> Coefficient Parameters.....	118

Table 5.23 The Estimates, Standard Deviations, and Relative Standard Deviations the <i>CL</i> Coefficient Parameters.....	122
Table 5.24 The Estimates, Standard Deviations, and Relative Standard Deviations the <i>Cm</i> Coefficient Parameters.....	125
Table 5.25 The Estimates, Standard Deviations, and Relative Standard Deviations the <i>CY</i> Coefficient Parameters.....	128
Table 5.26 The Estimates, Standard Deviations, and Relative Standard Deviations the <i>Cl</i> Coefficient Parameters.....	132
Table 5.27 The Estimates, Standard Deviations, and Relative Standard Deviations the <i>Cm</i> Coefficient Parameters.....	136
Table 5.28 Normalized Sensitivity Magnitudes (SM) for Longitudinal Coefficients in Longitudinal Maneuvers (Short-Period and Phugoid) (Most Influential Terms are Red-Colored).	143
Table 5.29 Normalized MSE values for lateral coefficients in dutch-roll and bank-to-bank maneuvers (most effective terms are red-colored).	146
Table 5.30 R^2 Values for Full and Reduced Models	147
Table 5.31 Tuned Longitudinal parameters with the OEM.....	150
Table 5.32 The Tuned Lateral Parameters with the OEM.....	153
Table 5.33 Tolerances for Phugoid Dynamics	161
Table 5.34 Theil's Inequality Coefficient (TIC) for Longitudinal Motion	167
Table 5.35 Theil's Inequality Coefficient (TIC) for Lateral/Directional Motion .	169
Table 5.36 Theil's Inequality Coefficient (TIC) for Longitudinal Motion	171
Table 5.37 Theil's Inequality Coefficient (TIC) for Combined Maneuvers	174
Table 5.38 Mean Squared Error Values with respect to Different Altitudes	188
Table 5.39 Drag Coefficient Parameter Estimates and Errors.....	192
Table 5.40 Drag Coefficient Parameter Estimates and Estimation Error – Continued	193
Table 5.41 Lift Coefficient Parameter Estimates and Errors	194
Table 5.42 Lift Coefficient Parameter Estimates and Errors	194

LIST OF FIGURES

FIGURES

Figure 1.1 Representation of Dynamic System in Time Domain	1
Figure 1.2 Aircraft Dynamics and Control	2
Figure 1.3 Quad-M Basics of Flight Vehicle System Identification	3
Figure 1.4 Aerodynamic Database Generation Methods with Examples	4
Figure 2.1 Aircraft Model	10
Figure 2.2 Axis Orientations	13
Figure 2.3 Generic Turbofan Engine Model Inputs and Outputs	25
Figure 2.4 Turbofan Engine Components	26
Figure 2.5 Turbofan Engine Simplified Thrust Model Block Diagram	27
Figure 2.6 Maximum Thrust Values at Different Mach Numbers and Altitudes ...	29
Figure 2.7 Major Types of Sensor Errors	30
Figure 2.8 Flowchart of the Linearization Process	33
Figure 2.9 Armijo Condition	38
Figure 3.1 Control Inputs for the Short Period, Phugoid, Dutch-Roll, and Bank-to-Bank Maneuvers	43
Figure 3.2 Flight Test Scope	43
Figure 4.1 Mathematical Model Required for the Equation Error and the Output Error Methods	59
Figure 4.2 Schematic of Data Preprocessing to Compute Aerodynamic Force and Moment Coefficients from Flight Measured Data	64
Figure 4.3 Flowchart of the Equation Error Method	65
Figure 4.4 Flowchart of the Output Error Method	69
Figure 4.5 Correlated-Based Binary Particle Swarm Optimization Flowchart	79
Figure 4.6 Search Mechanism of the PSO	82
Figure 4.7 Test and Training Error as a Function of Model Complexity	91
Figure 4.8. Model Analysis Engineering Flowchart	91

Figure 4.9. Resampling Methods. (a) Hold-out Cross-Validation (b) K-fold Cross-Validation	93
Figure 4.10 Geometry for Performance Calculation.	98
Figure 4.11 CD_0 Values for Different Gliding Flights.....	101
Figure 5.1 Training Dataset Results of CD Coefficient a) Time Histories of the Input Variables b) Time Histories of the Output variable	119
Figure 5.2 Residual Cross Plots and Cross Plot for CD in Training Dataset.	120
Figure 5.3 Testing Dataset Results of CD Coefficient a) Time Histories of the Input Variables b) Time Histories of the Output variable	121
Figure 5.4 Training Dataset Results of CL Coefficient a) Time Histories of the Input Variables b) Time Histories of the Output variable	123
Figure 5.5 Residual Cross Plots and Cross Plot for CL in Training Dataset.	124
Figure 5.6 Testing Dataset Results of CL Coefficient a) Time Histories of the Input Variables b) Time Histories of the Output variable	124
Figure 5.7 Training Dataset Results of Cm Coefficient a) Time Histories of the Input Variables b) Time Histories of the Output Variable	126
Figure 5.8 Residual Cross Plots and Cross Plot for Cm in Training Dataset.....	127
Figure 5.9 Testing Dataset Results of Cm Coefficient a) Time Histories of the Input Variables b) Time Histories of the Output Variable	127
Figure 5.10 Training Dataset Results of CY Coefficient for the Dutch Roll Motion a) Time Histories of the Input Variables b) Time Histories of the Output Variable.	129
Figure 5.11 Training Dataset Results of CY Coefficient for the Bank-To-Bank Motion a) Time Histories of the Input Variables b) Time Histories of the Output Variable	129
Figure 5.12 Residual Cross Plots and Cross Plot for CY in Training Dataset.....	130
Figure 5.13 Testing Dataset Results of CY Coefficient a) Time Histories of the Input Variables b) Time Histories of the Output variable	131
Figure 5.14 Dutch Roll Training Dataset Results of Cl Coefficient a) Time Histories of the Input Variables b) Time Histories of the Output Variable.....	133

Figure 5.15 Bank-To-Bank Training Dataset Results of Cl Coefficient a) Time Histories of the Input Variables b) Time Histories of the Output Variable	133
Figure 5.16 Residual Cross Plots and Cross Plot for Cl in Training Dataset	134
Figure 5.17 Testing Dataset Results of Cl Coefficient a) Time Histories of the Input Variables b) Time Histories of the Output variable	135
Figure 5.18 Dutch Roll Training Dataset Results of Cn Coefficient a) Time Histories of the Input Variables b) Time Histories of the Output Variable	136
Figure 5.19 Bank-To-Bank Training Dataset Results of Cn Coefficient a) Time Histories of the Input Variables b) Time Histories of the Output Variable	137
Figure 5.20 Residual Cross Plots and Cross Plot for Cn in Training Dataset	138
Figure 5.21 Testing Dataset Results of Cn Coefficient a) Time Histories of the Input Variables b) Time Histories of the Output Variable	138
Figure 5.22 Sensitivities of the CD parameters with a 1% change from their original value during longitudinal maneuvers.	139
Figure 5.23 Sensitivities of the CD parameters with a 1% change from their original value during lateral (dutch-roll) maneuver.	140
Figure 5.24 Sensitivities of the CL parameters with a 1% change from their original value during longitudinal maneuvers.	141
Figure 5.25 Sensitivities of the CL parameters with a 1% change from their original value during lateral (dutch-roll) maneuver.	141
Figure 5.26 Sensitivities of the Cm parameters with a 1% change from their original value during longitudinal maneuvers.	142
Figure 5.27 Sensitivities of the Cm parameters with a 1% change from their original value during lateral (dutch-roll) maneuver.	142
Figure 5.28 Sensitivities of the CY parameters with a 1% change from their original value during lateral (dutch-roll and bank-to-bank) maneuvers.....	144
Figure 5.29 Sensitivities of the CI parameters with a 1% change from their original value during lateral (dutch-roll and bank-to-bank) maneuvers.....	145

Figure 5.30 Sensitivities of the Cn parameters with a 1% change from their original value during lateral (dutch-roll and bank-to-bank) maneuvers.	146
Figure 5.31 Accuracy Spread of the Full Model for Longitudinal Coefficients. ..	147
Figure 5.32 Accuracy Spread of the Reduced Model for Longitudinal Coefficients.	148
Figure 5.33 Accuracy Spread of the Full Model for Lateral Coefficients.....	148
Figure 5.34 Accuracy Spread of the Reduced Model for Lateral Coefficients.	148
Figure 5.35 Reduced Longitudinal Model Output Comparison for Short-Period Maneuvers.	149
Figure 5.36 Full Longitudinal Model Output Comparison for Short-Period Maneuvers Keeping All Parameter Fixed.	150
Figure 5.37 The Full Longitudinal Model Output Comparison for Short-Period Maneuvers After Tuning $Cm\delta e$, $Cm\alpha$, $Cm\alpha_{101}$, and $Cm\delta lef$ Process.	151
Figure 5.38 The Lateral Model Output Comparison for Dutch-Roll Maneuvers Keeping All Parameters Fixed.....	152
Figure 5.39 The Lateral Model Output Comparison for Bank-To-Bank Maneuvers Keeping All Parameters Fixed.....	152
Figure 5.40 Full Lateral Model Output Comparison for Dutch-Roll Maneuvers After Tuning Lateral Parameters.	154
Figure 5.41 Full Lateral Model Output Comparison for Bank-To-Bank Maneuvers After Tuning Lateral Parameters.	154
Figure 5.42 Low-Speed Maneuvering Stability.	156
Figure 5.43 Mid Speed Maneuvering Stability.	156
Figure 5.44 High-Speed Maneuvering Stability.....	157
Figure 5.45 Longitudinal Static Stability.	158
Figure 5.46 Short Period Dynamics – at h = 10000 ft, CM = 0.35c and Ma = 0.35	159
Figure 5.47 Short Period Dynamics – at h = 10000 ft, CM = 0.35c and Ma = 0.50	159
Figure 5.48 Phugoid Dynamics – at h = 10000 ft, CM = 0.30c and Ma = 0.35....	160

Figure 5.49 Phugoid Dynamics – at $h = 10000$ ft, $CM = 0.30c$ and $Ma = 0.50$...	161
Figure 5.50 Dutch-Roll Dynamics – at $h = 10000$ ft, $CM = 0.35c$ and $Ma = 0.35$	162
Figure 5.51 Dutch-Roll Dynamics – at $h = 10000$ ft, $CM = 0.35c$ and $Ma = 0.50$	163
Figure 5.52 Bank-To-Bank Maneuver – at $h = 10000$ ft, $CM = 0.35c$ and $Ma = 0.35$	164
Figure 5.53 Bank-To-Bank Maneuver – at $h = 10000$ ft, $CM = 0.35c$ and $Ma = 0.50$	164
Figure 5.54 Bank-To-Bank Maneuver – at $h = 10000$ ft, $CM = 0.35c$ and $Ma = 0.35$ without any bias term on the initial conditions and control deflections	165
Figure 5.55 Longitudinal Dynamics – at $h = 10000$ ft, $CM = 0.30c$ and $Ma = 0.35$	166
Figure 5.56 Longitudinal Dynamics – at $h = 10000$ ft, $CM = 0.30c$ and $Ma = 0.50$	166
Figure 5.57 Lat/Dir Dynamics – at $h = 10000$ ft, $CM = 0.30c$ and $Ma = 0.35$	168
Figure 5.58 Lat/Dir Dynamics – at $h = 10000$ ft, $CM = 0.30c$ and $Ma = 0.50$	168
Figure 5.59 Short Period Dynamics – at $h = 10000$ ft, $CM = 0.30c$ and $Ma = 0.35$	170
Figure 5.60 Short Period Dynamics – at $h = 10000$ ft, $CM = 0.30c$ and $Ma = 0.50$	170
Figure 5.61 Combined Maneuvers – at $h = 10000$ ft, $CM = 0.30c$ and $Ma = 0.35$	172
Figure 5.62 Combined Maneuvers – at $h = 10000$ ft, $CM = 0.30c$ and $Ma = 0.50$	173
Figure 5.63 Short Period Dynamics – at $h = 10000$ ft, $CM = 0.30c$ and $Ma = 0.35$	175
Figure 5.64 Short Period Dynamics – at $h = 10000$ ft, $CM = 0.30c$ and $Ma = 0.50$	175
Figure 5.65 Dutch-Roll Dynamics – at $h = 10000$ ft, $CM = 0.30c$ and $Ma = 0.35$	176
Figure 5.66 Dutch-Roll Dynamics – at $h = 10000$ ft, $CM = 0.30c$ and $Ma = 0.50$	177

Figure 5.67 Bank-To-Bank Dynamics – at $h = 10000$ ft, $CM = 0.30c$ and $Ma = 0.35$	178
Figure 5.68 Bank-To-Bank Dynamics – at $h = 10000$ ft, $CM = 0.30c$ and $Ma = 0.50$	178
Figure 5.69 Example of a frequency sweep on longitudinal axis.....	179
Figure 5.70 Frequency Response Validation of $q\delta e$ – at $h = 10000$ ft, $CM = 0.30c$ and $Ma = 0.35$	180
Figure 5.71 Frequency Response Validation of $q\delta e$ – at $h = 10000$ ft, $CM = 0.30c$ and $Ma = 0.50$	180
Figure 5.72 Frequency Response Validation of $p\delta a$ – at $h = 10000$ ft, $CM = 0.30c$ and $Ma = 0.35$	181
Figure 5.73 Frequency Response Validation of $p\delta a$ – at $h = 10000$ ft, $CM = 0.30c$ and $Ma = 0.50$	181
Figure 5.74 Frequency Response Validation of $r\delta r$ – at $h = 10000$ ft, $CM = 0.30c$ and $Ma = 0.35$	182
Figure 5.75 Frequency Response Validation of $r\delta r$ – at $h = 10000$ ft, $CM = 0.30c$ and $Ma = 0.50$	182
Figure 5.76 Estimation Quality of Drag Coefficient	183
Figure 5.77 Estimation Quality of Lift coefficient	184
Figure 5.78 Estimation Quality of Pitch Moment Coefficient	184
Figure 5.79 Measured and Constructed Thrust, Lift Coefficient, and Drag Coefficient in Steady Level Flight	186
Figure 5.80 Measured and Constructed Thrust, Lift Coefficient, and Drag Coefficient in Steady Climb Flight.....	187
Figure 5.81 Measured and Constructed Thrust Coefficient at $h = 0$ ft	189
Figure 5.82 Measured and Constructed Thrust Coefficient at $h = 5000$ ft.....	189
Figure 5.83 Measured and Constructed Thrust Coefficient at $h = 10000$ ft	190
Figure 5.84 Measured and Constructed Thrust Coefficient at $h = 20000$ ft	190
Figure 5.85 Measured and Constructed Thrust Coefficient at $h = 30000$ ft	191

Figure 5.86 Convergence of Cost Function for Iterative Equation Error Method	192
Figure 5.87 Converge of Parameter Estimates for the Drag Coefficient	193
Figure 5.88 Converge of Parameter Estimates for Lift Coefficient	195
Figure 5.89 Estimation Quality of Drag Coefficient Where Wind Tunnel Data is Compared with Iterative EEM Method (First Iteration)	196
Figure 5.90 Estimation Quality of Drag Coefficient Where Wind Tunnel Data is Compared with Iterative EEM Method (Last Iteration)	197
Figure 5.91 Estimation Quality of Drag Coefficient Where Wind Tunnel Data is Compared with EEM Method (Actual Thrust)	197
Figure 5.92 Estimation Quality of Lift Coefficient Where Wind Tunnel Data is Compared with Iterative EEM Method (First Iteration)	198
Figure 5.93 Estimation Quality of Lift Coefficient Where Wind Tunnel Data is Compared with Iterative Eem Method (Last Iteration).....	199
Figure 5.94 Estimation Quality of Lift Coefficient Where Wind Tunnel Data is Compared with EEM Method (Actual Thrust)	200

LIST OF ABBREVIATIONS

ABBREVIATIONS

CM	Center of Mass
NR	Newton-Raphson
LSNR	Line Search Newton-Raphson
EOM	Equations of Motion
EEM	Equation Error Method
OEM	Output Error Method
SA	Sensitivity Analysis
FS	Feature Selection

LIST OF SYMBOLS

SYMBOLS

\mathcal{F}_B	body-fixed frame
\mathcal{F}_N	local navigation frame
$s(\cdot)$	shorthand notations for $\sin(\cdot)$
$c(\cdot)$	shorthand notations for $\cos(\cdot)$
$t(\cdot)$	shorthand notations for $\tan(\cdot)$
α	angle of attack
β	angle of sideslip
V_{TAS}	true airspeed
X, Y, Z	longitudinal, lateral, and vertical forces in \mathcal{F}_B
D, C, L	drag, crosswind, and lift forces in \mathcal{F}_W
l, m, n	roll, pitch, and yaw moments in \mathcal{F}_B
T	thrust force
C_T	nondimensional thrust coefficient
C_D	drag coefficient
C_C	crosswind coefficient
C_L	lift coefficient
C_l	roll moment coefficient
C_m	pitch moment coefficient
C_n	yaw moment coefficient

m	mass of the air vehicle
\vec{g}	acceleration due to gravity
\bar{q}	dynamic pressure
u, v, w	total x -, y -, and z - body axis velocity components
Φ, θ, ψ	Euler roll, pitch, and yaw angles of \mathcal{F}_B
p, q, r	roll, pitch, and yaw rates
$\dot{p}, \dot{q}, \dot{r}$	roll, pitch, and yaw accelerations
p_N, p_E, p_D	x -, y -, and z - axis position vector components of CM w.r.t. \mathcal{F}_N
h	altitude
γ, χ	Velocity-vector flight path angle and heading angle
δ_e	elevator deflection
δ_a	aileron deflection
δ_r	rudder deflection
δ_{th}	throttle setting
\vec{f}	The vector sum of all external forces
\vec{m}_B	The vector sum of all external moments referred to the vehicle CM (point B)
\vec{m}_P	The vector sum of all external moments referred to the arbitrary point P
\check{I}_B^B	Inertia matrix
\vec{a}_s	specific acceleration vector

CHAPTER 1

INTRODUCTION

1.1 System Identification

Developing mathematical models for physical systems based on imperfect observations or measurements is one of the oldest and most fundamental scientific endeavors. This procedure is referred to as system identification [1].

The system identification is linked to other problems in dynamics. The inputs u , the outputs z or y , and the system model functions f and g are three quantities representing a dynamic system described in state space, see Figure 1.1 [1].

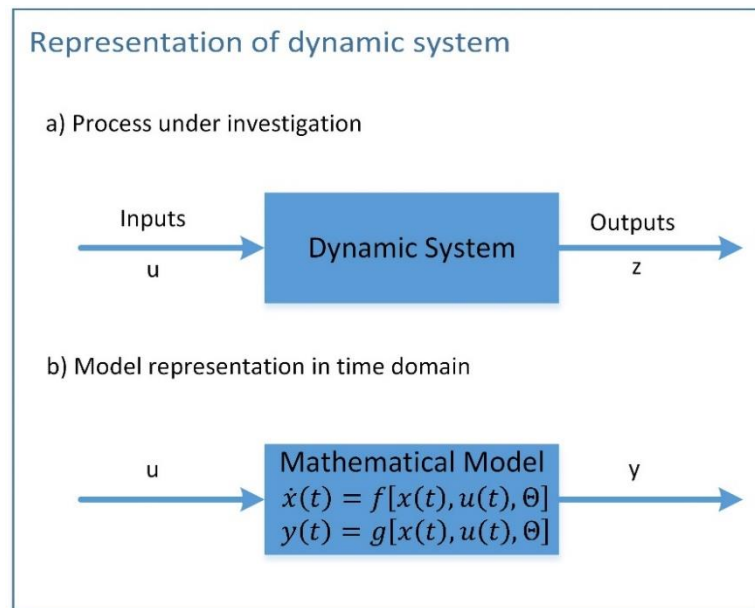


Figure 1.1 Representation of Dynamic System in Time Domain

The identification problem attempts to determine the system model f and g based on the given inputs u and outputs z .

Although the state variables x are not directly specified in the preceding description, they are implicitly mentioned since the outputs are functions of internal system state variables. Similarly, the system functions f and g contain unknown parameters $\vec{\Theta}$.

The process of establishing an appropriate mathematical model, usually containing differential equations, with unknown parameters that must be derived indirectly from observed data is known as system identification. System identification is one of the three general problems in aircraft dynamics and control, which can be understood in Figure 1.2 (duplicated from Ref. [2]).



Figure 1.2 Aircraft Dynamics and Control

Several critical elements of system identification include the following:

- Accessibility to input and output data,
- Asserting plausible models (i.e., class of systems),
- Selecting the most appropriate model from the given class (i.e., equivalency).

$$C_m = C_m(M, \alpha, \beta, p, q, r, \delta_e, \delta_a, \delta_r \dots) \quad (1.1)$$

which can be expanded as:

$$C_m = \frac{\partial C_m}{\partial \alpha} \alpha + \dots + \frac{\partial C_m}{\partial q} q + \dots + \frac{\partial C_m}{\partial \delta_e} \delta_e + \dots \quad (1.2)$$

The stability and control derivatives are the partial derivatives with regard to the motion variables and control inputs in the Taylor series expansion.

1.2 Modern Methods of Aircraft Parameter Estimation

Figure 1.3 depicts the four essential components of flight vehicle system identification: maneuver, measurements, methods, and models [1].

- 1) The design of the control input form to stimulate various flying modes of the flight vehicle motion.
- 2) The selection of instruments and filters.
- 3) The selection of the most appropriate identification approach.
- 4) Defining the structure of a possible mathematical model.

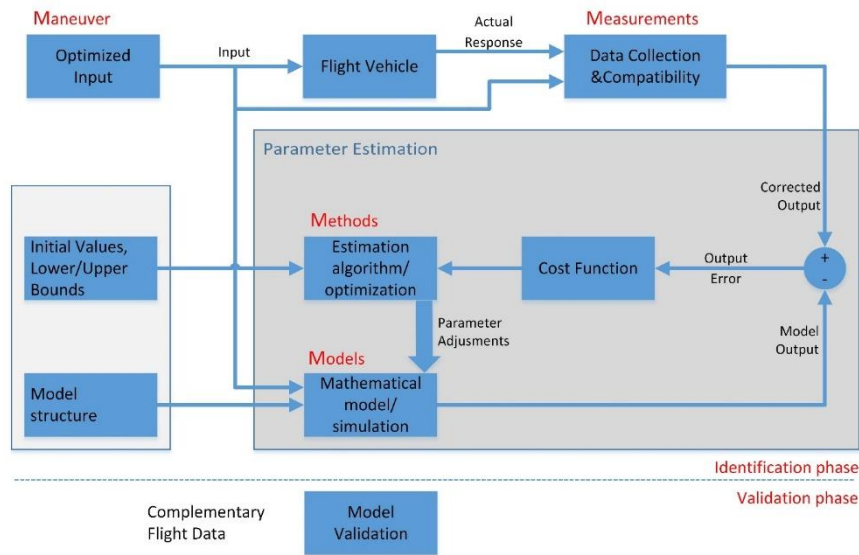


Figure 1.3 Quad-M Basics of Flight Vehicle System Identification

1.3 The Motivation for System Identification

Aircraft flight simulation is used extensively in modern aircraft design, certification, and pilot training. The fidelity of the aerodynamic dataset has an impact on how closely the aircraft in flight simulation matches the actual aircraft. The aerodynamic model is the core of a flight simulator. Inaccuracies in the aerodynamic model may result in a simulation failing in the qualification process [3]. Therefore, high-fidelity aerodynamic datasets are required to provide an accurate actual aircraft behavior to

the pilots. The aerodynamic dataset is obtained in a variety of ways. In increasing order of fidelity, these include semi-empirical datasheet methods, linear flow solvers, nonlinear flow solvers, small-scale wind tunnel tests, full-scale wind tunnel tests, and flight tests. The processing time and cost increase as fidelity increases.

Several computational and experimental approaches can be utilized to generate the aerodynamic database, depending on the cost and accuracy requirements of the design phase. References [4] [5].summarize these approaches and provide sample tools and classifications. As expected, the higher the cost of the aerodynamic database, the more accurate it is. The resource and time costs associated with each approach are often tens to hundreds of times more than those associated with the less accurate approach [6], as shown in Figure 1.4.

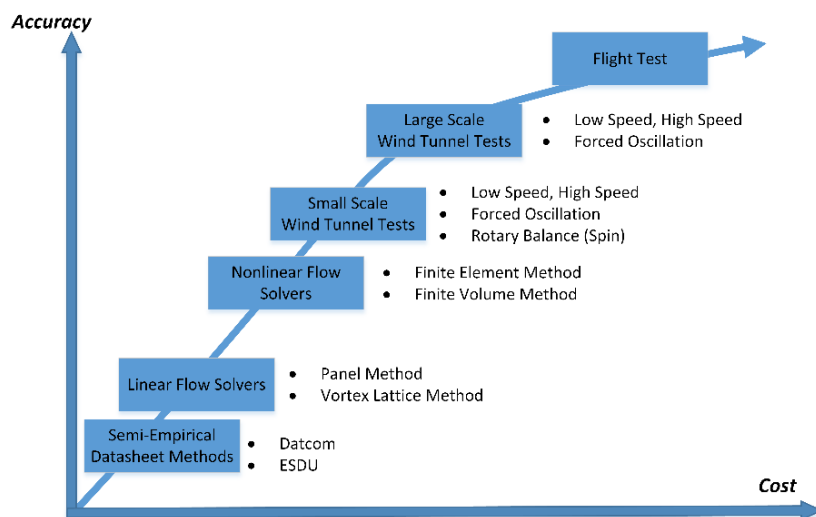


Figure 1.4 Aerodynamic Database Generation Methods with Examples

The semi-empirical approach is based on generalized and formalized experimental results. Datcom and ESDU are two well-known examples of this approach. As compared to other approaches, the computational effort is considerably decreased. A comprehensive aerodynamic dataset can be obtained in a matter of minutes. They do not require the generation of a computational grid.

Linear flow solvers are based on the principle of potential flow. This approach is exemplified by the panel and vortex lattice methods (VLM). They may contain corrections for the compressibility, boundary layer, dynamic motions, and nonlinear flow characteristics. They require computational grids; however, the grids are substantially smaller than those used by nonlinear flow solvers. VSAero, Panair, Tranair, and AVL are typical examples of panel and vortex lattice methods. While the linear flow regimes can be computed more precisely than the semi-empirical approach, the accuracy diminishes dramatically as the flow becomes non-linear [4]. Semi-empirical methods and linear flow solvers are commonly utilized in the conceptual design phase.

Nonlinear flow solvers attempt to define all conservation equations, including those for continuity, momentum, and energy equations, and deal with a variety of turbulence models, compressibility, and boundary layer-related issues. The nonlinear flow solvers consider the finite volume and finite element methods. Ansys-Fluent, Star-CCM+, Open Foam, CFL3D, and SU2 are well-known nonlinear flow solvers. This approach has been investigated in detail within a low angle of attack sweeps (linear region) in the subsonic-supersonic regions. Nonetheless, the results in the transonic region, including shock-induced separations and at a high angle of attack sweeps (nonlinear part), differ from the actual aerodynamic data due to volatile flow characteristics. It is challenging to determine dynamic effects, including forced oscillations and spin conditions, using these solvers. They demand more computational power than linear flow solvers due to the additional processing and computations [4].

In wind tunnel tests, based on scale similarity, the aerodynamic database is developed through experiments. A wind tunnel test model should be designed and manufactured to conduct these experiments, which is a substantially more expensive approach when compared to the computational approaches. However, wind tunnel tests are required to resolve highly unsteady flight conditions. In small-scale wind tunnels, scaling issues such as Reynolds number, aeroelastic characteristics, and so on exist so that a full-scale wind tunnel is preferred [7]. Supersonic aerodynamics,

forced oscillation, and spin characteristics can be obtained in small-scale wind tunnels while taking off-landing features are accurately observed in large-scale wind tunnels. Forced oscillation and high-speed tests can also be conducted in large-scale wind tunnels. Indeed, there is some deviation from actual aerodynamic data because of Reynolds correction, the experimental system errors, the effect of wind tunnel airflow quality, the interference of tunnel walls/supports, and other factors [6].

Flight tests are the final option for eliminating the errors in wind tunnel tests. The aerodynamic database can be developed from flight test data using comprehensive system identification methods [8] [9] [10] [11] [12] [13]. Aerodynamic data should be validated with flight tests prior to further aircraft development.

1.4 Literature Review

The field of system identification is vast and encompasses a broad range of topics. The primary objective of system identification is to establish the mathematical model structure that best reflects the dynamic system, which is not unique. Numerous model postulates may need to be examined. The parameters of a given model have been quantitatively quantified, often via statistical procedures. This process in the entire model development phase is referred to as parameter estimation [1]. Parameter estimation is described as a function that quantifies the difference between measured system and predicted model responses. The time domain and frequency domain techniques of system identification are summarized by Jategaonkar [1], Klein and Morelli [2], and Tischler and Remple [14]. Jategaonkar [1] discusses time-domain applications, while Tischler and Remple [14] and Morelli, Grauer, and Cooper [15] [16] discuss frequency-domain approaches, an overview and theoretical basis for each of the approaches mentioned above are provided in Morelli and Klein [2]. System identification in time and frequency domains are considered as competing methods. Both have advantages and disadvantages that are mutually beneficial [17] [18]. The time-domain is more intuitive since it refers to space where mathematical

functions are expressed in terms of time. Moreover, the parameters of a particular model have a physical meaning in the time domain [17] [18].

Numerous methods are available for system identification in the time-domain, including the equation-error method [1] [2] [6] [13] [19] [20] [21] [22], the output error method [1] [2] [13], the filter error method [1] [23] and the artificial neural network [6] [24] [25] [26] [27]. These methods are interchangeable [1] [9] [13] [28]. In this doctoral study, the equation-error and output-error methods are employed successively, e.g., the equation error method can be employed initially to determine the aerodynamic parameters. The acquired results are then used as the starting point for the output error method for fine-tuning. The equation-error and output-error estimation approaches can be distinguished from each other. Without knowledge of their history, non-state parameters such as non-dimensional force and moment coefficients are determined without knowing their history. This procedure is referred to as the equation-error method [1] [2] [29] [30]. The outputs of the system, such as the angle of attack, angular rates, etc., are integrated throughout the simulation, and therefore estimation technique is referred to as the output-error method [1] [2] [29] [30]. The predicted parameters of the output error technique converge mostly towards the truth ones. Nonetheless, this technique is extremely susceptible to non-convergent solutions in agile aircraft. A combined equation/output error is recommended to address this issue [29].

Selecting independent variables in the equation error method is often a problematic issue. There are many approaches for selecting regression models, and the first one is the expert-based selection. The statistical criteria and flight mechanic intuition are used to select model terms [12] [13] [31]. However, it requires extensive knowledge of Flight Mechanics. Subset selection is the second approach, which divides into two parts: best subset selection and stepwise selection [1] [2] [32]. The best subset selection entails choosing the optimal model from among all possible models. When there is a large number of predictors, the best subset selection suffers computationally [32] [33]. Due to computational constraints, the best subset selection cannot be applied with a vast predictor number. The stepwise methods,

which examine a much smaller set of models than the best subset selection, are appealing alternatives. The stepwise selection may be classified into three types: forward stepwise selection, backward stepwise selection, and hybrid selection. The stepwise approach is a kind of local search, and its main disadvantage is that it eventually converges to local optima [32]. In this doctorate study, the binary Particle Swarm Optimization is considered to identify the most related independent variables in the equation error method, which forms the contribution of the thesis.

In the first phase, the equation-error method is used firstly to identify aerodynamic parameters in the expert-based selection. The obtained results in the first phase are used as a starting point in the output-error process for fine-tuning, concerning FAA specified guidelines regarding tolerances on each variable for some maneuvers.

In chapter 2, aircraft modeling and trim are discussed. In chapter 3, data gathering is briefly covered. The methodology is presented in chapter 4. In chapter 5, the results are presented, and in chapter 6, the contributions are mentioned.

CHAPTER 2

AIRCRAFT MODELING AND TRIM

2.1 Air Vehicle Flight Simulation Model

The general equations of motion of a system of rigid bodies are described in many well-known textbooks, articles, and reports. Stevens, et.al. [34], Zipfel [35], Cook [36], Allerton [37], Etkin and Reid [38], Stengel [39], Raol and Singh [40], and Schmidt [41] are some examples. This section provides a cohesive framework for the definition of different coordinate systems, conventions, and associated equations derived under these definitions. The air-vehicle flight simulation model is based on [42] [43] [44].

Air-vehicle flight in 6 Degrees of Freedom (6-DoF) comprises three translational and three rotational motions along and about the three axes of its reference frame, respectively. The coordinate system associated with the body-fixed reference frame is often utilized to resolve the air vehicle's equations of motion. All forces and moments acting on the aircraft are transformed into the body coordinates. It is common to utilize the body reference frame as the resolution frame. Furthermore, the wind frame can be selected for model-based analyses. The wind frame is utilized as the resolution frame for the equations of motion in this research. Finally, based on the variable states, a set of equations including translational and rotational motions and kinematic relations is produced.

The equations of motion, aerodynamics, propulsion, weight and balance, landing gear, atmosphere, flight control system, actuator, and sensor models are all utilized to simulate an air vehicle in flight. Figure 2.1 is an example flow diagram. The objective of the equation of motion for flight dynamics is to provide adequate information on the motion of the air vehicle, in particular, the states of the air vehicle.

The other subsystem models are used to generate air-vehicle data for the EOM model.

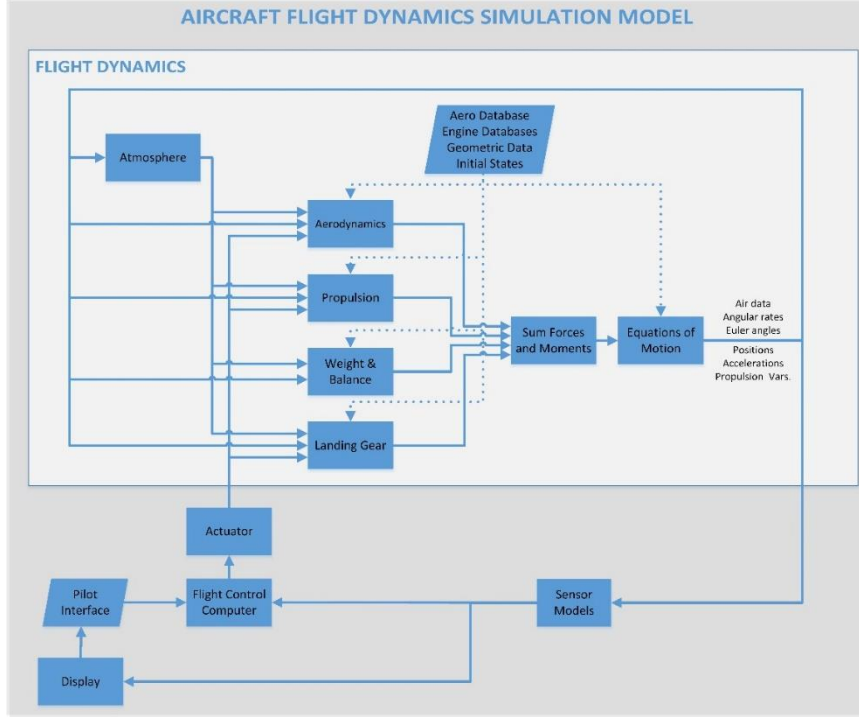


Figure 2.1 Aircraft Model

2.1.1 Definition of Reference Systems

Five frames must be introduced to model the motion of a rigid body air vehicle; These are described as follows:

Local Geodetic North-East-Down frame, $\mathcal{F}_N\{N; x_N y_N z_N\}$, with origin N, and with Nz_N axis directed vertically down along the local normal at the surface. $Nx_N y_N$ is the local horizontal plane, Nx_N axis points toward the north, and Nx_N axis points toward the east. This frame is used for navigation purposes and is often named the local navigation frame, which is the reason for using N to denote this frame [34] [38] [45].

Vehicle body-fixed frame, $\mathcal{F}_B\{B; x_B y_B z_B\}$ with origin B, instantaneous CM of the air vehicle. Bx_B axis is called the roll axis and points towards the nose of the air

vehicle, By_B is called the pitch axis and directed to the right when viewed from the rear, and Bz_B is called the yaw axis and points towards the fuselage belly.

Wind frame, $\mathcal{F}_W\{W; x_W y_W z_W\}$ with origin W, instantaneous CM of the air vehicle. Wx_W axis points towards the local air velocity vector, Bz_W points towards the symmetry plane of the air vehicle, and Wy_W forms a right-handed coordinate system.

Velocity frame, $\mathcal{F}_V\{V; x_V y_V z_V\}$, with origin V, is an additional frame (also known as flight path frame). Two angles γ and χ denote the instantaneous angular orientation of velocity coordinates with respect to local NED coordinates.

Propulsion frame, $\mathcal{F}_P\{P; x_P y_P z_P\}$, with the thrust application point P.

2.1.2 Nonlinear Equations of Motion

2.1.2.1 Force Equations

The generalized equations of motion (EOM) of an air vehicle can be expressed using the principles of Newton's Second Law for translational motion and Euler's Law for rotational movement. For conventional air vehicles, the body can be assumed to be rigid, symmetric about the XY-plane, and with all forces and moments acting about the center of mass. The translational motion for stationary, flat Earth is defined in tensor form as

$$\vec{a}_{B/N}^N = \mathcal{D}^N \vec{v}_{B/N}^N = \mathcal{D}^B \vec{v}_{B/N}^N + \vec{\omega}^{B/N} \times \vec{v}_{B/N}^N = \frac{1}{m} \vec{f} \quad (2.1)$$

Resolution of vector components in body coordinates are given as

$$\begin{aligned} \{\mathcal{D}^B \vec{v}_{B/N}^N\}^{(B)} &= \begin{bmatrix} \dot{u} \\ \dot{v} \\ \dot{w} \end{bmatrix}, & \{\vec{f}\}^{(B)} &= \begin{bmatrix} f_x \\ f_y \\ f_z \end{bmatrix}, & \{\vec{v}_{B/N}^N\}^{(B)} &= \begin{bmatrix} u \\ v \\ w \end{bmatrix}, \\ \{\vec{\omega}^{B/N}\}^{(B)} &= \begin{bmatrix} p \\ q \\ r \end{bmatrix} \end{aligned} \quad (2.2)$$

Ordinary differential equations of translational motion, obtained in coordinate-dependent component form in body coordinates and the body-axes accelerations, expanded out for each component, are given by

$$\begin{aligned} \begin{bmatrix} \dot{u} \\ \dot{v} \\ \dot{w} \end{bmatrix} &= \frac{1}{m} \begin{bmatrix} f_x \\ f_y \\ f_z \end{bmatrix} - \begin{bmatrix} p \\ q \\ r \end{bmatrix} \times \begin{bmatrix} u \\ v \\ w \end{bmatrix} \\ \dot{u} &= f_x/m - qw + rv \\ \dot{v} &= f_y/m - ru + pw \\ \dot{w} &= f_z/m - pv + qu \end{aligned} \quad (2.3)$$

When no specific landing gear contact forces are present, the accepted formulation for the resulting force is as follows:

$$\vec{f} = \vec{f}_a + \vec{f}_p + \vec{f}_g \quad (2.4)$$

where \vec{f}_a , \vec{f}_p and \vec{f}_g are the resultant forces due to aerodynamics, propulsion, and thrust, respectively.

The velocity of vehicle CM w.r.t. Earth $\vec{v}_{B/N}^N$ is expressed in terms of $\vec{v}_{B/W}^N$ (velocity of the CM w.r.t. the air mass) and $\vec{v}_{W/N}^N$ (velocity of the wind w.r.t. Earth) as

$$\vec{v}_{B/N}^N = \vec{v}_{B/W}^N + \vec{v}_{W/N}^N \quad (2.5)$$

so that $\vec{v}_{B/N}^N$ and $\vec{v}_{B/W}^N$ represent the same vector when omitting wind (i.e., when $\vec{v}_{W/N}^N = \vec{0}$).

Figure 2.2 illustrates the orientation of the wind coordinates in relation to the body coordinates. Note that wind has been omitted ($\vec{v}_{W/N}^N \equiv \vec{0}$ with $\vec{v}_{B/N}^N \equiv \vec{v}_{B/W}^N$), purely for ease of illustration of the aerodynamic wind angles α and β .

Using the definitions for the body-axes components of $\vec{v}_{B/N}^N$ and $\vec{v}_{W/N}^N$, together with the wind-axis component of $\vec{v}_{B/W}^N$ (the true airspeed, denoted by V_{TAS}), described by

$$\{\vec{v}_{B/N}^N\}^{(B)} = \begin{bmatrix} u \\ v \\ w \end{bmatrix}, \quad \{\vec{v}_{W/N}^N\}^{(B)} = \begin{bmatrix} u_W \\ v_W \\ w_W \end{bmatrix}, \quad \{\vec{v}_{B/W}^N\}^{(W)} = \begin{bmatrix} V_{TAS} \\ 0 \\ 0 \end{bmatrix} \quad (2.6)$$

the expression for true airspeed (TAS) relative to undisturbed air, V_{TAS} , which is defined as the magnitude of the velocity vector $\vec{v}_{B/W}^E$ of the CM w.r.t. the air mass, is obtained from

$$V_{TAS} = |\vec{v}_{B/W}^N| = \sqrt{\vec{v}_{B/W}^N \cdot \vec{v}_{B/W}^N}, \quad \vec{v}_{B/W}^N = \vec{v}_{B/N}^N - \vec{v}_{W/N}^N \quad (2.7)$$

so that the substitution gives

$$V_{TAS} = \sqrt{(u - u_W)^2 + (v - v_W)^2 + (w - w_W)^2} \quad (2.8)$$

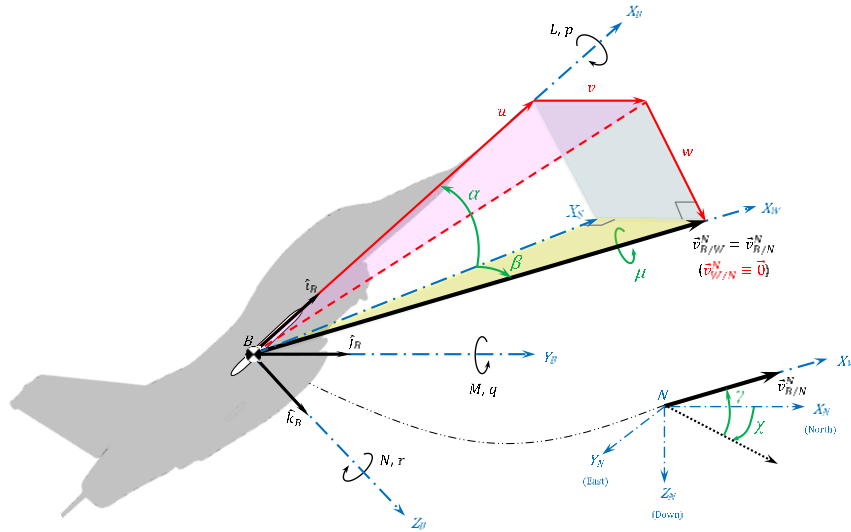


Figure 2.2 Axis Orientations

The transformation matrix from body fixed to wind axis, in terms of the combination of the transformation matrices from body-fixed to stability and stability to wind axes, is given as

$$\begin{aligned}
\check{T}^{(W,B)} &= \check{T}^{(W,S)} \check{T}^{(S,B)} \\
&= \begin{bmatrix} \cos \alpha & 0 & \sin \alpha \\ 0 & 1 & 0 \\ \sin \alpha & 0 & \cos \alpha \end{bmatrix} \begin{bmatrix} \cos \beta & \sin \beta & 0 \\ -\sin \beta & \cos \beta & 0 \\ 0 & 0 & 1 \end{bmatrix} \\
&= \begin{bmatrix} \cos \alpha \cos \beta & \sin \beta & \sin \alpha \cos \beta \\ -\cos \alpha \sin \beta & \cos \beta & -\sin \alpha \sin \beta \\ -\sin \alpha & 0 & \cos \alpha \end{bmatrix}
\end{aligned} \tag{2.9}$$

Using $s_{(\cdot)}$ and $c_{(\cdot)}$ as shorthand notations for $\sin(\cdot)$ and $\cos(\cdot)$ respectively, we get

$$\check{T}^{(W,B)} = \check{T}^{(W,B)} = \begin{bmatrix} c_\alpha c_\beta & s_\beta & s_\alpha c_\beta \\ -c_\alpha s_\beta & c_\beta & -s_\alpha s_\beta \\ -s_\alpha & 0 & c_\alpha \end{bmatrix} \tag{2.10}$$

The definitions for Cartesian incidence (wind) angles in the presence of wind are derived from the relation

$$[\check{T}^{(W,B)}]^T \{\vec{v}_{B/W}^E\}^{(W)} = \{\vec{v}_{B/N}^N\}^{(B)} - \{\vec{v}_{W/N}^N\}^{(B)} \tag{2.11}$$

expanding [Eq. (2.11)] in component form

$$\begin{bmatrix} c_\alpha c_\beta & s_\beta & s_\alpha c_\beta \\ -c_\alpha s_\beta & c_\beta & -s_\alpha s_\beta \\ -s_\alpha & 0 & c_\alpha \end{bmatrix}^T \begin{bmatrix} V_{TAS} \\ 0 \\ 0 \end{bmatrix} = \begin{bmatrix} u \\ v \\ w \end{bmatrix} - \begin{bmatrix} u_W \\ v_W \\ w_W \end{bmatrix} \tag{2.12}$$

obtaining the following trigonometric relationships for the angle of attack α and true sideslip angle β , respectively:

$$\alpha = \arctan_2[w - w_W \quad , \quad u - u_W], \quad -\pi < \alpha \leq \pi \tag{2.13}$$

$$\begin{aligned}
\beta &= \arcsin\left(\frac{v - v_W}{V_{TAS}}\right) = \arctan\left(\frac{v - v_W}{\sqrt{(u - u_W)^2 + (w - w_W)^2}}\right), \\
-\frac{\pi}{2} &< \beta < \frac{\pi}{2}
\end{aligned} \tag{2.14}$$

2.1.2.2 Moment Equations

The equations for rotational motion are represented in tensor form as

$$\begin{aligned}
\sum \vec{m}_B &= \mathcal{D}^N \vec{l}_B^{B/N} = \mathcal{D}^B \vec{l}_B^{B/N} + \vec{\omega}^{B/N} \times \vec{l}_B^{B/N}, \quad \vec{l}_B^{B/N} = \vec{I}_B^B \vec{\omega}^{B/N} \\
\sum \vec{m}_B &= \mathcal{D}^B (\vec{I}_B^B \vec{\omega}^{B/N}) + (\vec{\omega}^{B/N} \times \vec{I}_B^B \vec{\omega}^{B/N}) \\
&\approx \vec{I}_B^B (\mathcal{D}^B \vec{\omega}^{B/N}) + (\vec{\omega}^{B/N} \times \vec{I}_B^B \vec{\omega}^{B/N})
\end{aligned} \tag{2.15}$$

Where the components in body coordinates are

$$\begin{aligned}
\{\mathcal{D}^B \vec{\omega}^{B/N}\}^{(B)} &= \begin{bmatrix} \dot{p} \\ \dot{q} \\ \dot{r} \end{bmatrix}, \quad \{\vec{m}_B\}^{(B)} = \begin{bmatrix} l \\ m \\ n \end{bmatrix}, \\
\{\vec{\omega}^{B/N}\}^{(B)} &= \begin{bmatrix} p \\ q \\ r \end{bmatrix}, \quad \{\vec{I}_B^B\}^{(B)} = \begin{bmatrix} I_{XX} & -I_{XY} & -I_{XZ} \\ -I_{XY} & I_{YY} & -I_{YZ} \\ -I_{XZ} & -I_{YZ} & I_{ZZ} \end{bmatrix}
\end{aligned} \tag{2.16}$$

The coordinate-dependent component form in body coordinates as,

$$\begin{aligned}
&\{\mathcal{D}^B \vec{\omega}^{B/N}\}^{(B)} \\
&= [\{\vec{I}_B^B(t)\}^{(B)}]^{-1} \{ \{\vec{m}_B\}^{(B)} - \{\vec{\omega}^{B/N}\}^{(B)} \times \{\vec{I}_B^B(t)\}^{(B)} \{\vec{\omega}^{B/N}\}^{(B)} \}
\end{aligned} \tag{2.17}$$

Expanding Eq.(2.17) in component form

$$\begin{aligned}
\begin{bmatrix} \dot{p} \\ \dot{q} \\ \dot{r} \end{bmatrix} &= \begin{bmatrix} I_{XX} & -I_{XY} & -I_{XZ} \\ -I_{XY} & I_{YY} & -I_{YZ} \\ -I_{XZ} & -I_{YZ} & I_{ZZ} \end{bmatrix}^{-1} \left\{ \begin{bmatrix} l \\ m \\ n \end{bmatrix} \right. \\
&\quad \left. - \begin{bmatrix} p \\ q \\ r \end{bmatrix} \times \begin{bmatrix} I_{XX} & -I_{XY} & -I_{XZ} \\ -I_{XY} & I_{YY} & -I_{YZ} \\ -I_{XZ} & -I_{YZ} & I_{ZZ} \end{bmatrix} \begin{bmatrix} p \\ q \\ r \end{bmatrix} \right\}
\end{aligned} \tag{2.18}$$

Assuming further that the airplane has symmetry about the xz plane, then we have

$I_{XY} = I_{YZ} = 0$. Equation (2.18) now simplifies to

$$\begin{bmatrix} \dot{p} \\ \dot{q} \\ \dot{r} \end{bmatrix} = \begin{bmatrix} I_{XX} & 0 & -I_{XZ} \\ 0 & I_{YY} & 0 \\ -I_{XZ} & 0 & I_{ZZ} \end{bmatrix}^{-1} \left\{ \begin{bmatrix} l \\ m \\ n \end{bmatrix} - \begin{bmatrix} p \\ q \\ r \end{bmatrix} \times \begin{bmatrix} I_{XX} & 0 & -I_{XZ} \\ 0 & I_{YY} & 0 \\ -I_{XZ} & 0 & I_{ZZ} \end{bmatrix} \begin{bmatrix} p \\ q \\ r \end{bmatrix} \right\} \tag{2.19}$$

The inverse of inertia tensor is found as

$$\begin{bmatrix} I_{XX} & 0 & -I_{XZ} \\ 0 & I_{YY} & 0 \\ -I_{XZ} & 0 & I_{ZZ} \end{bmatrix}^{-1} = \frac{1}{\Gamma} \begin{bmatrix} I_{ZZ} & 0 & I_{XZ} \\ 0 & \Gamma/I_{YY} & 0 \\ I_{XZ} & 0 & I_{XX} \end{bmatrix} \tag{2.20}$$

where $\Gamma = I_{XX}I_{ZZ} - I_{XZ}^2$

Expanding out each component in Eq.(2.19), the body-axes angular accelerations are given by

$$\begin{aligned}\dot{p} &= \frac{I_{XZ}(I_{XX} - I_{YY} + I_{ZZ})pq - (I_{ZZ}^2 - I_{YY}I_{ZZ} + I_{XZ}^2)qr + I_{ZZ}l + I_{XZ}n}{I_{XX}I_{ZZ} - I_{XZ}^2} \\ \dot{q} &= \frac{(I_{ZZ} - I_{XX})pr - I_{XZ}(p^2 - r^2) + m}{I_{YY}} \\ \dot{r} &= \frac{(I_{XX}^2 - I_{XX}I_{YY} + I_{XZ}^2)pq - I_{XZ}(I_{XX} - I_{YY} + I_{ZZ})qr + I_{XZ}l + I_{XX}n}{I_{XX}I_{ZZ} - I_{XZ}^2}\end{aligned}\quad (2.21)$$

2.1.2.3 Kinematic Equations

The angular velocities in the navigation frame in body-axes are defined as

$$\begin{aligned}\begin{bmatrix} p \\ q \\ r \end{bmatrix} &= \begin{bmatrix} \dot{\phi} \\ 0 \\ 0 \end{bmatrix} + \begin{bmatrix} 1 & 0 & 0 \\ 0 & \cos \phi & \sin \phi \\ 0 & -\sin \phi & \cos \phi \end{bmatrix} \begin{bmatrix} 0 \\ \dot{\theta} \\ 0 \end{bmatrix} \\ &+ \begin{bmatrix} 1 & 0 & 0 \\ 0 & \cos \phi & \sin \phi \\ 0 & -\sin \phi & \cos \phi \end{bmatrix} \begin{bmatrix} \cos \theta & 0 & -\sin \theta \\ 0 & 1 & 0 \\ \sin \theta & 0 & \cos \theta \end{bmatrix} \begin{bmatrix} 0 \\ 0 \\ \dot{\psi} \end{bmatrix} \\ \begin{bmatrix} p \\ q \\ r \end{bmatrix} &= \begin{bmatrix} 1 & 0 & -\sin \theta \\ 0 & \cos \phi & \sin \phi \cos \theta \\ 0 & -\sin \phi & \cos \phi \cos \theta \end{bmatrix} \begin{bmatrix} \dot{\phi} \\ \dot{\theta} \\ \dot{\psi} \end{bmatrix}\end{aligned}\quad (2.22)$$

Taking the inverse, Euler-angle rates are governed by the following expressions

$$\begin{bmatrix} \dot{\phi} \\ \dot{\theta} \\ \dot{\psi} \end{bmatrix} = \begin{bmatrix} 1 & \sin \phi \tan \theta & \cos \phi \tan \theta \\ 0 & \cos \phi & -\sin \phi \\ 0 & \sin \phi / \cos \theta & \cos \phi / \cos \theta \end{bmatrix} \begin{bmatrix} p \\ q \\ r \end{bmatrix}\quad (2.23)$$

Using $s_{(\cdot)}$, $c_{(\cdot)}$, and $t_{(\cdot)}$ as shorthand notations for $\sin(\cdot)$, $\cos(\cdot)$, and $\tan(\cdot)$ respectively, we obtain

$$\begin{bmatrix} \dot{\phi} \\ \dot{\theta} \\ \dot{\psi} \end{bmatrix} = \begin{bmatrix} 1 & s_\phi t_\theta & c_\phi t_\theta \\ 0 & c_\phi & -s_\phi \\ 0 & s_\phi/c_\theta & c_\phi/c_\theta \end{bmatrix} \begin{bmatrix} p \\ q \\ r \end{bmatrix} \quad (2.24)$$

The rotation matrix from body fixed to navigation axis is

$$\check{T}^{(N,B)} = \begin{bmatrix} c_\psi & s_\psi & 0 \\ -s_\psi & c_\psi & 0 \\ 0 & 0 & 1 \end{bmatrix} \begin{bmatrix} c_\theta & 0 & -s_\theta \\ 0 & 1 & 0 \\ s_\theta & 0 & c_\theta \end{bmatrix} \begin{bmatrix} 1 & 0 & 0 \\ 0 & c_\phi & s_\phi \\ 0 & -s_\phi & c_\phi \end{bmatrix} \quad (2.25)$$

Multiplying each matrix, we get

$$\check{T}^{(N,B)} = \begin{bmatrix} c_\theta c_\psi & -c_\phi s_\psi + s_\phi s_\theta c_\psi & s_\phi s_\psi + c_\phi s_\theta c_\psi \\ c_\theta s_\psi & c_\phi c_\psi + s_\phi s_\theta s_\psi & -s_\phi c_\psi + c_\phi s_\theta s_\psi \\ -s_\theta & s_\phi c_\theta & c_\phi c_\theta \end{bmatrix} \quad (2.26)$$

Therefore, the desired kinematic expressions relating to the translational rates are given by

$$\{\vec{v}_{B/N}^N\}^{(N)} = \check{T}^{(N,B)} \{\vec{v}_{B/N}^B\}^{(B)} \quad (2.27)$$

Expanding Eq.(2.27) in component form

$$\begin{bmatrix} \dot{p}_N \\ \dot{p}_E \\ \dot{p}_D \end{bmatrix} = \begin{bmatrix} c_\theta c_\psi & -c_\phi s_\psi + s_\phi s_\theta c_\psi & s_\phi s_\psi + c_\phi s_\theta c_\psi \\ c_\theta s_\psi & c_\phi c_\psi + s_\phi s_\theta s_\psi & -s_\phi c_\psi + c_\phi s_\theta s_\psi \\ -s_\theta & s_\phi c_\theta & c_\phi c_\theta \end{bmatrix} \begin{bmatrix} u \\ v \\ w \end{bmatrix} \quad (2.28)$$

Expanding out \dot{p}_D the component in Eq.(2.28), we get

$$\dot{p}_D = -s_\theta u + s_\phi c_\theta v + c_\phi c_\theta w \quad (2.29)$$

Altitude rate is calculated as

$$\dot{h} = -\dot{p}_D = +s_\theta u - s_\phi c_\theta v - c_\phi c_\theta w \quad (2.30)$$

2.1.3 Auxiliary Equations

Flight path angle (γ) and heading angle (χ) are expressed in terms of the components of $\{\vec{v}_{B/N}^N\}^{(N)}$ and $\dot{h} = -\dot{p}_D$, respectively.

$$\gamma = \arcsin\left(\frac{\dot{h}}{|\vec{v}_{B/N}^N|}\right) = \arctan\left(\frac{\dot{h}}{\sqrt{\dot{p}_N^2 + \dot{p}_E^2}}\right), \quad -\frac{\pi}{2} < \gamma < \frac{\pi}{2} \quad (2.31)$$

$$\chi = \arctan_2[\dot{p}_E, \dot{p}_N], \quad -\pi < \chi \leq \pi \quad (2.32)$$

Accelerometers measure the specific linear accelerations. The body-axes components of specific linear accelerations at the vehicle center of mass, $\vec{a}_{sB/N}^N$, can be obtained excluding the gravity force, \vec{f}_g as

$$\vec{a}_{sB/N}^N = \frac{1}{m}(\vec{f} - \vec{f}_g) \quad (2.33)$$

When the air vehicle is flying, the force and moment caused by ground handling (landing gear) is equal to zero; thus, the total force excluding the gravity force is equal to aerodynamic (\vec{f}_a) and propulsive (\vec{f}_p) forces

$$\vec{a}_{sB/N}^N = \frac{1}{m}(\vec{f}_a + \vec{f}_p) \quad (2.34)$$

with the resolution of vector components into body coordinates as

$$\{\vec{a}_{sB/N}^N\}^{(B)} = \begin{bmatrix} a_{sx} \\ a_{sy} \\ a_{sz} \end{bmatrix}, \quad \{\vec{f}_a\}^{(B)} = \begin{bmatrix} X_a \\ Y_a \\ Z_a \end{bmatrix}, \quad \{\vec{f}_p\}^{(B)} = \begin{bmatrix} X_p \\ Y_p \\ Z_p \end{bmatrix} \quad (2.35)$$

Expanding Eq.(2.34) in component form and writing the specific accelerations for each axis component yields the following:

$$\begin{bmatrix} a_{sx} \\ a_{sy} \\ a_{sz} \end{bmatrix} = \frac{1}{m} \begin{bmatrix} X_a + X_p \\ Y_a + Y_p \\ Z_a + Z_p \end{bmatrix} \quad (2.36)$$

2.1.4 Off-Nominal Calculations

2.1.4.1 Determination of Velocity at Off-Nominal Point

Using the following definitions for the body-axes components of $\vec{v}_{B/N}^N$ and $\vec{v}_{P/N}^N$, and the body-axis component of $\vec{r}_{P/B}$ (displacement vector of an arbitrary point P w.r.t vehicle CM)

$$\begin{aligned} \{\vec{v}_{P/N}^N\}^{(B)} &= \begin{bmatrix} u_P \\ v_P \\ w_P \end{bmatrix}, & \{\vec{v}_{B/N}^N\}^{(B)} &= \begin{bmatrix} u \\ v \\ w \end{bmatrix}, & \{\vec{\omega}^{B/N}\}^{(B)} &= \begin{bmatrix} p \\ q \\ r \end{bmatrix}, \\ \{\vec{r}_{P/B}\}^{(B)} &= \begin{bmatrix} x_{P/B} \\ y_{P/B} \\ z_{P/B} \end{bmatrix} \end{aligned} \quad (2.37)$$

the velocity at any arbitrary point P on the vehicle is obtained as

$$\{\vec{v}_{P/N}^N\}^{(B)} = \{\vec{v}_{B/N}^N\}^{(B)} + \{\vec{\omega}^{B/N}\}^{(B)} \times \{\vec{r}_{P/B}\}^{(B)} \quad (2.38)$$

where $\{\vec{r}_{P/B}\}^{(B)} = -\{\vec{r}_{B/P}\}^{(B)}$

Expanding Eq.(2.38) in component form and writing the velocity transfer for each axis component yields

$$\begin{aligned} \begin{bmatrix} u_P \\ v_P \\ w_P \end{bmatrix} &= \begin{bmatrix} u \\ v \\ w \end{bmatrix} + \begin{bmatrix} p \\ q \\ r \end{bmatrix} \times \begin{bmatrix} x_{P/B} \\ y_{P/B} \\ z_{P/B} \end{bmatrix} \\ u_P &= u + qz_{P/B} - ry_{P/B} \\ v_P &= v + rx_{P/B} - pz_{P/B} \\ w_P &= w + py_{P/B} - qx_{P/B} \end{aligned} \quad (2.39)$$

2.1.4.2 Determination of the Specific Acceleration at Off-Nominal Point

The body-axes components of specific linear accelerations at an arbitrary point P (accelerometer sensor position), $\{\vec{a}_{sP/N}^N\}^{(B)}$, instead of the CM are obtained as

$$\begin{aligned} \{\vec{a}_{sP/N}^N\}^{(B)} &= \{\vec{a}_{sB/N}^N\}^{(B)} + \{\mathcal{D}^B \vec{\omega}^{B/N}\}^{(B)} \times \{\vec{r}_{P/B}\}^{(B)} \\ &\quad + \{\vec{\omega}^{B/N}\}^{(B)} \times (\{\vec{\omega}^{B/N}\}^{(B)} \times \{\vec{r}_{P/B}\}^{(B)}) \end{aligned} \quad (2.40)$$

with the resolution into vector components in body coordinates

$$\{\vec{a}_{sP/N}^N\}^{(B)} = \begin{bmatrix} a_{sx,P} \\ a_{sy,P} \\ a_{sz,P} \end{bmatrix}, \quad \{\vec{a}_{sB/N}^N\}^{(B)} = \begin{bmatrix} a_{sx} \\ a_{sy} \\ a_{sz} \end{bmatrix}, \quad \{\vec{r}_{P/B}\}^{(B)} = \begin{bmatrix} x_{P/B} \\ y_{P/B} \\ z_{P/B} \end{bmatrix} \quad (2.41)$$

Expanding Eq.(2.41) in component form and writing the results for each axis component yields

$$\begin{aligned} \begin{bmatrix} a_{sx,P} \\ a_{sy,P} \\ a_{sz,P} \end{bmatrix} &= \begin{bmatrix} a_{sx} \\ a_{sy} \\ a_{sz} \end{bmatrix} + \begin{bmatrix} \dot{p} \\ \dot{q} \\ \dot{r} \end{bmatrix} \times \begin{bmatrix} x_{P/B} \\ y_{P/B} \\ z_{P/B} \end{bmatrix} + \begin{bmatrix} p \\ q \\ r \end{bmatrix} \times \left(\begin{bmatrix} p \\ q \\ r \end{bmatrix} \times \begin{bmatrix} x_{P/B} \\ y_{P/B} \\ z_{P/B} \end{bmatrix} \right) \\ a_{sx,P} &= a_{sx} - (q^2 + r^2)x_{P/B} + (pq - \dot{r})y_{P/B} + (pr + \dot{q})z_{P/B} \\ a_{sy,P} &= a_{sy} + (pq + \dot{r})x_{P/B} - (p^2 + r^2)y_{P/B} + (qr - \dot{p})z_{P/B} \\ a_{sz,P} &= a_{sz} + (pr - \dot{q})x_{P/B} + (qr + \dot{p})y_{P/B} - (p^2 + q^2)z_{P/B} \end{aligned} \quad (2.42)$$

2.1.4.3 Transferring Moments to Off-Nominal Point

Using the following definitions for the body-axes components of \vec{m}_p , \vec{m}_B , and \vec{f} , together with the body-axis component of $\vec{r}_{P/B}$ (displacement vector of an arbitrary point P w.r.t vehicle CM)

$$\begin{aligned}\{\vec{m}_P\}^{(B)} &= \begin{bmatrix} l_P \\ m_P \\ n_P \end{bmatrix}, & \{\vec{m}_B\}^{(B)} &= \begin{bmatrix} l \\ m \\ n \end{bmatrix}, & \{\vec{f}\}^{(B)} &= \begin{bmatrix} f_x \\ f_y \\ f_z \end{bmatrix}, \\ \{\vec{r}_{P/B}\}^{(B)} &= \begin{bmatrix} x_{P/B} \\ y_{P/B} \\ z_{P/B} \end{bmatrix}\end{aligned}\tag{2.43}$$

the moments referred to any arbitrary point P on the vehicle is computed as

$$\{\vec{m}_P\}^{(B)} = \{\vec{m}_B\}^{(B)} + \{\vec{r}_{B/P}\}^{(B)} \times \{\vec{f}\}^{(B)}\tag{2.44}$$

where $\{\vec{r}_{P/B}\}^{(B)} = -\{\vec{r}_{B/P}\}^{(B)}$

Expanding in component form and writing the results for each axis component yields the following:

$$\begin{aligned}\begin{bmatrix} l_P \\ m_P \\ n_P \end{bmatrix} &= \begin{bmatrix} l \\ m \\ n \end{bmatrix} - \begin{bmatrix} x_{P/B} \\ y_{P/B} \\ z_{P/B} \end{bmatrix} \times \begin{bmatrix} f_x \\ f_y \\ f_z \end{bmatrix} \\ l_P &= l - f_z y_{P/B} + f_y z_{P/B} \\ m_P &= m + f_z x_{P/B} - f_x z_{P/B} \\ n_P &= n - f_y x_{P/B} + f_x y_{P/B}\end{aligned}\tag{2.45}$$

2.2 Forces and Moments

The sum of all applied forces and moments in the preceding equations arises from aerodynamics, gravity, and propulsion. Since gravity acts through the center of mass (CM) and the gravity field is uniform, there is no gravity moment acting on the air vehicle. The resultant force and moment are thus expressed as

$$\vec{f} = \vec{f}_a + \vec{f}_p + \vec{f}_g, \quad \vec{m}_B = \vec{m}_{B,a} + \vec{m}_{B,p}\tag{2.46}$$

where \vec{f}_a, \vec{f}_p and \vec{f}_g are the resultant forces due to aerodynamics, propulsion, and thrust, respectively.

Note that gravity force produces no external moment about the CM, so the total external moment is due to the total aerodynamic and propulsive moment alone.

2.2.1 Aerodynamic Forces and Moments

Aerodynamic forces and moments result from the relative motion of the air and the aircraft. Aerodynamic forces and moments can be represented using non-dimensional coefficients as follows:

$$\{\vec{f}_a\}^{(B)} = \begin{bmatrix} X_a \\ Y_a \\ Z_a \end{bmatrix} = \bar{q}S \begin{bmatrix} C_X \\ C_Y \\ C_Z \end{bmatrix} = \frac{1}{2}\rho V_{TAS}^2 \begin{bmatrix} C_X \\ C_Y \\ C_Z \end{bmatrix} \quad (2.47)$$

$$\{\vec{m}_{B,a}\}^{(B)} = \begin{bmatrix} l_a \\ m_a \\ n_a \end{bmatrix} = \bar{q}S \begin{bmatrix} bC_l \\ \bar{c}C_m \\ bC_n \end{bmatrix} \quad (2.48)$$

where \bar{q} is the dynamic pressure, V_{TAS} is the magnitude of the air-relative velocity (also called the airspeed), ρ is the air density, S is the wing reference area, b is the wingspan, and \bar{c} is the mean aerodynamic chord.

Dynamic pressure is calculated as follows:

$$\bar{q} = \frac{1}{2}\rho V_{TAS}^2 \quad (2.49)$$

The dimensionless force components resolved into the wind axes can be obtained using the transformation matrix in Eq. (2.10) as follows:

$$\begin{bmatrix} -C_D \\ -C_C \\ -C_L \end{bmatrix} = \begin{bmatrix} c_\alpha c_\beta & s_\beta & s_\alpha c_\beta \\ -c_\alpha s_\beta & c_\beta & -s_\alpha s_\beta \\ -s_\alpha & 0 & c_\alpha \end{bmatrix} \begin{bmatrix} C_X \\ C_Y \\ C_Z \end{bmatrix} \quad (2.50)$$

In overall, the non-dimensional force and moment coefficients are nonlinear in their dependence on the aircraft translational and angular velocity vector components, as well as the control surface deflections, and also their time derivatives and other non-dimensional quantities, such as Mach number and Reynolds number.

The aerodynamic force and moment coefficients are calculated using the following relationships and represented as a function of a combination of independent variables [2] [46] [47] [48] [49].

$$C_a = C_a(M, \alpha, \beta, p, q, r, \delta_e, \delta_a, \delta_r, \delta_{lef}, \delta_{sb}) \quad (2.51)$$

where a stands for X, Y, Z, l, m, n .

For longitudinal coefficients, the dependency is expressed as

$$\begin{aligned} C_a = & C_a(\alpha) + \Delta C_a(\beta, \alpha) + \Delta C_a(\delta_h, \alpha) + \Delta C_a(\delta_{LEF}, \alpha, \beta) \\ & + \frac{q\bar{c}}{2V_T} \left\{ \left[C_{a_q}(\alpha) + \Delta C_{a_q}(\alpha, \delta_{LEF}) \right] \right\} \end{aligned} \quad (2.52)$$

where a stands for X, Z, m .

For lateral coefficients, the dependency is expressed as

$$\begin{aligned} C_a = & C_a(\beta) + \Delta C_a(\beta, \alpha) + \Delta C_a(\delta_{LEF}, \alpha, \beta) \\ & + [\Delta C_a(\delta_a, \alpha, \beta) + \Delta C_a(\delta_a, \alpha, \beta, \delta_{LEF})] + [\Delta C_a(\delta_r, \alpha, \beta)] \\ & + \frac{b}{2V_T} \left\{ \left[C_{a_p}(\alpha) + \Delta C_{a_p}(\alpha, \delta_{LEF}) \right] p + \left[C_{a_r}(\alpha) + \Delta C_{a_r}(\alpha, \delta_{LEF}) \right] r \right\} \end{aligned} \quad (2.53)$$

where a stands for Y, l, m .

When the whole range of aircraft flight envelope is examined, these aerodynamic coefficients exhibit nonlinear correlations with their dependent variables. Polynomial functions or spline functions can be used to represent the nonlinearity in a postulated model. When the (equally spaced) nodes of an interval are used in the interpolation, exceptionally high degree polynomials exhibit oscillation. Conversely, spline functions can avoid the drawbacks of the polynomial representation. They are defined only on the subintervals and are very capable of approximating nonlinearities. In aerodynamic coefficients, parameters dependency on the angle of attack are represented via spline functions [2] in the form

$$\alpha_{\alpha_i}^m = (\alpha - \alpha_i)_+^m = \begin{cases} (\alpha - \alpha_i)^m & \alpha \geq \alpha_i \\ 0 & \alpha < \alpha_i \end{cases} \quad (2.54)$$

rather than the usual B-splines.

As an example, the aerodynamic structure for C_D is shown below. The structure of other longitudinal aerodynamic coefficients is similar.

$$\begin{aligned} C_D = & C_{D_0} + [C_{D_\alpha} \cdot \alpha + C_{D_{\alpha^2}} \cdot \alpha^2] + [C_{D_{\delta_e}} \cdot \delta_e + C_{D_{\delta_e \alpha}} \cdot \delta_e \cdot \alpha] \\ & + [C_{D_q} \cdot \frac{qc}{2V} + C_{D_{q\alpha}} \cdot \frac{qc}{2V} \cdot \alpha] \\ & + [C_{D_{\delta_{lef}}} \cdot \delta_{lef} + C_{D_{\delta_{lef} \alpha}} \cdot \delta_{lef} \cdot \alpha + C_{D_{\delta_{lef} \alpha_{10}^1}} \cdot \delta_{lef} \\ & \cdot (\alpha - \alpha_{10^\circ})_+ C_{D_{\delta_{lef} \alpha_{15}^1}} \cdot \delta_{lef} \cdot (\alpha - \alpha_{15^\circ})_+] \\ & + [C_{D_\beta} \cdot \beta + C_{D_{\beta_0^1}} \cdot (\beta - \beta_{0^\circ})_+ + C_{D_{\beta^2}} \cdot \beta^2] \end{aligned} \quad (2.55)$$

2.2.2 Propulsion Forces and Moments

Assuming that the thrust from the propulsion systems acts along the x body axis with an inclination angle of the engines, the applied force from propulsion is

$$\vec{f}_p = \begin{bmatrix} T \cos \alpha_T \\ 0 \\ -T \sin \alpha_T \end{bmatrix} \quad (2.56)$$

$$\vec{m}_{B,p} = \vec{f}_p \times \vec{r}_{EN/B} = \begin{bmatrix} 0 \\ T \cos \alpha_T z_{EN/B} + T \sin \alpha_T x_{EN/B} \\ 0 \end{bmatrix} \quad (2.57)$$

where $\vec{r}_{EN/B}$ ($x_{EN/B}, y_{EN/B}, z_{EN/B}$) is the position of the engine with respect to CM along the body-fixed coordinate axes.

2.2.2.1 Turbofan Engine Model Inputs and Outputs

The inputs and outputs of a generic turbofan engine in the context of a flight vehicle system identification are depicted in Figure 2.3 [50].

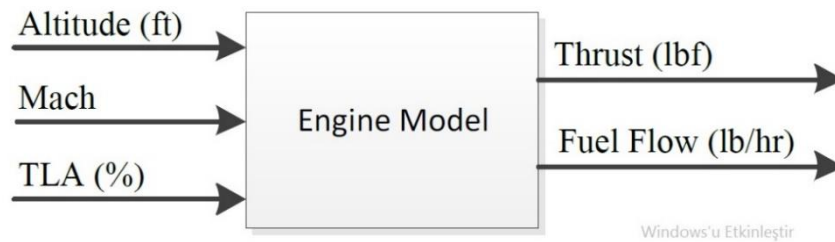


Figure 2.3 Generic Turbofan Engine Model Inputs and Outputs

2.2.2.2 Turbofan Engine Components

The turbofan engine operates according to a thermodynamic cycle. In this cycle, the air is ingested, compressed, combusted, expanded, and expelled from the engine throughout this cycle. As a result, thrust is generated to propel the flight vehicle. Five main engine components perform for this operation:

- the fan,
- low- and high-pressure compressors,
- combustion
- low- and high- pressure turbines
- nozzle.

Figure 2.4 illustrates these components.

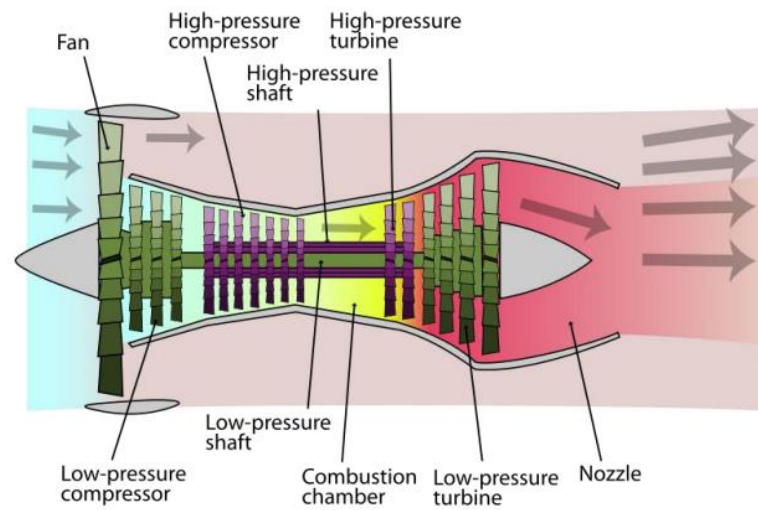


Figure 2.4 Turbofan Engine Components

The fan generates most of the thrust produced by a turbofan engine.

Compression works by adding energy to the pressure and heat already present to prepare the air for combustion. Compressors are classified into two types: low-pressure compressors and high-pressure compressors.

The combustor's function is to supplement the energy in the airflow by heat addition. Fuel is injected into the combustion chamber and mixed with the air. Following that, the mixture of fuel and air is subsequently ignited, drastically increasing the temperature and energizing the flow, propelling it back towards the high-pressure turbine.

The turbines extract energy from the flow and utilize it to drive the compressors and the fan. The rotating fan draws more air through the engine's core, thus completing the cycle, and it draws additional bypass air around the engine, thereby producing continual thrust.

The exhaust nozzle's purpose is to push the core flow out of the engine, thus generating extra thrust.

This is a continuous process, with each component performing a particular function to keep the engine functioning. In principle, the idea of a turbofan engine is

straightforward: add energy to the air passing through the engine and then extract this energy to power the fan and generate thrust.

2.2.2.3 Simplified Turbofan Thrust Model

This section introduces a mathematical engine model capable of estimating the thrust force for any flight condition.

Numerous researchers have concentrated their efforts on developing generic engine models with the least amount of data. Yadav, Kapadi, and Pashilkar [51] proposed an aero thermodynamic model for turbofan engine digital simulation. Similarly, Roberts and Eastbourn in Reference [52] proposed novel methods for developing a dynamic turbofan engine model using thermodynamic equations. Additionally, NASA Glenn Research Center developed a general high-bypass ratio, twin-spool commercial turbofan engine model [53]. However, the goal of this study is to provide a turbofan engine model to calculate the turbofan engine thrust force for any flight condition, and the models provided by [51] [52] [53] were found to be too complex for this purpose. As a result, several techniques to estimate the thrust force of a turbofan engine from simple equations were investigated.

Two sub-models comprise the engine model. The first sub-model is concerned with the static engine state, while the second sub-model is concerned with the engine dynamics (i.e., transient state). Figure 2.5 illustrates these sub-models. Each sub-model is discussed separately in the two following sections.

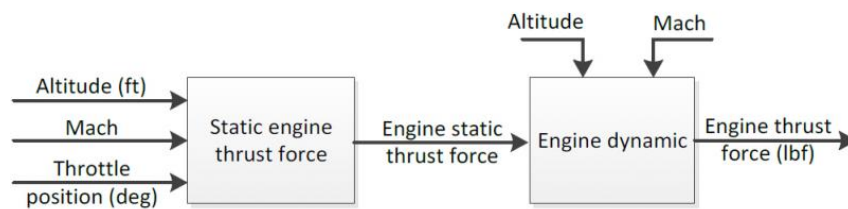


Figure 2.5 Turbofan Engine Simplified Thrust Model Block Diagram

2.2.2.3.1 Static Engine Model

Numerous simple static models exist in the literature [46] [47] [54] [55] [56], and [57], and it is shown that the model in Ref. [54] is superior to others.

There are three significant external variables and one internal variable which affects the thrust variation. The external variables include air density, Mach number, and altitude; internal variables include throttle position. The static model is described as follows:

$$\frac{T(h, M, \delta_{TLA})}{T_0} = \bar{\sigma}(h, M) \times \tilde{T}(h, M, \delta_{TLA}) \quad (2.58)$$

where $T(h, M, \delta_{TLA})$ is the engine static thrust force at the altitude h , the Mach number M and the throttle position δ_{TLA} , T_0 is the maximum thrust value, $\tilde{T}(h, M, \delta_{TLA})$ is the nondimensional thrust coefficient and $\bar{\sigma}$ is the relative air density ratio defined as:

$$\bar{\sigma}(h, M) = \frac{\rho(h)}{\rho_0} \left[1 + \frac{(\gamma - 1)}{2} M^2 \right]^{\frac{1}{\gamma-1}} \quad (2.59)$$

and $\tilde{T}(h, M, \delta_{TLA})$ is a polynomial defined as:

$$\tilde{T}(h, M, \delta_{TLA}) = \sum_{i=0}^n \sum_{j=0}^m \tilde{T}_{ij}(h) M^i \delta_{TLA}^j \quad (2.60)$$

where $\tilde{T}_{ij}(h)$ denotes the polynomial coefficients depending on the altitude h , and $\{n, m\}$ represent the order of \tilde{T} for Mach number and throttle position. The order of the polynomial for throttle position and the order of the polynomial to the Mach number are assigned as m and n , respectively. These numbers, m , and n , are optimized later to give better results, i.e., minor errors. In Figure 2.6, T_0 for different altitudes can be seen.

Mach	Thrust values at an altitude, ft					
	0	10000	20000	30000	40000	50000
T_{ide}						
0.2	635	425	690	1010	1330	1700
0.4	60	25	345	755	1130	1525
0.6	-1020	-710	-300	350	910	1360
0.8	-2700	-1900	-1300	-247	600	1100
1.0	-3600	-1400	-595	-342	-200	700
T_{mit}						
0.2	12680	9150	6313	4040	2470	1400
0.4	12610	9312	6610	4290	2600	1560
0.6	12640	9839	7090	4660	2840	1660
0.8	12390	10176	7750	5320	3250	1930
1.0	11680	9848	8050	6100	3800	2310
T_{max}						
0.2	21420	15700	11225	7323	4435	2600
0.4	22700	16860	12250	8154	5000	2835
0.6	24240	18910	13760	9285	5700	3215
0.8	26070	21075	15975	11115	6860	3950
1.0	28886	23319	18300	13484	8612	5057

Figure 2.6 Maximum Thrust Values at Different Mach Numbers and Altitudes

2.2.2.3.2 Transient (Dynamic) Engine Model

The transient engine dynamic response for a turbofan was modeled with a state equation as a first-order lag in the actual thrust to the commanded thrust as shown below [46] [47] [48] [50] [54]:

$$T_a = \frac{1}{\tau_{eng}} (T - T_a) \quad (2.61)$$

where τ_{eng} is the engine time constant, T_a is the actual thrust, and T is the steady-state thrust at defined altitude, Mach number, and throttle position. τ_{eng} is dependent on the flight condition. In this study, for aerodynamic identification purposes, τ_{eng} can be kept fixed, or the transient engine dynamics can be neglected not to increase the number of unknown parameters.

2.2.3 Gravity Force

Gravitational forces resolved into body coordinates are given as

$$\{\vec{f}_g\}^{(B)} = \begin{bmatrix} X_g \\ Y_g \\ Z_g \end{bmatrix} = \check{T}^{(N,B)} \begin{bmatrix} 0 \\ 0 \\ mg \end{bmatrix} = \begin{bmatrix} -mgs_\phi \\ mgs_\phi c_\theta \\ mgc_\phi c_\theta \end{bmatrix} \quad (2.62)$$

2.3 Sensor Models

This subsection discusses the sensor models that were used in the simulation model. The sensor models composed of an accelerometer and a rate gyroscope model. Stochastic and deterministic errors are the two main types of sensor errors that may appear. The most common types of sensor errors are depicted in Figure 2.7 [58].

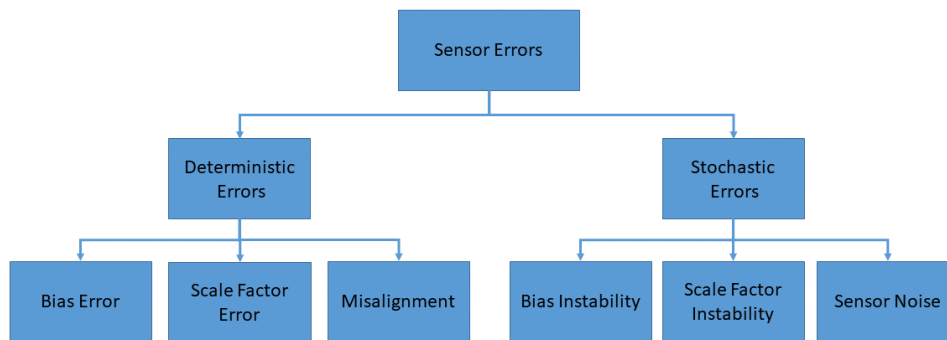


Figure 2.7 Major Types of Sensor Errors

Bias error, scale factor error, and misalignment are all examples of deterministic errors. The bias error is a constant offset between the output and the input values. Scale factor is a multiplier applied to a signal that is composed of the output to the input ratio over the measurement range. Misalignment is an orthogonality error resulting from a rigid-body rotation that offsets all axes relative to the expected input axes [59]. Generally, highly accurate mounting of the sensor is achievable; the misalignments are quite minor [1].

Errors that occur as a result of random bias or scale factor drift, as well as random sensor noise, are known as stochastic errors. Random variations in bias and scale factor are the low frequency components and their influence is minimal. The sensor noise is responsible for a large portion of the stochastic errors [58]. Sensor noise may be reduced via filtering. In sensor error models, random sensor noise is represented as a zero mean white noise.

The error model of any sensor is given by:

$$y_m = (1 + S_y + \delta S_y)y + (\Delta y + \delta \Delta y) + n_y \quad (2.63)$$

where S_y is the scale factor error, δS_y is the scale factor instability, Δy the unknown instrument bias, $\delta \Delta y$ is the bias instability and n_y is sensor noise in the measured variable. The measured quantity is denoted by the left-hand subscript m . The time constant is omitted since no time delay is introduced in the measured variables.

The characteristics for the sensor models are given in Table 2.1.

Table 2.1 Characteristics of the Sensor Models

Symbol	Accelerometer	Gyroscopes
Bias	0.005 g	10 deg/hr
Scale Factor Error	1000 ppm or 0.1%	500 ppm or 0.05%
Random Sensor Noise	0.005 g/h/ \sqrt{Hz}	0.004 deg/h/ \sqrt{Hz}

2.4 Aircraft Trim and Linearization

2.4.1 Dynamic Model Representation for Aircraft Trim

Mathematical model of the dynamic system can be represented in state-space form as

$$\begin{aligned} \dot{\vec{x}} &= f(\vec{x}, \vec{u}), \quad \vec{x}(t_0) = \vec{x}_0 \\ \vec{y} &= g(\vec{x}, \vec{u}) \end{aligned} \quad (2.64)$$

where \vec{x} is the $n_x \times 1$ column vector of state variables, \vec{u} is the $n_u \times 1$ control input vector and \vec{y} is the $n_y \times 1$ output vector.

Simplified linear models are valid over minor perturbations about the equilibrium points. The dynamic system equations can be linearized around a suitable operation point, results in

$$\begin{aligned}\dot{\vec{x}} &= A\vec{x} + B\vec{u}, \quad x(t_0) = x_0 \\ y &= C\vec{x} + D\vec{u}\end{aligned}\tag{2.65}$$

The system matrices A , B , C , and D are respectively denoted by

$$\begin{aligned}A_{ij} &= \frac{f_i(x + \epsilon e_j, u) - f_i(x - \epsilon e_j, u)}{2\epsilon}; i = 1, 2, \dots, n_{\dot{x}}; j = 1, 2, \dots, n_x \\ B_{ij} &= \frac{f_i(x, u + \epsilon e_j) - f_i(x, u - \epsilon e_j)}{2\epsilon}; i = 1, 2, \dots, n_{\dot{x}}; j = 1, 2, \dots, n_u \\ C_{ij} &= \frac{g_i(x + \epsilon e_j, u) - g_i(x - \epsilon e_j, u)}{2\epsilon}; i = 1, 2, \dots, n_y; j = 1, 2, \dots, n_x \\ D_{ij} &= \frac{g_i(x, u + \epsilon e_j) - g_i(x, u - \epsilon e_j)}{2\epsilon}; i = 1, 2, \dots, n_y; j = 1, 2, \dots, n_u\end{aligned}\tag{2.66}$$

where ϵ is a small positive scalar, e_j is the j th unit vector, and n_u , n_x , $n_{\dot{x}}$, and n_y stand for the number of elements in u , x , \dot{x} and y vectors, respectively.

Nonlinear equations must be solved to determine the trim condition. At least 12 states are needed to characterize aircraft motion. These are the translational, rotational, kinematic, and navigation equations. In A , B , C , and D system matrices, the columns correspond to the input/state vectors, while the rows correspond to state derivative/output vectors.

The input vector depends on the type of air vehicle. It typically comprises the deflections of an elevator, aileron, and rudder, as well as a throttle setting.

The air vehicle state, output, and input vectors are defined, respectively, as

$$\begin{aligned}\vec{x} &= [V, \alpha, \beta, \phi, \theta, \psi, p, q, r, p_N, p_E, h]^T \\ \vec{y} &= [a_z, a_y, \gamma]^T \\ \vec{u} &= [\delta_T, \delta_e, \delta_a, \delta_r]^T\end{aligned}\tag{2.67}$$

For a nonlinear, time-invariant system, the trim point is equivalent to the equilibrium point of the nonlinear system, which is represented by x_{eq} . In state-space, this equilibrium point, or trim condition, is described as $\dot{x} = 0$, with the set of control settings $u_{eq} = \text{constant}$ enabling steady-state possible. This solution generally can only be found numerically.

In this study, firstly, the Newton-Raphson method is utilized to determine the trim condition. Then the Line Search Newton-Raphson method is examined for its ability to provide global convergence to trim problems. To utilize the Newton-Raphson method, linearization is required; the procedure is shown in Figure 2.8 [31] [47] [48] [60]. The perturbations are selected as a fraction of the equilibrium values and maybe defined some prescribed values for an equilibrium value of zero.

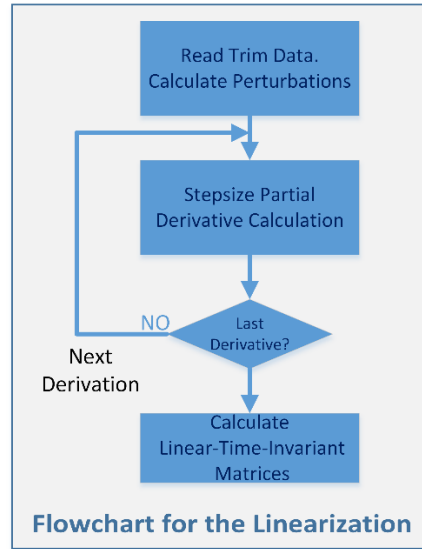


Figure 2.8 Flowchart of the Linearization Process

The following are the linearized steady-state equations of motion in matrix form, using the Jacobian matrix:

$$\begin{bmatrix} \dot{V} \\ \dot{\alpha} \\ \dot{\beta} \\ \dot{\phi} \\ \dot{\theta} \\ \dot{\psi} \\ \dot{p} \\ \dot{q} \\ \dot{r} \\ \dot{N} \\ \dot{E} \\ \dot{h} \end{bmatrix} = \begin{bmatrix} \frac{\partial \dot{V}}{\partial V} & \frac{\partial \dot{V}}{\partial \alpha} & \dots & \frac{\partial \dot{V}}{\partial h} \\ \frac{\partial \dot{\alpha}}{\partial V} & \frac{\partial \dot{\alpha}}{\partial \alpha} & \dots & \frac{\partial \dot{\alpha}}{\partial h} \\ \frac{\partial \dot{\beta}}{\partial V} & \frac{\partial \dot{\beta}}{\partial \alpha} & \dots & \frac{\partial \dot{\beta}}{\partial h} \\ \frac{\partial \dot{\phi}}{\partial V} & \frac{\partial \dot{\phi}}{\partial \alpha} & \dots & \frac{\partial \dot{\phi}}{\partial h} \\ \frac{\partial \dot{\theta}}{\partial V} & \frac{\partial \dot{\theta}}{\partial \alpha} & \dots & \frac{\partial \dot{\theta}}{\partial h} \\ \frac{\partial \dot{\psi}}{\partial V} & \frac{\partial \dot{\psi}}{\partial \alpha} & \dots & \frac{\partial \dot{\psi}}{\partial h} \\ \frac{\partial \dot{p}}{\partial V} & \frac{\partial \dot{p}}{\partial \alpha} & \dots & \frac{\partial \dot{p}}{\partial h} \\ \frac{\partial \dot{q}}{\partial V} & \frac{\partial \dot{q}}{\partial \alpha} & \dots & \frac{\partial \dot{q}}{\partial h} \\ \frac{\partial \dot{r}}{\partial V} & \frac{\partial \dot{r}}{\partial \alpha} & \dots & \frac{\partial \dot{r}}{\partial h} \\ \frac{\partial \dot{N}}{\partial V} & \frac{\partial \dot{N}}{\partial \alpha} & \dots & \frac{\partial \dot{N}}{\partial h} \\ \frac{\partial \dot{E}}{\partial V} & \frac{\partial \dot{E}}{\partial \alpha} & \dots & \frac{\partial \dot{E}}{\partial h} \\ \frac{\partial \dot{h}}{\partial V} & \frac{\partial \dot{h}}{\partial \alpha} & \dots & \frac{\partial \dot{h}}{\partial h} \end{bmatrix} \begin{bmatrix} V \\ \alpha \\ \beta \\ \phi \\ \theta \\ \psi \\ p \\ q \\ r \\ N \\ E \\ h \end{bmatrix} + \begin{bmatrix} \frac{\partial \dot{V}}{\partial \delta_e} & \dots & \frac{\partial \dot{V}}{\partial \delta_T} \\ \frac{\partial \dot{\alpha}}{\partial \delta_e} & \dots & \frac{\partial \dot{\alpha}}{\partial \delta_T} \\ \frac{\partial \dot{\beta}}{\partial \delta_e} & \dots & \frac{\partial \dot{\beta}}{\partial \delta_T} \\ \frac{\partial \dot{\phi}}{\partial \delta_e} & \dots & \frac{\partial \dot{\phi}}{\partial \delta_T} \\ \frac{\partial \dot{\theta}}{\partial \delta_e} & \dots & \frac{\partial \dot{\theta}}{\partial \delta_T} \\ \frac{\partial \dot{\psi}}{\partial \delta_e} & \dots & \frac{\partial \dot{\psi}}{\partial \delta_T} \\ \frac{\partial \dot{p}}{\partial \delta_e} & \dots & \frac{\partial \dot{p}}{\partial \delta_T} \\ \frac{\partial \dot{q}}{\partial \delta_e} & \dots & \frac{\partial \dot{q}}{\partial \delta_T} \\ \frac{\partial \dot{r}}{\partial \delta_e} & \dots & \frac{\partial \dot{r}}{\partial \delta_T} \\ \frac{\partial \dot{N}}{\partial \delta_e} & \dots & \frac{\partial \dot{N}}{\partial \delta_T} \\ \frac{\partial \dot{E}}{\partial \delta_e} & \dots & \frac{\partial \dot{E}}{\partial \delta_T} \\ \frac{\partial \dot{h}}{\partial \delta_e} & \dots & \frac{\partial \dot{h}}{\partial \delta_T} \end{bmatrix} \begin{bmatrix} \delta_e \\ \delta_a \\ \delta_r \\ \delta_T \end{bmatrix} \quad (2.68)$$

2.4.2 Numerical Methods for Aircraft Trim

2.4.2.1 Newton-Raphson Method

A Newton-Raphson method is a practical approach for solving equations numerically. It is based on the straightforward concept of linear approximation. In a generalized vector form, the Newton-Raphson method is expressed as

$$\vec{F}(\vec{\Theta}) = 0 \quad (2.69)$$

where $\vec{\Theta} \in \mathbb{R}^n$ is an unknown vector parameter with $n \geq 1$ components, and $\vec{F}: \mathbb{R}^n \rightarrow \mathbb{R}^n$ is a vector-valued function, that is,

$$\vec{F}(\vec{\Theta}) = \begin{bmatrix} F_1(\vec{\Theta}) \\ F_2(\vec{\Theta}) \\ \vdots \\ F_n(\vec{\Theta}) \end{bmatrix} = \begin{bmatrix} F_1(\Theta_1, \Theta_2, \dots, \Theta_n) \\ F_2(\Theta_1, \Theta_2, \dots, \Theta_n) \\ \vdots \\ F_n(\Theta_1, \Theta_2, \dots, \Theta_n) \end{bmatrix} = 0 \quad (2.70)$$

where each $F_i: \mathbb{R}^n \rightarrow \mathbb{R}$, $i = 1, 2, \dots, n$, is a scalar-valued function of n variables. A vector Θ^* for which Eq. 15 is satisfied is called a solution or root of the nonlinear equations.

To derive the formulas for the NR method, Taylor series for the function F at the point Θ_k is written as

$$\vec{F}(\vec{\Theta}_k + \alpha_k \vec{p}_k) \approx F(\vec{\Theta}_k) + \alpha_k \nabla \vec{F}(\vec{\Theta}_k)^T \vec{p}_k \quad (2.71)$$

where p_k is a search direction that improves the solution in some sense, the scalar α_k is the step length that determines the next point, and $\nabla F(\Theta_k)^T$ is the transpose of the Jacobian matrix of F at the point Θ_k . Then Eq. (2.71) can be rewritten as

$$\vec{F}(\vec{\Theta}_k + \alpha_k \vec{p}_k) \approx \vec{F}(\vec{\Theta}_k) + \alpha_k J(\vec{\Theta}_k)^T \vec{p}_k \quad (2.72)$$

If $J(\Theta_k)$ is nonsingular, then solving the equation

$$\vec{F}(\vec{\Theta}^*) \approx \vec{F}(\vec{\Theta}_k) + \alpha_k J(\Theta_k) \vec{p}_k = 0 \quad (2.73)$$

$\alpha_k p_k$ can be obtained as

$$\alpha_k \vec{p}_k = -J(\vec{\Theta}_k)^{-1} \vec{F}(\vec{\Theta}_k) \quad (2.74)$$

In the Newton-Raphson method,

$$\alpha_k = 1 \quad (2.75)$$

and p reduces to

$$\vec{p}_k = -J(\vec{\Theta}_k)^{-1} \vec{F}(\vec{\Theta}_k) \quad (2.76)$$

Algorithm 1: Newton-Raphson Method for Nonlinear Equations

1. Choose initial condition x_0 and maximum iteration number k_{mx}
2. **for** $k = 0$ to k_{max}
3. Calculate a solution to p_k to the Newton equations,
4. $\vec{p}_k = -J(\vec{\Theta}_k)^{-1} \vec{F}(\vec{\Theta}_k)$
5. $\vec{\Theta}_{k+1} = \vec{\Theta}_k + \vec{p}_k$
6. **end for**

Newton-Raphson method needs the knowledge of the Jacobian of the nonlinear function. The derivatives in the scalar-valued function can be approximated numerically with a finite difference approach. This strategy is based on Taylor's theorem. By observing the change in function values in response to small perturbations of the unknowns near a given point x , the derivatives can be approximated. The partial derivative of the scalar-valued function f_i with respect to the j^{th} independent variable can be approximated by the central-difference formula

$$\begin{aligned} \frac{\partial F_i}{\partial \theta_j}(x) &= \lim_{\epsilon \rightarrow 0} \frac{F_i(\theta_1, \dots, \theta_{j-1}, \theta_j + \epsilon e_j, \theta_{j+1}, \dots, \theta_n) - F_i(\theta_1, \dots, \theta_{j-1}, \theta_j - \epsilon e_j, \theta_{j+1}, \dots, \theta_n)}{2\epsilon} \quad (2.77) \\ &\approx \frac{F_i(\theta + \epsilon e_j) - F_i(\theta - \epsilon e_j)}{2\epsilon} \end{aligned}$$

where ϵ is a small positive scalar and e_j is the j th unit vector.

Now considering the function $F_i : \mathbb{R}^n \rightarrow \mathbb{R}$, which is a scalar-valued function of n independent variables, $\vec{\theta}$ the variable can be written componentwise as $\vec{\theta} = (\theta_1, \theta_2, \dots, \theta_n)$. The gradient vector, the n vector of first derivatives of F_i can be built up by merely applying Eq. (2.77) for $j = 1, 2, \dots, n$. This process requires the evaluation of f at the points $\theta + \epsilon e_j$, $j = 1, 2, \dots, n$, and $\theta - \epsilon e_j$, $j = 1, 2, \dots, n$: a total of $2n$ points.

The vector of the first derivatives of f_i , the scalar-valued function is called the gradient of the function and is denoted as

$$\nabla F_i(\vec{\theta}) \equiv \left[\frac{\partial F_i(\theta)}{\partial \theta_1} \quad \frac{\partial F_i(\theta)}{\partial \theta_2} \quad \dots \quad \frac{\partial F_i(\theta)}{\partial \theta_n} \right]^T \quad (2.78)$$

To define the Jacobian, the vector-valued function, $F(\Theta)$, is used:

$$\vec{F}(\vec{\Theta}) = \begin{bmatrix} F_1(\vec{\Theta}) \\ F_2(\vec{\Theta}) \\ \vdots \\ F_n(\vec{\Theta}) \end{bmatrix} = \begin{bmatrix} F_1(\Theta_1, \Theta_2, \dots, \Theta_n) \\ F_2(\Theta_1, \Theta_2, \dots, \Theta_n) \\ \vdots \\ F_n(\Theta_1, \Theta_2, \dots, \Theta_n) \end{bmatrix} \quad (2.79)$$

where each of the functions, F_i is a scalar-valued function. Then ∇F is the matrix with entries

$$(\nabla F(\vec{\Theta}))_{ji} \equiv \frac{\partial F_i(\vec{\Theta})}{\partial \Theta_j} \quad (2.80)$$

Note that the i th column of $\nabla F(x)$ is the gradient of f_i . It can be shown as

$$\nabla F(\vec{\Theta}) = [\nabla F_1(\Theta) \quad \nabla F_2(\Theta) \quad \dots \quad \nabla F_i(\Theta) \quad \dots \quad \nabla F_n(\Theta)] \quad (2.81)$$

The Jacobian of F at the point Θ is defined as $\nabla F(\Theta)^T$ and represented as

$$J(\Theta) = \nabla F(\vec{\Theta})^T \quad (2.82)$$

The Jacobian is the matrix with entries

$$(J(\Theta))_{ij} \equiv \frac{\partial F_i(\Theta)}{\partial \Theta_j} \quad (2.83)$$

where i represents the equation index, and j represents the independent variable index.

2.4.2.2 Line Search Newton-Raphson Method

A line search strategy can be used to make the Newton-Raphson Method more robust. To begin, a merit function needs to be defined, a scalar-valued function of x whose value indicates whether a new candidate iterate is better or worse than the current iterates, in terms of progress towards a solution of f . The most often used merit function is the Euclidean norm $\|\cdot\|_2$, defined as

$$\|F(\Theta)\|_2 = \sqrt{\sum_{i=1}^n F_i^2(\Theta)} \quad (2.84)$$

The algorithm used in Line Search Newton-Raphson uses the sufficient decrease condition, known as the Armijo condition, which is the only difference from the Newton-Raphson method:

$$\|F(\Theta_k + \alpha_k p_k)\|_2 \leq \|F(\Theta_k) + c\alpha_k \nabla F(\Theta_k)^T p_k\|_2 \quad (2.85)$$

The norm of the Armijo condition is illustrated in Figure 2.9 [61]

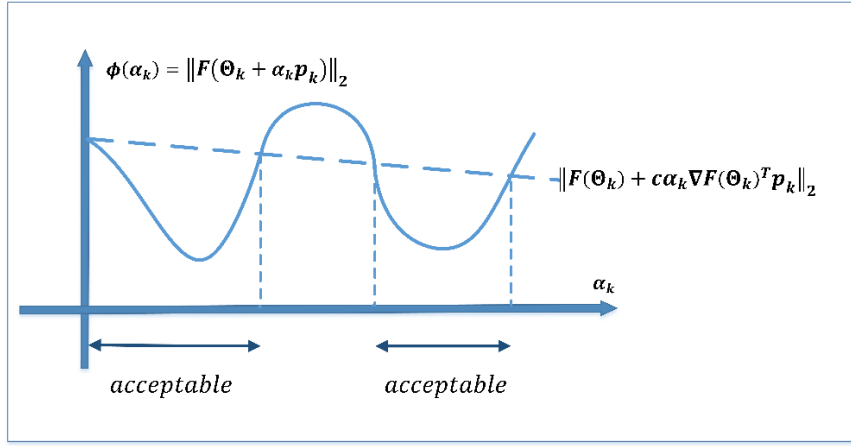


Figure 2.9 Armijo Condition

If the initial point (Θ_0) is away from the solution; the Armijo condition is applied to the Newton-Raphson method to help convergence.

Algorithm 2: Line Search Newton-Raphson Method for Nonlinear Equations

1. Choose initial condition x_0 , maximum iteration number k_{max} , and c
2. **for** $k = 0$ to k_{max}
3. Calculate a solution to p_k to the Newton equations,
4. $\vec{p}_k = -J(\vec{\Theta}_k)^{-1}F(\vec{\Theta}_k)$
5. **if** $\alpha = 1$ satisfies the Armijo condition
6. Set $\alpha_k = 1$
7. **else**
8. Perform Armijo condition line search to find $\alpha_k > 0$ that satisfies Eq. (2.85)
9. **end if**
10. $\vec{\Theta}_{k+1} = \vec{\Theta}_k + \vec{p}_k$
11. **end for**

Procedure 1: Armijo Condition Line Search

1. Choose ρ with $0 < \rho < 1$ and $\bar{\alpha} = 1$; set $\alpha_k \leftarrow \bar{\alpha}$
2. **while** $\|F(\Theta_k + \alpha_k p_k)\|_2 \leq \|F(\Theta_k) + c\alpha_k \nabla f(\Theta_k)^T p_k\|_2$ **do**
3. $\alpha_k \leftarrow \rho \alpha_k$
4. **end while**
5. Terminate with α_k

2.4.3 Steady-State Flight Conditions (Trim Conditions)

The steady-state flight is important since it is the starting condition for flight simulation and a flight condition in which the aircraft is linearized. As far as flight dynamics are concerned, the steady-state flight is defined as a condition when all force and moment components in the body-fixed coordinate system are constant or zero. Additionally, aerodynamic angles and the angular rate components must be constant, with zero derivatives. As a result, the following basic restrictions are specified as follows:

$$\begin{aligned} \text{Linear accelerations:} \quad & \dot{V}, \dot{\alpha}, \dot{\beta} \text{ (or } \dot{u}, \dot{v}, \dot{w}) \equiv 0 \\ \text{Angular accelerations:} \quad & \dot{p}, \dot{q}, \dot{r} \equiv 0 \end{aligned} \tag{2.86}$$

When the steady-state conditions $\dot{p}, \dot{q}, \dot{r} = 0$ are satisfied, the aerodynamic and thrust moments must be zero or constant, indicating that the angular rates to be zero or constant. The conditions $\dot{V}, \dot{\alpha}, \dot{\beta}$ (or $\dot{u}, \dot{v}, \dot{w}$) = 0 necessitates that the airspeed, angle of attack, and sideslip angle be constant, and thus the aerodynamic forces must be zero or constant. As a result, additional constraints based on widely used steady-state flight (trim) conditions are defined as:

$$\begin{aligned} \text{Straight and level flight:} \quad & \dot{\phi}, \dot{\theta}, \dot{\psi}, \gamma, p, q, r \equiv 0 \quad V, h = \text{user defined} \\ \text{Steady climb or descent:} \quad & \dot{\phi}, \dot{\theta}, \dot{\psi}, p, q, r \equiv 0 \quad V, h, \gamma, \delta_t = \text{user defined} \\ \text{Steady turn:} \quad & \dot{\phi}, \dot{\theta}, \gamma \equiv 0 \quad V, h, \phi = \text{use defined} \end{aligned}$$

The reader is referred to Ref. [42] [43] for the detailed knowledge of the trim conditions stated above.

CHAPTER 3

FLIGHT DATA GATHERING AND ANALYSIS

3.1 Flight Data Gathering

The flight test data used in this study are collected from a high-fidelity F-16 simulator. The stability and control augmentation systems have been developed using the aircraft model to carry out the maneuvers. The stability and control derivatives are estimated mainly from the aircraft's dynamic reaction to control inputs. Typically, a variety of maneuvers are required to stimulate dynamic motion about different axes utilizing separate inputs on each control. In general, it is suggested to begin each maneuver with a trimmed level flight to allow for 5 to 10 seconds of steady flight before applying particular control inputs and provide adequate time for the aircraft to oscillate depending on the mode of motion [1] [13]. Trim data for discrete flight conditions defined in Mach numbers ($M = 0.2$ to $M = 0.6$), altitudes ($h = 0$ ft to $h = 40000$ ft) and different flight path angles ($\gamma = -5^\circ$ to $\gamma = 5^\circ$) are collected to generate a preliminary engine thrust model. Maneuvers for system identification (individual models), with two different altitudes and six different speed combinations, are performed out in twelve different trim points in this study. Control inputs of the pilot have been designed to do short-period, phugoid, Dutch-roll, and bank-to-bank maneuvers. The angles of attack and sideslip are covered between $-5^\circ \leq \alpha \leq 18^\circ$ and $-8^\circ \leq \beta \leq 8^\circ$. The longitudinal maneuvers covered an angle of attack range of 0° - 18° . The lateral maneuvers covered an angle of attack range of 4° - 13° and an angle of sideslip range -8° - 8° , respectively. Aircraft geometry, nominal mass, and inertia properties are given in Table 3.1 and Table 3.2

Table 3.1 F-16 Aircraft Geometry and Mass Properties

Property	Symbol	Value	Units
Mass	m	9295	kg
Wingspan	b	30	m
Wing area	S	300	m
Mean aerodynamic chord	\bar{c}	11.32	m
Reference moment center (x -direction)	x_{MC}	$0.35\bar{c}$	m
Reference moment center (y -direction)	y_{MC}	0	m
Reference moment center (z -direction)	z_{MC}	0	m
Center of mass (x -direction)	x_B	$0.3\bar{c}$ - $0.38\bar{c}$	m
Center of mass (y -direction)	y_B	0	m
Center of mass (z -direction)	z_B	0	m

Table 3.2 Aircraft Inertia Tensor in kg-m²

Symbol	Value	Symbol	Value	Symbol	Value
I_{XX}	12875	I_{XY}	0	I_{XZ}	1331
I_{YX}	0	I_{YY}	75674	I_{YZ}	0
I_{ZX}	1331	I_{ZY}	0	I_{ZZ}	85552

3.1.1 Optimized Maneuvers

The primary objective of the system identification maneuvers detailed in this section is to stimulate associated modes of the aircraft motion adequately. In general, while exciting a specific mode, it should be avoided by exciting other modes. The short period, phugoid, Dutch roll, and bank-to-bank maneuvers are described in detail below and shown in Figure 3.1.

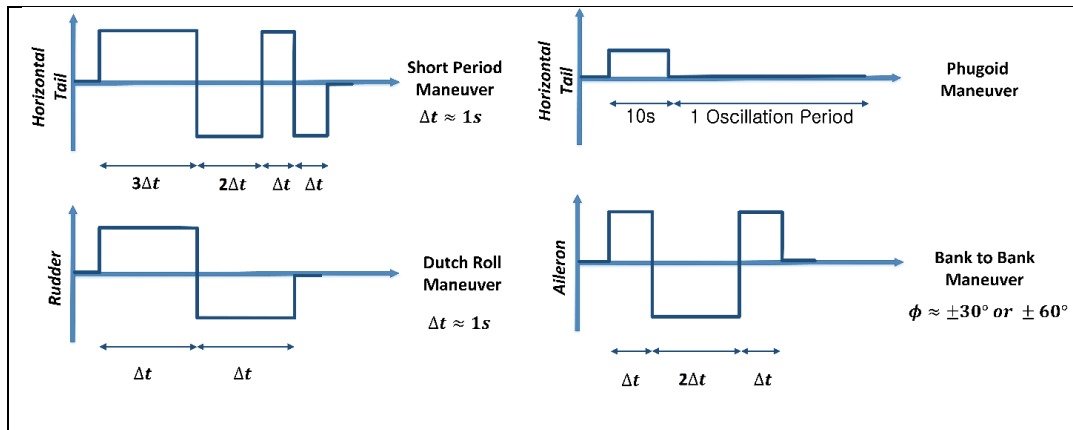


Figure 3.1 Control Inputs for the Short Period, Phugoid, Dutch-Roll, and Bank-to-Bank Maneuvers

The pilot's control inputs are applied to stimulate the different modes of air vehicle via short-period, phugoid, Dutch-roll, and bank-to-bank maneuvers. All test procedures began with level flight trim conditions. Trims were not performed at idle or maximum power settings since the aerodynamic coefficients are not affected by thrust change. The flight test scope is shown in Figure 3.2.

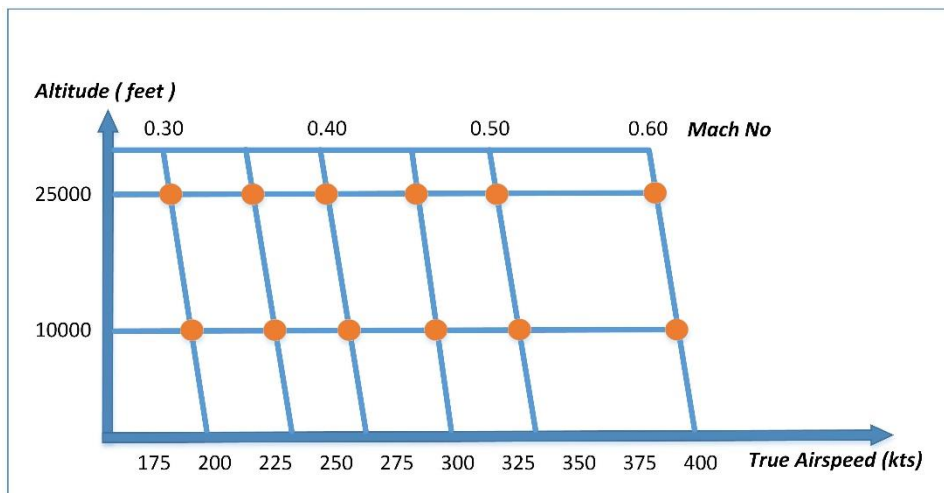


Figure 3.2 Flight Test Scope

3.1.1.1 Short Period Mode (SP)

It is a multi-step 3-2-1-1 elevator input that excites the short period motion with a variation of approximately 4 degrees in angle of attack and 0.5g in vertical

acceleration. It provides enormous information for estimating the vertical and pitching motion derivatives [1].

3.1.1.2 Dutch Roll (DR)

The Dutch Roll maneuver provides knowledge for predicting the lateral motion variables [1]. This maneuver is excited by rudder inputs. Multiple oscillations cycles are often seen. The maximum change in the sideslip angle is typically in the range of ± 4 degrees or 0.1g lateral acceleration. The Dutch roll maneuvers are performed at different trim speeds and altitudes since the lateral-direction derivatives depend on the angle of attack.

3.1.1.3 Bank to Bank (BTB)

Bank-to-Bank maneuver provides extra knowledge on lateral-direction motion variables relating to rolling rate and aileron deflection [1]. Aileron input is applied, rolling the aircraft from wings-level to 30 degrees banking on one side; this is continued by changing input and smoothly transitioning to the wings-level and the opposite bank angle, and then back to wings-level condition. The aileron adjustment causes a rapid change in roll rate and acceleration.

3.1.2 Optimal Input Design

Several different input patterns can be applied to induce oscillatory motion: pulse, doublet, 3-2-1-1 signal, and modifications of the 3-2-1-1 signal. The procedures described by Jategaonkar in Ref. [1] (pages 41–52) are used as guidelines. A pulse input is the most straightforward way to trigger the oscillatory motion. After a certain amount of time has passed, the control is released, allowing the aircraft to oscillate freely without pilot inputs. A pulse input quickly obtains the excitation of long-period modes (e.g., phugoid), but the fast-reacting modes (short-period, dutch-roll)

are more critical than long-period modes. A doublet is a more often utilized input to stimulate the dynamic motion. The doublet input generates a symmetrical signal from a two-sided pulse. Its excitation power varies with time steps, and tuning time steps is critical. Extending the logic of the doublet input, 3-2-1-1 multi-step input can be utilized, which offers a much broader excitation power spectrum than the doublet input. This is why the 3-2-1-1 signal outperforms the doublet input. The other virtue of the 3-2-1-1 is its simplicity and ability to be executed manually. When flown manually, inputs do not have highly sharp edges due to the pilot's filtering effect. It is worth noting that the exact form and time step are not critical. The 3-2-1-1 input on the elevator is suggested to excite the short-period motion, while the doublet input on the rudder is recommended to excite the dutch roll motion. Although the 3-2-1-1 input can be designed for dutch roll excitation, it is weakly damped in comparison to the short period, and therefore a doublet input is found to be sufficient for excitation of the dutch roll. In the following subsections, how to choose the optimal time step is mentioned.

3.1.2.1 Short Period Mode (SP)

Firstly, the longitudinal linearized matrices are obtained from the nonlinear simulation model for the discrete flight conditions performed by maneuvers.

$$\begin{bmatrix} \Delta \dot{u} \\ \Delta \dot{w} \\ \Delta \dot{q} \\ \Delta \dot{\theta} \end{bmatrix} = \begin{bmatrix} \frac{\partial \dot{u}}{\partial u} & \frac{\partial \dot{u}}{\partial w} & \frac{\partial \dot{u}}{\partial q} & \frac{\partial \dot{u}}{\partial \theta} \\ \frac{\partial \dot{w}}{\partial u} & \frac{\partial \dot{w}}{\partial w} & \frac{\partial \dot{w}}{\partial q} & \frac{\partial \dot{w}}{\partial \theta} \\ \frac{\partial \dot{q}}{\partial u} & \frac{\partial \dot{q}}{\partial w} & \frac{\partial \dot{q}}{\partial q} & \frac{\partial \dot{q}}{\partial \theta} \\ \frac{\partial \dot{\theta}}{\partial u} & \frac{\partial \dot{\theta}}{\partial w} & \frac{\partial \dot{\theta}}{\partial q} & \frac{\partial \dot{\theta}}{\partial \theta} \end{bmatrix}_0 \begin{bmatrix} \Delta u \\ \Delta w \\ \Delta q \\ \Delta \theta \end{bmatrix} + \begin{bmatrix} \frac{\partial \dot{u}}{\partial \delta_e} \\ \frac{\partial \dot{w}}{\partial \delta_e} \\ \frac{\partial \dot{q}}{\partial \delta_e} \\ \frac{\partial \dot{\theta}}{\partial \delta_e} \end{bmatrix}_0 \Delta \delta_e \quad (3.1)$$

where subscript 0 represents the equilibrium (trim) point.

Two complex conjugate pairs of eigenvalues result from the four states, corresponding to two stable oscillatory modes. It is possible to determine the natural frequency and period of these pairs of eigenvalues. Because the periods of these

modes are separated by more than an order of magnitude, they are easily distinguished as the short-period and phugoid modes. The phugoid mode has a low damping factor, whereas the short-period mode has a moderate damping factor.

Typically, the time step for the 3-2-1-1 input is set such that the short period's natural frequency falls in the middle of the upper third of the input spectrum. This leads to an estimate for Δt_{3211} given by

$$\Delta t_{3211} \approx \frac{1.6}{\omega_{n_{SP}}} \approx \frac{\pi}{2\omega_{n_{SP}}} \approx \frac{1}{4} \cdot \text{period of oscillation} \quad (3.2)$$

or

$$\Delta t_{3211} \approx \frac{2.1}{\omega_{n_{SP}}} \approx \frac{1}{3} \cdot \text{period of oscillation} \quad (3.3)$$

where $\omega_{n_{SP}}$ is the short period frequency.

3.1.2.2 Dutch Roll (DR)

Firstly, the lateral linearized matrices are obtained from the nonlinear simulation model for the discrete flight conditions performed by maneuvers.

$$\begin{bmatrix} \Delta \dot{v} \\ \Delta \dot{p} \\ \Delta \dot{r} \\ \Delta \dot{\phi} \end{bmatrix} = \begin{bmatrix} \frac{\partial \dot{v}}{\partial v} & \frac{\partial \dot{v}}{\partial p} & \frac{\partial \dot{v}}{\partial r} & \frac{\partial \dot{v}}{\partial \phi} \\ \frac{\partial \dot{p}}{\partial v} & \frac{\partial \dot{p}}{\partial p} & \frac{\partial \dot{p}}{\partial r} & \frac{\partial \dot{p}}{\partial \phi} \\ \frac{\partial \dot{r}}{\partial v} & \frac{\partial \dot{r}}{\partial p} & \frac{\partial \dot{r}}{\partial r} & \frac{\partial \dot{r}}{\partial \phi} \\ 0 & c_\phi & -s_\phi & 0 \end{bmatrix}_0 \begin{bmatrix} \Delta v \\ \Delta p \\ \Delta r \\ \Delta \phi \end{bmatrix} + \begin{bmatrix} \frac{\partial \dot{v}}{\partial \delta_a} & \frac{\partial \dot{v}}{\partial \delta_r} \\ \frac{\partial \dot{p}}{\partial \delta_a} & \frac{\partial \dot{p}}{\partial \delta_r} \\ \frac{\partial \dot{r}}{\partial \delta_a} & \frac{\partial \dot{r}}{\partial \delta_r} \\ 0 & 0 \end{bmatrix}_0 \begin{bmatrix} \Delta \delta_a \\ \Delta \delta_r \end{bmatrix} \quad (3.4)$$

where subscript 0 represents the equilibrium (trim) point.

There are two real eigenvalues and a pair of complex conjugate eigenvalues for lateral/directional motion. The conjugate pairs of eigenvalues represent the dutch roll mode, which is characterized by a rolling and yawing motion with some sideslipping. The natural frequency and period of this pair of eigenvalues can be calculated.

The time step for the doublet input is usually chosen as

$$\Delta t_{DBLT} = \frac{2.3}{\omega_{n_{DR}}} \approx \frac{1}{3} \cdot \text{period of oscillation} \quad (3.5)$$

where $\omega_{n_{DR}}$ is the dutch roll frequency.

3.1.3 Flight Test Instrumentation and Measurement

The quality of measured data influences the parameter estimation accuracy. To use system identification methods effectively, accurate measurements of control inputs and motion variables are recommended.

For the estimate of rigid-body aerodynamic models, a sampling frequency of 20-25 Hz is typically adequate [1] [2]. Since simulation results are recorded at a 20 Hz sampling rate. To identify the aerodynamic model, a typical set of measured quantities are as follows [1] [2]

- Control surface deflections $(\delta_a, \delta_h, \delta_r, \delta_{lef}, \delta_{sb})$,
- The linear accelerations (a_x, a_y, a_z) ,
- Angular rates (p, q, r) ,
- Euler angles (θ, ϕ, ψ) ,
- Air data (M, α, β) ,
- Static pressure, static temperature, and altitude (P_s, T_s, h) ,
- Propulsion parameters (δ_t, T)

The resolution of flight test instrumentation is shown in Table 3.3 [60]

Table 3.3 Flight Test Instrumentation Accuracy and Resolution

SENSOR	RANGE	ACCURACY	RESOLUTION
Pitch Attitude	∓ 90 [deg]	∓ 0.5 [deg]	0.1 [deg]
Roll Attitude	∓ 90 [deg]	∓ 0.5 [deg]	0.1 [deg]
Heading	0 to 360 [deg]	∓ 0.5 [deg]	0.2 [deg]
Pitch Rate	∓ 100 [deg/s]	∓ 0.5 [deg/s]	0.1 [deg/s]
Roll Rate	∓ 300 [deg/s]	∓ 1.0 [deg/s]	0.2 [deg/s]
Yaw Rate	∓ 100 [deg/s]	∓ 0.5 [deg/s]	0.1 [deg/s]
Axial Acceleration	∓ 5 [g]	∓ 0.02 [g]	0.01 [g]
Lateral Acceleration	∓ 5 [g]	∓ 0.02 [g]	0.01 [g]
Normal Acceleration	-5 to 10 [g]	∓ 0.02 [g]	0.01 [g]
Angle of Attack	-45 to 70 [deg]	∓ 0.3 [deg]	0.1 [deg]
Angle of Sideslip	∓ 45 [deg]	∓ 0.3 [deg]	0.1 [deg]
Pressure Altitude	0 to 60000 [ft]	∓ 150 [ft]	20 [ft]
Radar Altitude	0 to 1000 [ft]		
True Airspeed	0 to 1500 [kt]	∓ 2 [kt]	1 [kt]
Mach Number	0 to 2.4 [ft]	∓ 0.005	0.005
Elevator Position	Limits of Travel	∓ 0.2 [deg]	0.2 [deg]
Aileron Position	Limits of Travel	∓ 0.1 [deg]	0.1 [deg]
Rudder Position	Limits of Travel	∓ 0.2 [deg]	0.2 [deg]
Flap Position	Limits of Travel	∓ 0.2 [deg]	0.2 [deg]

3.2 Flight Data Analysis

It is a known fact that errors in measurements can severely degrade the estimation results from flight data [1] [12] [31]. Two data preprocessing steps were taken before the model identification to avoid parameter estimation errors.

3.2.1 Flight Data Prefiltering

It is recommended to record raw data, and occasionally eliminating high-frequency noise is required prior to using the signals. The numerical differentiation of measured angular rates, followed by filtering, is preferred to generate the angular accelerations. To accomplish this, digital filters based on a linear combination of input values are used extensively. They do not introduce any delay in the filtered values owing to symmetry. This study uses Spencer's low-pass digital filter, based on 15 points, the present value, and the preceding as well as the following seven data points as formulated as follows:

$$y_n = \frac{1}{320} [-3u_{n-7} - 6u_{n-6} - 5u_{n-5} + 3u_{n-4} + 21u_{n-3} + 46u_{n-2} + 67u_{n-1} + 74u_n + 67u_{n+1} + 46u_{n+2} + 21u_{n+3} + 3u_{n+4} - 5u_{n+5} - 6u_{n+6} - 3u_{n+7}] \quad (3.6)$$

For all data points except for the first and the last seven, the above equation can be accurately applied. A filter that uses fewer data points is applied to the two ends of the time series to make it smooth. The first two and the last two data points cannot be adequately filtered due to a lack of adequate information. Ensure to use the procedure. The following filter for two data points can be incorporated:

$$y_n = \frac{1}{96} [7u_{n-2} + 24u_{n-1} + 34u_n + 24u_{n+1} + 7u_{n+2}] \quad (3.7)$$

3.2.2 Flight Path Reconstruction

Secondly, flight path reconstruction [1] [2] [62], which is also called the data compatibility check, is utilized. The goal of flight path reconstruction is to guarantee that kinematically consistent and error-free flight measurements are obtained. Flight data are kinematically consistent if the integrated state variables (e.g., the air data obtained from linear accelerations, or the attitude angles obtained from the rotational kinematics) match up with direct measurements [28]. Flightpath reconstruction

involves two main parts: 1) state integration 2) observer equations for comparison of estimated (reconstructed) and measured outputs. The state integration consists of integrating translational dynamics, integrating rotational kinematics, and integrating navigational kinematics. Generally, accurate mounting of the sensor is possible; misalignments are very minimal. Additionally, these correction components are often less than the measurement noise. For these reasons, we generally ignore these corrections in practice [1]. Some drifts in the estimated and measured outputs suggest introducing time lags (delays), biases, and/or scale factors in the measurement signals (e.g., linear accelerations, angular rates, angle of attack, and angle of sideslip) as well as time-invariant atmospheric wind speeds [1] [2] [9] [22] [63]. The output error technique is used to estimate the time lags, biases, and/or scale factors in the measurement signals and time-invariant atmospheric wind speeds. Since the body-fixed axes system is defined with respect to CM, the measured accelerations and velocity components were transferred from the sensor locations to the CM [1] [64].

Any typically measured variable can be expressed as

$$y_m(t) = K_y y(t - \tau) + \Delta y \quad (3.8)$$

where K_y is the calibration factor, Δy the unknown instrument bias, and τ the time delay in the measured variable. The subscript m on the left-hand side indicates the measured quantity. The time constant is omitted since no time delay is introduced in the measured variables. The equation turns out to be

$$y_m(t) = K_y y(t) + \Delta y \quad (3.9)$$

The state variable, control input, and observation vectors for data compatibility are given in Table 3.4.

Table 3.4 Input, State, Observation, and Unknown Variables Vectors for Data Compatibility

Symbol	Description	Variables
u	Control Input Vector	$[a_{s_x,AS}, a_{s_y,AS}, a_{s_z,AS}, p, q, r]$
x	State Variable Vector	$[u, v, w, \phi, \theta, \psi, p_D]$
y	Observation Vector	$[V, \alpha, \beta, \phi, \theta, \psi, h]$
Θ	Unknown Variables	$[\Delta a_{s_x}, \Delta a_{s_y}, \Delta a_{s_z}, \Delta p, \Delta q, \Delta r, K_\alpha, \Delta \alpha, K_\beta, \Delta \beta]$

As seen in Table 3.4, the linear accelerations and angular rates' the scale factors are not included. This is because scale factors are highly correlated with biases and lead to poor quantitative identifiability. Furthermore, scale factor errors are negligible in the high precision accelerometers and rate gyros, and their calibrating is more accurate than that of other measured variables. The bias errors are also negligible for the same reason, but they are included in the model to prevent drifting in the integrated variables.

It is worth noting that the sensor errors Δa_{s_y} , Δp , Δq , K_β , and $\Delta \beta$ appear as bias parameters within the estimation model, but their determination for the longitudinal variable consistency procedure is not critical. For practical use, it is recommended to divide maneuvers as longitudinal and lateral. The procedure to estimate longitudinal and lateral error terms is as follows: First, the flight data from longitudinal maneuvers are concatenated, and primary longitudinal unknown variables are estimated. And then, the time history plots are observed, and primary variables related to longitudinal maneuvers are frozen. Finally, lateral maneuvers are utilized to estimate the primary lateral variables. Table 3.5 summarizes the primary variables for different maneuvers.

Table 3.5 Maneuvers and Primary Unknown Variables for Data Compatibility.

Maneuvers	Primary Variables
Longitudinal (Short-Period, Phugoid)	$[\Delta a_{s_x}, \Delta a_{s_z}, \Delta q, K_\alpha, \Delta \alpha]$
Lateral (Dutch-Roll, Bank-to-Bank)	$[\Delta a_{s_y}, \Delta p, \Delta r, K_\beta, \Delta \beta]$

State and observation equations for flight path reconstruction are given in the coming subsections.

3.2.2.1 State Equations

The following transformation is used to compute the body-axes specific accelerations at the CM from the specific accelerations measured at the accelerometer sensor position (AS):

$$\begin{aligned}
 & \begin{bmatrix} a_{s_x} \\ a_{s_y} \\ a_{s_z} \end{bmatrix} \\
 &= \begin{bmatrix} a_{s_x, AS_m} - \Delta a_{s_x} \\ a_{s_y, AS_m} - \Delta a_{s_y} \\ a_{s_z, AS_m} - \Delta a_{s_z} \end{bmatrix} - \begin{bmatrix} \dot{p} \\ \dot{q} \\ \dot{r} \end{bmatrix} \times \begin{bmatrix} x_{AS/B} \\ y_{AS/B} \\ z_{AS/B} \end{bmatrix} \\
 & \quad - \begin{bmatrix} p_m - \Delta p \\ q_m - \Delta q \\ r_m - \Delta r \end{bmatrix} \times \left(\begin{bmatrix} p_m - \Delta p \\ q_m - \Delta q \\ r_m - \Delta r \end{bmatrix} \times \begin{bmatrix} x_{AS/B} \\ y_{AS/B} \\ z_{AS/B} \end{bmatrix} \right)
 \end{aligned} \tag{3.10}$$

The complete set of nonlinear system equations are given by

$$\begin{aligned}
 \begin{bmatrix} \dot{x}_1 \\ \dot{x}_2 \\ \dot{x}_3 \end{bmatrix} &= \begin{bmatrix} \dot{u} \\ \dot{v} \\ \dot{w} \end{bmatrix} = \begin{bmatrix} a_{s_x} \\ a_{s_y} \\ a_{s_z} \end{bmatrix} + \begin{bmatrix} -g s_\phi c_{\theta_m} \\ g s_\phi c_{\theta_m} \\ g c_\phi c_{\theta_m} \end{bmatrix} - \begin{bmatrix} p_m - \Delta p \\ q_m - \Delta q \\ r_m - \Delta r \end{bmatrix} \times \begin{bmatrix} u \\ v \\ w \end{bmatrix} \\
 \begin{bmatrix} \dot{x}_4 \\ \dot{x}_5 \\ \dot{x}_6 \end{bmatrix} &= \begin{bmatrix} \dot{\phi} \\ \dot{\theta} \\ \dot{\psi} \end{bmatrix} = \begin{bmatrix} 1 & s_\phi t_\theta & c_\phi t_\theta \\ 0 & c_\phi & -s_\phi \\ 0 & s_\phi / c_\theta & c_\phi / c_\theta \end{bmatrix} \begin{bmatrix} p \\ q \\ r \end{bmatrix} \\
 \dot{x}_7 &= \dot{p}_D = \begin{bmatrix} -s_\theta & s_\phi c_\theta & c_\phi c_\theta \end{bmatrix} \begin{bmatrix} u \\ v \\ w \end{bmatrix}
 \end{aligned} \tag{3.11}$$

3.2.2.2 Observation Equations

The velocity components along the body axes at the air data boom (subscript ADB) are computed from velocity components along the body axes at CM as follows:

$$\begin{bmatrix} u_{ADB} \\ v_{ADB} \\ w_{ADB} \end{bmatrix} = \begin{bmatrix} u \\ v \\ w \end{bmatrix} + \begin{bmatrix} p_m - \Delta p \\ q_m - \Delta q \\ r_m - \Delta r \end{bmatrix} \times \begin{bmatrix} x_{ADB/B} \\ y_{ADB/B} \\ z_{ADB/B} \end{bmatrix} \quad (3.12)$$

The observation equations are given by

$$\begin{aligned} y_1 &= V_{ADB} = \sqrt{(u_{ADB})^2 + (v_{ADB})^2 + (w_{ADB})^2} \\ y_2 &= \alpha_{ADB} = K_\alpha \left(\tan^{-1} \frac{w_{ADB}}{u_{ADB}} \right) + \Delta\alpha \\ y_3 &= \beta_{ADB} = K_\beta \left(\tan^{-1} \frac{v_{ADB}}{u_{ADB}} \right) + \Delta\beta \\ y_4 &= \phi \\ y_5 &= \theta \\ y_6 &= \psi \\ y_7 &= -p_D \end{aligned} \quad (3.13)$$

CHAPTER 4

METHODOLOGY

4.1 Model Description

The following general nonlinear system provides a mathematical model of the dynamic system in state space [1] [2] [60]:

$$\begin{aligned}\dot{\vec{x}}(t) &= f[\vec{x}(t), \vec{u}(t), \vec{\beta}] + F(\lambda)\vec{w}(t), & \vec{x}(t_0) &= \vec{x}_0 \\ \vec{y}(t) &= g[\vec{x}(t), \vec{u}(t), \vec{\beta}]\end{aligned}\tag{4.1}$$

where \vec{x} is the $n_x \times 1$ state variables vector, \vec{u} is the $n_u \times 1$ control input vector, \vec{y} is the $n_y \times 1$ system output vector, $\vec{\beta}$ is the $n_\beta \times 1$ system parameter vector, n_x and n_y are the dimensional system functions, and f and g are general nonlinear scalar-valued functions. Along with the deterministic control input \vec{u} , the system is also excited by process noise $\vec{w}(t)$, a stochastic input, which is usually nonmeasurable $n_w \times 1$ column vector. The matrix F represents the additive process (state) noise distribution matrix.

Due to the impossibility of measuring the system parameters $\vec{\beta}$, they must be estimated from discrete measurements $\vec{z}(t_k)$ of the model outputs $\vec{y}(t_k)$. The output equation is formulated as

$$\vec{z}(t_k) = \vec{y}(t_k) + G\vec{v}(t_k)\tag{4.2}$$

where k is the discrete-time index and $\vec{v}(t_k)$ is the $n_v \times 1$ measurement noise vector. The measurement noise vector is assumed to be characterized by a sequence of independent Gaussian random variables with zero mean and identity covariance. The matrix G represents the additive measurement noise distribution matrix.

Apart from the system parameters β , it is assumed that the elements λ of process noise distribution matrix F , and the starting conditions x_0 are also unknown. As a result, the unknown parameter vector is as follows:

$$\vec{\Theta} = [\vec{\beta}^T \quad \vec{\lambda}^T \quad \vec{x}_0^T]^T \quad (4.3)$$

In this study, there is no stochastic input, process noise. So, the formulation becomes

$$\begin{aligned} \dot{\vec{x}}(t) &= f[\vec{x}(t), \vec{u}(t), \vec{\beta}] + F(\lambda)\vec{w}(t), \quad \vec{x}(t_0) = \vec{x}_0 \\ \vec{y}(t) &= g[\vec{x}(t), \vec{u}(t), \vec{\beta}] \\ \vec{z}(t_k) &= \vec{y}(t_k) + G\vec{v}(t_k) \end{aligned} \quad (4.4)$$

and the unknown vector is

$$\vec{\Theta} = [\vec{\beta}^T \quad \vec{x}_0^T]^T \quad (4.5)$$

In the aircraft system identification problem, $\vec{\beta}$ correspond to aerodynamic forces and moments related parameters.

4.2 Integration of State Equations

There are many algorithms to integrate the state equations numerically. The Euler, Runge-Kutta 2nd and Runge-Kutta 4th order integration methods are concentrated in the study. The Euler integration needs just one evaluation of the state derivative function at each time point; the Runge-Kutta 2nd and 4th order algorithms need two and four evaluations. The computational burden is related to the number of function evaluations [31]. The Euler integration is the fastest, while the Runge-Kutta 4th is the slowest. The higher-order integration algorithms provide more accurate results than low-order integration formulas.

The Runge-Kutta 4th is usually suggested for rigid body system identification. Due to adverse error propagation, the Euler integration is not recommended, especially for long-duration maneuvers and sampling rates larger than 20 milliseconds [31].

However, second-order integration suffices [65]. For substantial problems, the computational time can be reduced by starting with a more straightforward integration method, the Euler method, the Runge-Kutta 2nd order method, and a few iterations or convergence switching over to a higher-order algorithm Runge-Kutta 4th order method.

4.3 Parameter Estimation Methods

For regression, the sum of squared errors as an objective function (cost function) is used and given in Eq. (4.6).

$$f(\vec{\Theta}) = \frac{1}{N} \sum_{k=1}^N \left(\vec{z}(t_k) - \vec{y}(\vec{\Theta}; \vec{u}(t_k)) \right)^T \left(\vec{z}(t_k) - \vec{y}(\vec{\Theta}; \vec{u}(t_k)) \right) \quad (4.6)$$

This problem can be solved using any minimization optimization problem. Gauss-Newton algorithm is one of the most widely used minimization algorithms and is selected for this study.

The parameter estimation process is frequently usually unstable, in that a little change in measurement might result in a large change in the estimated model. Inverse problems that develop because of this scenario are referred to as ill-conditioned problems. Regularization is the process of enhancing the stability of the inversion process by introducing extra constraints that bias the result. Tikhonov regularization is the most often used approach for regularization. Another possibility is to employ the bounds constraint technique, which is inserting lower and upper bounds in model parameters [66]. The unconstrained optimization problem may be modified to include these lower and upper bounds. This results in the formulation of a linearly constrained optimization problem as [67]:

$$\min_{\vec{\Theta}} f(\vec{\Theta}) \text{ subject to } \vec{\Theta}_{min} \leq \vec{\Theta} \leq \vec{\Theta}_{max} \quad (4.7)$$

In standard form,

$$\min_{\vec{\Theta}} f(\vec{\Theta}) \text{ subject to } c_1: \vec{\Theta} - \vec{\Theta}_{min} \geq 0, c_2: \vec{\Theta}_{max} - \vec{\Theta} \geq 0 \quad (4.8)$$

Barrier methods [61] provide an effective solution to this constrained optimization problem. The constrained optimization problem is reconstructed as an unconstrained problem with logarithmic barrier terms added to the objective function. As a point approaches the boundary of an optimization problem's feasible area, a logarithmic barrier term increases to infinity. For regions that are possible further from the boundary, the logarithmic terms are negligible. The new optimization problem (combined objective/barrier function) is formulated for the inequality-constrained optimization problem.

$$f(\vec{\Theta}; \mu) \leftarrow f(\vec{\Theta}) - \mu [\log(\vec{\Theta} - \vec{\Theta}_{min}) + \log(\vec{\Theta}_{max} - \vec{\Theta})] \quad (4.9)$$

To estimate aerodynamic parameters defined in the model postulate, equation error and output error methods in the time domain are used to analyze simulated data. In the first phase, the equation-error method is utilized firstly to identify aerodynamic parameters, and in the second phase, the result from the equation-error process is used as a starting point in the output-error method for fine-tuning.

The mathematical model required for the equation error and the output error methods is shown in Figure 4.1.

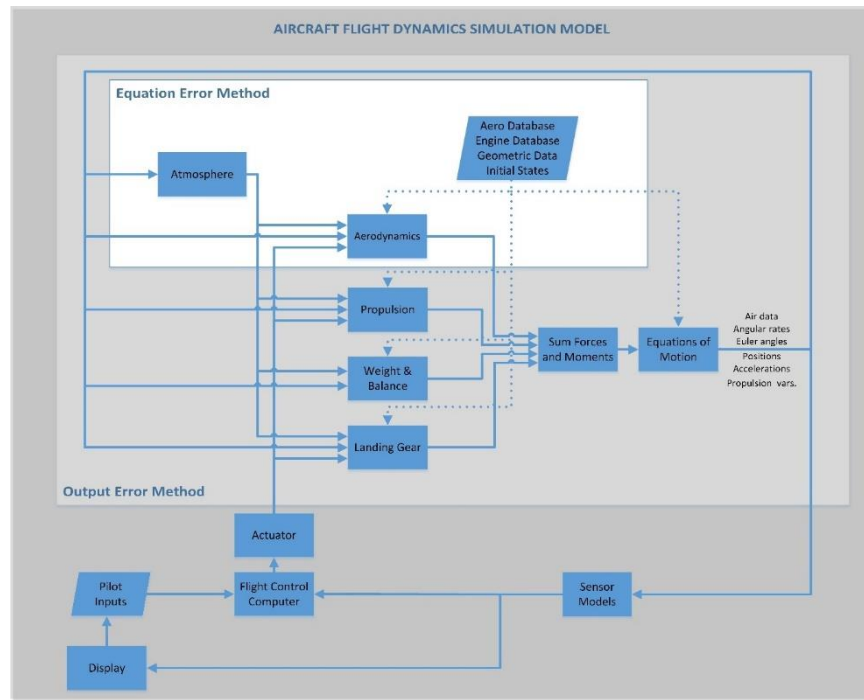


Figure 4.1 Mathematical Model Required for the Equation Error and the Output Error Methods

4.3.1 Gauss-Newton Algorithm

In this part, the derivation of the Gauss-Newton algorithm is presented in two parts: (1) Newton's algorithm and (2) Gauss–Newton's algorithm. Before the derivation, let us introduce some commonly used terminologies:

In least-squares problems, the observed values, \vec{z} , are compared with the model prediction vector, \vec{y} , and the difference between these values is referred to as the residual vector, \vec{r} . The objective (cost) function f incorporates the residual and is denoted by the following form:

$$\begin{aligned}
f(\vec{\Theta}) &= \frac{1}{N} \sum_{j=1}^N \left(\vec{z}_j - \vec{y}(\vec{\Theta}; \vec{u}_j) \right)^2 \\
&= \frac{1}{N} \sum_{i=1}^N \left(\vec{z}_j - \vec{y}_j(\vec{\Theta}) \right)^2 \\
&= \frac{1}{N} \sum_{j=1}^N \vec{r}_j(\vec{\Theta})^2
\end{aligned} \tag{4.10}$$

where N is the number of data points, $\vec{\Theta} \in \mathbb{R}^m$ denotes variable vector with $m \geq 1$ components, also called unknowns or parameters, and \vec{u} is the control input vector. During training, the unknown variables are repeatedly adjusted to minimize the objective function: mean square error.

The vector of first derivatives of f is called the function gradient and is notated as a first-order derivative of the objective function.

$$\nabla f(\vec{\Theta}) = \left[\frac{\partial f(\vec{\Theta})}{\partial \Theta_1} \quad \dots \quad \frac{\partial f(\vec{\Theta})}{\partial \Theta_m} \right]^T \tag{4.11}$$

The matrix of second derivatives of f is called the Hessian matrix or simply the Hessian and is notated as $\nabla^2 f$. It is the matrix with entries.

$$[\nabla^2 f(\vec{\Theta})]_{ij} = \frac{\partial^2 f(\vec{\Theta})}{\partial \Theta_i \partial \Theta_j} \tag{4.12}$$

To define the Jacobian, a vector-valued function, $\vec{r}: \mathbb{R}^n \rightarrow \mathbb{R}^m$, that is used:

$$\vec{r}(\vec{\Theta}) = \begin{bmatrix} r_1(\vec{\Theta}) \\ r_2(\vec{\Theta}) \\ \vdots \\ r_N(\vec{\Theta}) \end{bmatrix} = \begin{bmatrix} r_1(\Theta_1, \Theta_2, \dots, \Theta_m) \\ r_2(\Theta_1, \Theta_2, \dots, \Theta_m) \\ \vdots \\ r_N(\Theta_1, \Theta_2, \dots, \Theta_m) \end{bmatrix} \tag{4.13}$$

where each $r_j: \mathbb{R}^m \rightarrow \mathbb{R}$, $j = 1, 2, \dots, N$, is a scalar-valued function of m variables.

The Jacobian is the matrix with entries.

$$\left(J(\vec{\Theta})\right)_{ij} \equiv \frac{\partial r_i(\vec{\Theta})}{\partial \Theta_j} \quad (4.14)$$

where i represents the equation index, and j represents the independent variable index. Then, we have

$$\begin{aligned} \nabla f(\vec{\Theta}) &= \frac{1}{N} 2 \sum_{j=1}^N r_j(\vec{\Theta}) \nabla r_j(\vec{\Theta}) \\ &= \frac{2}{N} J(\vec{\Theta})^T \vec{r}(\vec{\Theta}) \end{aligned} \quad (4.15)$$

and

$$\begin{aligned} \nabla^2 f(\vec{\Theta}) &= \frac{2}{N} \left[\sum_{j=1}^N \nabla r_j(\vec{\Theta}) \nabla r_j(\vec{\Theta})^T + \sum_{j=1}^N r_j(\vec{\Theta}) \nabla^2 r_j(\vec{\Theta}) \right] \\ &= \frac{2}{N} \left[J(\vec{\Theta})^T J(\vec{\Theta}) + \sum_{j=1}^N r_j(\vec{\Theta}) \nabla^2 r_j(\vec{\Theta}) \right] \end{aligned} \quad (4.16)$$

One of the critical search directions is the Newton direction. This direction is obtained using the second-order Taylor series approximation to $f([\vec{\Theta}]^k + \vec{p}^k)$ and is computed as follows:

$$\nabla^2 f([\vec{\Theta}]^k) [\vec{p}^k]^N = -\nabla f([\vec{\Theta}]^k) \quad (4.17)$$

and then uses a line search to determine

$$[\vec{\Theta}]^{k+1} = [\vec{\Theta}]^k + [\vec{p}^k]^N \quad (4.18)$$

The computation of the Hessian matrix is a critical step in the implementation of Newton's method. While Newton's method produces excellent local convergence, it has some drawbacks:

- The Newton algorithm does not work if the Hessian is not invertible.

- The Newton algorithm may not converge.
- The Newton algorithm can converge to a saddle point instead of to a local minimum.

Gauss-Newton's technique is regarded as just a modification of Newton's method. The Hessian is approximated by the first term of Eq. (4.16), assuming $J(\vec{\theta})^T J(\vec{\theta})$ is often more crucial than the second summation term. The direction is computed from Eqs. (4.15)(4.16)(4.18) and dividing both sides by as follows $\frac{2}{N}$,

$$J(\vec{\theta}^k)^T J(\vec{\theta}^k) [\vec{p}^k]^{GN} = -J(\vec{\theta}^k)^T \vec{r}(\vec{\theta}^k) \quad (4.19)$$

and then uses a line search to determine

$$\vec{\theta}^{k+1} = \vec{\theta}^k + [\vec{p}^k]^{GN} \quad (4.20)$$

While the Gauss-Newton technique often works well in practice, it is based on Newton's method and, therefore, may fail for the same reasons as Newton's Method. Additionally, when the matrix $J(\vec{\theta})^T J(\vec{\theta})$ is singular, the technique can fail.

4.3.2 Equation Error Method

Non-state parameters which are not integrated throughout the simulation, such as force and moment coefficients, are determined without considering their history. This technique is referred to as the equation-error method and is computationally efficient since it does not require integration of the assumed model.

The equation-error method is one of the earliest analytical methods for estimating aircraft dynamic model parameters from flight data. Instead of matching the states or outputs, the equation-error method matches state time-derivative knowledge from the dynamic system. When using this approach, model outputs does not need to be integrated since the matching is done directly in those equations themselves (hence

the name “equation-error”). This method works well with data from inherently unstable aircraft flying under closed-loop feedback control [1] [68].

This technique is used to calculate the aerodynamic parameter estimates by minimizing the cost function which is obtained nondimensional force and moment coefficients and the estimated model values. The non-dimensional force and moment coefficients are calculated by replacing measured and known quantities.

For the equation error estimation, the control input, state variables, measured / model output vectors, and unknown (estimated) variables are shown in Table 4.1.

Table 4.1 Input, State Variable, and Output Vectors and Unknown Variables for the Equation Error Method.

Symbol	Description	Variables
\vec{u}	Control Input Vector	$[V, \alpha, \beta, p, q, r, \delta_{lef}, \delta_e, \delta_a, \delta_r, \delta_{sb}, M]$
\vec{x}	State Variable Vector	$[\]$
\vec{y}	Model Observation Vector	$[C_X, C_Y, C_Z, C_l, C_m, C_n]$
$\vec{\theta}$	Unknown Variables	$[C_X, C_Y, C_Z, C_l, C_m, C_n]$ Model Variables

The model structure for each aerodynamic coefficient is found separately since this approach simplifies the training task and focuses on one coefficient each time.

Some properties of the equation error method can be summarized as:

- The equation error method minimizes the equation error between measured and estimated dependent variables
- Presents a single shot solution; no iterations are required
- Easy to implement, involves simple matrix operations
- Preferred for a nonlinear and unstable system

4.3.2.1 Observation Equations

Because the aerodynamic forces and moments are not directly measured, a preprocessing step is necessary in the case of aerodynamic parameter identification. Aerodynamic force and moment coefficients can be computed using the measurements of the associated variables such as linear accelerations, and angular rates, mass properties, and other external forces and moments as shown in Figure 4.2.

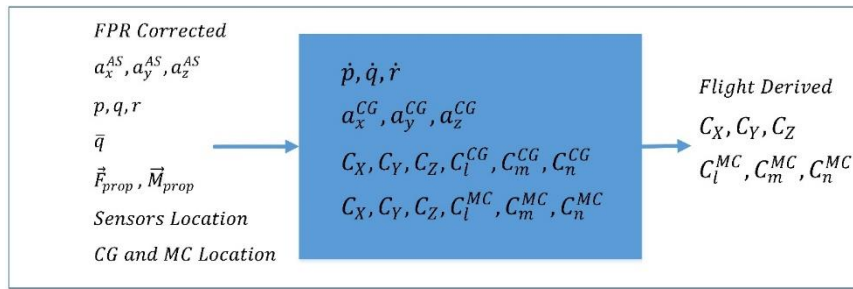


Figure 4.2 Schematic of Data Preprocessing to Compute Aerodynamic Force and Moment Coefficients from Flight Measured Data

To summarize, the equation-error method minimize the cost function to estimate aerodynamic parameters, and the non-dimensional force and moment coefficients are computed by replacing measured and known quantities. Since thrust-related forces and moments are determined from the manufacturer engine database, the equation error approach is utilized in order to simulate the functional dependence of aerodynamic forces and moments on aircraft control, state and output variables. See Figure 4.3 (modified from Ref. [69][p.15][Fig. 12]).

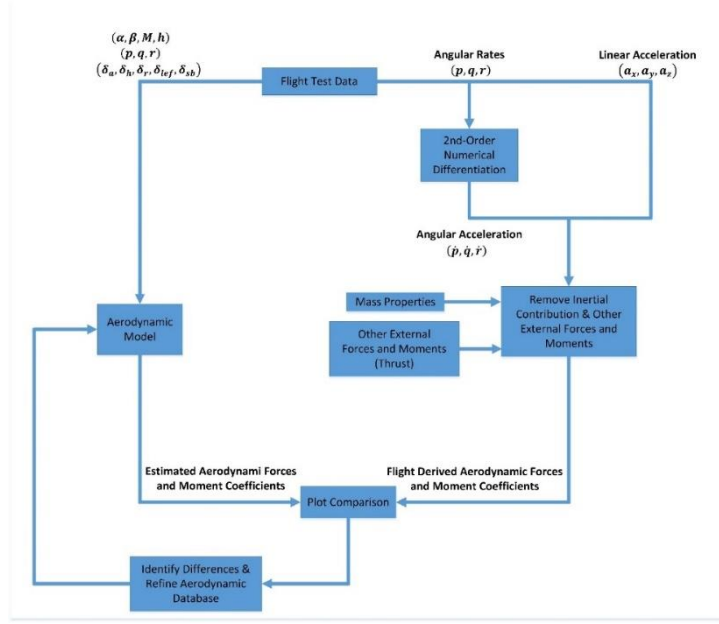


Figure 4.3 Flowchart of the Equation Error Method

How to compute the nondimensional force and moment coefficients are shown in the following equations. The body-axes specific accelerations at the CM are computed from measured accelerations at the accelerometer sensor position using the following transformation:

$$\begin{bmatrix} a_{sx} \\ a_{sy} \\ a_{sz} \end{bmatrix} = \begin{bmatrix} a_{sx,AS} \\ a_{sx,AS} \\ a_{sz,AS} \end{bmatrix} - \begin{bmatrix} \dot{p} \\ \dot{q} \\ \dot{r} \end{bmatrix} \times \begin{bmatrix} x_{AS/B} \\ y_{AS/B} \\ z_{SA/B} \end{bmatrix} - \begin{bmatrix} p \\ q \\ r \end{bmatrix} \times \left(\begin{bmatrix} p \\ q \\ r \end{bmatrix} \times \begin{bmatrix} x_{AS/B} \\ y_{AS/B} \\ z_{AS/B} \end{bmatrix} \right) \quad (4.21)$$

The body-axes aerodynamic force coefficients are obtained as follows:

$$\begin{bmatrix} C_X \\ C_Y \\ C_Z \end{bmatrix} = \frac{1}{\bar{q}S} \left(m \begin{bmatrix} a_{sx} \\ a_{sy} \\ a_{sz} \end{bmatrix} - \begin{bmatrix} T \\ 0 \\ 0 \end{bmatrix} \right) \quad (4.22)$$

The non-dimensional force components resolved in the wind axis can be obtained using the transformation matrix from body to wind and written as follows:

$$\begin{bmatrix} C_D \\ C_C \\ C_L \end{bmatrix} = -\frac{1}{\bar{q}S} \begin{bmatrix} c_\alpha c_\beta & s_\beta & s_\alpha c_\beta \\ -c_\alpha s_\beta & c_\beta & -s_\alpha s_\beta \\ -s_\alpha & 0 & c_\alpha \end{bmatrix} \begin{bmatrix} m a_{sx} - T \\ m a_{sy} \\ m a_{sz} \end{bmatrix} \quad (4.23)$$

The aerodynamic body-axes moments at the CM are computed as follows:

$$\begin{bmatrix} l_a \\ m_a \\ n_a \end{bmatrix} = \begin{bmatrix} p \\ q \\ r \end{bmatrix} \times \begin{bmatrix} I_{XX} & -I_{XY} & -I_{XZ} \\ -I_{XY} & I_{YY} & -I_{YZ} \\ -I_{XZ} & -I_{YZ} & I_{ZZ} \end{bmatrix} \begin{bmatrix} p \\ q \\ r \end{bmatrix} + \begin{bmatrix} I_{XX} & -I_{XY} & -I_{XZ} \\ -I_{XY} & I_{YY} & -I_{YZ} \\ -I_{XZ} & -I_{YZ} & I_{ZZ} \end{bmatrix} \begin{bmatrix} \dot{p} \\ \dot{q} \\ \dot{r} \end{bmatrix} \quad (4.24)$$

The body axes rolling, pitching, and yawing coefficients referred to CM are obtained by

$$\begin{bmatrix} C_l \\ C_m \\ C_n \end{bmatrix} = \frac{1}{\bar{q}S} \begin{bmatrix} 1/b & 0 & 0 \\ 0 & 1/\bar{c} & 0 \\ 0 & 0 & 1/b \end{bmatrix} \begin{bmatrix} l_a \\ m_a \\ n_a \end{bmatrix} \quad (4.25)$$

The moment coefficients referred to aerodynamic moment reference point (MRP) on the vehicle is obtained as

$$\begin{aligned} C_{l_{MRP}} &= C_l - C_Z \frac{x_{MRP/B}}{b} + C_Y \frac{z_{MRP/B}}{b} \\ C_{m_{MRP}} &= C_m - C_X \frac{z_{MRP/B}}{\bar{c}} + C_Z \frac{x_{MRP/B}}{\bar{c}} \\ C_{n_{MRP}} &= C_n - C_Y \frac{x_{MRP/B}}{b} + C_X \frac{y_{MRP/B}}{b} \end{aligned} \quad (4.26)$$

4.3.2.2 Sensitivity Analysis

Since the output error method is a computationally expensive technique and updating all parameters obtained with the equation error method is not feasible, identifying the most influential parameters in each aerodynamic coefficient model is necessary. To do so, sensitivity analysis is utilized. The sensitivity analysis aims to determine the most effective longitudinal and lateral/directional terms, which is tuned in the output error method.

Sensitivity analysis is the process of determining how different types of uncertainty in the model input influence the model's uncertainty. The sensitivity analysis is considered how the parameters of a model influence the optimization cost function from a parameter estimation viewpoint. Sensitivity analysis is employed to assess

the impact of a model's parameters on the output by ranking them in order of importance.

The derivative-based method for sensitivity analysis is known as local sensitivity analysis. A parameter's sensitivity to the cost function equals the partial derivative of the cost function with regard to that value. The term "local" leads to concept that all derivatives are computed at a single point. This method works well for basic cost functions. Local sensitivity analysis is a method that is performed one at a time (OAT). OAT methods examine the impact of only one parameter on the cost function at a time while keeping the other parameters constant.

4.3.2.2.1 Quantifying Parameter Sensitivity

To quantify the parameter sensitivity, aerodynamic coefficient parameters with the optimum model structure are estimated for each coefficient and recorded as baseline parameters, and the cost function is recorded as baseline cost function. Then each parameter is changed by 1% from its baseline value. The model is simulated with the same control input vectors, and the resulting cost function is calculated and recorded. Finally, the sensitivity magnitude is computed as

$$\vec{S}_i = \frac{f_i(\vec{\Theta} + 0.01 \cdot \vec{\Theta}_i, \vec{u}) - f(\vec{\Theta}, \vec{u})}{f(\vec{\Theta}, \vec{u})}; i = 1, 2, \dots, n_{\Theta} \quad (4.27)$$

where $\vec{\Theta}$ is the baseline parameter vector, \vec{u} the control input vector $f(\vec{\Theta}, \vec{u})$ the base cost function, $f_i(\vec{\Theta} + 0.01 \cdot \vec{\Theta}_i, \vec{u})$ the resulting cost function for the i^{th} parameter in the model, and \vec{S}_i the sensitivity magnitude for the i^{th} parameter in the model.

Since the optimum parameters are varied, the resulting cost function increased, and sensitivity magnitude is always positive. To make a more consistent comparison for each coefficient, values of sensitivity magnitudes are normalized by the most significant sensitivity magnitude.

$$\vec{S}_{n_i} = \frac{\vec{S}_i}{\max(\vec{S})}; i = 1, 2, \dots, n_{\Theta} \quad (4.28)$$

This is carried out for each parameter in each aerodynamic coefficient. Parameters with greater sensitivity magnitudes highly influence the model output and are selected to be tuned in the second phase. On the other hand, parameters with less influence have lower sensitivity magnitudes. For the rest of the study, the parameters whose normalized sensitivity magnitude fell below 5% are not tuned in the second phase (output error method).

4.3.3 Output Error Method

Since the outputs of the system, such as the angle of attack, angle of sideslip, roll-pitch-yaw rates, and so on, are integrated throughout the simulation, the technique is referred to as the output-error method. The output-error method can be regarded of as a technique in which the model is used to match the dynamic system's states or outputs. A model which uses the parameter estimates obtained with equation error method does not achieve the necessary fit the dynamic system's measured outputs since that is not what is being optimized. Any mismatch in equation-error model is integrated over time, and numerical integration of unstable systems may result in numerical divergence during the simulation. Unless the modeling errors caused by from the equation-error parameter estimation are minimal in amplitude (magnitude) and zero in mean, the result can be a considerable difference between measured outputs and the model outputs calculated using the equations of motion. In the output-error case, the discrepancy between measured and model outputs is deliberately reduced via the parameter estimation adjustment. The estimates obtained with the equation-error method are used as initial guesses, which are bounded at ± 10 of the initial values. The output error method has been the most commonly used time-domain method for estimating aerodynamic parameters from flight data since its establishment [1]. The flowchart of the output-error method is

shown in Figure 4.4. The result obtained in the equation error method is used as a starting point in the output method for fine-tuning.

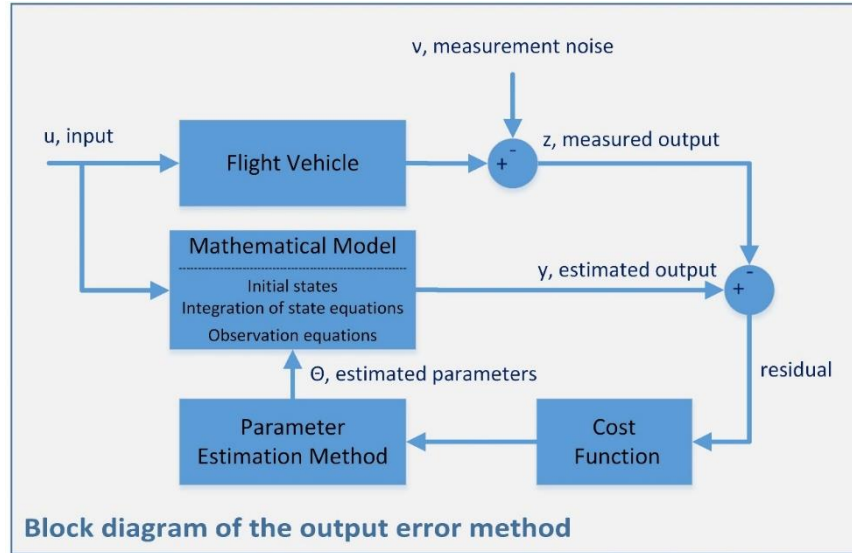


Figure 4.4 Flowchart of the Output Error Method

In longitudinal maneuvers, drag, lift, and pitch moment coefficients are the primary concern, and side force, roll moment, and yaw moment coefficients are the secondary concern and vice versa. Hence, longitudinal and lateral/directional dynamics are considered decoupled.

Additional terms, which are the measured variables, are added to the control input vector u . These measured additional terms were then considered as pseudo-inputs. By including the pseudo-control inputs, the size of the model is lowered and the impacts of additional motion variables, which are not considered as state variables, are taken into consideration. For instance, in the longitudinal decoupled model with the forward speed, vertical speed, pitch rate, pitch attitude, and pressure altitude (u, w, q, θ, h) as state variables, and elevator deflection, δ_e , as input, we may include the variables relating to the lateral-directional motion as pseudo inputs. The opposite is also true in that we may evaluate the lateral-directional motion using conventional variables of longitudinal motion, such as angle of attack, as pseudo inputs. The use

of pseudo-control inputs enables the effects of other motion variables, which are not regarded as state variables.

4.3.3.1 Longitudinal Dynamics

4.3.3.1.1 Reduced Longitudinal Model

A reduced longitudinal model is first employed to reduce the model size and unknown parameters. The aim of using this model is to tune the parameters of the drag and lift coefficients. After tuning the drag and lift coefficient parameters, the identification of pitch moment becomes easier.

For the output error estimation, the control input, state variables, measured / model output vectors, and unknown (estimated) variables for the reduced longitudinal motion are shown in Table 4.2.

Table 4.2 Input, State Variable, and Output Vectors and Unknown Variables in the Reduced Longitudinal Motion for the Output Error Method

Symbol	Description	Variables
\vec{u}	Control Input Vector	$[\delta_e, \delta_{lef}, v, p, q, r, \phi, \theta, C_C, \dot{p}, \rho, T]$
\vec{x}	State Variable Vector	$[u, w]$
\vec{y}	Model Observation Vector	$[V_{ADB}, \alpha_{ADB}]$
$\vec{\theta}$	Unknown Variables	$[C_D \text{ and } C_L]$ Model Variables

4.3.3.1.1.1 State Equations

True airspeed V , angle of attack α , angle of sideslip β and dynamic pressure are calculated as follows:

$$\begin{aligned}
V &= \sqrt{(u)^2 + (v_m)^2 + (w)^2} \\
\alpha &= \left(\tan^{-1} \frac{w}{u} \right) \\
\beta &= \left(\sin^{-1} \frac{v_m}{V} \right) \\
\bar{q} &= \frac{1}{2} \rho_m V^2
\end{aligned} \tag{4.29}$$

The non-dimensional drag, lift, and pitch moment coefficients are computed as

$$\begin{aligned}
C_D &= C_D(\alpha, \beta, q^*, \delta_e, \delta_{lef}) \\
C_L &= C_L(\alpha, \beta, q^*, \delta_e, \delta_{lef})
\end{aligned} \tag{4.30}$$

The aerodynamic force coefficients at the body axis are transformed to

$$\begin{bmatrix} C_X \\ C_Y \\ C_Z \end{bmatrix} = \left(\bar{q} S \begin{bmatrix} c_\alpha c_\beta & s_\beta & s_\alpha c_\beta \\ -c_\alpha s_\beta & c_\beta & -s_\alpha s_\beta \\ -s_{\alpha_m} & 0 & c_\alpha \end{bmatrix} \right)^T \begin{bmatrix} -C_D \\ -C_{C_m} \\ -C_L \end{bmatrix} \tag{4.31}$$

The body-axis accelerations are given by

$$\begin{bmatrix} \dot{x}_1 \\ \dot{x}_2 \end{bmatrix} = \begin{bmatrix} \dot{u} \\ \dot{v} \\ \dot{w} \end{bmatrix} = \left(\bar{q} S \begin{bmatrix} C_X \\ C_Y \\ C_Z \end{bmatrix} + \begin{bmatrix} T_m \\ 0 \\ 0 \end{bmatrix} \right) + \begin{bmatrix} -g s_{\phi_m} \\ g s_{\phi_m} c_{\theta_m} \\ g c_{\phi_m} c_{\theta_m} \end{bmatrix} - \begin{bmatrix} p_m \\ q_m \\ p_m \end{bmatrix} \times \begin{bmatrix} u \\ v_m \\ w \end{bmatrix} \tag{4.32}$$

4.3.3.1.2 Observation Equations

The velocity components along the body axes at the air data boom (subscript ADB) are computed from velocity components along the body axes at CM as follows:

$$\begin{aligned}
\begin{bmatrix} u_{ADB} \\ v_{ADB} \\ w_{ADB} \end{bmatrix} &= \begin{bmatrix} u \\ v_m \\ w \end{bmatrix} + \begin{bmatrix} p_m \\ q \\ r_m \end{bmatrix} \times \begin{bmatrix} x_{ADB/B} \\ y_{ADB/B} \\ z_{ADB/B} \end{bmatrix} \\
V_{ADB} &= \sqrt{(u_{ADB})^2 + (v_{ADB})^2 + (w_{ADB})^2} \\
\alpha_{ADB} &= \left(\tan^{-1} \frac{w}{u} \right)
\end{aligned} \tag{4.33}$$

The observation equations are given by

$$\begin{aligned}
y_1 &= V_{ADB} \\
y_2 &= \alpha_{ADB}
\end{aligned} \tag{4.34}$$

4.3.3.1.2 Full Longitudinal Model

After updating the lift and drag coefficient in the reduced longitudinal model, the full longitudinal model is utilized to tune the pitch moment.

For the output error estimation, the control input, state variables, measured / model output vectors, and unknown (estimated) variables for the full longitudinal motion are shown in Table 4.3.

Table 4.3 Input, State Variable, and Output Vectors and Unknown Variables in the Full Longitudinal Motion for the Output Error Method.

Symbol	Description	Variables
\vec{u}	Control Input Vector	$[\delta_e, \delta_{lef}, v, p, r, \phi, C_C, \dot{p}, \rho, T]$
\vec{x}	State Variable Vector	$[u, w, q, \theta, h]$
\vec{y}	Model Observation Vector	$[V_{ADB}, \alpha_{ADB}, q, \theta, h, a_{s_z, AS}]$
$\vec{\theta}$	Unknown Variables	$[C_D, C_L, \text{and } C_m]$ Model Variables

4.3.3.1.2.1 State Equations

True airspeed V , angle of attack α , angle of sideslip β and dynamic pressure are calculated as follows:

$$\begin{aligned} V &= \sqrt{(u)^2 + (v_m)^2 + (w)^2} \\ \alpha &= \left(\tan^{-1} \frac{w}{u} \right) \\ \beta &= \left(\sin^{-1} \frac{v_m}{V} \right) \\ \bar{q} &= \frac{1}{2} \rho_m V^2 \end{aligned} \tag{4.35}$$

The non-dimensional drag, lift, and pitch moment coefficients are computed as

$$\begin{aligned} C_D &= C_D(\alpha, \beta, q^*, \delta_e, \delta_{lef}) \\ C_L &= C_L(\alpha, \beta, q^*, \delta_e, \delta_{lef}) \\ C_{m_{MRP}} &= C_m(\alpha, \beta, q^*, \delta_e, \delta_{lef}) \end{aligned} \tag{4.36}$$

The aerodynamic force coefficients at the body axis are transformed to

$$\begin{bmatrix} C_X \\ C_Y \\ C_Z \end{bmatrix} = \left(\bar{q} S \begin{bmatrix} c_\alpha c_\beta & s_\beta & s_\alpha c_\beta \\ -c_\alpha s_\beta & c_\beta & -s_\alpha s_\beta \\ -s_{\alpha_m} & 0 & c_\alpha \end{bmatrix}^T \begin{bmatrix} -C_D \\ -C_{C_m} \\ -C_L \end{bmatrix} \right) \tag{4.37}$$

The pitching moment coefficient referred to the CM are computed by the following formula

$$C_m = C_{m_{MRP}} - C_X \frac{z_{MRP/B}}{\bar{c}} + C_Z \frac{x_{MRP/B}}{\bar{c}} \tag{4.38}$$

The body-axis accelerations are given by

$$\begin{bmatrix} \dot{x}_1 \\ \dot{x}_2 \end{bmatrix} = \begin{bmatrix} \dot{u} \\ \dot{v} \\ \dot{w} \end{bmatrix} = \left(\bar{q} S \begin{bmatrix} C_X \\ C_Y \\ C_Z \end{bmatrix} + \begin{bmatrix} T_m \\ 0 \\ 0 \end{bmatrix} \right) + \begin{bmatrix} -g s_{\phi_m} \\ g s_{\phi_m} c_{\theta} \\ g c_{\phi_m} c_{\theta} \end{bmatrix} - \begin{bmatrix} p_m \\ q \\ p_m \end{bmatrix} \times \begin{bmatrix} u \\ v_m \\ w \end{bmatrix} \tag{4.39}$$

The equations for rotational motion are represented as

$$\dot{x}_3 = \dot{q} = \frac{(I_{ZZ} - I_{XX})p_m r_m - I_{XZ}(p_m^2 - r_m^2) + \bar{q}S\bar{c}c_m}{I_{YY}} \quad (4.40)$$

The Euler-pitch angle rate is obtained by

$$\dot{x}_4 = \dot{\theta} = \cos \phi_m q - \sin \phi_m r_m \quad (4.41)$$

The altitude rate is obtained by

$$[\dot{x}_5] = [\dot{h}] = -[-s_\theta u + s_{\phi_m} c_\theta v_m + c_{\phi_m} c_\theta w] \quad (4.42)$$

4.3.3.1.2.2 Observation Equations

The velocity components along the body axes at the air data boom (subscript ADB) are computed from velocity components along the body axes at CM as follows:

$$\begin{bmatrix} u_{ADB} \\ v_{ADB} \\ w_{ADB} \end{bmatrix} = \begin{bmatrix} u \\ v_m \\ w \end{bmatrix} + \begin{bmatrix} p_m \\ q \\ r_m \end{bmatrix} \times \begin{bmatrix} x_{ADB/B} \\ y_{ADB/B} \\ z_{ADB/B} \end{bmatrix} \quad (4.43)$$

$$V_{ADB} = \sqrt{(u_{ADB})^2 + (v_{ADB})^2 + (w_{ADB})^2}$$

$$\alpha_{ADB} = \left(\tan^{-1} \frac{w}{u} \right)$$

The specific acceleration at CM is computed as

$$a_{s_z} = \frac{1}{m}(\bar{q}SC_z) \quad (4.44)$$

The specific acceleration referred to accelerometer sensor is computed as

$$\begin{aligned} y_6 &= a_{s_z, AS} \\ &= a_{s_z} + (p_m r_m - \dot{q})x_{AS/B} + (q r_m + \dot{p}_m)y_{AS/B} \\ &\quad - (p_m^2 + q_m^2)z_{AS/B} \end{aligned} \quad (4.45)$$

The observation equations are given by

$$\begin{aligned}
y_1 &= V_{ADB} \\
y_2 &= \alpha_{ADB} \\
y_3 &= q \\
y_4 &= \theta \\
y_5 &= h \\
y_6 &= a_{s_z,AS}
\end{aligned} \tag{4.46}$$

4.3.3.2 Lateral/Directional Dynamics

For the output error estimation, the control input, state variables, measured / model output vectors, and unknown (estimated) variables for the longitudinal motion are shown in Table 4.3.

Table 4.4 Input, State Variable, and Output Vectors and Unknown Variables in the Lateral Motion for the Output Error Method

Symbol	Description	Variables
\vec{u}	Control Input Vector	$[\delta_a, \delta_r, \delta_{lef}, u, w, q, \theta, C_X, C_Z, \rho, T]$
\vec{x}	State Variable Vector	$[v, p, r, \phi]$
\vec{y}	Model Output Vector	$[\beta_{ADB}, p, r, \phi, a_{s_y,AS}]$
$\vec{\theta}$	Unknown Variables	$[C_Y, C_L, C_n]$ Model Variables

4.3.3.2.1 State Equations

True airspeed V , angle of attack α , and angle of sideslip β are calculated as follows:

$$\begin{aligned}
V &= \sqrt{(u_m)^2 + (v)^2 + (w_m)^2} \\
\alpha &= \left(\tan^{-1} \frac{w_m}{u_m} \right) \\
\beta &= \left(\sin^{-1} \frac{v}{V} \right)
\end{aligned} \tag{4.47}$$

The non-dimensional drag, lift, and pitch moment coefficients are computed as

$$\begin{aligned}
C_Y &= C_Y(\alpha, \beta, p^*, r^*, \delta_a, \delta_r, \delta_{lef}) \\
C_{l_{MRP}} &= C_l(\alpha, \beta, p^*, r^*, \delta_a, \delta_r, \delta_{lef}) \\
C_{n_{MRP}} &= C_n(\alpha, \beta, p^*, r^*, \delta_a, \delta_r, \delta_{lef})
\end{aligned} \tag{4.48}$$

Dynamic pressure is calculated as follows:

$$\bar{q} = \frac{1}{2} \rho_m V \tag{4.49}$$

The following formula computes the roll and yaw moment coefficients referred to the CM

$$\begin{aligned}
C_l &= C_{l_{MRP}} - C_{Z_m} \frac{y_{MRP/B}}{\bar{c}} + C_Y \frac{z_{MRP/B}}{\bar{c}} \\
C_n &= C_{n_{MRP}} - C_Y \frac{x_{MRP/B}}{\bar{c}} + C_{X_m} \frac{y_{MRP/B}}{\bar{c}}
\end{aligned} \tag{4.50}$$

The body-axis accelerations are given by

$$\dot{x}_1 = \dot{v} = \bar{q} S C_Y / m - r u_m + p w_m \tag{4.51}$$

The equations for rotational motion are represented in tensor form as

$$\begin{aligned}
\dot{x}_2 &= \dot{p} \\
&= \frac{I_{XZ}(I_{XX} - I_{YY} + I_{ZZ})pq_m - (I_{ZZ}^2 - I_{YY}I_{ZZ} + I_{XZ}^2)q_m r + I_{ZZ}\bar{q}Sbc_l + I_{XZ}\bar{q}Sbc_n}{I_{XX}I_{ZZ} - I_{XZ}^2} \\
\dot{x}_3 &= \dot{r} \\
&= \frac{(I_{XX}^2 - I_{XX}I_{YY} + I_{XZ}^2)pq_m - I_{XZ}(I_{XX} - I_{YY} + I_{ZZ})q_m r + I_{XZ}\bar{q}Sbc_l + I_{XX}\bar{q}Sbc_n}{I_{XX}I_{ZZ} - I_{XZ}^2}
\end{aligned} \tag{4.52}$$

The Euler-roll angle rate is obtained by

$$\dot{x}_4 = \dot{\phi} = p + \sin \phi \tan \theta_m q_m - \cos \phi \tan \theta_m r \quad (4.53)$$

4.3.3.2.2 Observation Equations

The velocity components along the body axes at the air data boom (subscript ADB) are computed from velocity components along the body axes at CM as follows:

$$\begin{bmatrix} u_{ADB} \\ v_{ADB} \\ w_{ADB} \end{bmatrix} = \begin{bmatrix} u_m \\ v \\ w_m \end{bmatrix} + \begin{bmatrix} p \\ q_m \\ r \end{bmatrix} \times \begin{bmatrix} x_{ADB/B} \\ y_{ADB/B} \\ z_{ADB/B} \end{bmatrix} \quad (4.54)$$

$$\beta_{ADB} = \left(\sin^{-1} \frac{v_{ADB}}{V_{ADB}} \right)$$

The specific acceleration at CM is computed

$$a_{sy} = \frac{1}{m} (\bar{q} S C_Y) \quad (4.55)$$

The specific acceleration referred to as accelerometer sensor is

$$\begin{aligned} y_5 &= a_{sy,AS} \\ &= a_{sy} + (pq_m + \dot{r})x_{AS/B} - (p^2 + r^2)y_{AS/B} + (q_m r - \dot{p})z_{AS/B} \end{aligned} \quad (4.56)$$

The observation equations are given by

$$\begin{aligned} y_1 &= \beta_{ADB} \\ y_2 &= p \\ y_3 &= r \\ y_4 &= \phi \\ y_5 &= a_{sy,P} \end{aligned} \quad (4.57)$$

4.4 Model Structure Determination and Validation

This section covers the means of determining the accuracy, reliability, and usefulness of the specified model. For each coefficient, each model structure represents a multi-input, single-output subspace. This strategy enables more adaptability and simplifies the training process.[11]. The primary goal of aerodynamic model development is to optimize the model structure. Simplicity is preferable but yet possessing a significant level of complexity. Although restricting the number of terms used simplifies computing, it is essential to use the correct terms to ensure accuracy. Choosing which terms to include in each coefficient model is a tedious process and named feature selection. There are numerous well-known methods for selecting appropriate terms (feature selection), including Stepwise Regression, Multivariate Orthogonal Functions (MOFs), and Generalized Additive Models (GAMs). The aerodynamic model structure used in this study is based on the one developed by Grauer and Morelli in Ref [23]. Grauer and Morelli used multivariate orthogonal function modeling to investigate measured wind tunnel aerodynamic datasets for eight aircraft over a wide variety of flight regimes. The most critical modeling terms (the number of selected instances is high) for each coefficient are selected as frozen model terms. The remaining model terms for longitudinal and lateral coefficients are selected using expert-based selection and a correlation-based binary particle swarm optimization method, respectively. Certain additions and rejections to the structure of the underlying aerodynamic model are made using quantitative and qualitative graphical findings analyzed by Jategaonkar [65] and resampling methods analyzed by Millidere et al. in Ref. [24].

4.4.1 The Correlation Based Particle Swarm Optimization

The lateral/directional coefficients are identified using the correlation-based particle swarm optimization. Initial model terms pool are generated based on a set of base regressors and a maximum term order. And then, pairwise correlation among the

model terms is compared, and certain terms are removed. Finally, binary Particle Swarm Optimization is utilized to generate the best subset of the remaining terms. The flowchart of this process is shown in Figure 4.5.

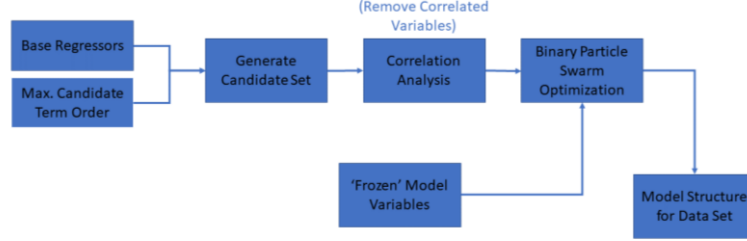


Figure 4.5 Correlated-Based Binary Particle Swarm Optimization Flowchart

4.4.1.1 Generating Candidate Pool

For lateral aerodynamic coefficients, candidate model terms are as follows:

$$\begin{aligned}
 C_a = & \sum_{i=0}^3 \sum_{j=0}^2 (C_{a\beta^i\alpha^j}) \beta^i \alpha^j + \sum_{i=1}^1 \sum_{j=0}^2 \sum_{k=0}^1 (C_{a\delta_{lef}^i\alpha^j\beta^k}) \delta_{lef}^i \alpha^j \beta^k \\
 & + \sum_{i=1}^1 \sum_{j=0}^2 \sum_{k=0}^1 (C_{a\delta_a^i\alpha^j\beta^k}) \delta_a^i \alpha^j \beta^k \\
 & + \sum_{i=1}^1 \sum_{j=1}^1 \sum_{k=0}^2 \sum_{l=0}^1 (C_{a\delta_a^i\delta_{lef}^j\alpha^k\beta^l}) \delta_a^i \delta_{lef}^j \alpha^k \beta^l \\
 & + \sum_{i=1}^1 \sum_{j=0}^2 \sum_{k=0}^1 (C_{a\delta_r^i\alpha^j\beta^k}) \delta_r^i \alpha^j \beta^k + \sum_{i=1}^1 \sum_{j=0}^2 (C_{ap^{*i}\alpha^j}) p^{*i} \alpha^j \\
 & + \sum_{i=1}^1 \sum_{j=0}^2 \sum_{k=1}^1 (C_{ap^{*i}\alpha^j\delta_{lef}^k}) p^{*i} \alpha^j \delta_{lef}^k + \sum_{i=1}^1 \sum_{j=0}^2 (C_{ar^{*i}\alpha^j}) r^{*i} \alpha^j \\
 & + \sum_{i=1}^1 \sum_{j=0}^2 \sum_{k=1}^1 (C_{ar^{*i}\alpha^j\delta_{lef}^k}) r^{*i} \alpha^j \delta_{lef}^k
 \end{aligned} \tag{4.58}$$

where $a = Y, l, m$.

The simplest way to generate regressor pool is to utilize the conventional regressors such as α , β , δ_{lef} , δ_a , δ_r , p^* , and r^* for lateral/directional coefficients. If there are no useful terms in the regressor pool, the quality of the model never improves.

Some model terms defined by Ref. [23] are so critical so that these terms are frozen for the model structure. After deciding frozen terms, to avoid correlations of model terms, the correlation between the model terms is checked before implementing binary particle swarm optimization. That is why this procedure is called the correlation-based binary particle swarm optimization technique.

4.4.1.2 Pearson's Correlation Coefficient

Pairwise correlation is a statistic that indicates the linear relationship between two or more variables. Correlation is used to select variables since the appropriate variables are strongly associated with the output. Additionally, variables should be associated with the output but not with one another. When two terms are correlated, the model requires just one of them, since the second provides no new information.

Given paired data $\{(x_1, y_1), \dots, (x_n, y_n)\}$ consisting of n pairs, the Pearson's correlation coefficient, r_{xy} , is defined as [70]

$$r_{xy} = \frac{\sum_{i=1}^n (x_i - \bar{x})(y_i - \bar{y})}{\sqrt{\sum_{i=1}^n (x_i - \bar{x})^2} \sqrt{\sum_{i=1}^n (y_i - \bar{y})^2}} \quad (4.59)$$

where:

n is the sample size

x_i, y_i are the individual sample points indexed with i

\bar{x}, \bar{y} are the mean for x and y samples

The value of Pearson's correlation ranges from -1 to +1. When the coefficient approaches to one end, then there is a high correlation. A value of 0 indicates that variables are not linearly dependent on one another. If the variables are correlated, we can eliminate the one with lower correlation coefficient value with the output variable. Additionally, we may calculate multiple correlation coefficients to determine if more than two variables are correlated to each other. This is referred to as multi-collinearity.

4.4.1.3 Binary Particle Swarm Optimization

Particle swarm optimization (PSO) is a population-based stochastic optimization technique [71]. This method is very popular because to its simplicity and low computing cost [72]. The PSO offers many advantages over other global optimization methods, including ease of implementation, and minimal number of hyperparameters to adjust. PSO has been effectively used in a wide range of fields, including parameter estimation as well as artificial neural network training, and feature selection [73] [74] [75] [76] [77] [78] [79].

PSO begins with a collection of random particles (solutions) and then seek for optimal solutions. Each particle is updated by using personal best and global best at each iteration. Personal best refers to best solution (fitness) of the particle. Global best refers the best value attained by any particle in the population [71].

Following the determination of particle's personal and global best values, the particle's velocity and positions are updated using the following equations [71] :

$$\vec{v}_i^{k+1} = w\vec{v}_i^k + c_1r_1(\vec{p}_i^k - \vec{x}_i^k) + c_2r_2(\vec{g}^k - \vec{x}_i^k) \quad (4.60)$$

$$\vec{x}_i^{k+1} = \vec{x}_i^k + \vec{v}_i^{k+1} \quad (4.61)$$

where \vec{v}_i^k is the particle velocity, \vec{x}_i^k is the current particle solution, r_1 and r_2 are random numbers between 0 and 1 and c_1 and c_2 acceleration coefficients.

The search mechanism of the PSO is illustrated in Figure 4.6.

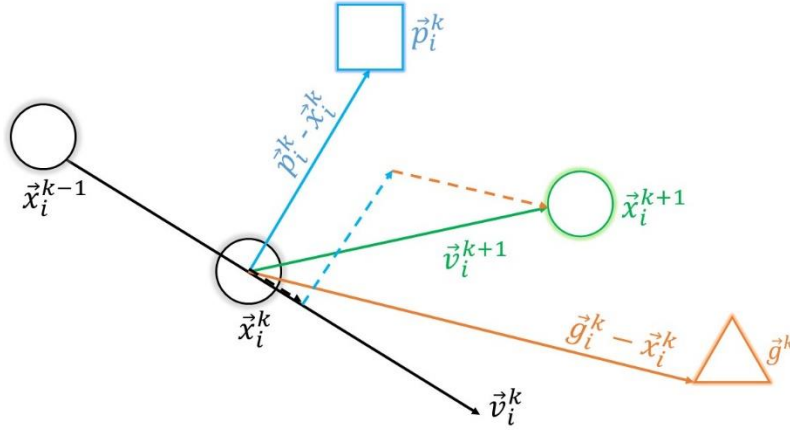


Figure 4.6 Search Mechanism of the PSO

The first term in equation (4.60) is referred to as the inertia component. It maintains the particle's original direction. The second term is called the cognitive component, which serve as the particle's memory, leading it to return to its optimal regions of the search space on individual basis. The last term is referred to the social component. It leads the particle to gravitate toward the best global solution the swarm has discovered so far.

The binary variant of this method has been developed to address binary problems. A transfer function which is the essential component of the binary version maps search space from continuous to discrete.

Two distinct components differentiate the continuous and binary versions of PSO: a new transfer function and a different position update method. The transfer function is used to map search space from continuous to binary, and the updating process changes the positions of particles in binary search spaces between 0 and 1.

Particles can move around the search space in the continuous version of PSO by employing position vectors. As a result, the notion of position updating for particles may be simply realized by adding velocities to positions through equation (4.61). However, position updating is different in the binary space [26]. Due to fact that

binary space contains just two integers (“0” and “1”), the operation of position updating cannot be accomplished using equation (4.61). As a result, a method should be developed for altering agents’ positions from “0” to “1” or vice versa. In other words, a relationship between velocity and position must be established [80].

Essentially, changing the position in discrete binary spaces entails flipping between "0" and "1" values. This flipping should be dependent on the agents' velocities. The issue here is how to update the positions in a binary space using the idea of velocity in a real space. The notion is to adjust an agent's location based on the likelihood of its velocity. To do this, a transfer function is required to convert velocity values to probability values for position updates.

Two concerns must be addressed when recasting the feature selection as an optimization problem. The first concern is with the solution's representation. Given that binary nature of feature selection, we chose to express the solution as a binary vector, with 1 values indicating that the associated feature is selected and 0 values indicating that it is not. The size of the solution corresponds to the number of features in each dataset. The second concern is with the objective function's design. In the binary PSO feature selection task, the predicted squared error (PSE) metric is used.[23] [81] is used as the objective function to choose the model without overparameterizing the model.

$$PSE = \frac{1}{N} \sum_{i=1}^N \left(\vec{z}_j - \vec{y}_j(\vec{\Theta}) \right)^2 + \sigma^2 \frac{n}{N} \quad (4.62)$$

The first component in the PSE reduces monotonically with each additional modeling term and quantifies the model fit error and is referred to as mean squared fit error. The second component is the overfit penalty, which rises monotonically with each additional model term and prevents the model from being over-parameterized, resulting in poor prediction outcomes. With each additional model term, one component increases continually whereas the other term decreases continually, ensuring that PSE is always minimum at a single point. By selecting this

point as the number of modeling terms, a model with low mean squared fit error and high prediction capacity is developed. The variance σ^2 is formulated as follows: [23]

$$\sigma^2 = \frac{1}{N-1} \sum_{i=1}^N (\bar{z}_i - \bar{\bar{z}})^2 \quad (4.63)$$

The general steps of the BPSO algorithm are as follows:

- a. Define the objective function to be minimized, Eq. (4.62).
- b. Each particle is assigned a random value.
- c. Initialize the hyperparameters of PSO: w (Table 4.8), c_1 and c_2 (Table 4.9).
- d. Repeat the following steps e to g until meeting the end condition.
- e. The velocities of each particle are updated using Eq. (4.60).
- f. Utilize Table 4.5 or Table 4.6 to determine the probability of changing the components of position vector.
- g. Update the position vectors using (4.65) or (4.66).

4.4.1.3.1 Hyperparameters of Binary Particle Swarm Optimization

The BPSO algorithm is an extremely efficient approach for solving feature selection problems. However, certain components of the feature selection process, called hyperparameters, are not updated autonomously. The hyperparameter is not the variable that is optimized through the feature selection process, but rather the variable specified by previous information, e.g., transfer function scheme, inertia weight updating strategy, and the value of acceleration coefficients [80]. The setting for these hyperparameters has a considerable impact on the performance of BPSO, and there are no universally optimal default values for various problems and data sets. The fundamental issue in designing a BPSO is determining the optimal hyperparameters. The brute force technique is applied to find the best hyperparameters. The numbers of population and generation number are taken to be 20 and 30, respectively. The dimension number is the number of terms in the

generated pool. Each configuration is run 30 times, and the min, max, mean, and standard deviation of the PSE are recorded. The mean values are compared, and the one giving the minimum mean value is selected as the best configuration.

4.4.1.3.1.1 Transfer Function Scheme

Binary PSO depends on a transfer function to convert a continuous search space to a discrete search space for its core component. S-shaped and v-shaped transfer functions are the two main families of transfer functions described in the literature. A transfer function's range should be restricted to the range [0,1]. All real values of velocity are transformed to probability values in the range [0,1] using an equation (4.64) that uses a sigmoid function [80].

$$T(v_i^{k+1}) = \frac{1}{1 + e^{-v_i^{k+1}}} \quad (4.64)$$

Position vectors may be updated as follows with the likelihood of their velocities once velocities have been converted to probability values:

$$x_i^{k+1} = \begin{cases} 1 & \text{if } rand < T(v_i^{k+1}) \\ 0 & \text{if } rand \geq T(v_i^{k+1}) \end{cases} \quad (4.65)$$

The other s-shaped transfer functions are listed in Table 4.5.

Table 4.5 S-Shaped Family of Transfer Functions

Name	Transfer Function
S1	$T(x) = \frac{1}{1 + e^{-2x}}$
S2	$T(x) = \frac{1}{1 + e^{-x}}$
S3	$T(x) = \frac{1}{1 + e^{-x/2}}$
S4	$T(x) = \frac{1}{1 + e^{-x/3}}$

Table 4.6 lists the most common v-shaped transfer functions.

Table 4.6 V-Shaped Family of Transfer Functions

Name	Transfer Function
V1	$T(x) = \left \operatorname{erf}\left(\frac{\sqrt{\pi}}{2}x\right) \right $
V2	$T(x) = \tanh(x) $
V3	$T(x) = \left \frac{x}{\sqrt{1+x^2}} \right $
V4	$T(x) = \left \frac{2}{\pi} \arctan\left(\frac{\pi}{2}x\right) \right $

Because v-shaped functions are distinct from the s-shaped ones, additional rules for changing their positions are required. Position vectors should be updated using a formula based on velocities when using these types of transfer functions.

$$x_i^{k+1} = \begin{cases} (x_i^k)^{-1} & \text{if } rand < T(v_i^{k+1}) \\ x_i^k & \text{if } rand \geq T(v_i^{k+1}) \end{cases} \quad (4.66)$$

where $(x_i^k)^{-1}$ is the complement of x_i^k .

Table 4.7 Different Transfer Functions

No	1	2	3	4	5	6	7	8
Name	S1	S2	S3	S4	V1	V2	V3	V4

4.4.1.3.1.2 Inertia Weight Updating Strategy

Each population-based algorithm undergoes two main phases of optimization: exploration and exploitation. By maintaining a favorable balance between those phases, the algorithm may converge to the global optima in an acceptable amount of time. The ideal solution for any algorithm is to begin the search process by using the exploration operator more than the exploitation operator. One of the hyperparameters

that control this balance is the inertia weight. There are many strategies for the inertia weight in the literature [79] [82] [83] [84]. In this study, only ten different inertia weight update strategies, which are listed in Table 4.8, are tested as follows:

Table 4.8 Different Inertia Weight Update Strategies

No	Name of the Inertia Weight	Formula of the Inertia Weight
1	Constant Inertia Weight	$w = 0.2$
2	Constant Inertia Weight	$w = 0.5$
3	Constant Inertia Weight	$w = 0.7$
4	Constant Inertia Weight	$w = 1.0$
5	Linear Decreasing Inertia Weight	$w^k = w_{max} - (w_{max} - w_{min}) \frac{k}{k_{max}}$ $w_{min} = 0.2, w_{max} = 0.8$
6	Nonlinear Decreasing Inertia Weight	$\left(\frac{2}{k}\right)^{0.3}$
7	Linear Increasing Inertia Weight	$w^k = w_{min} + (w_{max} - w_{min}) \frac{k}{k_{max}}$ $w_{min} = 0.2, w_{max} = 0.8$
8	Simulated Annealing Inertia Weight	$w^k = w_{min} + (w_{max} - w_{min}) 0.99^k$ $w_{min} = 0.2, w_{max} = 0.8$
9	Random Inertia Weight	$w^k = 0.5 + \frac{rand}{2}$
10	Global-Local Best Inertia Weight	$w_i^k = 1.1 - \frac{\vec{g}^k}{\vec{p}_i^k}$

4.4.1.3.1.3 The Value of Acceleration Coefficients

The second hyperparameter that controls this balance is the acceleration coefficients. To have a good balance, the sum of c_1 and c_2 must be equal to 4 [71].

$$c_1 + c_2 = 4 \quad (4.67)$$

There are many options for c_1 and c_2 selection, but just 2 options are evaluated for this study. In the first one, both of them are set to 2. And in the second option, c_1 decreases from 3.5 to 0.5 and c_2 grows linearly from 0.5 to 3.5 to balance exploration and exploitation.

Table 4.9 Different Acceleration Update Strategies

No	Name of the Inertia Weight	The Formula of the Inertia Weight
1	Constant Accelerations	$c_1 = 2$ $c_2 = 2$
2	Adaptive Accelerations	$c_1 = 3.5 - 3 \frac{k}{k_{max}}$ $c_2 = 0.5 + 3 \frac{k}{k_{max}}$

4.4.2 Statistical Accuracy

Firstly, it is checked if the expected value is reasonable. The magnitude of the order must be close to real value. Otherwise, we are doing something wrong. And then, we check the standard deviation, coefficient of variation (relative standard deviation), and correlation matrix results. The coefficient of variation should not exceed 50%.

The coefficient of variation is a statistic that indicates the degree of relative variability. It is the ratio of the standard deviation to the estimate. The larger the coefficient, the more dispersion around mean. The smaller the coefficient, the more accurate the estimate. The formula for the coefficient of variation is as follows:

$$CoV = \left| \frac{\sigma}{\Theta} \right| \times 100\% \quad (4.68)$$

where σ is the standard deviation and Θ is the estimate.

4.4.3 Qualitative Graphical Results

Time History Plots: Comparing the time histories of measured and estimated responses is a standard procedure to evaluate the model fidelity qualitatively. Any discrepancies in the match between the two responses often provide important clues to improve the model fidelity.

Cross Plots: In addition to plotting time histories of measured and estimated responses, cross plots of arbitrary two variables, such as lift coefficient versus angle of attack, Rolling and yawing moment coefficients versus angle of sideslip, drag coefficient versus lift coefficient, are occasionally necessary. These cross plots are helpful for gaining more insight into the modeling aspects.

Cross Plots of Residuals; the test of the residuals is a valuable indication of the validity of assumptions made. The low spread of residual cantered around zero is desirable, whereas non-flat spread indicates that the model needs improvement with the observed variable.

4.4.4 Resampling Methods

To determine how effective the equation error method on a given dataset is, how well its estimations resemble the measured data is examined. The mean squared error is the most often used metric in regression problems:

$$\text{MSE}_{\text{Train}} = \frac{1}{n_{\text{train}}} \sum_{i=1}^{n_{\text{train}}} (z_i - y_i)^2 \quad (4.69)$$

where n_{train} is the number of samples in the training dataset, z_i and y_i are the actual and the estimated values for the i^{th} observation in the training set.

Rather than how well the method performs on the training data, what matters is how well the trained model performs on the data in the testing dataset, which has not been used to train the network. That is,

$$\text{MSE}_{Test} = \frac{1}{n_{test}} \sum_{i=1}^{n_{test}} (z_i - y_i)^2 \quad (4.70)$$

should be computed for assessing the model, where n_{test} is the number of samples in the testing dataset, z_i and y_i are the actual and the estimated values for the i th observation in the testing dataset we have separated aside.

Adding many variables (increasing complexity), which decreases the training MSE, has no effect on reducing the test MSE. Overfitting occurs when a given method yields a small training MSE but a high test MSE. The small changes in the training data may have a significant effect on the estimated model. In this instance, the random error is modeled rather than the pattern hidden in the data. This is not the desired case [32]. Such a case is demonstrated in Figure 4.7 [33]. The resampling methods, essential tools in modern statistics, are discussed to minimize this undesired case [32] [33]

The performance of the regression model is a crucial criterion for determining the optimal variable selection. In the beginning, the available dataset is split into two sets, training dataset, and testing dataset. The testing dataset, which is not seen in the identification phase, is used to evaluate the ultimate performance of the identified model. However, during the identification phase, it is worth noting that the training dataset may be utilized in a variety of ways to evaluate the identified model, including train-validation split, cross-validation sets, or random resamples. The use of such methods is illustrated in Figure 4.8, in which the enclosed box indicates that several iterations may be required to obtain the final trained model to be assessed by the testing dataset. Below we describe some commonly used validation techniques to determine how well the trained model might work on the testing dataset. For more information on the subject, the reader is referred to Ref. [33].

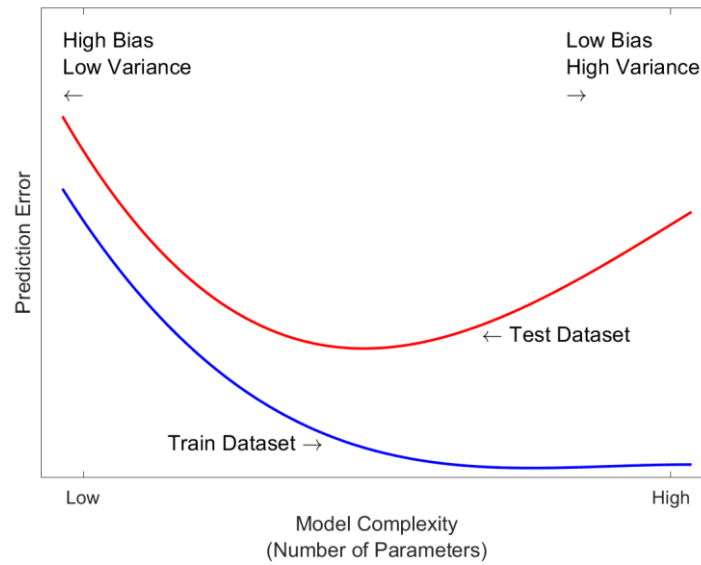


Figure 4.7 Test and Training Error as a Function of Model Complexity

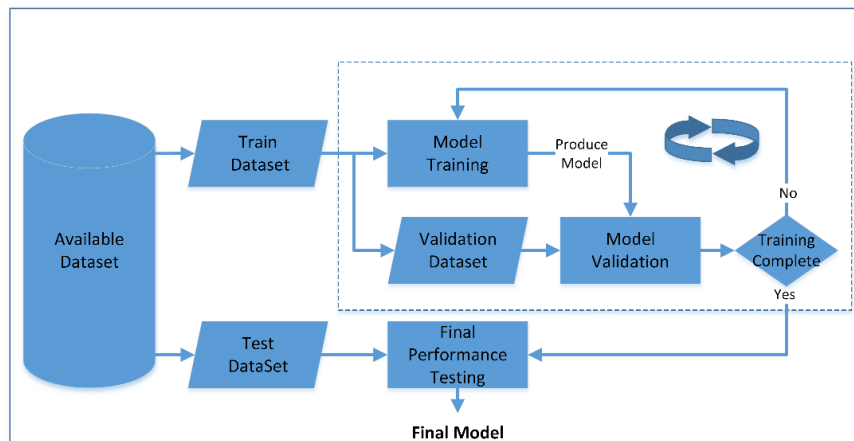


Figure 4.8. Model Analysis Engineering Flowchart

4.4.4.1 Train Validation Split

It is a straightforward procedure that comprises randomly partitioning the available training dataset into two parts: a training dataset and a validation dataset, illustrated in Figure 4.9.a. The model is fitted to the newly generated training dataset, and the performance of the fitted model is evaluated in the validation set. The trained model is then used for the testing dataset. Generally, the training data consists of %80 of

the available data set. This simple approach is easy to implement, but it has a significant drawback: testing MSE can be highly variable, depending on which observations are included in the training and the validation datasets.

4.4.4.2 K-fold Cross-Validation

This procedure addresses the drawback of the train-validation split approach. This approach divides the set of observations randomly into k groups, or folds, of approximately equal size, illustrated in Figure 4.9.b. The first fold is used to validate the model, while the remaining $k - 1$ folds are used to train the model. The mean square error for the validation set (first fold) is computed. This procedure is repeated k times; each time, a new group of observations is used as a validation set. As a consequence, k estimates of the validation MSEs are produced. The k -fold cross-validation error estimate is then computed by the average [32] [33]

$$CV_{(k)} = \frac{1}{k} \sum_{i=1}^k MSE_{val_i} \quad (4.71)$$

In comparison to the hold-out cross-validation approach, which produces inconsistent results when applied with varying splits owing to unpredictability in the train and validation splits, performing a k -fold cross-validation is more robust in that regard. Generally, the number of folds, k , to be used in this approach for a given n observations, as recommended in [85], is

$$k = \min \{ \sqrt{n}, 10 \} \quad (4.72)$$

Figure 4.9 illustrates the resampling techniques.

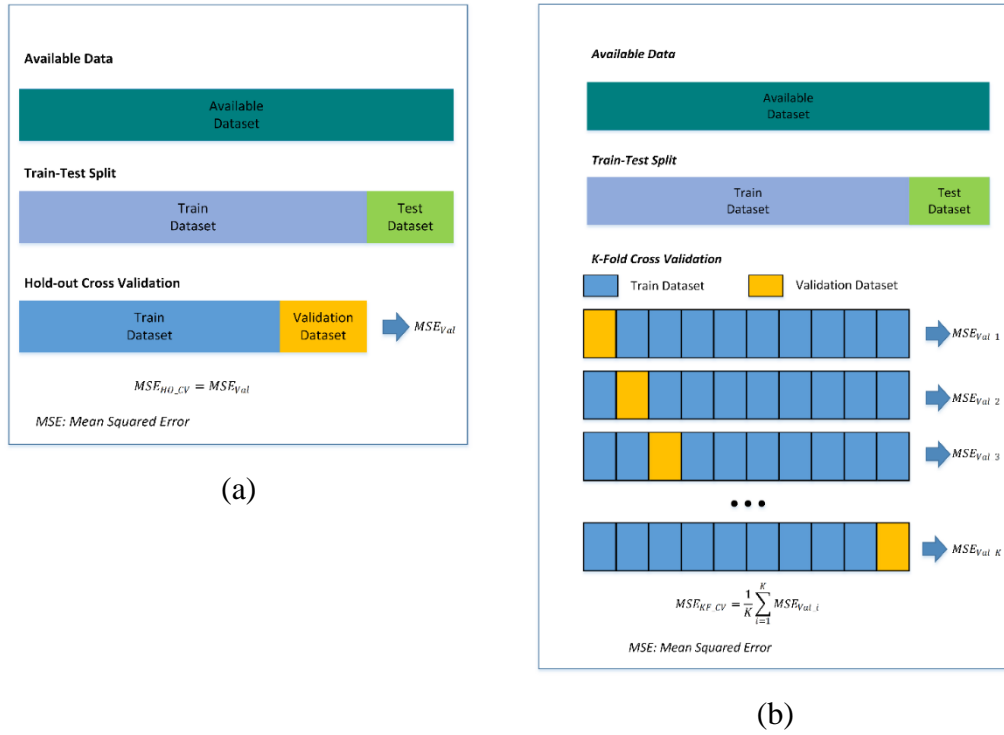


Figure 4.9. Resampling Methods. (a) Hold-out Cross-Validation (b) K-fold Cross-Validation

4.4.5 Proof-of-Match (POM)

The estimated model's capacity is evaluated by comparing the measured responses to the model's predictions with the duplicated control inputs. This process is referred to as proof-of-match in the context of flight vehicles, and it is a critical part of flight simulator certification and acceptance. Throughout this process, the estimated aerodynamic model is kept fixed [1] [2] [13]. According to a fundamental principle of sciences, supplementary flight data and flight maneuvers are utilized to verify the model capability.

Additionally, the FAA has established standards, which defines the criteria for evaluating, qualifying, and maintaining Flight System Training Devices (FSTD). The standards include six appendices: these are requirements, full flight simulators, objective tests, subjective evaluation, sample documents, wind shear training, and FSTD directives, respectively [86].

The simulation should begin under the identical initial conditions as in the flight. The initial conditions must be adjusted appropriately to fit the flight conditions. The control inputs and outputs during the actual flight test are exposed to measurement errors and noise. Similarly, the estimated models are imprecise. As a result, aerodynamic coefficients also should be adjusted. A practical methodology is to introduce minor biases on the initial conditions, the measured control deflections, and the aerodynamic coefficients. The effective aerodynamic parameters in several maneuvers are listed in Table 4.10 [87].

Table 4.10 Effective Aerodynamic Parameters in Proof-of-Match Maneuvers

Maneuver	Maneuver Parameters	Model Parameters
Short Period	a. Frequency	$C_{m\alpha}$
Phugoid	a. Time to double/half	C_D
	b. Period	C_D
Longitudinal Static Stability (LSS)	a. Stick position gradient	$C_{m\alpha}, C_{m\delta_e}$
	b. AOA gradient	$C_{L\alpha}$
Maneuvering Longitudinal Stability	a. Stick position gradient	$C_{m\alpha}, C_{m\delta_e}, C_{m_0}$
	b. AOA gradient	$C_{L\alpha}$
Steady State Trim	a. Airspeed, Weight, AOA	$C_{L\alpha}$
	b. Longitudinal Trim	$C_{L_{TRIM}}$
	c. Throttle Position	C_D and T balance
Dutch Roll	a. Frequency:	$C_{n\beta}$
	b. Damping:	C_{nr}
Bank To Bank	a. Initial roll response to partial deflection inputs	$C_{l\delta_a}, C_{lp}$
	b. Full deflection rolls	$C_{n\delta_a}, C_{np}$
Steady State Sideslip	a. Bank/Rudder slope	$C_{n\beta}, C_{n\delta_r}$
	b. Bank/Beta slope	$C_{Y\beta}$
	c. Aileron/Bank slope	$C_{l\delta_a}, C_{lp}$

To avoid subjective assessment of the match between measured system responses and model predicted outputs, FAA has established standards for each variable in terms of tolerances. As an example, Table 4.11 specifies many flight tests, including the tolerances and flight conditions for each validation test. The reader is referred to Refs. [86] [88] for a complete list of validation tests.

Table 4.11 FAA Validation Tests and Tolerance Values

Test Number	Maneuver	Parameters	Tolerance
2.c.5	Longitudinal Trim	Elevator Pitch Angle	± 1.0 deg ± 1.0 deg
2.c.6	Longitudinal Maneuvering Stability	Elevator	± 1.0 deg or $\pm 10\%$
2.c.7	Longitudinal Static Stability	Elevator	± 1.0 deg or $\pm 10\%$
2.c.9	Phugoid Dynamics	Period Time to $\frac{1}{2}$ or 2	$\pm 10\%$ $\pm 10\%$
2.c.10	Short Period Dynamics	Pitch Angle Pitch Rate Normal Acceleration	± 1.5 deg ± 1.5 deg ± 0.1 g
2.d.2 and 2.d.3	Bank To Bank	Roll Rate Yaw Rate Lateral Acceleration Sideslip Angle Bank Angle	± 2 deg ± 2 deg ± 0.1 g ± 1.5 deg ± 2.0 deg or $\pm 10\%$
2.d.7	Dutch Roll	Roll Rate Yaw Rate Lateral Acceleration Sideslip Angle	± 2 deg ± 2 deg ± 0.1 g ± 1.5 deg
2.d.8	Steady State Sideslip	Sideslip Angle Bank Angle Aileron	± 1.5 deg ± 2 deg or $\pm 10\%$ ± 2.0 deg

Longitudinal parameter matching is performed in two phases. The static part of aerodynamic coefficients is validated with Longitudinal Maneuvering Stability and Longitudinal Static Stability tests. The dynamic portion of the aerodynamic coefficient is confirmed with the Short-Period, Phugoid, and Trust Variation tests [8].

4.4.6 Theil's Inequality Coefficient

Residual analysis is a popular statistical method for determining how well a model fits the data. Theil's inequality coefficient is used as the criteria. It sheds light on the relationship between the two time series, in this instance the measured and model responses (\vec{z} and \vec{y}). Theil's inequality coefficient for each of the variables is defined as [1]

$$U_i = \frac{\sqrt{\frac{1}{N} \sum_{i=1}^N [z_i(t_k) - y_i(t_k)]^2}}{\sqrt{\frac{1}{N} \sum_{i=1}^N [z_i(t_k)]^2} + \sqrt{\frac{1}{N} \sum_{i=1}^N [y_i(t_k)]^2}}, i = 1, 2, \dots, n_y \quad (4.73)$$

where N is the total number of data points, \vec{z} is the measurement vector, \vec{y} is the model output vector and n_y is the dimension of the output vector. Eq. provides n_y separate Theil's inequality coefficients corresponding to the number of outputs.

U is the normalized index, constrained within the zero and unity interval. $U = 0$ denotes a perfect fit, and $U = 1$ denotes to the maximal inequality. As a rule of thumb, the maximum acceptable values of this coefficient is in the range of 0.25 to 0.30. The TIC value will be investigated for the conditions stated below:

- Zero input initial condition
- Noise driven behavior
- Combination of short-period, dutch-roll, and bank-to-bank maneuvers
- Short-period, dutch-roll, and bank-to-bank maneuvers with respect to strong control deflection inputs

4.4.7 Range of Model Applicability in Frequency Domain

Even though validation tests are often carried out in the time domain, the application range of the estimated model may be shown more clearly in frequency domain. This is especially critical for systems with flight control systems or in situations where aeroelastic effects may be dominating.

The magnitude and phase angle bode plots illustrate the model's accuracy and validity range in the frequency domain. For a perfect match, we'll require 0-dB magnitude and 0-deg phase angle throughout the whole frequency range. MUAD (Maximum Unnoticeable Added Dynamics) limits are used to define the magnitude and phase mismatch thresholds at which a pilot would notice a difference in the aircraft's response characteristics, similarly to how they are used in time domain verification in terms of tolerances [14]. To maintain adequate fidelity, the size and phase of the error function should be maintained within these bounds.

Tischler [14] suggested using the MUAD limits as a fidelity criterion for FAA level D simulations. DLR researchers separately developed and used the same technique of mismatching frequency domain boundaries to identify the impacts of unnoticed dynamics in helicopters and to evaluate the accuracy of in-flight simulations.

The procedure to compute the frequency responses can be found in Ref. [14]. Pitch-rate response to elevator input (q/δ_e), roll-rate response to aileron input (p/δ_a), and yaw-rate response to rudder input (r/δ_r) at different trim settings will be investigated.

4.5 Thrust Calculation from Steady State Flight Tests

4.5.1 Introduction to Flight Performance

This section discusses flight mechanics, which is the study of aircraft translational motions. Figure 4.10 illustrates the geometry for flight mechanics [89].

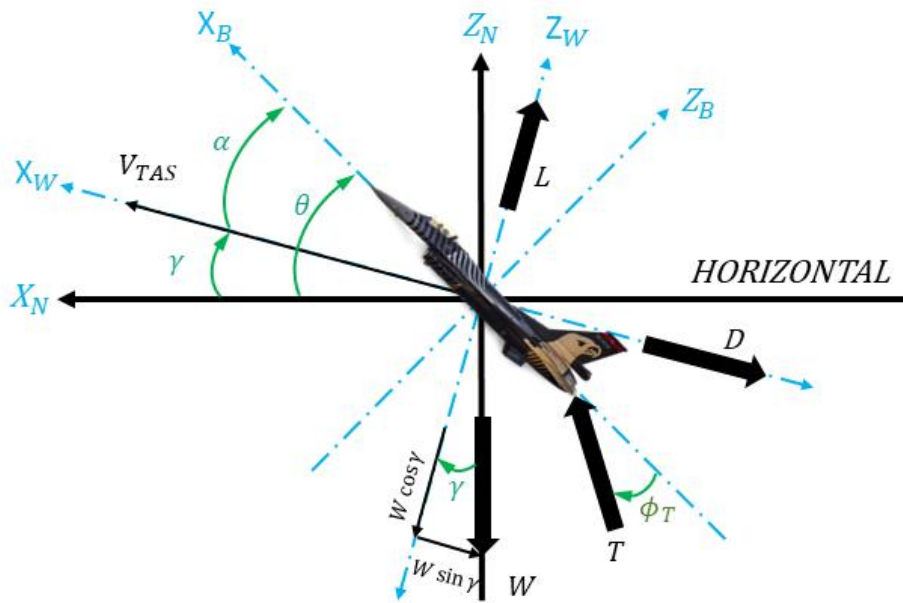


Figure 4.10 Geometry for Performance Calculation.

The climb angle, γ , is the angle between the horizontal and the wind (stability) X-axis. Summing forces in the Xs and Zs directions yield Eqs. (4.74) and (4.75).

$$\sum F_x = T \cos(\alpha + \alpha_T) - D - W \sin \gamma \quad (4.74)$$

$$\sum F_z = T \sin(\alpha + \alpha_T) + L - W \cos \gamma \quad (4.75)$$

where T is thrust, D is drag, L is lift, W is weight, α is the angle of attack, γ is flight path angle and α_T is thrust incidence angle.

For most aircraft and in F16 aircraft, the thrust axis has little incidence with respect to the wind axis, i.e., $\alpha_T = 0$. So Eqs. (4.74) and (4.75) are simplified as follows:

$$\sum F_x = T \cos \alpha - D - W \sin \gamma \quad (4.76)$$

$$\sum F_z = L - W \cos \gamma \quad (4.77)$$

In Eqs. (4.76) and (4.77), the drag (D) and lift (L) is as follows:

$$D = q S_{Ref} C_D \quad (4.78)$$

$$L = q S_{Ref} C_L \quad (4.79)$$

where $q = 1/2 \rho V_{TAS}^2$ is the dynamic pressure and S_{Ref} is the reference area.

4.5.2 Steady State Flight

If the aircraft is flying in steady-state flight, the sum of the forces must equal to zero, $\sum F_x = \sum F_z = 0$. This leads to Eqs. (4.80) and (4.81), the purest versions of the translational equations of motion.

$$T \cos \alpha - D - W \sin \gamma = 0 \quad (4.80)$$

$$L - W \cos \gamma = 0 \quad (4.81)$$

From Eqs. (4.80) and (4.81), we get that

$$C_D = \frac{D}{q S_{Ref}} \quad (4.82)$$

$$C_L = \frac{L}{q S_{Ref}} \quad (4.83)$$

There is a relation between C_D and C_L as shown below [1] [3] [48] [89].

$$C_D = C_{D0} + \frac{1}{\pi e A R} C_L^2 \quad (4.84)$$

$$= C_{D0} + KC_L^2$$

where C_{D0} is the drag coefficient at zero angle of attack, e is Oswald efficiency factor, and AR is the aspect ratio.

For swept-wing aircraft, Oswald efficiency, e , is assumed to be as follows [89] :

$$e = 4.61(1 - 0.045 \times AR^{0.68})(\cos \Lambda_{LE})^{0.15} - 3.1 (\Lambda_{LE} > 30 \text{ deg}) \quad (4.85)$$

where AR is the aspect ratio, and Λ_{LE} is the leading-edge swept angle.

In F16 aircraft, AR equals 3 and Λ_{LE} equals to 40° . So Eq. (4.85) turns out to be Eq. (4.86).

$$\begin{aligned} e &= 4.61(1 - 0.045 \times AR^{0.68})(\cos \Lambda_{LE})^{0.15} - 3.1 (\Lambda_{LE} > 30 \text{ deg}) \\ &= 4.61(1 - 0.045 \times 3^{0.68})(\cos 40)^{0.15} - 3.1 \\ &= 0.9086 \end{aligned} \quad (4.86)$$

In a flight, the weight of the aircraft, and we can measure the angle of attack, α , and flight path angle, γ , and true airspeed, V_{TAS} are measured, and the air density ρ is calculated using the standard atmosphere model. So the only unknown components in Eqs. (4.80) and (4.81) are L and D , i.e. C_D and C_L coefficients. Hence, using Eqs. (4.80)(4.81)(4.82)(4.83)(4.84) and (4.86), we can conclude that if we know C_{D0} coefficients, we can find C_D and C_L aerodynamic coefficients using Newton-Raphson algorithm discussed in Subsection 2.4.2.1. How to calculate C_{D0} in flight are covered in the next subsection.

4.5.3 Gliding Flight

In gliding flight, $T = 0$ and the sum of the forces must equal to zero, $\sum F_x = \sum F_x = 0$. This leads to Eqs. (4.87) and (4.88).

$$D - W \sin \gamma = 0 \quad (4.87)$$

$$L - W \cos \gamma = 0 \quad (4.88)$$

From Eqs. (4.82) and (4.83), we get that

$$C_D = \frac{W \sin \gamma}{qS_{Ref}} \quad (4.89)$$

$$C_L = \frac{W \cos \gamma}{qS_{Ref}} \quad (4.90)$$

Using Eq. (4.84), we can calculate C_{D0} .

$$C_{D0} = C_D - \frac{1}{\pi eAR} C_L^2 \quad (4.91)$$

We collected some flight data for gliding flights, and we get the results in Figure 4.11. The averaged C_{D0} value for the flight is 0.0208, $\bar{C}_{D0} = 0.0208$, and it is very close to actual value, 0.0202.

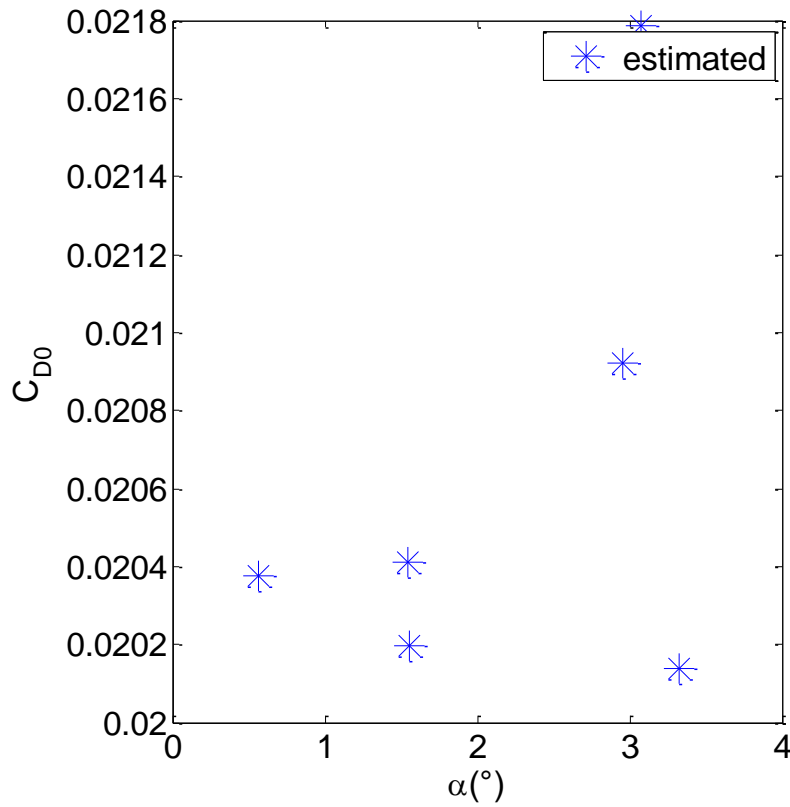


Figure 4.11 C_{D0} Values for Different Gliding Flights

4.5.4 Calculating Thrust Using Newton-Raphson Algorithm

Now we can go back to our primary concern, calculating the thrust coefficient from equations in Section 4.5.2 using the Newton-Raphson algorithm already discussed in Section 2.4.2.1.

Now we should construct the F function to be solved in the Newton-Raphson algorithm. Using Eqs. (4.80), (4.81), (4.82), (4.83), and (4.84), we get the following formula in which there are two equations and two unknowns which are T and C_L .

$$F(1) = 0 = T \cos \alpha - (C_{D0} + KC_L^2)qS_{Ref} - W \sin \gamma \quad (4.92)$$

$$F(2) = 0 = C_L qS_{Ref} - W \cos \gamma$$

where $F = \begin{bmatrix} F(1) \\ F(2) \end{bmatrix}$ and $x = \begin{bmatrix} T \\ C_L \end{bmatrix}$.

4.6 Iterative Equation Error Method

When the thrust force is known, the equation error method is used to find the reasonable starting point in the Output Error Method.

But when there is no available thrust data, thrust is calculated using assumption from Steady State Flight Tests (Section 4.5), and a preliminary simplified turbofan engine thrust model is developed (Section 2.2.2.3). All optimization-based design techniques need a good preliminary design as a starting point. There is no assurance that search engine discovers a suitable solution. The classical methods are used for the preliminary design. And then iterative equation error method is employed.

The iterative equation error method approach consisted of a starting point and then used a systematic method to obtain a refined solution estimate. In the end, it is expected to obtain a solution that simultaneously satisfies the given output vector.

The process is started by choosing a reasonable starting point for an unknown parameter vector, $\Theta^{(0)}$. Specific estimations do not lead to a converged solution if

the starting point is far from optimum. The unknown parameter vector is subdivided into two components, namely, Θ_F and Θ_E . The vector with the subscript F contains fixed coefficients, and the other with the index E contains the parameters to be estimated. The starting point can be substituted into cost function, which can be used firstly to calculate a new estimate for C_D coefficient parameters. the fixed parameters, then these new estimates of C_D coefficient parameters along with the previous estimates for \tilde{T}_{ND} is substituted into cost function to compute a new estimate for C_L coefficient parameters. This process is repeated to calculate a new estimate for \tilde{C}_T coefficient. Then the entire procedure is repeated until percent relative error, ε_a , fall below a prespecified stopping criterion, ε_s or the maximum number of iterations is achieved. The motivation of using the iterative equation error method is as follows: the drag coefficient parameters and thrust coefficient parameters are nearly collinear or linearly dependent, and the classical methods cannot decipher between parameters, and resulting parameter estimates are biased with large uncertainties and leads to poor regression results.

For the iterative equation error estimation, the control input, state variables, measured / model output vectors, and unknown (estimated) variables are shown in Table 4.12.

Table 4.12 Input, State Variable, and Output Vectors and Unknown Variables for the Iterative Equation Error Method.

Symbol	Description	Variables
\vec{u}	Control Input Vector	$[V, \alpha, \beta, p, q, r, \delta_{lef}, \delta_{th}, \delta_e, \delta_a, \delta_r, \delta_{sb}, M]$
\vec{x}	State Variable Vector	$[\]$
\vec{y}	Observation Vector	$[a_{sX}, a_{sZ}]$
$\vec{\Theta}$	Unknown Variables	$[C_D, C_L, C_T]$ Model Variables

Algorithm1: The Iterative Equation Error Method Algorithm

1: Specify a tolerable error, ε_s
2: Choose the maximum number of iterations, $iter_{max}$
3: Choose output vector as $z = [a_x^{cg}, a_z^{cg}]$
4: Define cost function to be minimized, $J(\theta) = \frac{1}{N} \sum_{t=1}^N [z(t) - g(x(t), \theta)]^2$
5: Choose an initial guess $\theta^{(0)} = \begin{bmatrix} (C_{D_i}, i = 1, \dots, n_{C_D})^T, (C_{L_i}, i = 1, \dots, n_{C_L})^T, \\ (\tilde{C}_{T_i}, i = 1, \dots, n_{\tilde{C}_T})^T \end{bmatrix}^T$
6: **for** $k = 1$ **to** $iter_{max}$ **do**
7: **for** $j = 1$ **to** 3 **do**
8: Resolve unknown parameter vector into fixed (θ_F) and estimated (θ_E)
9: **if** $j = 1$ **then**
10: $\theta_E^{(k)} = [(C_{D_i}, i = 1, \dots, n_{C_D})^T]^T$
11: $\theta_F^{(k)} = [(C_{L_i}, i = 1, \dots, n_{C_L})^T, (\tilde{T}_{ND_i}, i = 1, \dots, n_{\tilde{T}_{ND}})^T]^T$
12: **elseif** $j = 2$ **then**
13: $\theta_E^{(k)} = [(C_{L_i}, i = 1, \dots, n_{C_L})^T]^T$
14: $\theta_F^{(k)} = [(C_{D_i}, i = 1, \dots, n_{C_D})^T, (\tilde{T}_{ND_i}, i = 1, \dots, n_{\tilde{T}_{ND}})^T]^T$
15: **elseif** $j = 3$ **then**
16: $\theta_E^{(k)} = [(\tilde{T}_{ND_i}, i = 1, \dots, n_{\tilde{T}_{ND}})^T]^T$
17: $\theta_F^{(k)} = [(C_{D_i}, i = 1, \dots, n_{C_D})^T, (C_{L_i}, i = 1, \dots, n_{C_L})^T]^T$
18: **end if**
19: $\theta_E^{(k+1)} = argmin J(\theta_F^{(k)}, \theta_E^{(k)})$
20: **end for**
21: Calculate percent relative error, $\varepsilon_a = \left| \frac{\theta^{(k+1)} - \theta^{(k)}}{\theta^{(k+1)}} \right| \times 100\%$
22: **if** $\varepsilon_a < \varepsilon_s$ **then**
23: Stop
24: **end if**
25: **end for**

CHAPTER 5

RESULTS AND DISCUSSION

5.1 Case 1: Availability of Engine Database from Manufacturer

5.1.1 Phase 1.1: Model Structure Determination

The longitudinal aerodynamic coefficients are determined using expert based method. This technique requires flight mechanics intuition and statistical knowledge. The reader is referred to Section 4.4.2, 4.4.3 and 4.4.4.

The lateral/directional aerodynamic coefficients are determined using the hybrid BPSO approach and results are presented in the next subsections. The algorithm starts by generating 44 candidate model variables (terms). And then, pairwise correlation of the output variable with model variables and pairwise correlation among the model variables is calculated. If the variables are correlated among themselves, i.e., the correlation is higher than 0.95, the variables with a lower correlation coefficient value with the output variable are dropped. Almost half of the variables are dropped after correlation analysis, and finally the binary Particle Swarm Optimization algorithm is run to decide the best subset.

5.1.1.1 C_Y Force Coefficient

In the Table 5.1, the correlated variables are shown. The total number of dropped variables is 24 for C_Y coefficient.

Table 5.1 The Dropped Variables of C_Y model after Correlation Analysis

Variable	Dropped Variables
$C_{Y\beta}$	$\{C_{Y\delta_a\beta}, C_{Y\delta_a\delta_{lef}\beta}\}$
$C_{Y\beta\alpha}$	$\{C_{Y\delta_a\alpha\beta}, C_{Y\delta_a\delta_{lef}\alpha\beta}, C_{Y\delta_{lef}\beta}\}$
$C_{Y\beta\alpha^2}$	$\{C_{Y\delta_a\alpha^2\beta}, C_{Y\delta_a\delta_{lef}\alpha^2\beta}, C_{Y\delta_{lef}\alpha\beta}, C_{Y\delta_{lef}\alpha^2\beta}\}$
$C_{Y\delta_a}$	$\{C_{Y\delta_a\delta_{lef}}\}$
$C_{Yp\alpha}$	$\{C_{Yp\delta_{lef}}, C_{Yp\alpha^2}, C_{Yp\alpha\delta_{lef}}\}$
$C_{Y\delta_r\alpha}$	$\{C_{Y\delta_r\alpha^2}\}$
$C_{Yr\alpha}$	$\{C_{Yr\delta_{lef}}\}$
$C_{Yr\alpha^2}$	$\{C_{Yr\alpha\delta_{lef}}, C_{Yr\alpha^2\delta_{lef}}\}$
$C_{Y\delta_a\alpha}$	$\{C_{Y\delta_a\delta_{lef}\alpha}, C_{Y\delta_a\alpha^2}, C_{Y\delta_a\delta_{lef}\alpha^2}, C_{Y\delta_{lef}\alpha}, C_{Y\alpha}, C_{Y\delta_{lef}\alpha}, C_{Y\alpha^2}\}$

The remaining variables after correlation analysis are listed from most influential to the least influential as shown in Table 5.2.

Table 5.2 The Remaining Variables of C_Y Model after Correlation Analysis

Remaining Set of Variables
$\{ \mathbf{C_{Y\beta}}, C_{Y\beta^3}, C_{Y\beta\alpha}, C_{Y\beta^3\alpha}, \mathbf{C_{Yp}}, C_{Y\beta^3\alpha^2}, C_{Y\beta\alpha^2}, \mathbf{C_{Y\delta_a}}, C_{Yp\alpha}, C_{Yp\alpha^2\delta_{lef}}, C_{Y\delta_r\beta}, \mathbf{C_{Y\delta_r}} \}$ $\{ C_{Y\delta_r\alpha\beta}, C_{Y\delta_r\alpha}, C_{Y\delta_r\alpha^2\beta}, C_{Yr\alpha}, \mathbf{C_{Yr}}, C_{Yr\alpha^2}, C_{Y\delta_a\alpha}, C_{Y\delta_{lef}\alpha^2} \}$

In Table 5.2, some variables are represented in bold, because these variables are considered the most influential variables for a generic aircraft in Ref. [23] and are kept fixed in this study.

After fixing the variables recommended by Ref. [23] , the optimized variables are listed in Table 5.3.

Table 5.3 The Optimized Variables of C_Y Model

#	Variable	#	Variable	#	Variable
1	$C_{Y\beta^3}$	6	$C_{Yp\alpha}$	11	$C_{Y\delta_r\alpha^2\beta}$
2	$C_{Y\beta\alpha}$	7	$C_{Yp\alpha^2\delta_{lef}}$	12	$C_{Yr\alpha}$
3	$C_{Y\beta^3\alpha}$	8	$C_{Y\delta_r\beta}$	13	$C_{Yr\alpha^2}$
4	$C_{Y\beta^3\alpha^2}$	9	$C_{Y\delta_r\alpha\beta}$	14	$C_{Y\delta_\alpha\alpha}$
5	$C_{Y\beta\alpha^2}$	10	$C_{Y\delta_r\alpha}$	15	$C_{Y\delta_{lef}\alpha^2}$

There is total 160 configurations for different acceleration schemes (AS), transfer functions (TF) and inertia weight schemes (IWS). Table 5.4 gives the best fitness, worst fitness, mean fitness and standard deviations for the best 10 BPSO configurations with respect to mean fitness. It can be seen that mean fitness produced by Acceleration Scheme (AS) 1, Transfer Function (TF) 1, and Inertia Weight Scheme (IWS) 9 is the least with the lowest standard deviation as compared to other configurations. All configurations achieve the same best fitness, but Conf. 1 has better consistency.

Table 5.4 The Results of the Best 10 BPSO Configurations for C_Y Model

Conf #	AS	TF	IWS	Best Fitness	Worst Fitness	Mean Fitness	Std. Dev
1	1	1	9	2.56E-06	2.66E-06	2.57E-06	3.3E-08
2	1	1	7	2.56E-06	2.69E-06	2.58E-06	3.8E-08
3	2	8	7	2.56E-06	2.83E-06	2.58E-06	6.3E-08
4	2	2	4	2.56E-06	2.66E-06	2.58E-06	4.2E-08
5	1	1	8	2.56E-06	2.72E-06	2.58E-06	4.7E-08
6	2	1	4	2.56E-06	2.81E-06	2.59E-06	6.9E-08
7	2	1	8	2.56E-06	2.73E-06	2.59E-06	4.8E-08
8	1	3	4	2.56E-06	2.72E-06	2.59E-06	5.0E-08
9	1	1	4	2.56E-06	2.72E-06	2.59E-06	5.5E-08
10	2	8	6	2.56E-06	2.74E-06	2.59E-06	4.9E-08

In Table 5.5, the optimal subsets for the best fitness for the best 10 configurations are listed. The optimal subsets are the same. The optimal subset includes the 3rd, 5th, 9th, 14th, and 15th variables.

Table 5.5 The Optimal Subset of the Best 10 BPSO Configuration for C_Y Model

	Variables														
	1	2	3	4	5	6	7	8	9	10	11	12	13	14	15
Conf #	1	0	0	1	0	1	0	0	0	1	0	0	0	1	1
	2	0	0	1	0	1	0	0	0	1	0	0	0	1	1
	3	0	0	1	0	1	0	0	0	1	0	0	0	1	1
	4	0	0	1	0	1	0	0	0	1	0	0	0	1	1
	5	0	0	1	0	1	0	0	0	1	0	0	0	1	1
	6	0	0	1	0	1	0	0	0	1	0	0	0	1	1
	7	0	0	1	0	1	0	0	0	1	0	0	0	1	1
	8	0	0	1	0	1	0	0	0	1	0	0	0	1	1
	9	0	0	1	0	1	0	0	0	1	0	0	0	1	1
	10	0	0	1	0	1	0	0	0	1	0	0	0	1	1

Table 5.6 display displays the modeling terms as well as the number of instances in which they were selected for all configurations. The 14th and 15th variables were selected for each configuration. The 3rd, 5th, and 9th variables were selected for 158, 143 and 127 out of 160 instances, respectively. The best solutions are obtained for 133 instances out of 160 configurations. The modeling terms which appeared in more than half of the configurations are represented in bold and they are exactly the same with first the best configuration.

Table 5.6 The Number of Instances the Model Variables are Selected Using All BPSO Configurations for C_Y Model

Variables														
1	2	3	4	5	6	7	8	9	10	11	12	13	14	15
2	1	158	16	143	0	0	0	134	0	17	0	0	160	160

5.1.1.2 C_I Moment Coefficient

In Table 5.7, the correlated variables of C_I model are shown. The total number of dropped variables is 24 for C_I coefficient.

Table 5.7 The Dropped Variables of C_I model after Correlation Analysis

Variable	Dropped Variables
$C_{lr\alpha}$	$\{C_{lr\delta_{lef}}\}$
$C_{lr\alpha^2}$	$\{C_{lr\alpha\delta_{lef}}, C_{lr\alpha^2\delta_{lef}}\}$
$C_{l\beta\alpha}$	$\{C_{l\delta_{lef}\beta}, C_{l\delta_a\alpha\beta}, C_{l\delta_a\delta_{lef}\alpha\beta}\}$
$C_{l\beta\alpha^2}$	$\{C_{l\delta_{lef}\alpha\beta}, C_{l\delta_a\alpha^2\beta}, C_{l\delta_a\delta_{lef}\alpha^2\beta}, C_{l\delta_{lef}\alpha^2\beta}\}$
$C_{l\beta}$	$\{C_{l\delta_a\beta}, C_{l\delta_a\delta_{lef}\beta}\}$
$C_{l\delta_r\alpha^2}$	$\{C_{l\delta_r\alpha}\}$
$C_{l\delta_a}$	$\{C_{l\delta_a\delta_{lef}}\}$
$C_{lp\alpha}$	$\{C_{lp\delta_{lef}}, C_{lp\alpha^2}, C_{lp\alpha\delta_{lef}}\}$
$C_{l\delta_{lef}}$	$\{C_{l\alpha}, C_{l\delta_{lef}\alpha}, C_{l\alpha^2}, C_{l\delta_a\alpha}, C_{l\delta_a\delta_{lef}\alpha}, C_{l\delta_a\alpha^2}, C_{l\delta_a\delta_{lef}\alpha^2}\}$

The remaining variables after correlation analysis are listed from most influential to the least influential as shown in Table 5.8.

Table 5.8 The Remaining Variables of C_l Model after Correlation Analysis

Remaining Set of Variables	
$\left\{ C_{l_{r\alpha}}, \mathbf{C_{l_r}}, C_{l_{r\alpha^2}}, C_{l_{\beta\alpha}}, C_{l_{\beta\alpha^2}}, C_{l_{\beta^3\alpha^2}}, C_{l_{\beta^3\alpha}}, \mathbf{C_{l_\beta}}, C_{l_{\beta^3}}, C_{l_{\delta_r\alpha^2}}, \mathbf{C_{l_{\delta_r}}}, \mathbf{C_{l_{\delta_a}}} \right\}$ $\left\{ , C_{l_{\delta_r\alpha^2\beta}}, C_{l_{\delta_r\beta}}, \mathbf{C_{l_p}}, C_{l_{\delta_r\alpha\beta}}, C_{l_{p\alpha}}, C_{l_{\delta_{lef}}}, C_{l_{p\alpha^2\delta_{lef}}}, C_{l_{\delta_{lef}\alpha^2}} \right\}$	

In Table 5.8, some variables are represented in bold, because these variables are considered the most influential variables for a generic aircraft in Ref. [23] and are kept fixed in this study.

After fixing the variables recommended by Ref. [23] , the optimized variables are listed in Table 5.9.

Table 5.9 The Optimized Variables of C_l Model

#	Variable	#	Variable	#	Variable
1	$C_{l_{r\alpha}}$	6	$C_{l_{\beta^3\alpha}}$	11	$C_{l_{\delta_r\alpha\beta}}$
2	$C_{l_{r\alpha^2}}$	7	$C_{l_{\beta^3}}$	12	$C_{l_{p\alpha}}$
3	$C_{l_{\beta\alpha}}$	8	$C_{l_{\delta_r\alpha^2}}$	13	$C_{l_{\delta_{lef}}}$
4	$C_{l_{\beta\alpha^2}}$	9	$C_{l_{\delta_r\alpha^2\beta}}$	14	$C_{l_{p\alpha^2\delta_{lef}}}$
5	$C_{l_{\beta^3\alpha^2}}$	10	$C_{l_{\delta_r\beta}}$	15	$C_{l_{\delta_{lef}\alpha^2}}$

There is total 160 configurations for different acceleration schemes, transfer functions and inertia weight schemes. Table 5.10 gives the best fitness, worst fitness, mean fitness and standard deviations for the best 10 BPSO configurations with respect to mean fitness. It can be seen that mean fitness produced by Acceleration Scheme (AS) 1, Transfer Function (TF) 1, and Inertia Weight (IW) 8 is the least with the lowest standard deviation as compared to other configurations. All configurations achieve the same best fitness, but Conf. 1 has better consistency.

Table 5.10 The Results of the Best 10 BPSO Configurations for C_l Model

Conf #	AS	TF	IWS	Best Fitness	Worst Fitness	Mean Fitness	Std. Dev
1	2	1	8	4.318E-08	4.341E-08	4.327E-08	5.351E-11
2	2	1	4	4.318E-08	4.384E-08	4.328E-08	1.480E-10
3	2	2	4	4.318E-08	4.374E-08	4.330E-08	1.560E-10
4	1	1	9	4.318E-08	4.384E-08	4.332E-08	1.699E-10
5	1	1	3	4.318E-08	4.421E-08	4.336E-08	2.735E-10
6	1	3	4	4.318E-08	4.410E-08	4.336E-08	2.497E-10
7	1	1	4	4.318E-08	4.434E-08	4.337E-08	2.878E-10
8	1	2	9	4.318E-08	4.395E-08	4.337E-08	2.062E-10
9	2	1	9	4.318E-08	4.414E-08	4.337E-08	3.079E-10
10	2	6	2	4.318E-08	4.421E-08	4.338E-08	2.809E-10

In Table 5.11, the optimal subsets for the best fitness for the best 10 configurations are listed. The optimal subset includes the 3rd, 6th, 10th, 13th, and 15th variables.

Table 5.11 The Optimal Subset of the Best 10 BPSO Configuration for C_l Model

		Variables														
Conf #		1	2	3	4	5	6	7	8	9	10	11	12	13	14	15
	1	1	0	1	1	0	0	1	0	0	0	1	1	1	0	1
	2	1	0	1	1	0	0	1	0	0	0	1	1	1	0	1
	3	1	0	1	1	0	0	1	0	0	0	1	1	1	0	1
	4	1	0	1	1	0	0	1	0	0	0	1	1	1	0	1
	5	1	0	1	1	0	0	1	0	0	0	1	1	1	0	1
	6	1	0	1	1	0	0	1	0	0	0	1	1	1	0	1
	7	1	0	1	1	0	0	1	0	0	0	1	1	1	0	1
	8	1	0	1	1	0	0	1	0	0	0	1	1	1	0	1
	9	1	0	1	1	0	0	1	0	0	0	1	1	1	0	1
	10	1	0	1	1	0	0	1	0	0	0	1	1	1	0	1

Table 5.12 displays the modeling terms as well as the number of instances in which they were selected for all configurations. The 3rd, 13th and 15th variables were selected for each configuration. The best solutions are obtained for 118 instances out of 160 configurations. The modeling terms which appeared in more than half of the configurations are represented in bold.

Table 5.12 The Number of Instances the Model Variables are Selected Using All BPSO Configurations for C_l Coefficient

Variables														
1	2	3	4	5	6	7	8	9	10	11	12	13	14	15
140	0	160	127	0	42	118	0	0	30	130	123	160	0	160

5.1.1.3 C_n Moment Coefficient

In Table 5.13, the correlated and dropped variables of C_n model are shown.

Table 5.13 The Dropped Variables of C_n model after Correlation Analysis

Variable	Dropped Variables
$C_{n\beta}$	$\{C_{n\delta_a\beta}, C_{n\delta_a\delta_{lef}\beta}\}$
$C_{n\delta_a}$	$\{C_{n\delta_a\delta_{lef}}\}$
$C_{n\beta\alpha}$	$\{C_{n\delta_a\alpha\beta}, C_{l\delta_a\delta_{lef}\alpha\beta}, C_{l\delta_{lef}\beta}\}$
$C_{np\alpha}$	$\{C_{np\delta_{lef}}, C_{np\alpha^2}, C_{np\alpha\delta_{lef}}\}$
$C_{n\beta\alpha^2}$	$\{C_{l\delta_a\alpha^2\beta}, C_{l\delta_a\delta_{lef}\alpha^2\beta}, C_{l\delta_{lef}\alpha\beta}, C_{l\delta_{lef}\alpha^2\beta}\}$
$C_{n\delta_r\alpha^2}$	$\{C_{n\delta_r\alpha}\}$
$C_{n\delta_a\alpha}$	$\{C_{n\delta_a\delta_{lef}\alpha}, C_{n\delta_a\alpha^2}, C_{n\delta_a\delta_{lef}\alpha^2}, C_{n\delta_{lef}\alpha}, C_{n\alpha^2}, C_{n\delta_{lef}}, C_{n\alpha}\}$
$C_{nr\alpha\delta_{lef}}$	$\{C_{nr\alpha^2\delta_{lef}}, C_{nr\alpha^2}\}$
$C_{nr\delta_{lef}}$	$\{C_{nr\alpha}\}$

The remaining variables after correlation analysis are listed from most influential to the least influential as shown in Table 5.14.

Table 5.14 The Remaining Variables of C_n Model after Correlation Analysis

Remaining Set of Variables
$\left\{ \mathbf{C_{n\beta}}, \mathbf{C_{n\beta^3}}, \mathbf{C_{np}}, \mathbf{C_{n\delta_a}}, C_{n\beta^3\alpha}, C_{n\beta\alpha}, C_{np\alpha}, C_{n\beta^3\alpha^2}, C_{n\beta\alpha^2}, C_{np\alpha^2\delta_{lef}}, C_{n\delta_r\beta} \right\}$ $\left\{ , C_{n\delta_r\alpha\beta}, C_{n\delta_r\alpha^2}, \mathbf{C_{n\delta_r}}, C_{n\delta_r\alpha^2\beta}, C_{n\delta_a\alpha}, C_{nr\alpha\delta_{lef}}, C_{nr\delta_{lef}}, \mathbf{C_{l_r}}, C_{l\delta_{lef}\alpha^2} \right\}$

In Table 5.14, some variables are represented in bold, because these variables are considered the most influential variables for a generic aircraft in Ref. [23] and are kept fixed in this study.

After fixing the variables recommended by Ref. [23] , the optimized variables are shown in Table 5.15.

Table 5.15 The Optimized Variables of C_n Model

#	Variable	#	Variable	#	Variable
1	$C_{n\beta^3\alpha}$	6	$C_{np\alpha^2\delta_{lef}}$	11	$C_{n\delta_a\alpha}$
2	$C_{n\beta\alpha}$	7	$C_{n\delta_r\beta}$	12	$C_{nr\alpha\delta_{lef}}$
3	$C_{np\alpha}$	8	$C_{n\delta_r\alpha\beta}$	13	$C_{nr\delta_{lef}}$
4	$C_{n\beta^3\alpha^2}$	9	$C_{n\delta_r\alpha^2}$	14	$C_{l\delta_{lef}\alpha^2}$
5	$C_{n\beta\alpha^2}$	10	$C_{n\delta_r\alpha^2\beta}$		

There is total 160 configurations for different acceleration schemes, transfer functions and inertia weight schemes. Table 5.16 gives the best fitness, worst fitness, mean fitness and standard deviations for the best 10 BPSO configurations with respect to mean fitness. All configurations achieve the same best fitness, but Conf. 1 has better consistency.

Table 5.16 The Results of the Best 10 BPSO Configurations for C_n Model

Conf #	AS	TF	IWS	Best Cost	Worst Cost	Mean Cost	Std. Dev
1	1	1	9	1.045E-07	1.114E-07	1.061E-07	2.21E-09
2	2	2	4	1.045E-07	1.110E-07	1.063E-07	2.34E-09
3	1	1	3	1.045E-07	1.110E-07	1.066E-07	2.54E-09
4	1	2	4	1.045E-07	1.128E-07	1.066E-07	2.85E-09
5	1	1	8	1.045E-07	1.142E-07	1.067E-07	2.72E-09
6	2	3	4	1.045E-07	1.113E-07	1.067E-07	2.43E-09
7	1	6	5	1.045E-07	1.101E-07	1.068E-07	2.31E-09
8	1	3	4	1.045E-07	1.114E-07	1.069E-07	2.78E-09
9	1	6	2	1.045E-07	1.153E-07	1.070E-07	3.14E-09
10	2	1	4	1.045E-07	1.110E-07	1.070E-07	2.46E-09

In Table 5.17, the optimal subsets for the best fitness for the best 10 configurations are listed. The optimal subset includes the 1st, 3rd, 5th, 8th, and 14th variables.

Table 5.17 The Optimal Subset of the Best 10 BPSO Configuration for C_n Model

		Variables													
Conf #		1	2	3	4	5	6	7	8	9	10	11	12	13	14
	1	0	1	1	0	1	0	0	1	0	0	0	0	0	1
	2	0	1	1	0	1	0	0	1	0	0	0	0	0	1
	3	0	1	1	0	1	0	0	1	0	0	0	0	0	1
	4	0	1	1	0	1	0	0	1	0	0	0	0	0	1
	5	0	1	1	0	1	0	0	1	0	0	0	0	0	1
	6	0	1	1	0	1	0	0	1	0	0	0	0	0	1
	7	0	1	1	0	1	0	0	1	0	0	0	0	0	1
	8	0	1	1	0	1	0	0	1	0	0	0	0	0	1
	9	0	1	1	0	1	0	0	1	0	0	0	0	0	1
	10	0	1	1	0	1	0	0	1	0	0	0	0	0	1

Table 5.18 displays the modeling terms as well as the number of instances in which they were selected for all configurations. The 3rd, 13th and 15th variables were selected for each configuration. The 2nd and 8th variables were selected for 158 and 149 out of 160 instances, respectively. The best solutions are obtained for 146 instances out of 160 configurations. The modeling terms which appeared in more than half of the configurations are represented in bold.

Table 5.18 The Number of Instances the Model Variables are Selected Using All BPSO Configurations for C_n Coefficient

Variables													
1	2	3	4	5	6	7	8	9	10	11	12	13	14
0	158	160	1	160	2	0	149	0	11	0	0	0	160

5.1.1.4 Model Structure Evaluation Using BPSO For Lateral/Directional Coefficients

Each configuration yields good performance. At least 80% of best solutions among 30 trials for each configuration are the same. But to make overall evaluation for BPSO hyperparameters, a fitness scaling function is introduced. Fitness scaling function scales the raw scores based on the rank of each individual. The rank of an individual is its position in the sorted scores. An individual with rank r has scaled fitness score proportional to $1/\sqrt{r}$. The scaled score of the most fit individual is proportional to 1, the scaled score of the next most fit is proportional to $1/\sqrt{2}$. Table 5.19 shows the best 10 BPSO Configurations with respect to fitness scaling sum. S1 type transfer function is seen 6 times out of 10 times. The 9th Inertia Weight Scheme is ranked first, but the 7th and 4th schemes are repeated most.

Table 5.19 The Results of the Best 10 BPSO Configurations with respect to Fitness Scaling Sum (FSS) for Lateral/Directional Coefficients

Conf #	AS	TF	IWS	FSS
1	1	1	9	3.000
2	1	1	7	2.121
3	2	8	7	1.732
4	2	2	4	1.500
5	1	1	8	1.342
6	2	1	4	1.225
7	2	1	8	1.134
8	1	3	4	1.061
9	1	1	4	1.000
10	2	8	6	0.949

The correlation of each hyperparameter were calculated with respect to fitness sum and shown in Table 5.20. As shown in Table 5.20, the most correlated hyperparameter with fitness sum is transfer function selection, and acceleration scheme selection is the least correlated and does not affect the performance of BPSO.

Table 5.20 Correlation Analysis of BPSO Hyperparameters with respect to Fitness Scaling Sum for Lateral/Directional Coefficients

Correlation	AS	TF	IWS
FSS	0.0158	-0.1563	0.0519

The normalized fitness scaling sum for each hyperparameter and selection are tabulated in Table 5.21. The results of Table 5.21 supported the results of Table 5.20. The normalized fitness scaling sums of Acceleration Scheme 1 and 2 are almost the same so anyone of them can be used. The normalized fitness scaling sum of S1 transfer function is the highest and almost double of next best alternative so that S1 is preferred. Among inertia weight schemes, the most influential ones are 4th, 7th and

9th inertia weight strategies which are Constant Inertia Weight, Linear Increasing Inertia Weight, and Random Inertia Weight.

Table 5.21 Normalized Fitness Scaling Sum for Each Hyperparameter Selections

Type	AS	TF	IWS
1	49.39	22.82	7.44
2	50.61	12.55	9.19
3		9.12	10.03
4		7.15	12.97
5		10.97	8.92
6		11.60	8.58
7		12.08	12.78
8		13.71	10.16
9			12.57
10			7.37
Sum	100	100	100

5.1.2 Phase 1.2: Equation Error Method

The results of longitudinal (C_D , C_D and C_m) and lateral (C_Y , C_l and C_n) aerodynamic coefficients, obtained with Equation Error Method, are provided in this section.

5.1.2.1 C_D Force Coefficient

The resulting model structure for the C_D coefficient is as follows:

$$\begin{aligned}
C_D = & C_{D_0} + [C_{D_\alpha} \cdot \alpha + C_{D_{\alpha^2}} \cdot \alpha^2] + [C_{D_{\delta_e}} \cdot \delta_e + C_{D_{\delta_e \alpha}} \cdot \delta_e \cdot \alpha] \\
& + [C_{D_q} \cdot \frac{qc}{2V} + C_{D_{q\alpha}} \cdot \frac{qc}{2V} \cdot \alpha] \\
& + [C_{D_{\delta_{lef}}} \cdot \delta_{lef} + C_{D_{\delta_{lef} \alpha}} \cdot \delta_{lef} \cdot \alpha + C_{D_{\delta_{lef} \alpha_{10}^1}} \cdot \delta_{lef} \\
& \cdot (\alpha - \alpha_{10^\circ})_+ + C_{D_{\delta_{lef} \alpha_{15}^1}} \cdot \delta_{lef} \cdot (\alpha - \alpha_{15^\circ})_+] \\
& + [C_{D_\beta} \cdot \beta + C_{D_{\beta_0^1}} \cdot (\beta - \beta_{0^\circ})_+ + C_{D_{\beta^2}} \cdot \beta^2]
\end{aligned} \tag{5.1}$$

The parameter estimates of C_D is tabulated in Table 5.22. As shown in Table 5.22, the relative standard deviation for each coefficient is below 50. It indicates that estimates are reasonable.

Table 5.22 The Estimates, Standard Deviations, and Relative Standard Deviations of the C_D Coefficient Parameters

Index	Parameter	Estimate	Std. Dev.	Rel. Std. Dev
1	C_{D_0}	1.92E-02	6.11E-05	0.32
2	C_{D_α}	-9.04E-02	3.39E-03	3.75
3	$C_{D_{\alpha^2}}$	4.02E+00	2.49E-02	0.62
4	$C_{D_{\delta_e}}$	-1.10E-01	1.53E-03	1.4
5	$C_{D_{\delta_e \alpha}}$	1.01E+00	8.93E-03	0.88
6	C_{D_q}	-5.75E-01	4.61E-02	8.02
7	$C_{D_{q\alpha}}$	2.20E+01	2.73E-01	1.24
8	$C_{D_{\delta_{lef}}}$	6.92E-02	1.91E-03	2.76
9	$C_{D_{\delta_{lef} \alpha}}$	-9.49E-01	1.57E-02	1.65
10	$C_{D_{\delta_{lef} \alpha_{10}^1}}$	-2.49E-01	2.49E-03	1
11	$C_{D_{\delta_{lef} \alpha_{15}^1}}$	5.83E-01	3.38E-03	0.58
12	C_{D_β}	3.47E-02	1.16E-03	3.34
13	$C_{D_{\beta_0^1}}$	-7.17E-02	2.32E-03	3.24
14	$C_{D_{\beta^2}}$	1.05E+00	1.13E-02	1.08

The time history results for C_D in the training dataset is given in Figure 5.1.

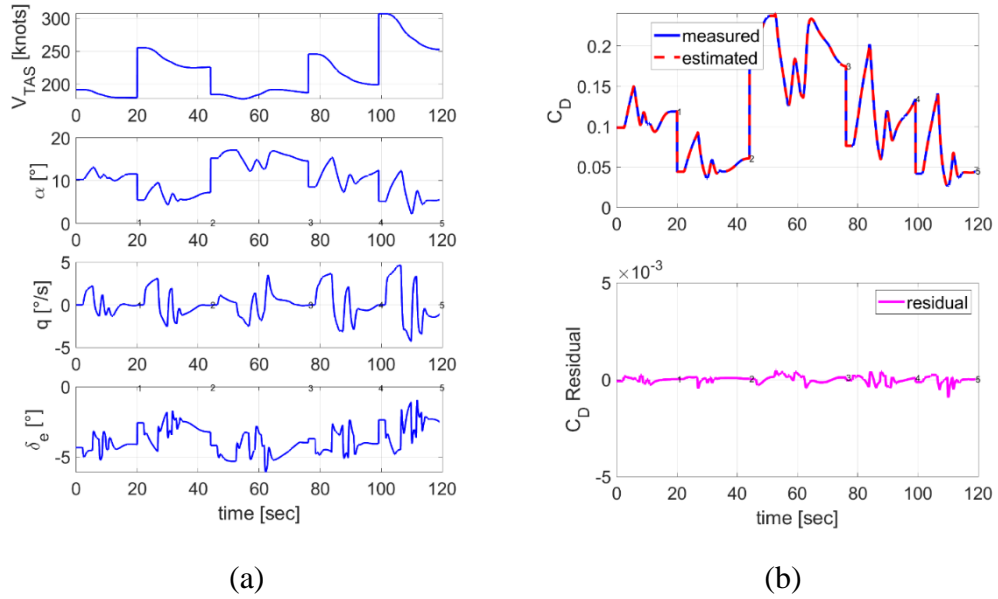


Figure 5.1 Training Dataset Results of C_D Coefficient a) Time Histories of the Input Variables b) Time Histories of the Output variable

No discrepancy is observed in Figure 5.1.

Residual cross plot for C_D with respect to air data, angular rates, and control surface deflections and cross plot for C_D with respect to the angle of attack in the training dataset are given in Figure 5.2. As stated earlier, in the residual cross plot, the flat spread of residual centered around zero is ideal, whereas non-flat spread indicates that the model needs improvement with the observed variable.

In Figure 5.2, higher β effect to residual error, can be seen in the cross plot of C_D vs β . As seen in figure, higher β cause more residual error. However, residual error is still small, and it is in an acceptable range (residual up to 50 drag count is acceptable).

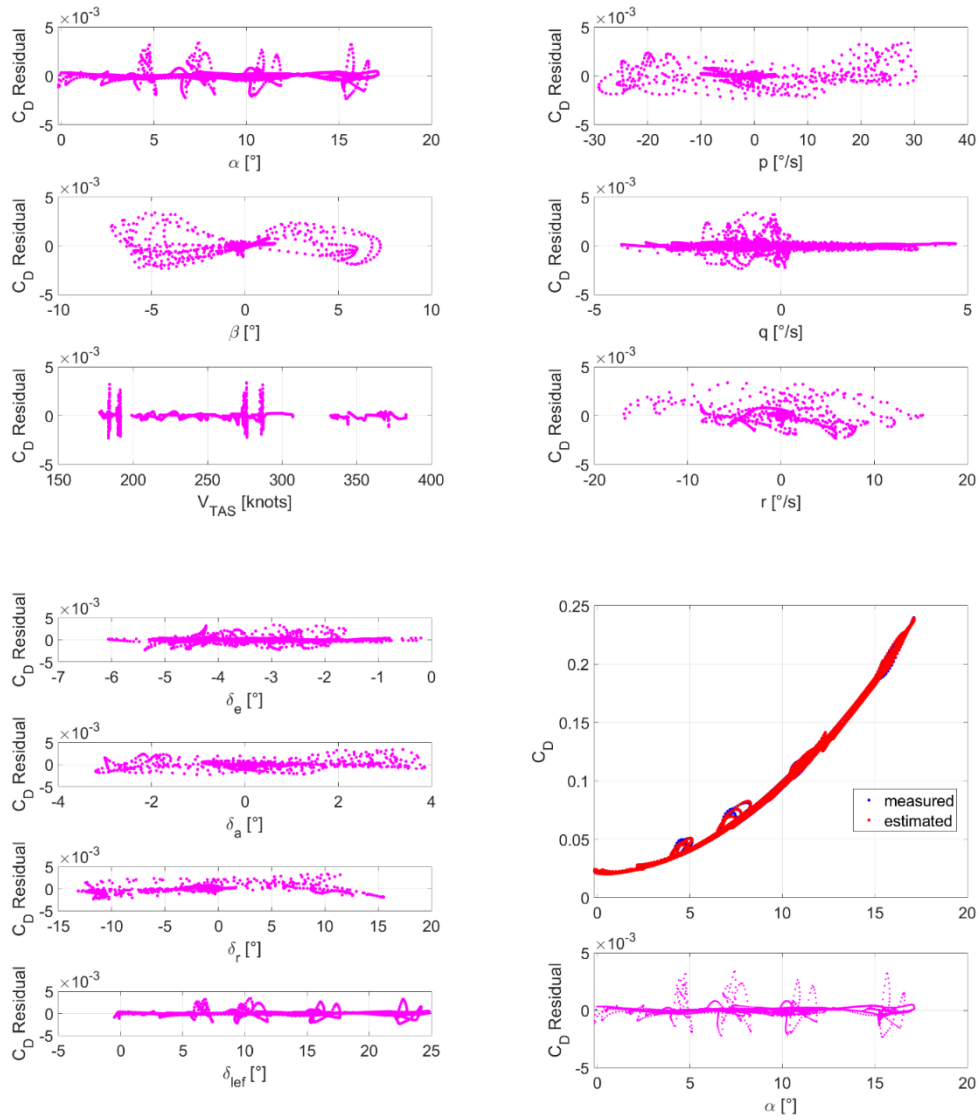


Figure 5.2 Residual Cross Plots and Cross Plot for C_D in Training Dataset.

As stated earlier, the results of training data are significant, but the final performance of the aerodynamic model should be tested with testing data reserved and are not used in the identification phase. The time history results for C_D in the testing dataset are shown in Figure 5.3.

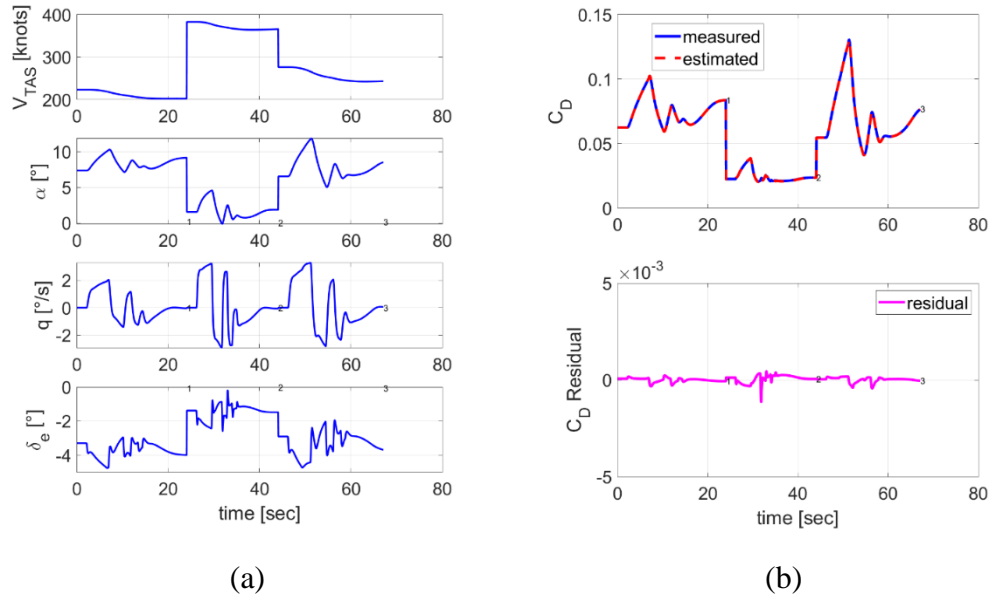


Figure 5.3 Testing Dataset Results of C_D Coefficient a) Time Histories of the Input Variables b) Time Histories of the Output variable

In Figure 5.3, the time history of C_D coefficient for testing dataset is plotted. Measured and estimated data are almost the same. As seen in this figure, the residual error is so tiny (less than 5×10^{-3}) that our aerodynamic coefficient model for C_D is acceptable.

5.1.2.2 C_L Force Coefficient

The resulting model structure for C_L coefficient is as follows:

$$\begin{aligned}
C_L = & \left[C_{L_0} + C_{L_\alpha} \cdot \alpha + C_{L_{\alpha_5^1}} \cdot (\alpha - \alpha_{5^\circ})_+ + C_{L_{\alpha_{10}^1}} \cdot (\alpha - \alpha_{10^\circ})_+ + C_{L_{\alpha_{15}^1}} \right. \\
& \cdot (\alpha - \alpha_{15^\circ})_+ \left. + \left[C_{L_{\delta_e}} \cdot \delta_e + C_{L_{\delta_e \alpha}} \cdot \delta_e \cdot \alpha + C_{L_{\delta_e \alpha^2}} \cdot \delta_e \cdot \alpha^2 \right] \right. \\
& + \left[C_{L_q} \cdot \frac{qc}{2V} \right] \\
& + \left[C_{L_{\delta_{lef}}} \cdot \delta_{lef} + C_{L_{\delta_{lef} \alpha}} \cdot \delta_{lef} \cdot \alpha + C_{L_{\delta_{lef} \alpha_5^1}} \cdot \delta_{lef} \cdot (\alpha - \alpha_{5^\circ})_+ \right. \\
& + C_{L_{\delta_{lef} \alpha_{10}^1}} \cdot \delta_{lef} \cdot (\alpha - \alpha_{10^\circ})_+ + C_{L_{\delta_{lef} \alpha_{15}^1}} \cdot \delta_{lef} \cdot (\alpha - \alpha_{15^\circ})_+ \left. \right] \\
& + \left[C_{L_\beta} \cdot \beta + C_{L_{\beta_0^1}} \cdot (\beta - \beta_{0^\circ})_+ \right]
\end{aligned} \tag{5.2}$$

The parameter estimates of C_L is tabulated in Table 5.23. As shown in Table 5.23, the relative standard deviation for each coefficient is below 50, which indicates that estimates uncertainty is very low.

Table 5.23 The Estimates, Standard Deviations, and Relative Standard Deviations the C_L Coefficient Parameters.

Index	Parameter	Estimate	Std. Dev.	Rel. Std. Dev
1	C_{L_0}	9.97E-02	9.34E-05	0.09
2	C_{L_α}	3.75E+00	2.28E-03	0.06
3	$C_{L_{\alpha_5^1}}$	1.42E-01	2.64E-03	1.85
4	$C_{L_{\alpha_{10}^1}}$	1.26E-01	5.27E-03	4.19
5	$C_{L_{\alpha_{15}^1}}$	-1.83E+00	4.75E-02	2.59
6	$C_{L_{\delta_e}}$	4.92E-01	3.51E-03	0.71
7	$C_{L_{\delta_e \alpha}}$	-5.45E-01	4.82E-02	8.84
8	$C_{L_{\delta_e \alpha^2}}$	5.41E+00	1.52E-01	2.82
9	C_{L_q}	3.01E+01	2.80E-02	0.09
10	$C_{L_{\delta_{lef}}}$	-1.85E-01	1.85E-03	1
11	$C_{L_{\delta_{lef} \alpha}}$	5.61E-01	1.51E-02	2.69
12	$C_{L_{\delta_{lef} \alpha_5^1}}$	4.48E-01	1.49E-02	3.32
13	$C_{L_{\delta_{lef} \alpha_{10}^1}}$	-8.98E-01	1.41E-02	1.57
14	$C_{L_{\delta_{lef} \alpha_{15}^1}}$	3.16E+00	1.08E-01	3.42
15	C_{L_β}	6.15E-02	5.28E-04	0.86
16	$C_{L_{\beta_0^1}}$	-1.23E-01	8.01E-04	0.65

The time history results for C_L in the training dataset is given in Figure 5.4.

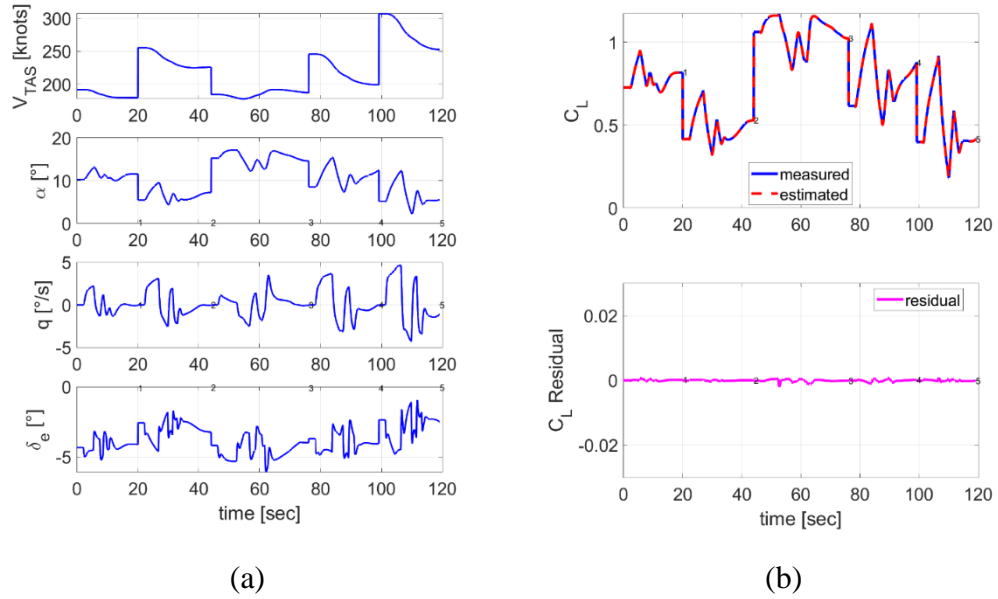
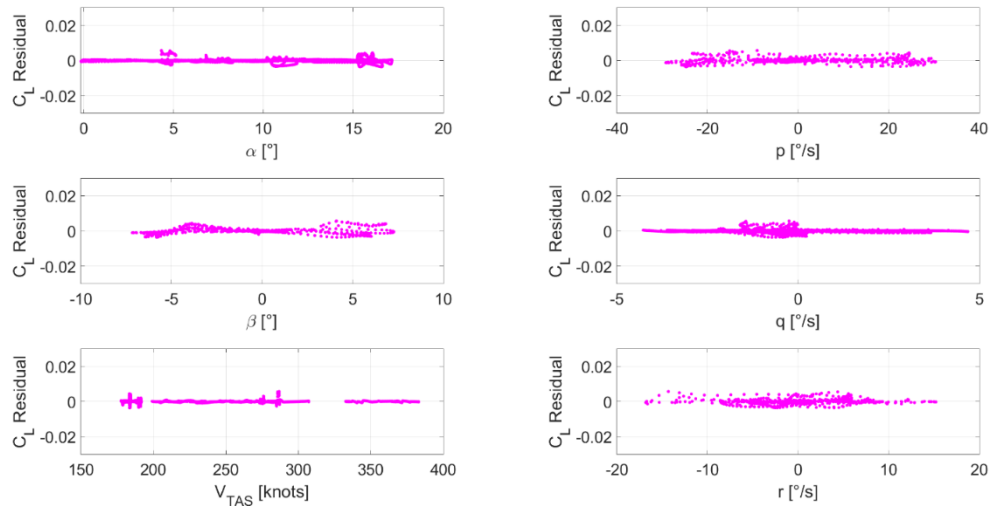


Figure 5.4 Training Dataset Results of C_L Coefficient a) Time Histories of the Input Variables b) Time Histories of the Output variable

Residual cross plot for C_L with respect to air data, angular rates, and control surface deflections and cross plot for C_L with respect to the angle of attack in the training dataset are given in Figure 5.5.



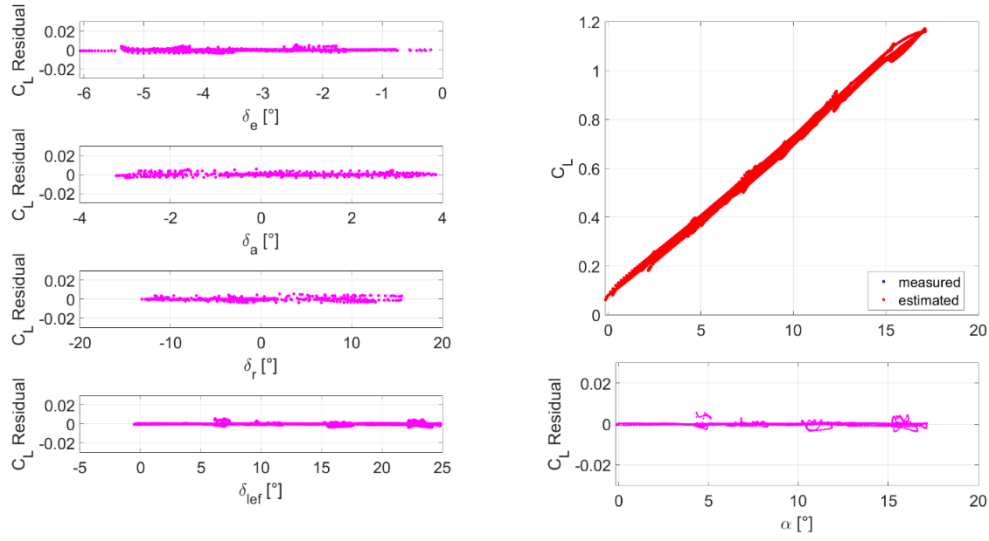


Figure 5.5 Residual Cross Plots and Cross Plot for C_L in Training Dataset.

The time history results for C_L in the testing dataset are shown in Figure 5.6.

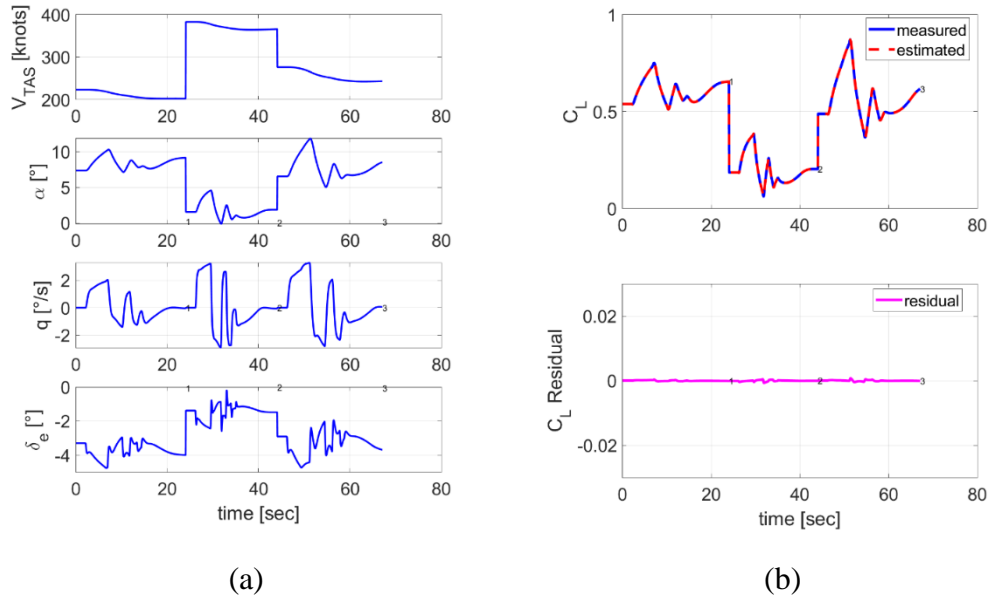


Figure 5.6 Testing Dataset Results of C_L Coefficient a) Time Histories of the Input Variables b) Time Histories of the Output variable

5.1.2.3 C_m Moment Coefficient

The resulting model structure for C_m coefficient is as follows:

$$\begin{aligned}
C_m = & \left[C_{m_0} + C_{m_\alpha} \cdot \alpha + C_{m_{\alpha_5^1}} \cdot (\alpha - \alpha_{5^\circ})_+ + C_{m_{\alpha_{10}^1}} \cdot (\alpha - \alpha_{10^\circ})_+ \right. \\
& \left. + C_{m_{\alpha_{15}^1}} \cdot (\alpha - \alpha_{15^\circ})_+ \right] \\
& + \left[C_{m_{\delta_e}} \cdot \delta_e + C_{m_{\delta_e \alpha}} \cdot \delta_e \cdot \alpha + C_{m_{\delta_e \alpha_{10}^1}} \cdot \delta_e \cdot (\alpha - \alpha_{10^\circ})_+ \right] \\
& + \left[C_{m_q} \cdot \frac{qc}{2V} + C_{m_{q\alpha}} \cdot \frac{qc}{2V} \cdot \alpha \right] \\
& + \left[C_{m_{\delta_{lef}}} \cdot \delta_{lef} + C_{m_{\delta_{lef} \alpha}} \cdot \delta_{lef} \cdot \alpha + C_{m_{\delta_{lef} \alpha_{10}^1}} \cdot \delta_{lef} \cdot (\alpha - \alpha_{10^\circ})_+ \right. \\
& \left. + C_{m_{\delta_{lef} \alpha_{15}^1}} \cdot \delta_{lef} \cdot (\alpha - \alpha_{15^\circ})_+ \right] \\
& + \left[C_{m_\beta} \cdot \beta + C_{m_{\beta_0^1}} \cdot (\beta - \beta_{0^\circ})_+ + C_{m_{\beta\alpha}} \cdot \beta \cdot \alpha \right]
\end{aligned} \tag{5.3}$$

The parameter estimates of C_m is tabulated in Table 5.24. As shown in Table 5.24, the relative standard deviation for each coefficient is below 50. It indicates that estimates are reasonable.

Table 5.24 The Estimates, Standard Deviations, and Relative Standard Deviations the C_m Coefficient Parameters.

Index	Parameter	Estimate	Std. Dev.	Rel. Std. Dev
1	C_{m_0}	-8.00E-03	4.60E-05	0.57
2	C_{m_α}	1.69E-01	1.31E-03	0.77
3	$C_{m_{\alpha_5^1}}$	-2.87E-02	1.45E-03	5.05
4	$C_{m_{\alpha_{10}^1}}$	4.65E-01	3.62E-03	0.78
5	$C_{m_{\alpha_{15}^1}}$	-1.26E+00	2.72E-02	2.16
6	$C_{m_{\delta_e}}$	-5.94E-01	1.64E-03	0.28
7	$C_{m_{\delta_e \alpha}}$	1.95E-01	1.26E-02	6.48
8	$C_{m_{\delta_e \alpha_{10}^1}}$	-1.03E+00	2.70E-02	2.63
9	C_{m_q}	-5.13E+00	3.72E-02	0.72
10	$C_{m_{q\alpha}}$	-4.93E+00	2.07E-01	4.21
11	$C_{m_{\delta_{lef}}}$	-7.68E-02	1.01E-03	1.32
12	$C_{m_{\delta_{lef} \alpha}}$	-1.19E-01	5.75E-03	4.81
13	$C_{m_{\delta_{lef} \alpha_{10}^1}}$	-6.48E-01	8.11E-03	1.25
14	$C_{m_{\delta_{lef} \alpha_{15}^1}}$	2.13E+00	6.18E-02	2.89
15	C_{m_β}	1.55E-02	5.57E-04	3.6
16	$C_{m_{\beta_0^1}}$	-6.36E-02	4.59E-04	0.72
17	$C_{m_{\beta\alpha}}$	1.57E-01	2.94E-03	1.87

The time history results for C_m in the training dataset is given in Figure 5.7.

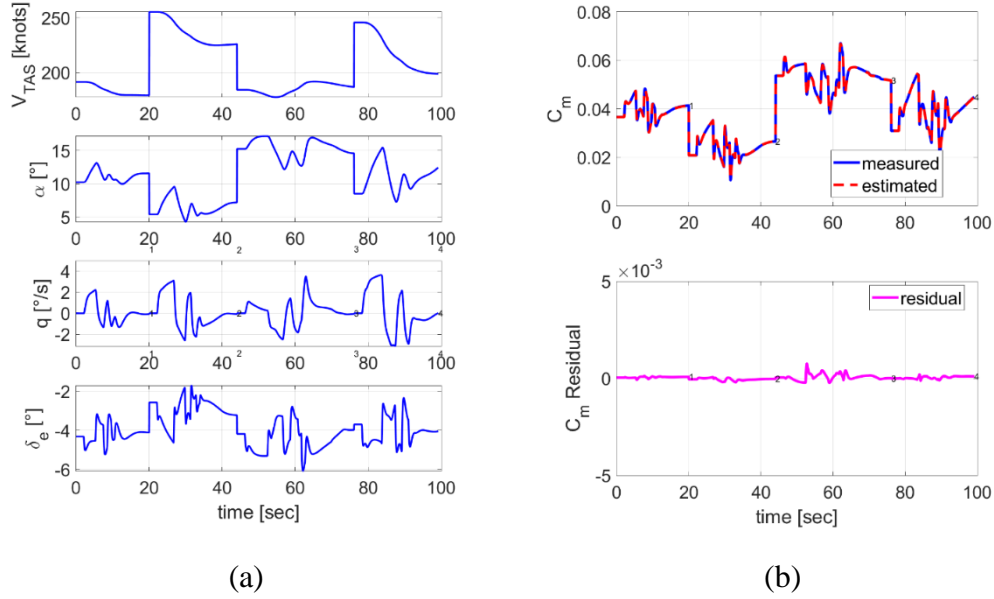
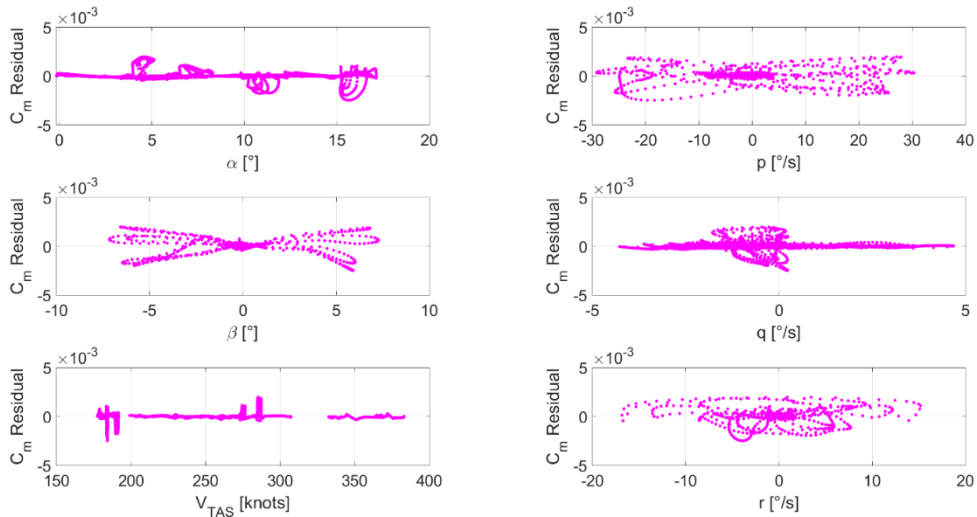


Figure 5.7 Training Dataset Results of C_m Coefficient a) Time Histories of the Input Variables b) Time Histories of the Output Variable

Residual cross plot for C_m with respect to air data, angular rates, and control surface deflections and cross plot for C_m with respect to the angle of attack in the training dataset are given in Figure 5.8.



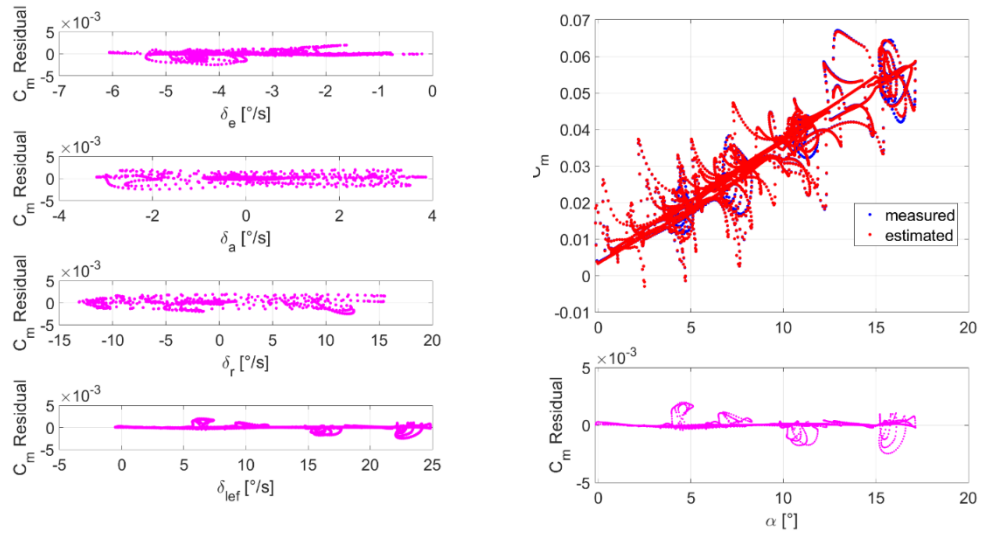


Figure 5.8 Residual Cross Plots and Cross Plot for C_m in Training Dataset.

The time history results for C_m in the testing dataset are shown in Figure 5.9.

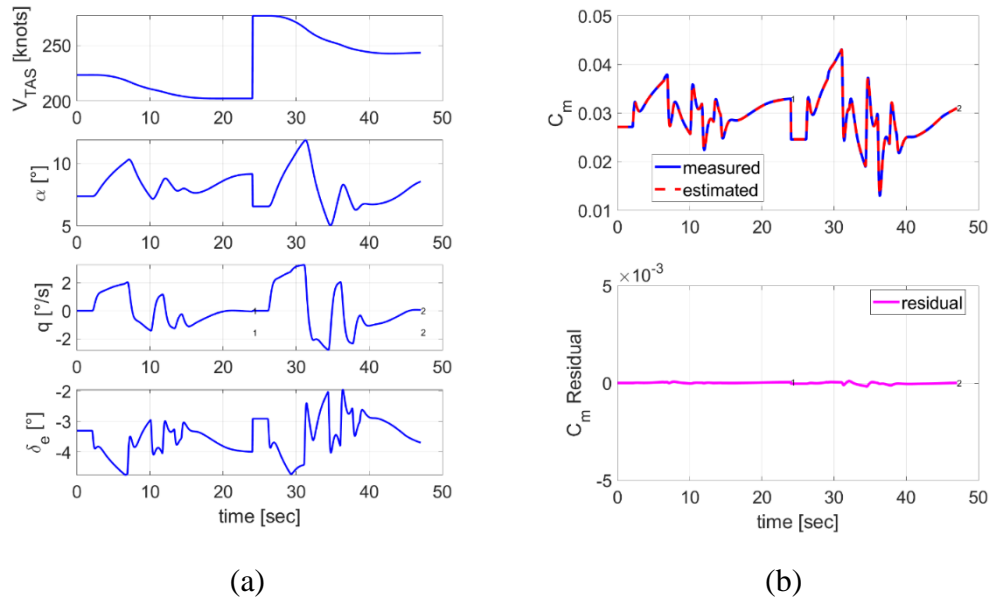


Figure 5.9 Testing Dataset Results of C_m Coefficient a) Time Histories of the Input Variables b) Time Histories of the Output Variable

5.1.2.4 C_Y Force Coefficient

The resulting model structure for C_Y coefficient is as follows:

$$\begin{aligned}
C_Y = & C_{Y_0} + \left[C_{Y_\beta} \cdot \beta + \beta \cdot \alpha^2 + C_{Y_{\beta^3\alpha}} \cdot \beta^3 \cdot \alpha \right] \\
& + \left[C_{Y_{\delta_r}} \cdot \delta_r + C_{Y_{\delta_r\alpha\beta}} \cdot \delta_r \cdot \alpha \cdot \beta \right] + \left[C_{Y_{\delta_a}} \cdot \delta_a + C_{Y_{\delta_a\alpha}} \cdot \delta_a \cdot \alpha \right] \\
& + \left[C_{Y_p} \cdot \frac{pb}{2V} \right] + \left[C_{Y_r} \cdot \frac{rb}{2V} \right] + \left[C_{Y_{\delta_{lef}\alpha^2}} \cdot \delta_{lef} \cdot \alpha^2 \right]
\end{aligned} \tag{5.4}$$

The parameter estimates of C_Y is tabulated in Table 5.25. As shown in Table 5.25, the relative standard deviation for each coefficient is below 50. It indicates that estimates are reasonable.

Table 5.25 The Estimates, Standard Deviations, and Relative Standard Deviations the C_Y Coefficient Parameters

Index	Parameter	Estimate	Std. Dev.	Rel. Std. Dev
1	C_{Y_0}	-5.09E-03	3.13E-05	0.61
2	C_{Y_β}	-1.07E+00	2.33E-03	0.22
3	$C_{Y_{\beta\alpha^2}}$	1.63E+00	4.15E-02	2.55
4	$C_{Y_{\beta^3\alpha}}$	-4.51E+01	1.05E+00	2.33
5	$C_{Y_{\delta_r}}$	1.68E-01	4.44E-04	0.26
6	$C_{Y_{\delta_r\alpha\beta}}$	-8.99E-01	3.23E-02	3.60
7	$C_{Y_{\delta_a}}$	7.58E-02	4.80E-03	6.34
8	$C_{Y_{\delta_a\alpha}}$	-3.26E-02	2.52E-02	37.04
9	C_{Y_p}	1.22E-01	4.04E-03	3.33
10	C_{Y_r}	5.09E-01	1.00E-02	1.96
11	$C_{Y_{\delta_{lef}\alpha^2}}$	3.36E-02	3.41E-03	10.15

The time history results for C_Y in the training dataset for the dutch roll maneuver is given in Figure 5.10.

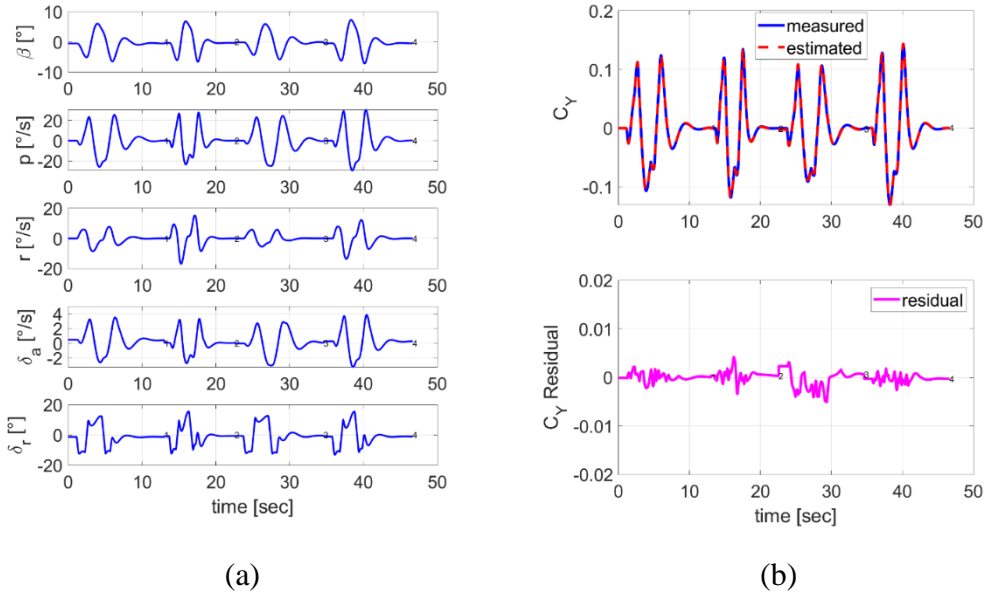


Figure 5.10 Training Dataset Results of C_Y Coefficient for the Dutch Roll Motion
a) Time Histories of the Input Variables b) Time Histories of the Output Variable

The time history results of C_Y in the training dataset for the bank-to-bank motion is given in Figure 5.11.

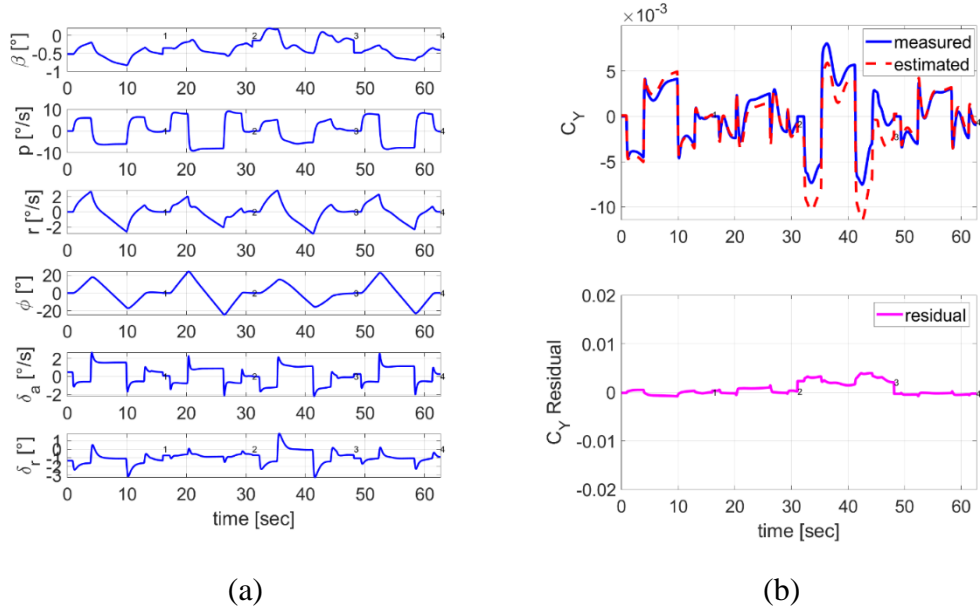


Figure 5.11 Training Dataset Results of C_Y Coefficient for the Bank-To-Bank Motion
a) Time Histories of the Input Variables b) Time Histories of the Output Variable

Residual cross plot for C_Y with respect to air data, angular rates, and control surface deflections and cross plot for C_Y with respect to the angle of attack in the training dataset are given in Figure 5.12.

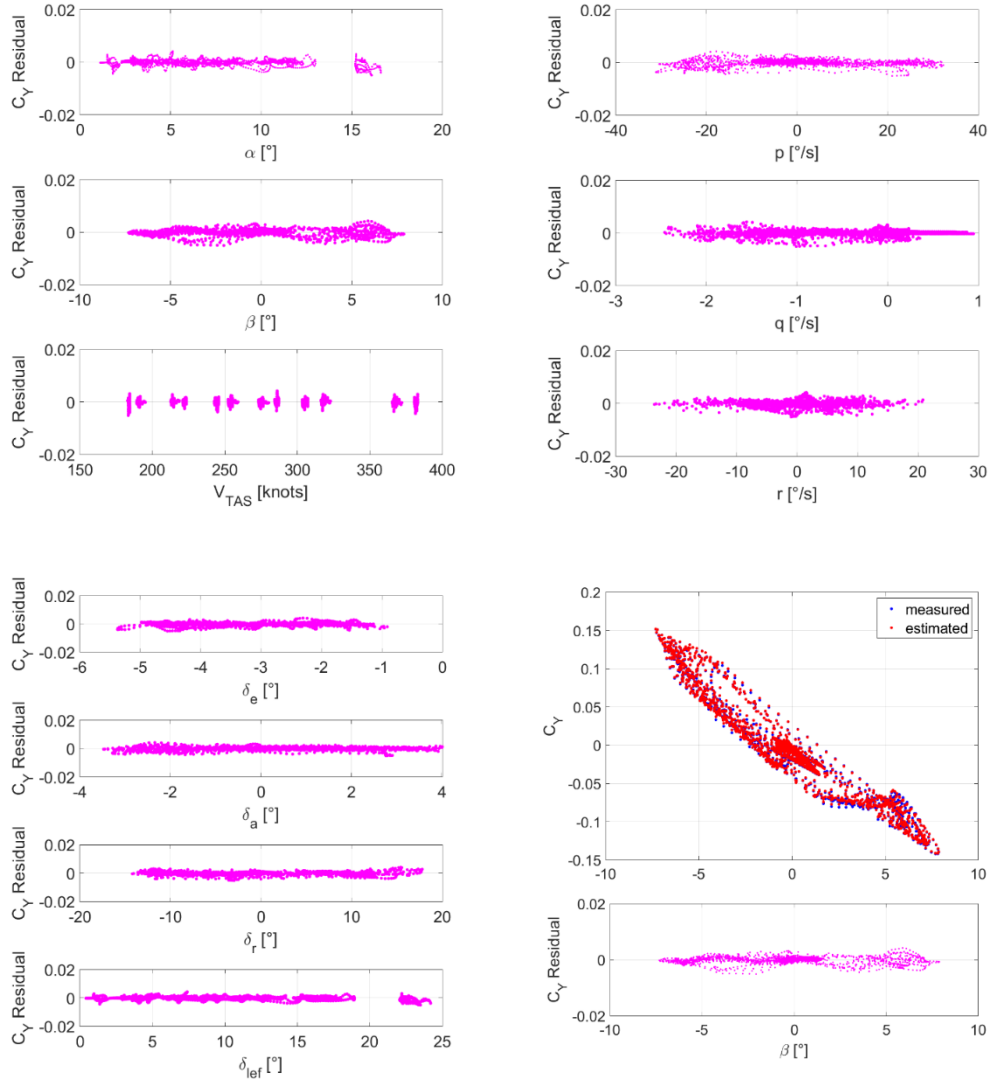


Figure 5.12 Residual Cross Plots and Cross Plot for C_Y in Training Dataset

The time history results for C_Y in the testing dataset are shown in Figure 5.13.

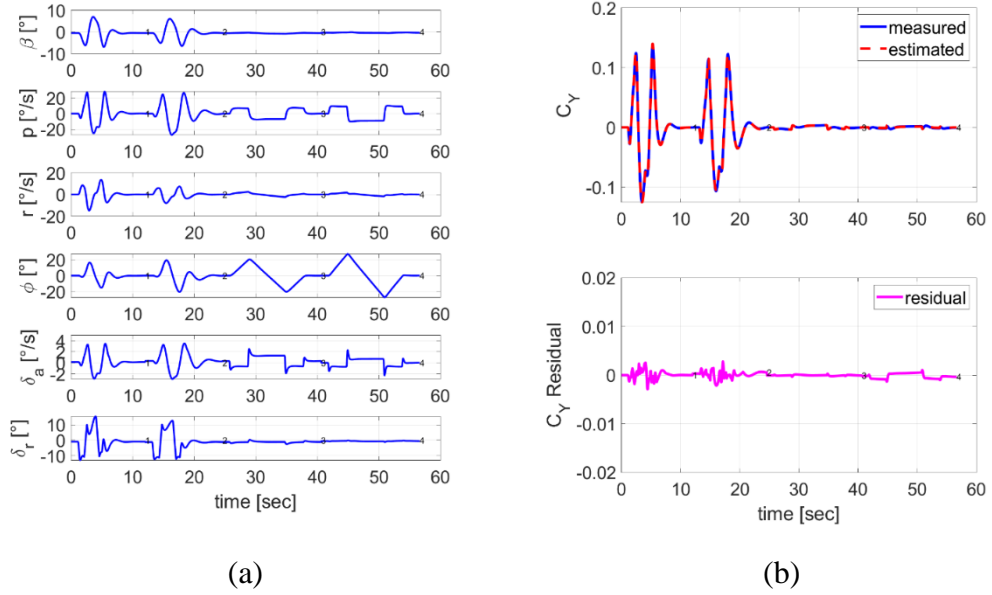


Figure 5.13 Testing Dataset Results of C_Y Coefficient a) Time Histories of the Input Variables b) Time Histories of the Output variable

5.1.2.5 C_l Moment Coefficient

The resulting model structure for C_l coefficient is as follows:

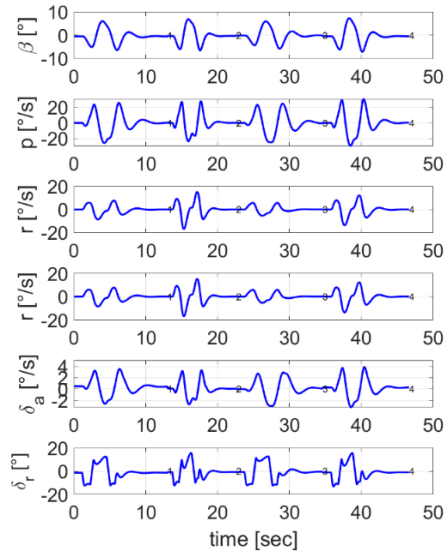
$$\begin{aligned}
 C_l = C_{l_0} &+ \left[C_{l_\beta} \cdot \beta + C_{l_{\beta\alpha}} \cdot \beta \cdot \alpha + C_{l_{\beta\alpha^2}} \cdot \beta \cdot \alpha^2 + C_{l_{\beta^3}} \cdot \beta^3 \right] \\
 &+ \left[C_{l_{\delta_r}} \cdot \delta_r + C_{l_{\delta_r\alpha\beta}} \cdot \delta_r \cdot \alpha \cdot \beta \right] + \left[C_{l_{\delta_a}} \cdot \delta_a \right] \\
 &+ \left[C_{l_p} \cdot \frac{pb}{2V} + C_{l_{p\alpha}} \cdot \frac{pb}{2V} \cdot \alpha \right] + \left[C_{l_r} \cdot \frac{rb}{2V} + C_{l_{r\alpha}} \cdot \frac{rb}{2V} \cdot \alpha \right] \\
 &+ \left[C_{l_{\delta_{lef}}} \cdot \delta_{lef} + C_{l_{\delta_{lef}\alpha^2}} \cdot \delta_{lef} \cdot \alpha^2 \right]
 \end{aligned} \tag{5.5}$$

The parameter estimates of C_l is tabulated in Table 5.26. As shown in Table 5.26, the relative standard deviation for each coefficient is below 50. It indicates that estimates are reasonable.

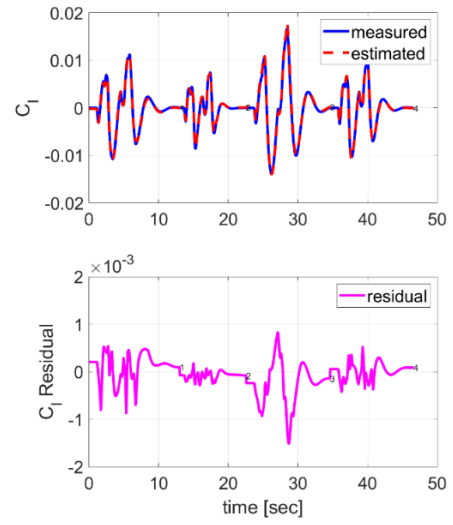
Table 5.26 The Estimates, Standard Deviations, and Relative Standard Deviations the C_l Coefficient Parameters.

Index	Parameter	Estimate	Std. Dev.	Rel. Std. Dev
1	C_{l_0}	-3.75E-04	5.75E-06	1.53
2	C_{l_β}	-8.88E-02	6.97E-04	0.79
3	$C_{l_{\beta\alpha}}$	-4.19E-01	1.09E-02	2.60
4	$C_{l_{\beta\alpha^2}}$	-2.89E-01	3.86E-02	13.33
5	$C_{l_{\beta^3}}$	-5.14E-01	2.07E-02	4.03
6	$C_{l_{\delta_r}}$	2.66E-02	6.00E-05	0.23
7	$C_{l_{\delta_r\alpha\beta}}$	-1.09E-01	4.25E-03	3.91
8	$C_{l_{\delta_a}}$	-1.30E-01	1.90E-04	0.15
9	C_{l_p}	-2.05E-01	6.66E-04	0.32
10	$C_{l_{p\alpha}}$	7.40E-02	3.99E-03	5.39
11	C_{l_r}	4.12E-02	1.68E-03	4.07
12	$C_{l_{r\alpha}}$	3.42E-01	1.18E-02	3.45
13	$C_{l_{\delta_{lef}}}$	2.43E-03	4.93E-05	2.03
14	$C_{l_{\delta_{lef}\alpha^2}}$	-3.01E-02	6.92E-04	2.30
12	$C_{l_{r\alpha}}$	3.42E-01	1.18E-02	3.45
13	$C_{l_{\delta_{lef}}}$	2.43E-03	4.93E-05	2.03
14	$C_{l_{\delta_{lef}\alpha^2}}$	-3.01E-02	6.92E-04	2.30

The time history results for C_l in the dutch roll training dataset is given in Figure 5.14.



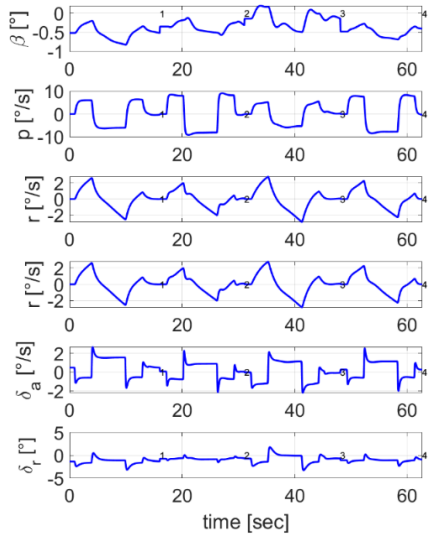
(a)



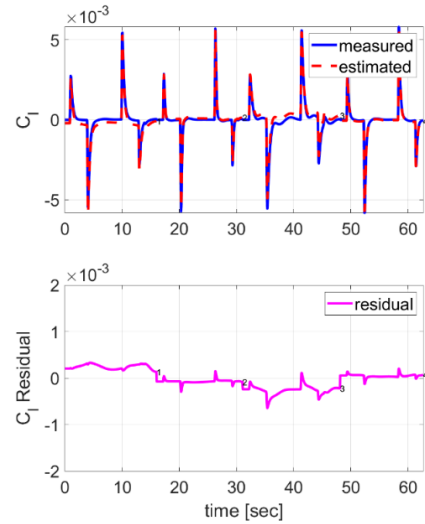
(b)

Figure 5.14 Dutch Roll Training Dataset Results of C_l Coefficient a) Time Histories of the Input Variables b) Time Histories of the Output Variable

The time history results for C_l in the bank-to-bank training dataset is given in Figure 5.15.



(a)



(b)

Figure 5.15 Bank-To-Bank Training Dataset Results of C_l Coefficient a) Time Histories of the Input Variables b) Time Histories of the Output Variable

Residual cross plot for C_l with respect to air data, angular rates, and control surface deflections and cross plot for C_l with respect to the angle of attack in the training dataset are given in Figure 5.16.

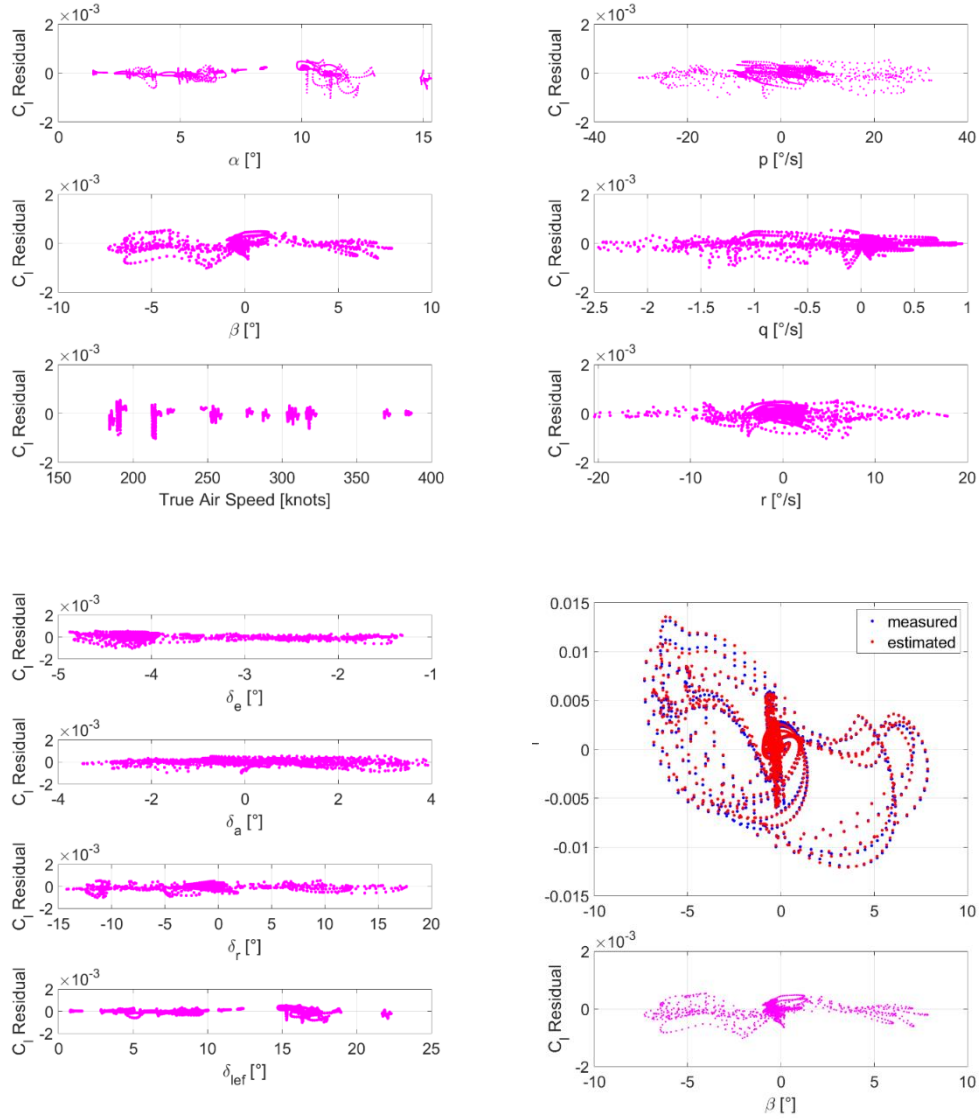


Figure 5.16 Residual Cross Plots and Cross Plot for C_l in Training Dataset

The time history results for C_l in the testing dataset are shown in Figure 5.17.

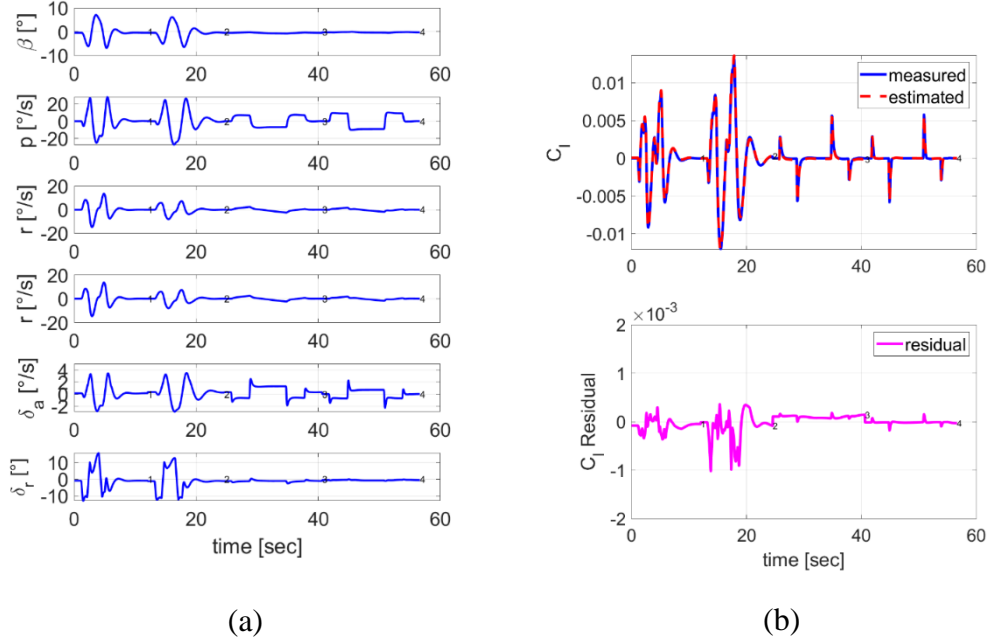


Figure 5.17 Testing Dataset Results of C_l Coefficient a) Time Histories of the Input Variables b) Time Histories of the Output variable

5.1.2.6 C_n Moment Coefficient

The resulting model structure for C_n coefficient is as follows:

$$\begin{aligned}
 C_n = & C_{n_0} + \left[C_{n_\beta} \cdot \beta + C_{n_{\beta\alpha}} \cdot \beta \cdot \alpha + C_{n_{\beta^3}} \cdot \beta^3 \right] \\
 & + \left[C_{n_{\delta_r}} \cdot \delta_r + C_{n_{\delta_r\alpha\beta}} \cdot \delta_r \cdot \alpha \cdot \beta \right] + \left[C_{n_{\delta_a}} \cdot \delta_a \right] \\
 & + \left[C_{n_p} \cdot \frac{pb}{2V} + C_{n_{p\alpha}} \cdot \frac{pb}{2V} \cdot \alpha + C_{n_{p\alpha^2}} \cdot \frac{pb}{2V} \cdot \alpha^2 \right] + \left[C_{n_r} \cdot \frac{rb}{2V} \right] \\
 & + \left[C_{n_{\delta_{lef}\alpha^2}} \cdot \delta_{lef} \cdot \alpha^2 \right]
 \end{aligned} \tag{5.6}$$

The parameter estimates of C_n is tabulated in Table 5.27. As shown in Table 5.27, the relative standard deviation for each coefficient is below 50. It indicates that estimates are reasonable.

Table 5.27 The Estimates, Standard Deviations, and Relative Standard Deviations the C_m Coefficient Parameters.

Index	Parameter	Estimate	Std. Dev.	Rel. Std. Dev
1	C_{n_0}	3.33E-05	5.31E-06	15.91
2	C_{n_β}	1.86E-01	5.17E-04	0.28
3	$C_{n_{\beta\alpha}}$	-3.89E-02	2.26E-03	5.83
4	$C_{n_{\beta^3}}$	2.98E+00	2.60E-02	0.87
5	$C_{n_{\delta_r}}$	-8.57E-02	7.52E-05	0.09
6	$C_{n_{\delta_r\alpha\beta}}$	2.45E-01	5.40E-03	2.20
7	$C_{n_{\delta_a}}$	-2.64E-02	3.95E-04	1.50
8	C_{n_p}	5.54E-02	2.12E-03	3.83
9	$C_{n_{p\alpha}}$	-1.03E+00	2.33E-02	2.27
10	$C_{n_{p\alpha^2}}$	2.75E+00	6.36E-02	2.31
11	C_{n_r}	-1.95E-01	1.61E-03	0.83
12	$C_{n_{\delta_{lef}\alpha^2}}$	-1.50E-02	5.82E-04	3.89

The time history results for C_n in the dutch roll and bank to-bank training datasets are given in Figure 5.18 and Figure 5.19, respectively.

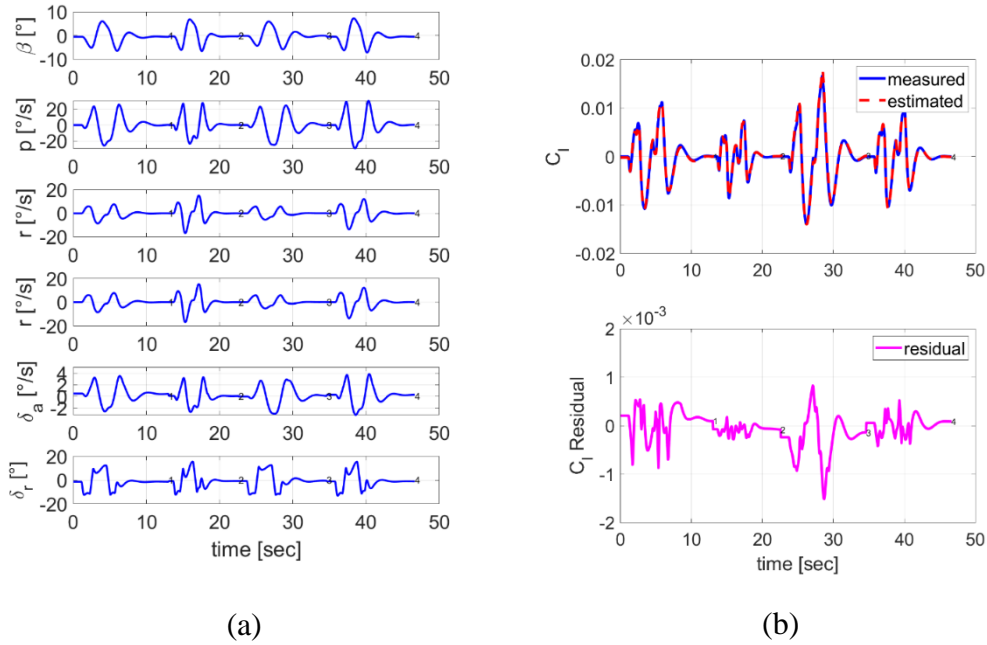
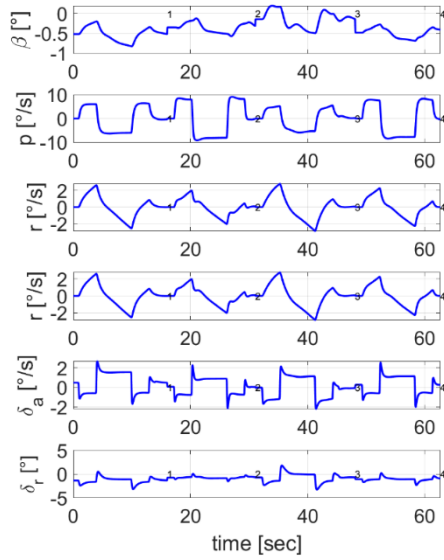
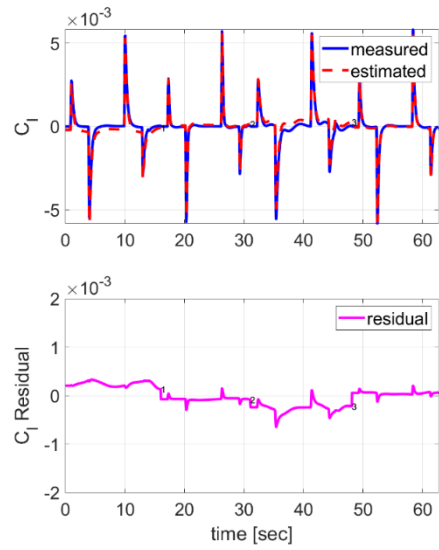


Figure 5.18 Dutch Roll Training Dataset Results of C_n Coefficient a) Time Histories of the Input Variables b) Time Histories of the Output Variable



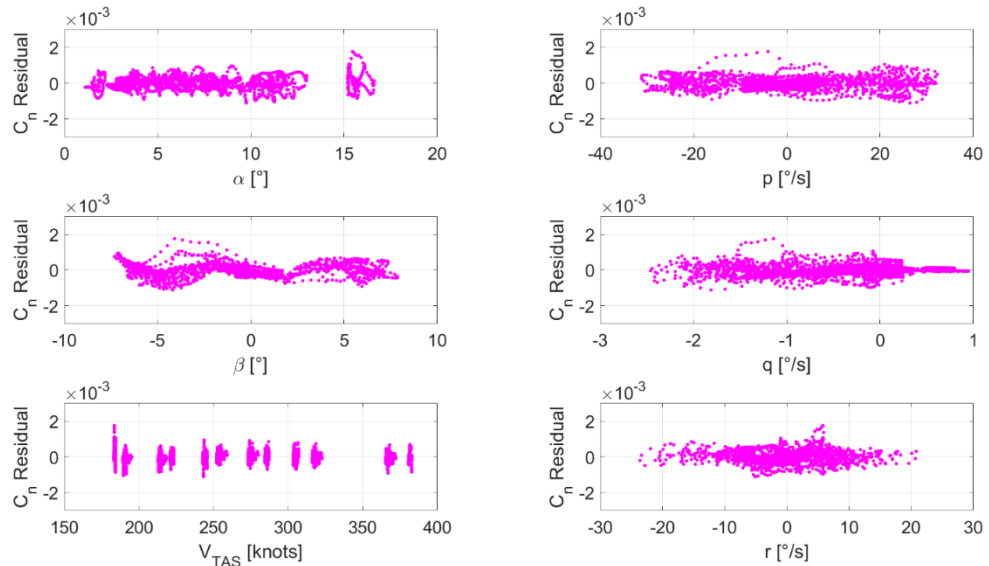
(a)



(b)

Figure 5.19 Bank-To-Bank Training Dataset Results of C_n Coefficient a) Time Histories of the Input Variables b) Time Histories of the Output Variable

Residual cross plot for C_n with respect to air data, angular rates, and control surface deflections and cross plot for C_n with respect to the angle of attack in the training dataset are given in Figure 5.20.



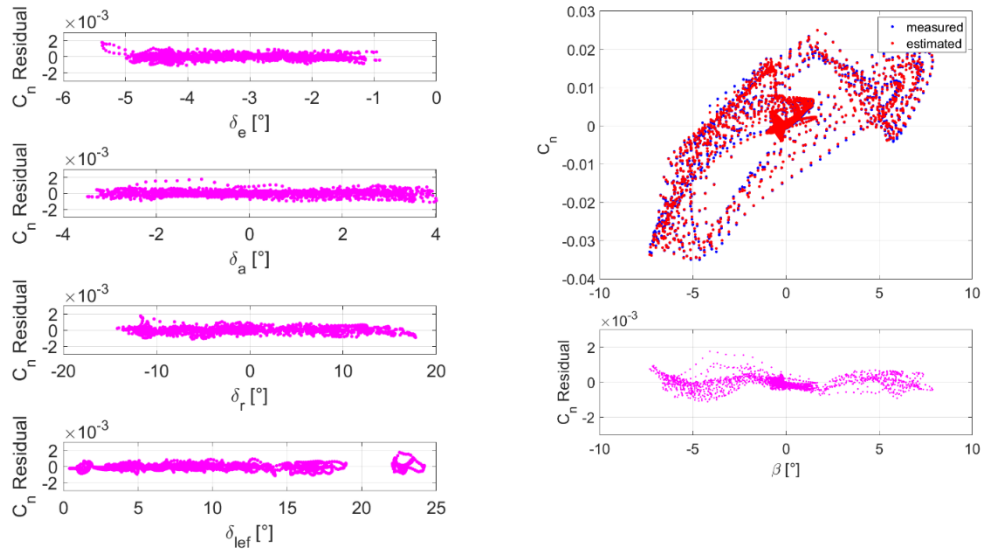


Figure 5.20 Residual Cross Plots and Cross Plot for C_n in Training Dataset

The time history results for C_n in the testing dataset are shown in Figure 5.21.

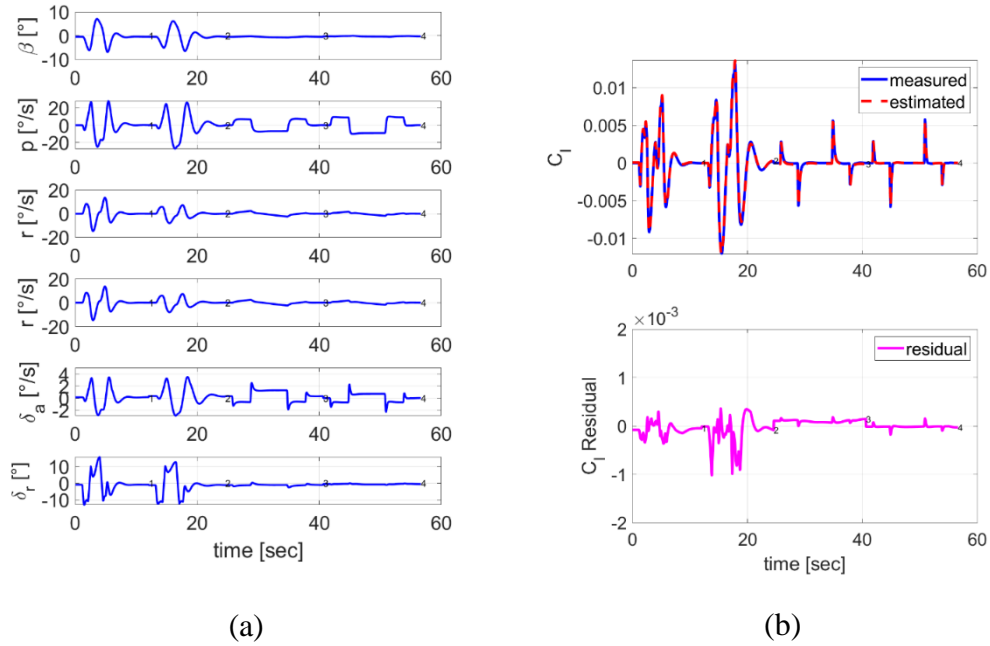


Figure 5.21 Testing Dataset Results of C_n Coefficient a) Time Histories of the Input Variables b) Time Histories of the Output Variable

5.1.3 Phase 1.3: Sensitivity Analysis

In this section, sensitivity analysis results are presented for each coefficient. We will determine the parameters that highly influence the aerodynamic coefficients in this phase. In Phase 2, we will only tune these most influential parameters since updating all parameters in the output error method is time-consuming, and the minimization problem can be ill-conditioned in this phase.

5.1.3.1 C_D Force Coefficient

The parameters of C_D coefficient are determined using short-period, phugoid, and dutch-roll maneuvers. That is why sensitivity analysis is done for longitudinal maneuvers, lateral maneuvers, and both of them. In the coming figures, normalized cost value for each parameter of C_D are observed for different maneuvers. It is concluded that in this case, the most influential parameters are $C_{D\alpha^2}$ and $C_{D\delta_{lef}\alpha}$. The other parameters have a normalized sensitivity magnitude of less than 5% of the most significant term's ($C_{D\alpha^2}$) magnitude.

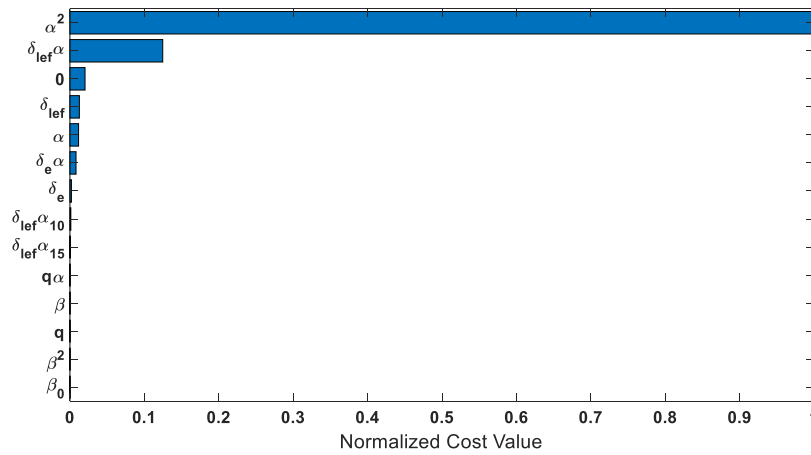


Figure 5.22 Sensitivities of the C_D parameters with a 1% change from their original value during longitudinal maneuvers.

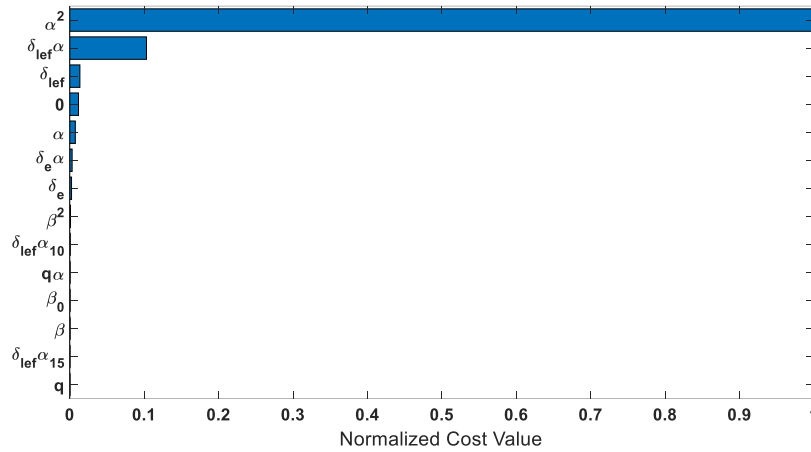


Figure 5.23 Sensitivities of the C_D parameters with a 1% change from their original value during lateral (dutch-roll) maneuver.

5.1.3.2 C_L Force Coefficient

The parameters of C_L coefficient are determined using short-period, phugoid, and dutch-roll maneuvers. That is why sensitivity analysis is done for longitudinal maneuvers, lateral maneuvers, and both of them. In the coming figures, normalized cost value for each parameter of C_L are observed for different maneuvers. It is concluded that in this case, the most influential parameters are $C_{L\alpha}$. This result is not surprising since it is already covered in Table 4.10. The other parameters have a normalized sensitivity magnitude of less than 5% of the most significant term's ($C_{L\alpha}$) magnitude and will not be tuned in Phase 2.

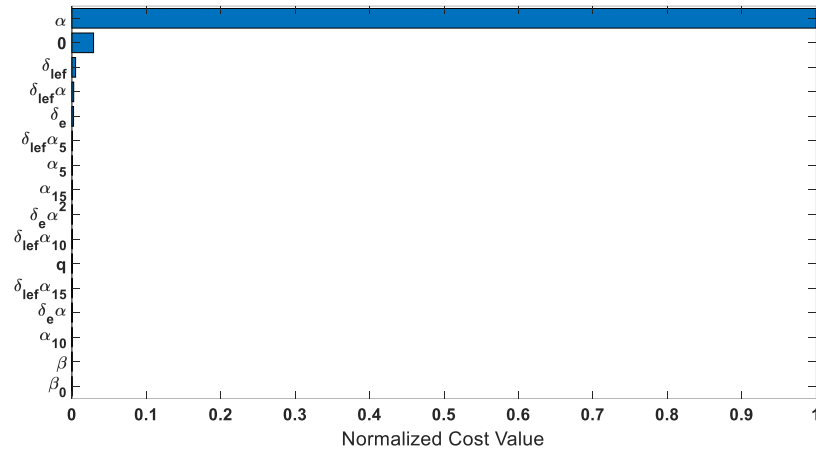


Figure 5.24 Sensitivities of the C_L parameters with a 1% change from their original value during longitudinal maneuvers.

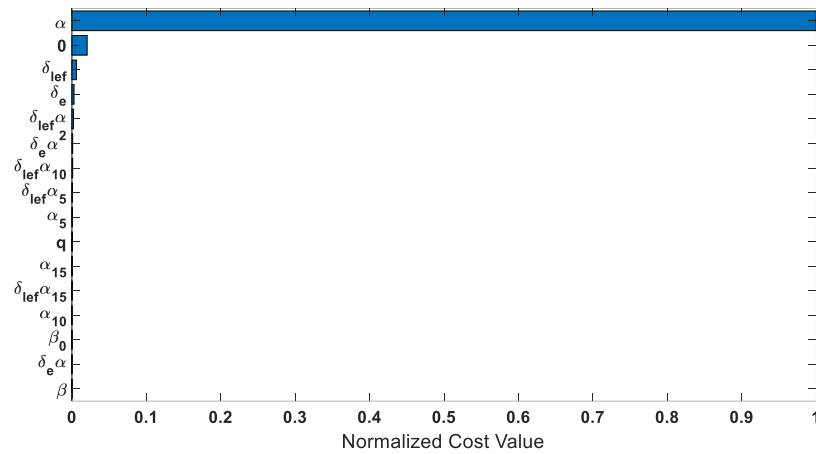


Figure 5.25 Sensitivities of the C_L parameters with a 1% change from their original value during lateral (dutch-roll) maneuver.

5.1.3.3 C_m Moment Coefficient

The parameters of C_m coefficient are determined using short-period, phugoid, and dutch-roll maneuvers. That is why sensitivity analysis is done for longitudinal maneuvers, lateral maneuvers, and both of them. In the coming figures, normalized cost value for each parameter of C_m are observed for different maneuvers. It is

concluded that in this case, the most influential parameters are $C_{m\delta_e}$, $C_{m\alpha}$, $C_{m\alpha_{10}^1}$, and $C_{m\delta_{lef}}$. This result is not also surprising since it is already covered in Table 4.10. The other parameters have a normalized sensitivity magnitude of less than 5% of the most significant term's ($C_{m\delta_e}$) magnitude and will not be tuned in Phase 2.

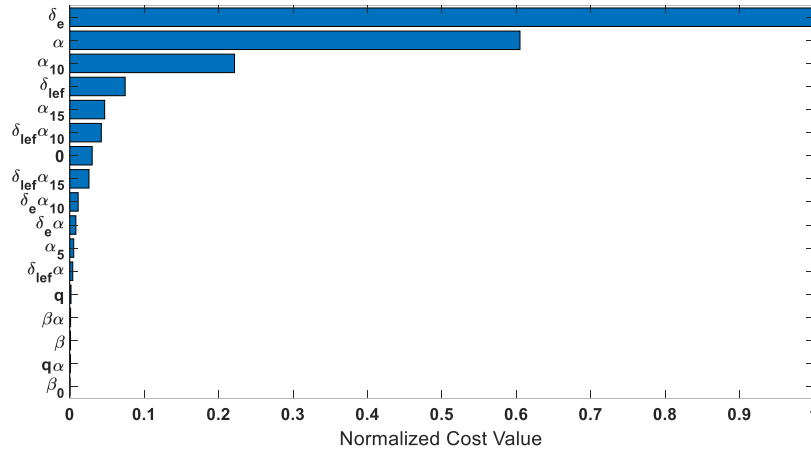


Figure 5.26 Sensitivities of the C_m parameters with a 1% change from their original value during longitudinal maneuvers.

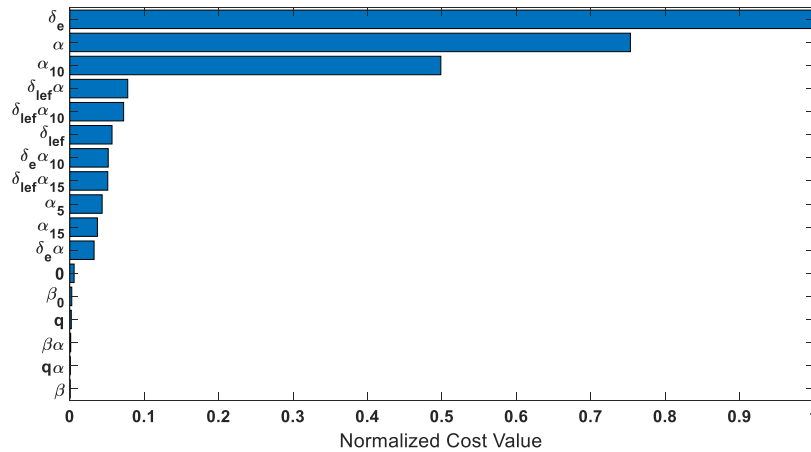


Figure 5.27 Sensitivities of the C_m parameters with a 1% change from their original value during lateral (dutch-roll) maneuver.

So far, the sensitivity of longitudinal coefficients is covered. It is noted that for longitudinal and lateral maneuvers, the rank of influential parameters is almost the

same, and there are no lateral terms in the most influential parameters of longitudinal coefficients. So in the second phase, there is no need to use lateral maneuvers to update the longitudinal coefficient parameters. The number of tuned parameters is decreased to 7 out of 47 terms. The tuned parameters are shown in red-colored in Table 5.28

Table 5.28 Normalized Sensitivity Magnitudes (SM) for Longitudinal Coefficients in Longitudinal Maneuvers (Short-Period and Phugoid) (Most Influential Terms are Red-Colored).

Index	Parameter	Normalized SM	Parameter	Normalized SM	Parameter	Normalized SM
1	C_{D_0}	0.0072	C_{L_0}	0.0291	C_{m_0}	0.0301
2	C_{D_α}	0.0257	C_{L_α}	1.0000	C_{m_α}	0.6049
3	$C_{D_\alpha^2}$	1.0000	$C_{L_{\alpha_5^1}}$	0.0005	$C_{m_{\alpha_5^1}}$	0.0053
4	$C_{D_{\delta_e}}$	0.0020	$C_{L_{\alpha_{10}^1}}$	0.0001	$C_{m_{\alpha_{10}^1}}$	0.2213
5	$C_{D_{\delta_e\alpha}}$	0.0118	$C_{L_{\alpha_{15}^1}}$	0.0005	$C_{m_{\alpha_{15}^1}}$	0.0469
6	C_{D_q}	0.0000	$C_{L_{\delta_e}}$	0.0022	$C_{m_{\delta_e}}$	1.0000
7	$C_{D_{q\alpha}}$	0.0000	$C_{L_{\delta_e\alpha}}$	0.0002	$C_{m_{\delta_e\alpha}}$	0.0082
8	$C_{D_{\delta_{lef}}}$	0.0063	$C_{L_{\delta_e\alpha^2}}$	0.0005	$C_{m_{\delta_e\alpha_{10}^1}}$	0.0112
9	$C_{D_{\delta_{lef}\alpha}}$	0.1604	C_{L_q}	0.0003	C_{m_q}	0.0016
10	$C_{D_{\delta_{lef}\alpha_{10}^1}}$	0.0016	$C_{L_{\delta_{lef}}}$	0.0049	$C_{m_{q\alpha}}$	0.0004
11	$C_{D_{\delta_{lef}\alpha_{15}^1}}$	0.0001	$C_{L_{\delta_{lef}\alpha}}$	0.0024	$C_{m_{\delta_{lef}}}$	0.0744
12	C_{D_β}	0.0001	$C_{L_{\delta_{lef}\alpha_5^1}}$	0.0006	$C_{m_{\delta_{lef}\alpha}}$	0.0040
13	$C_{D_{\beta_0^1}}$	0.0000	$C_{L_{\delta_{lef}\alpha_{10}^1}}$	0.0004	$C_{m_{\delta_{lef}\alpha_{10}^1}}$	0.0423
14	$C_{D_{\beta^2}}$	0.0000	$C_{L_{\delta_{lef}\alpha_{15}^1}}$	0.0003	$C_{m_{\delta_{lef}\alpha_{15}^1}}$	0.0258
15			C_{L_β}	0.0000	C_{m_β}	0.0009
16			$C_{L_{\beta_0^1}}$	0.0000	$C_{m_{\beta_0^1}}$	0.0000
17					$C_{m_{\beta\alpha}}$	0.0011

5.1.3.4 C_Y Force Coefficient

The parameters of C_Y coefficient is determined using dutch-roll and bank-to-bank maneuvers. To obtain lateral/directional parameters, these maneuvers are combined to prevent collinearity. But it was observed that the magnitude C_Y is much higher in the dutch-roll maneuvers; hence it was expected that C_Y is most affected with dutch-

roll maneuvers. In Figure 5.28, normalized cost value for each parameter of C_Y are observed for different maneuvers. It is concluded that in this case, the most influential parameters are $C_{Y\beta}$, $C_{Y\delta_r}$, and $C_{Y\delta_{lef}}$. The other parameters have a normalized sensitivity magnitude of less than 5% of the most significant term's ($C_{Y\beta}$) magnitude.

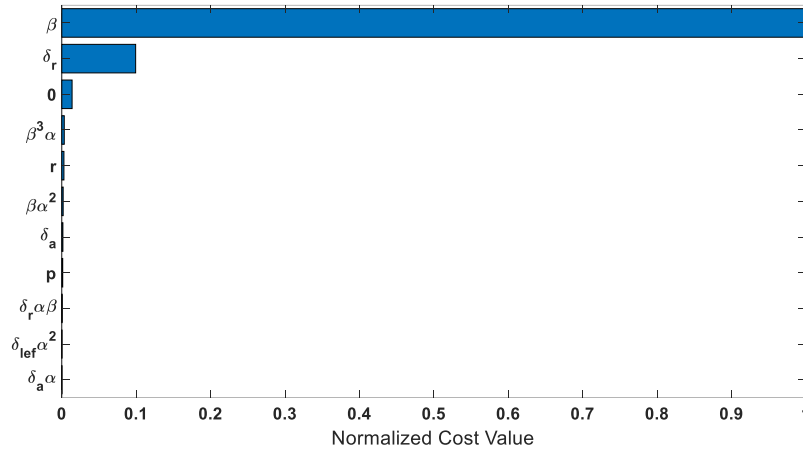


Figure 5.28 Sensitivities of the C_Y parameters with a 1% change from their original value during lateral (dutch-roll and bank-to-bank) maneuvers.

5.1.3.5 C_l Moment Coefficient

The parameters of C_l coefficient are determined using dutch-roll and bank-to-bank maneuvers. To obtain lateral/directional parameters, these maneuvers are combined to prevent collinearity. In Figure 5.29, the normalized cost value for each parameter of C_l are observed for combined dutch-roll and bank-to-bank maneuvers. It is concluded that in this case, the most influential parameters are $C_{l\delta_a}$, $C_{l\beta}$, C_{lp} , $C_{l\beta\alpha}$ and $C_{l\delta_r}$. The other parameters have a normalized sensitivity magnitude of less than 5% of the most significant term's ($C_{l\delta_a}$) magnitude.

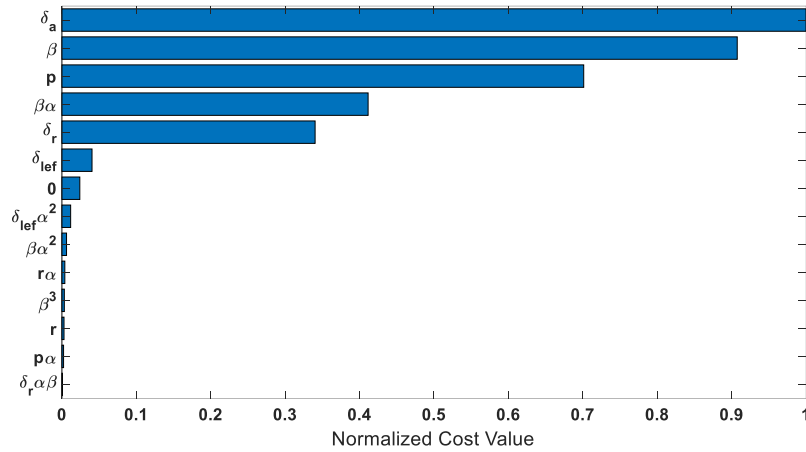


Figure 5.29 Sensitivities of the C_l parameters with a 1% change from their original value during lateral (dutch-roll and bank-to-bank) maneuvers

5.1.3.6 C_n Moment Coefficient

The parameters of C_n coefficient are determined using dutch-roll and bank-to-bank maneuvers. To obtain lateral/directional parameters, these maneuvers are combined to prevent collinearity. In Figure 5.30, the normalized cost value for each parameter of C_n are observed for combined dutch-roll and bank-to-bank maneuvers. It is concluded that in this case, the most influential parameters are $C_{n\delta_r}$, $C_{n\beta}$, and $C_{n\beta\alpha}$. The other parameters have a normalized sensitivity magnitude of less than 5% of the most significant term's ($C_{n\delta_r}$) magnitude.

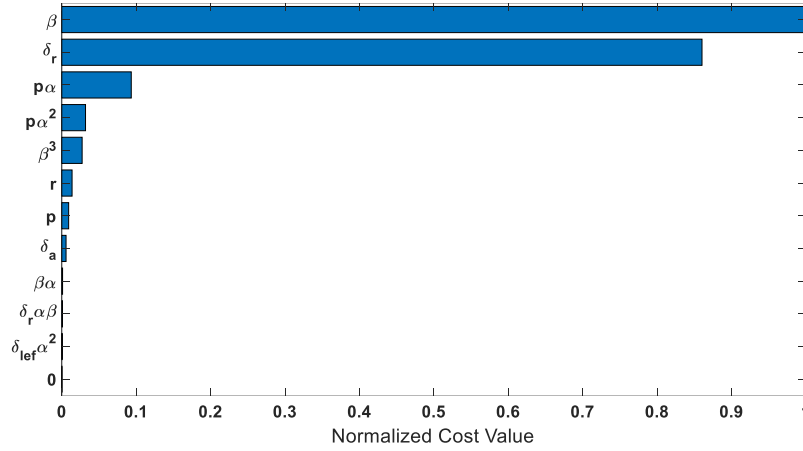


Figure 5.30 Sensitivities of the C_n parameters with a 1% change from their original value during lateral (dutch-roll and bank-to-bank) maneuvers.

The sensitivity of lateral coefficients is also covered. The number of tuned parameters is decreased to 10 out of 38 terms. The tuned parameters are shown in red-colored in Table 5.29.

Table 5.29 Normalized MSE values for lateral coefficients in dutch-roll and bank-to-bank maneuvers (most effective terms are red-colored).

Index	Parameter	Normalized SM	Parameter	Normalized SM	Parameter	Normalized SM
1	C_{Y0}	0.0138	C_{l0}	0.0240	C_{n0}	0.000
2	$C_{Y\beta}$	1.0000	$C_{l\beta}$	0.9075	$C_{n\beta}$	1.000
3	$C_{Y\beta\alpha^2}$	0.0018	$C_{l\beta\alpha}$	0.4115	$C_{n\beta\alpha}$	0.001
4	$C_{Y\beta^3\alpha}$	0.0033	$C_{l\beta\alpha^2}$	0.0062	$C_{n\beta^3}$	0.027
5	$C_{Y\delta_r}$	0.0993	$C_{l\beta^3}$	0.0032	$C_{n\delta_r}$	0.860
6	$C_{Y\delta_r\alpha\beta}$	0.0004	$C_{l\delta_r}$	0.3402	$C_{n\delta_r\alpha\beta}$	0.001
7	$C_{Y\delta_a}$	0.0015	$C_{l\delta_r\alpha\beta}$	0.0006	$C_{n\delta_a}$	0.006
8	$C_{Y\delta_a\alpha}$	0.0000	$C_{l\delta_a}$	1.0000	C_{np}	0.009
9	C_{Yp}	0.0013	C_{lp}	0.7012	$C_{np\alpha}$	0.093
10	C_{Yr}	0.0029	$C_{lp\alpha}$	0.0022	$C_{np\alpha^2}$	0.032
11	$C_{Y\delta_{lef}\alpha^2}$	0.0000	C_{lr}	0.0028	C_{nr}	0.014
12			$C_{lr\alpha}$	0.0039	$C_{n\delta_{lef}\alpha^2}$	0.001
13			$C_{l\delta_{lef}}$	0.0404		
14			$C_{l\delta_{lef}\alpha^2}$	0.0117		

To show the fitting capacity of the sensitive parameters, R^2 of predicted and observed data are computed for full and reduced model. In Table 5.30, we can compare results of R^2 when using all parameters and when keeping only the most sensitive parameters and dropping other parameters in the model for all aerodynamic coefficients.

Table 5.30 R^2 Values for Full and Reduced Models

Approach	Coefficient of Determination(R^2)					
	C_D	C_L	C_m	C_Y	C_l	C_n
Full Model	1.0000	1.0000	0.9996	0.9973	0.9968	0.9986
Reduced Model	0.9860	0.9983	0.9751	0.9937	0.9884	0.9813

Figure 5.31 to Figure 5.34 shows the qualitative accuracy spreads of the full and reduced models for each coefficient. All points are clustered along the equality line; the predicted values are close to the actual value, which shows that sensitive parameters covers the most proportion of total variation. Reduced models exhibit better fits in the force coefficients. C_m coefficient is the most critical coefficient as seen in Figure 5.32.

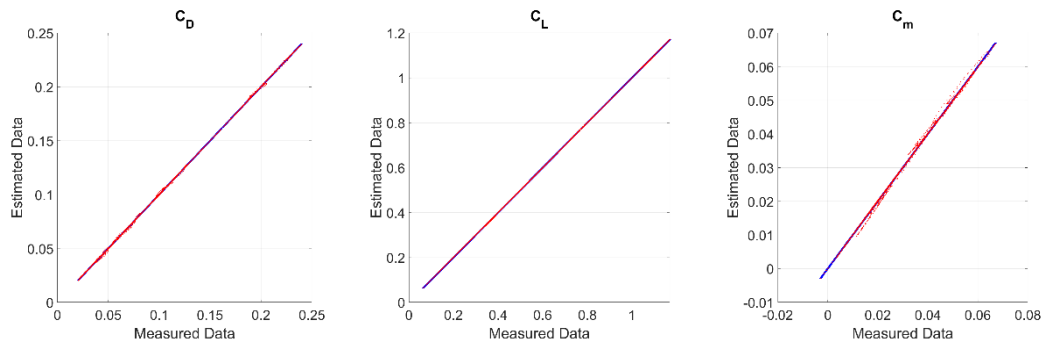


Figure 5.31 Accuracy Spread of the Full Model for Longitudinal Coefficients.

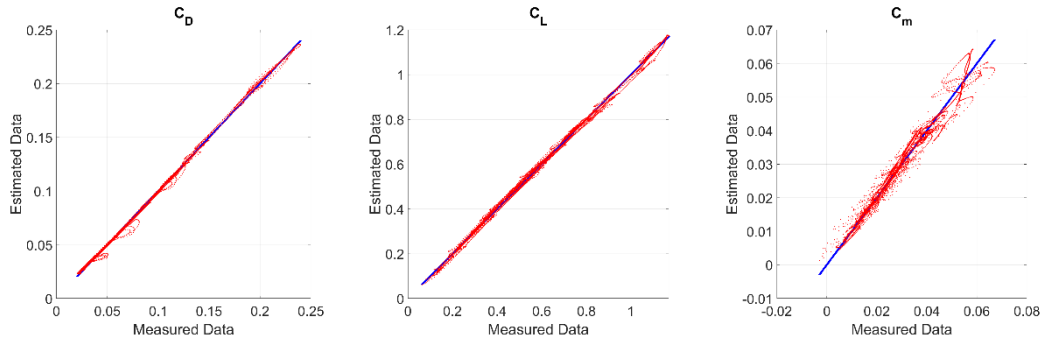


Figure 5.32 Accuracy Spread of the Reduced Model for Longitudinal Coefficients.

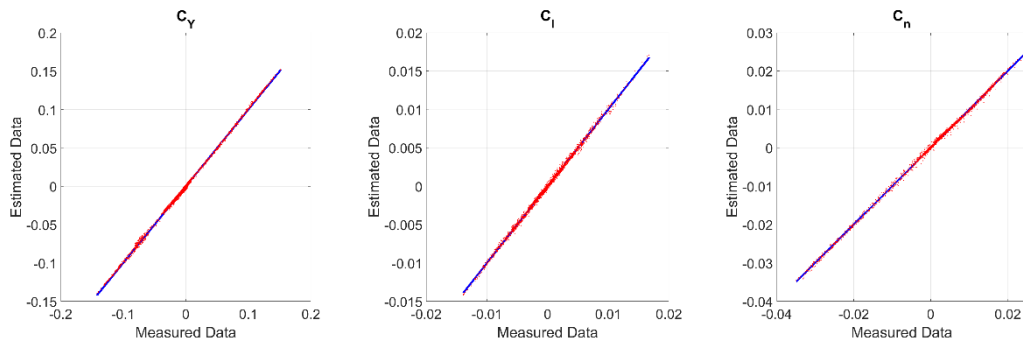


Figure 5.33 Accuracy Spread of the Full Model for Lateral Coefficients.

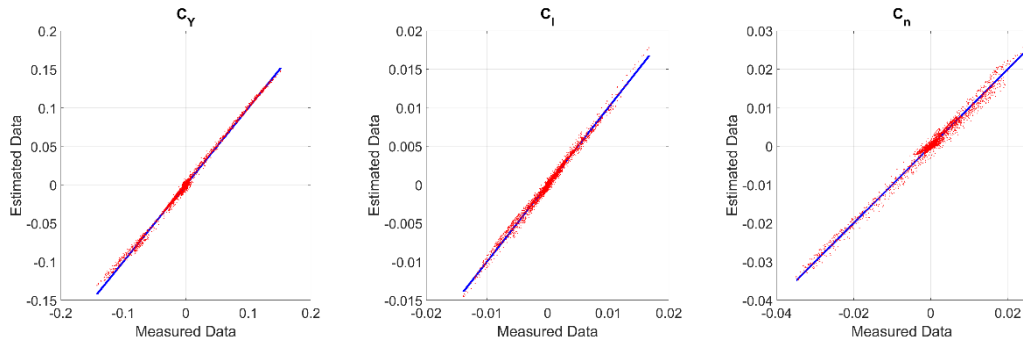


Figure 5.34 Accuracy Spread of the Reduced Model for Lateral Coefficients.

5.1.4 Phase 2: Output Error Method

So far, the results obtained with the equation error method (Phase 1.1) are entirely satisfactory. The results of Phase 1.1 are implemented in the 6DOF simulation model. The aerodynamic model is kept fixed, and the same initial conditions and inputs are given. Phase 2 is employed now to tune the most sensitive parameters

(determined in Phase 1.2). The parameter tuning by the output error method is done in two steps: longitudinal and lateral dynamics.

5.1.4.1 Longitudinal Dynamics

First, the reduced longitudinal model is used for a series of short-period maneuvers to observe the drag and lift characteristics: see Figure 5.35.

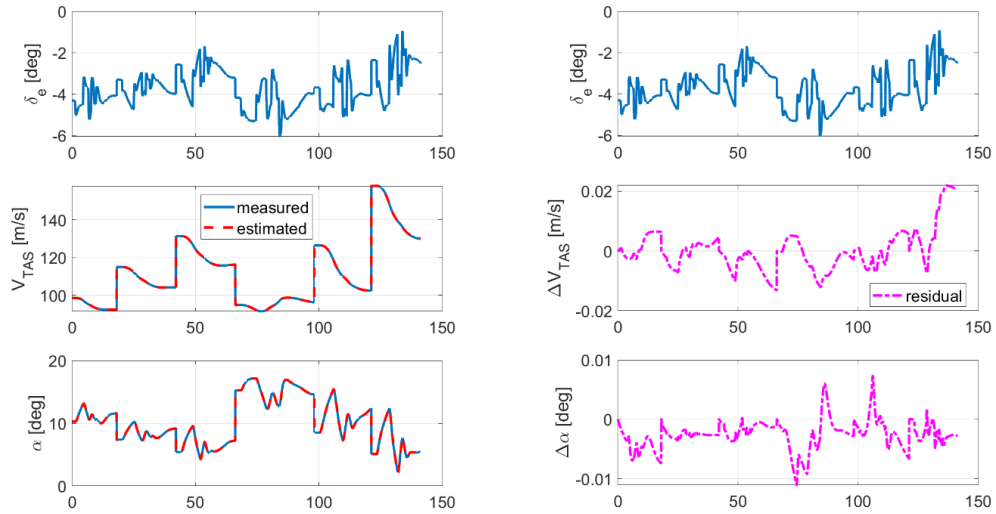


Figure 5.35 Reduced Longitudinal Model Output Comparison for Short-Period Maneuvers.

Without tuning any drag or lift coefficients parameter, there is a good match between measured and simulated data, as seen in Figure 5.35. It means that drag and lift characteristics are accurately captured in Phase 1.1, and there is no need for any tuning.

And then, the full longitudinal model is used for a series of short-period maneuvers to observe the pitch moment characteristic keeping all parameters obtained with EEM fixed. The specified initial conditions are reasonably accurate, but for the first and fourth maneuvers, the simulation shows drifts in V_{TAS} , α , q , and θ variables that are attributed to minor errors in the aerodynamic pitching coefficient see Figure 5.36. For other short-period maneuvers, there is a good match between measured and simulated data and tuning just a few C_m parameters will be enough for fine-tuning.

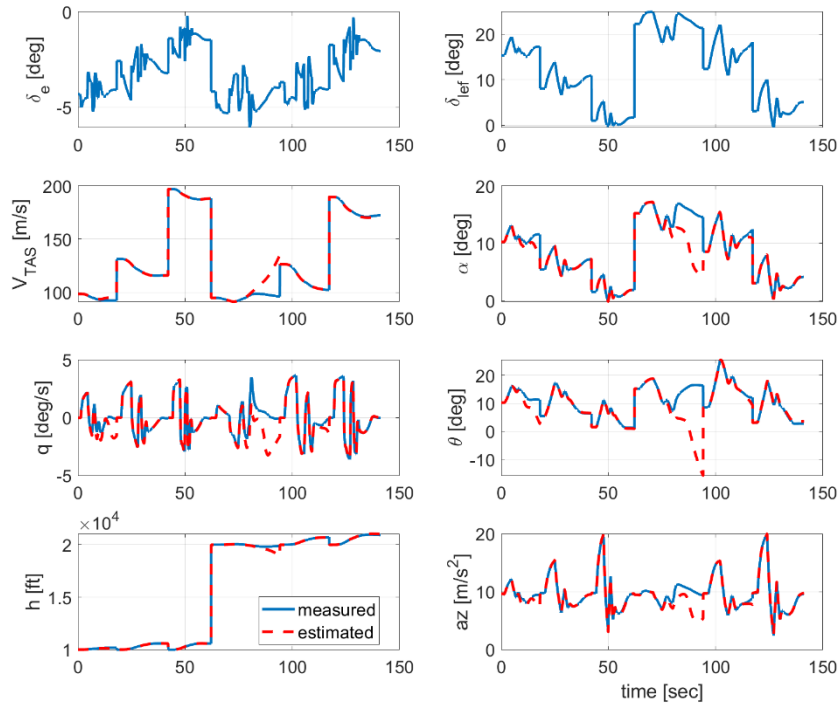


Figure 5.36 Full Longitudinal Model Output Comparison for Short-Period Maneuvers Keeping All Parameter Fixed.

After tuning the aerodynamic coefficients determined in Phase 1.2 ($C_{m_{\delta_e}}$, $C_{m_{\alpha}}$, $C_{m_{\alpha_{10}^1}}$, and $C_{m_{\delta_{lef}}}$), the updated longitudinal parameters can be seen in Table 5.31.

Table 5.31 Tuned Longitudinal parameters with the OEM.

Index	Parameter	EEM Estimate	OEM Estimate	Relative Change (%)
1	$C_{m_{\alpha}}$	1.69E-01	1.60E-01	5.38
2	$C_{m_{\alpha_{10}^1}}$	4.65E-01	4.71E-01	1.23
3	$C_{m_{\delta_e}}$	-5.94E-01	-6.00E-01	1.02
4	$C_{m_{\delta_{lef}}}$	-7.68E-02	-7.28E-02	5.22

There is a good match between measured data and simulated data after tuning process, as seen in Figure 5.37.

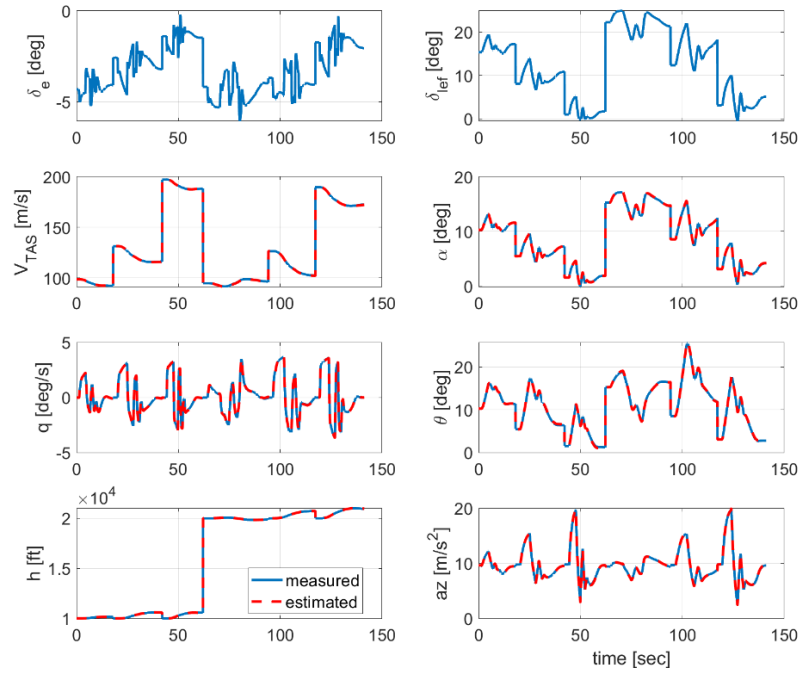


Figure 5.37 The Full Longitudinal Model Output Comparison for Short-Period Maneuvers After Tuning $C_{m\delta_e}$, $C_{m\alpha}$, $C_{m\alpha_{10}^1}$, and $C_{m\delta_{lef}}$ Process.

5.1.4.2 The Lateral/Directional Dynamics

The lateral model is used for a series of dutch-roll and bank-to-bank maneuvers to observe the side force, roll moment, and pitch moment characteristic keeping all parameters (obtained with EEM) fixed. There is a good match in dutch-roll maneuvers except for just a small duration drift in ϕ variable in Figure 5.38. However, the model predicted output is not within the acceptable range for Level-D model fidelity in dutch-roll maneuvers as seen in Figure 5.39.

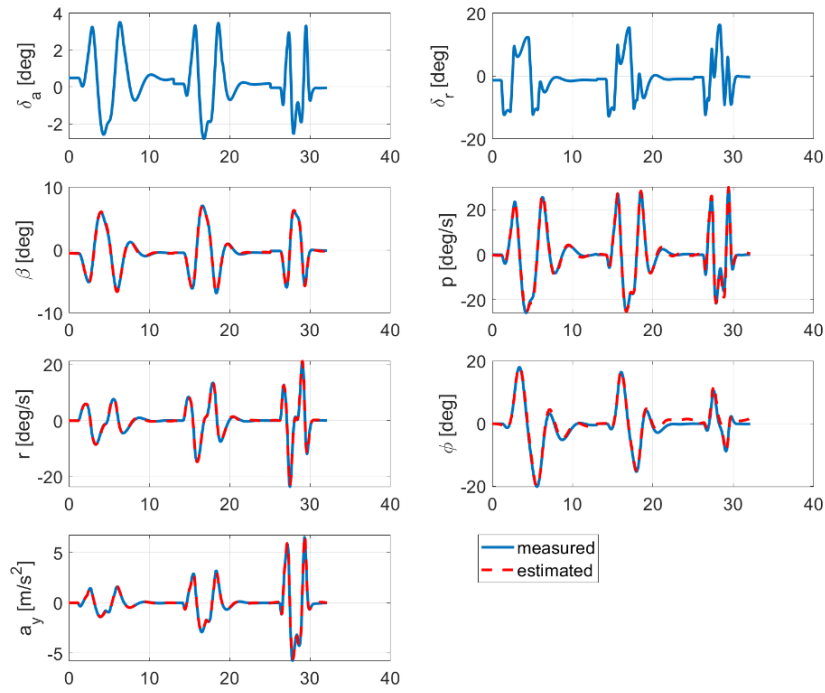


Figure 5.38 The Lateral Model Output Comparison for Dutch-Roll Maneuvers Keeping All Parameters Fixed.

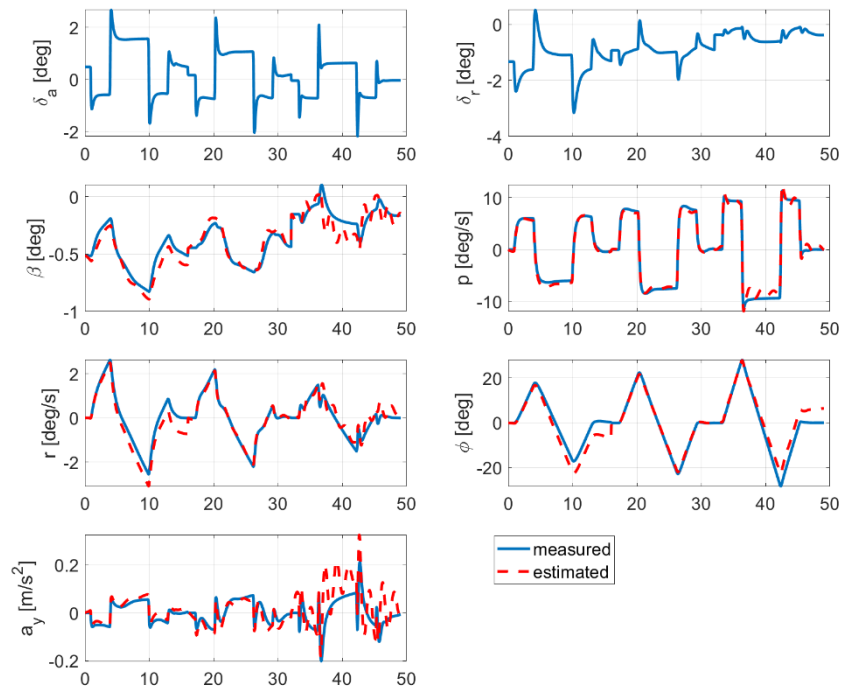


Figure 5.39 The Lateral Model Output Comparison for Bank-To-Bank Maneuvers Keeping All Parameters Fixed.

Note that dutch-roll and bank-to-bank maneuvers are shown in separate figures for the sake of better visualization. The most influential lateral parameters are tuned together in combined dutch-roll and bank-to-bank maneuvers. The tuned lateral parameters and their relative changes are seen in Table 5.32.

Table 5.32 The Tuned Lateral Parameters with the OEM.

Index	Parameter	EEM Estimate	OEM Estimate	Relative Change (%)
1	$C_{Y\beta}$	-1.07E+00	-1.072E-01	0.202
2	$C_{Y\delta_r}$	1.68E-01	1.72E-01	2.516
3	$C_{l\beta}$	-8.88E-02	-8.89E-02	0.101
4	$C_{l\beta\alpha}$	-4.19E-01	-4.54E-01	8.747
5	$C_{l\delta_r}$	2.66E-02	2.75E-02	0.028
6	$C_{l\delta_a}$	-1.30E-01	-1.33E-01	2.920
7	C_{lp}	-2.05E-01	-2.14E-01	4.717
8	$C_{n\beta}$	1.86E-01	1.84E-01	1.156
9	$C_{n\delta_r}$	-8.57E-02	-8.63E-02	0.701
10	$C_{np\alpha}$	7.40E-02	7.64E-02	3.219

After tuning the lateral aerodynamic coefficients, there is a better match between measured data and model-predicted data, as seen in Figure 5.40 and Figure 5.41. The small drifts in ϕ variable in dutch roll maneuvers were eliminated. And the model predicted output is within the allowed band for Level-D model fidelity in bank-to-bank maneuvers, as seen in Figure 5.41.

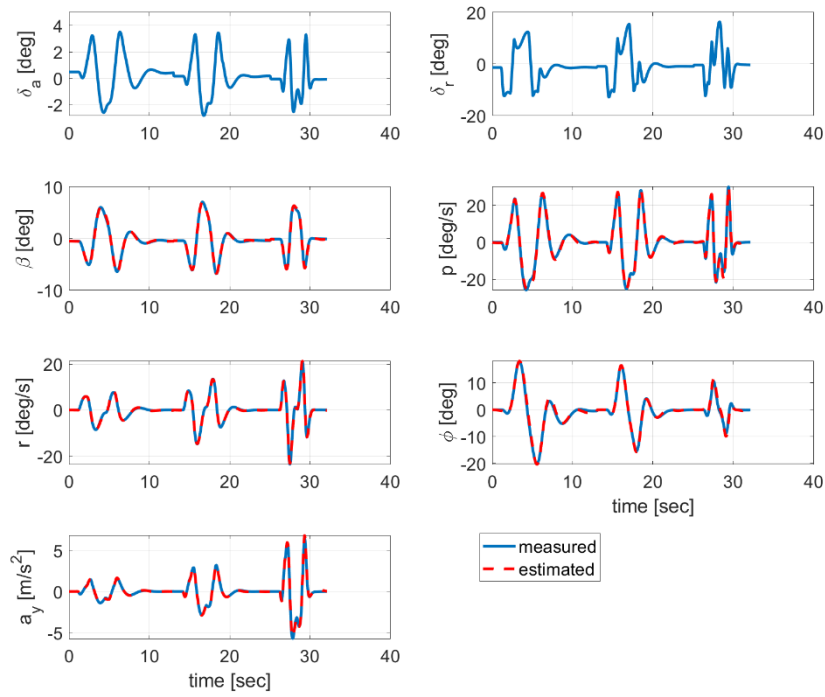


Figure 5.40 Full Lateral Model Output Comparison for Dutch-Roll Maneuvers After Tuning Lateral Parameters.

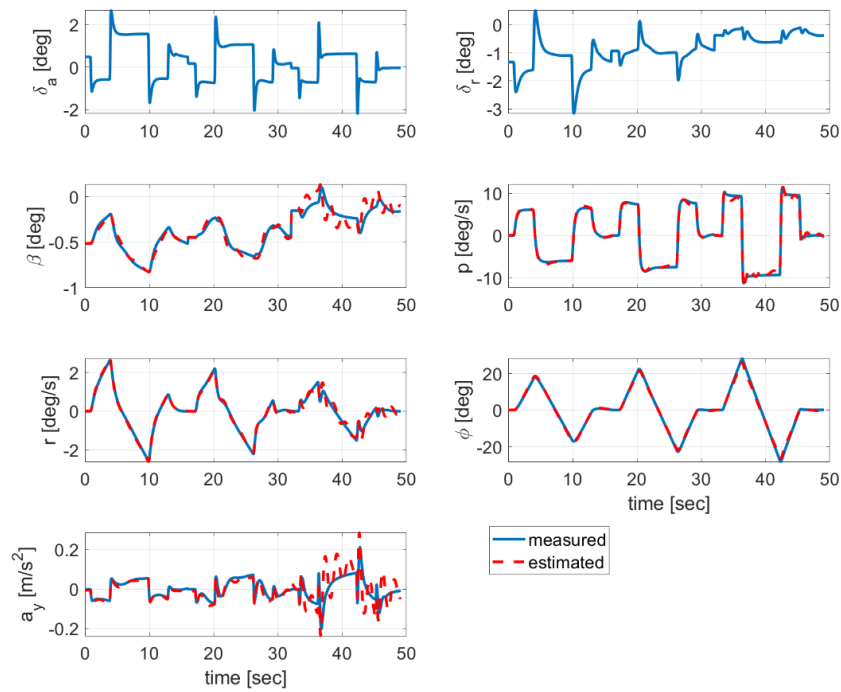


Figure 5.41 Full Lateral Model Output Comparison for Bank-To-Bank Maneuvers After Tuning Lateral Parameters.

5.1.5 Phase 3: Model Validation

5.1.5.1 Proof of Match Results

Proof of Match is the final testing in Flight Simulator Certification and is done with a validation dataset not used in the training phase.

To summarize, firstly, the parameters of aerodynamic coefficients are estimated using the EEM. Then, the most influential parameters are found using sensitivity analysis. And then, the most influential parameters are tuned using the OEM for longitudinal and lateral maneuvers. And finally, the model and parameters are kept fixed, and the performance of the identified model is evaluated using proof-of-match (POM) results. When assessing proof-of-match results for dynamic maneuvers, the minor biases on the initial conditions and the control deflections (up-to- 0.5 deg) are permitted [1].

Longitudinal parameter matching is performed in two phases. The static part of longitudinal aerodynamic coefficients is validated with Longitudinal Maneuvering Stability and Longitudinal Static Stability tests. The dynamic portion of the longitudinal aerodynamic coefficient is confirmed with the Short-Period maneuver.

Lateral parameter matching is confirmed with Dutch-Roll and Bank-To-Bank maneuvers.

5.1.5.1.1 Longitudinal Maneuvering Stability

The purpose of this test is to show that the maneuvering stability simulation correspond to the aircraft. The test is conducting by establishing a steady-state condition at various intermediate bank angles and increasing it to the maximum angle. A vital aspect of this test is obtaining an accurate trim condition that allows steady turning flight at specified bank angles. Steady-state aircraft trim conditions for turning flight can be found using the techniques in Section 2.4.3. The results are

a "snapshot" of the steady turning aircraft at the specified bank angle and the trim airspeed (three different airspeeds). Altitude is set to constant in each case.

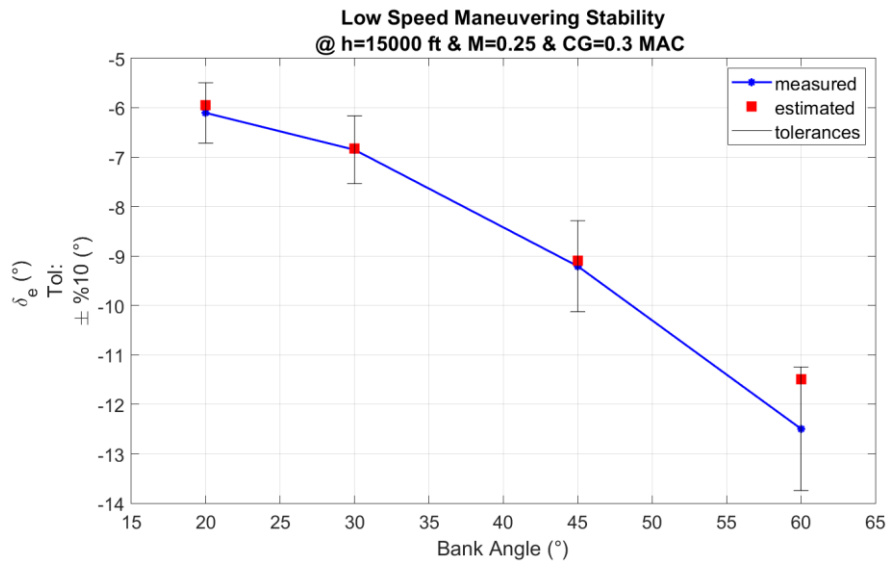


Figure 5.42 Low-Speed Maneuvering Stability.

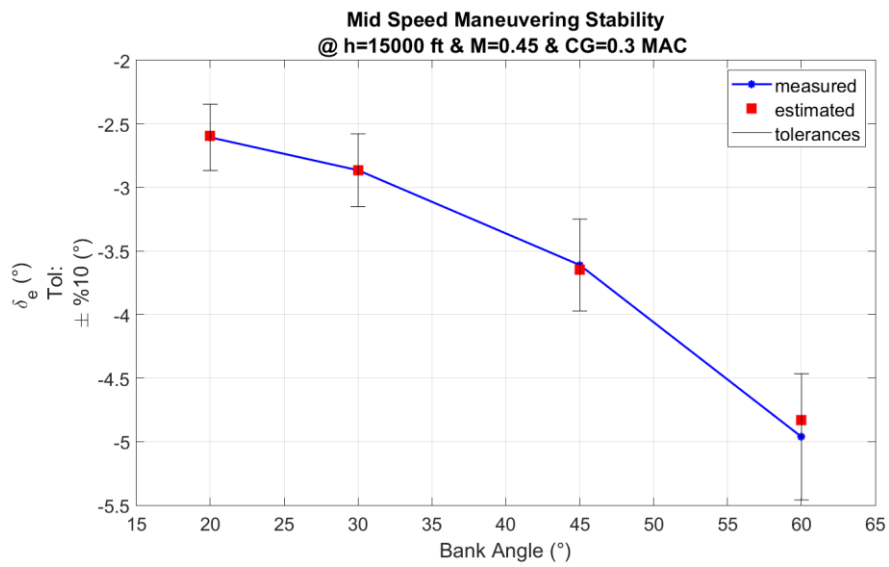


Figure 5.43 Mid Speed Maneuvering Stability.

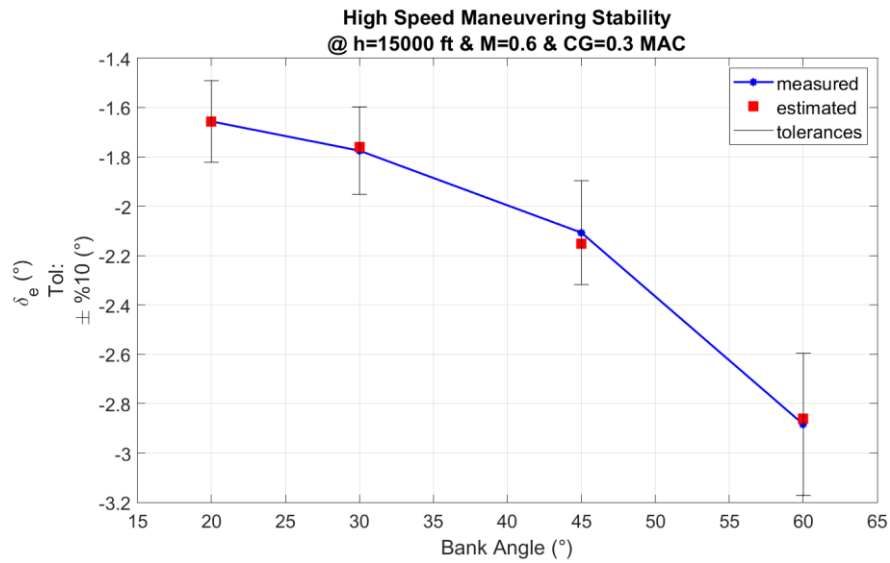


Figure 5.44 High-Speed Maneuvering Stability.

The tolerance bounds are lower and upper values in which the estimated results are expected to lie between. Figure 5.42, Figure 5.43, and Figure 5.44 show that the predicted results are in those tolerance bounds. It means our estimated coefficients are compatible with the actual aircraft. The predicted results are closer to tolerance bounds, which means that the residual between the estimated and measures is a bit higher at low airspeed.

5.1.5.1.2 Longitudinal Static Stability

The purpose of this test is to establish that the simulator's static longitudinal stability characteristics are consistent with those of the aircraft. The longitudinal control command is used to the air vehicle to get a deviation from trimmed airspeed, and elevator deflection is used to maintain a steady-state condition at various airspeeds, as shown in Figure 5.45.

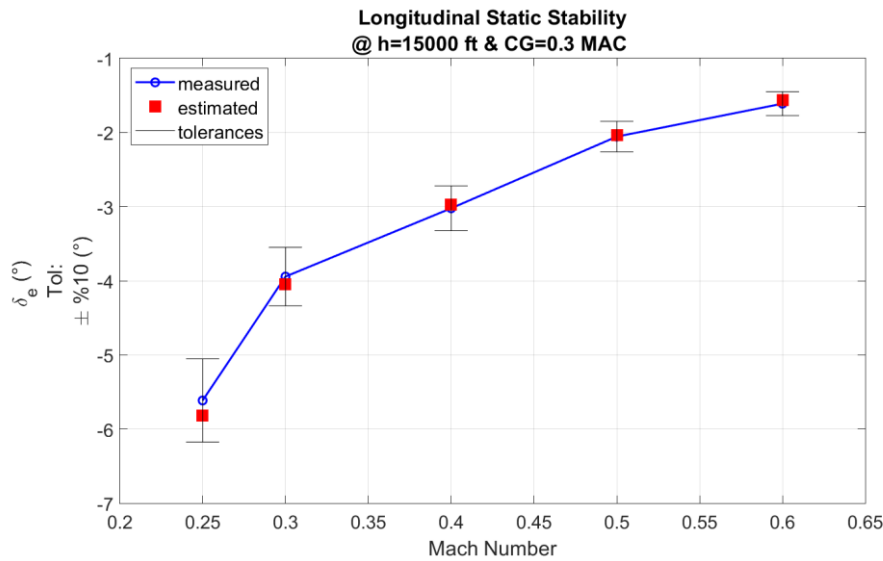


Figure 5.45 Longitudinal Static Stability.

The estimated results are in tolerance bounds. It means our estimated coefficients are compatible with the actual aircraft. The estimated results are closer to tolerance bounds at low airspeed, corresponding to a high angle of attack values. As we already observed in the cross plot of aerodynamic coefficients residual with respect to the angle of attack, the residual between the estimated and measured values at a high angle of attack is slightly higher.

5.1.5.1.3 Short Period Maneuver

Short period dynamics are determined by exciting the short period mode under the cruise condition by applying a doublet or 3-2-1-1 longitudinal control input. Oscillation in the short-period mode are often highly damped and has a period of a few seconds. The aircraft is rapidly pitched around the center of gravity, resulting basically variation in the angle-of-attack.

Figure 5.46 and Figure 5.47 shows the measured and predicted data comparison of short-period motions at 10000 ft, $CM = 0.35\bar{c}$ and two different speed ($Ma = 0.35$, $Ma=0.50$) flight condition. The model adequacy is quite apparent from the figures.

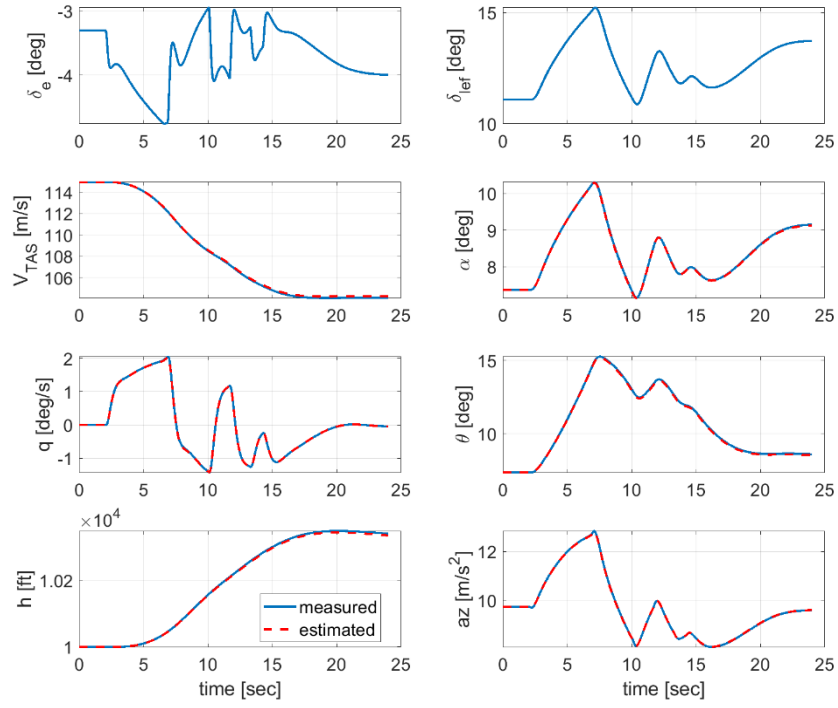


Figure 5.46 Short Period Dynamics – at $h = 10000$ ft, $CM = 0.35\bar{c}$ and $Ma = 0.35$

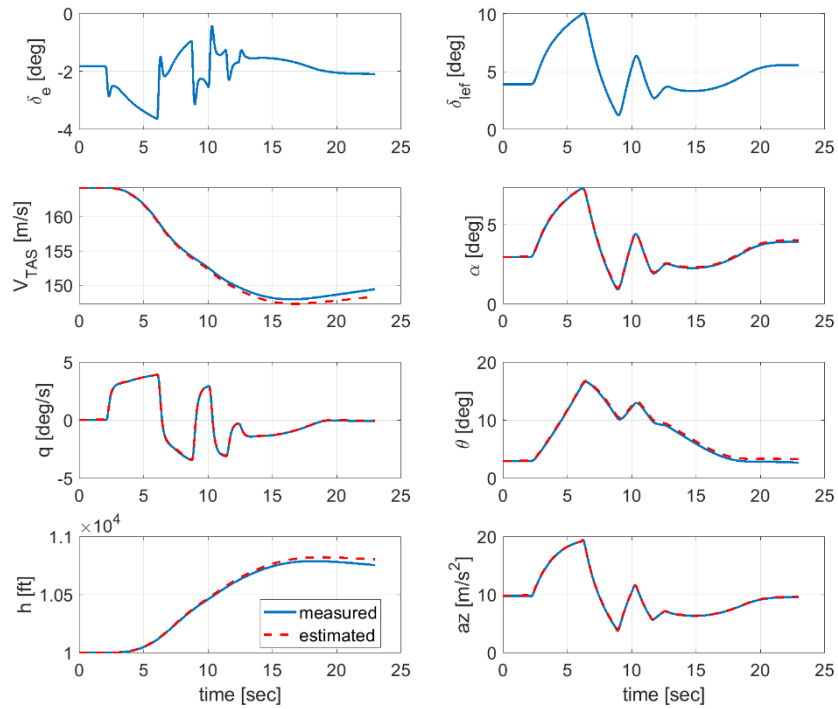


Figure 5.47 Short Period Dynamics – at $h = 10000$ ft, $CM = 0.35\bar{c}$ and $Ma = 0.50$

5.1.5.1.4 Phugoid Maneuver

The phugoid mode exhibit significant amplitude variation of airspeed, pitch angle, and altitude, but almost no variation in the angle-of-attack. Three complete cycles should be included in the test (six overshoots after input is completed).

Figure 5.48 and Figure 5.49 show the measured and predicted data comparison of phugoid motions at 10000 ft, $CM = 0.30\bar{c}$ and two different speed ($Ma = 0.35$, $Ma=0.50$) flight condition. The model adequacy is quite apparent from the figures.

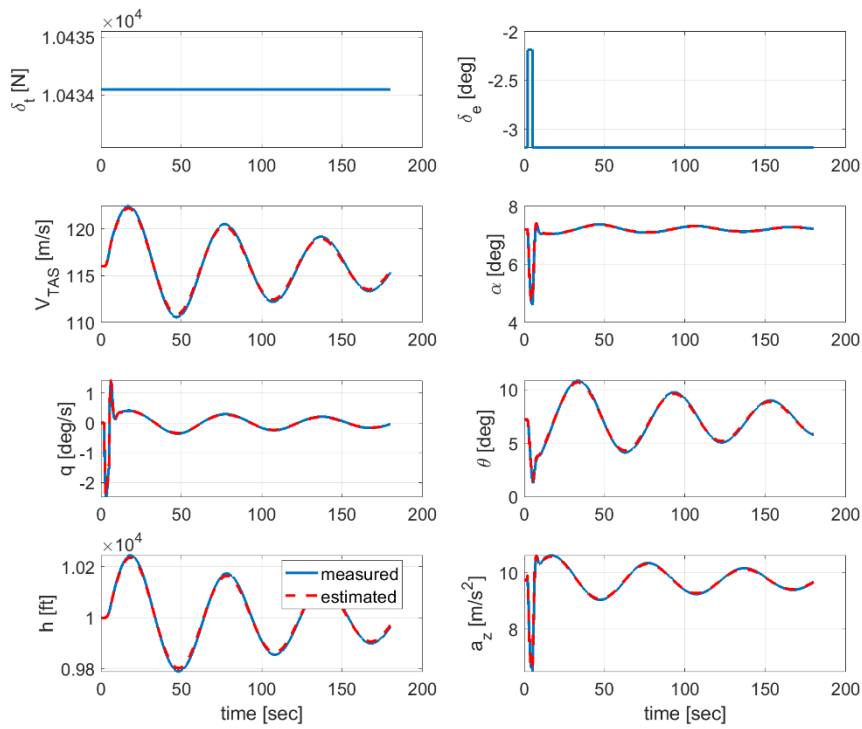


Figure 5.48 Phugoid Dynamics – at $h = 10000$ ft, $CM = 0.30\bar{c}$ and $Ma = 0.35$

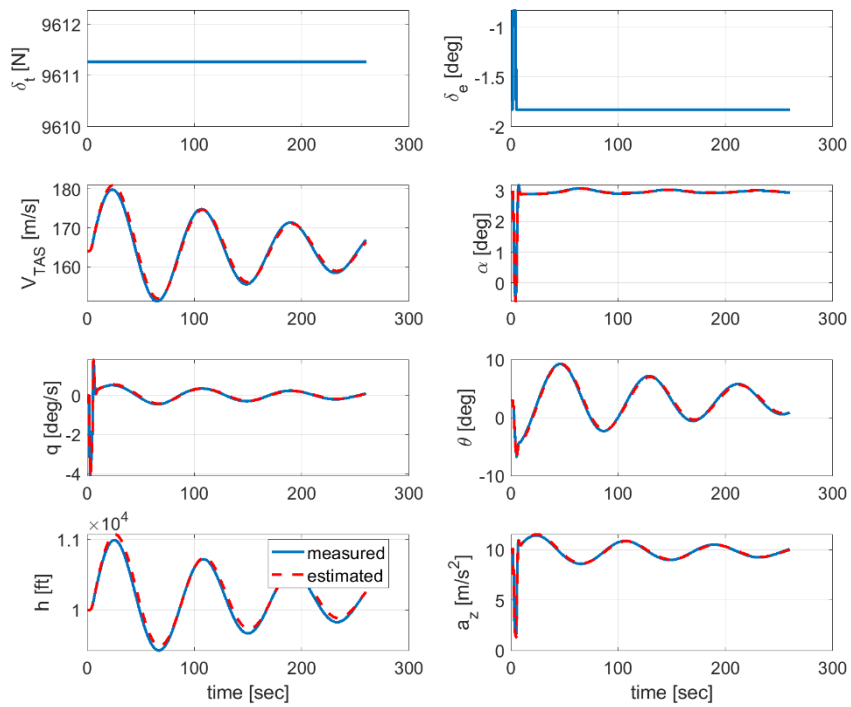


Figure 5.49 Phugoid Dynamics – at $h = 10000$ ft, $CM = 0.30\bar{c}$ and $Ma = 0.50$

Table 5.33 shows the period of the measured data and estimated model for phugoid dynamics. The estimated results are in 10% tolerance bounds of the actual results. It means our estimated coefficients are compatible with the actual aircraft.

Table 5.33 Tolerances for Phugoid Dynamics

(Flight Condition 1)		(Flight Condition 2)		
	Measured	Model	Measured	Model
Period	62.12	62.17	86.41	87.15

5.1.5.1.5 Dutch-Roll Maneuver

Dutch roll mode are evaluated using a doublet pedal input, allowing the aircraft to react freely for at least six oscillation cycles. The amount of rudder deflection should be limited to about 25% of the entire rudder pedal.

Figure 5.50 and Figure 5.51 show the measured and predicted data comparison of dutch-roll motions at 10000 ft, $CM = 0.35\bar{c}$ and two different speed ($Ma = 0.35$, $Ma=0.50$) flight condition. The model adequacy is quite apparent from the figures.

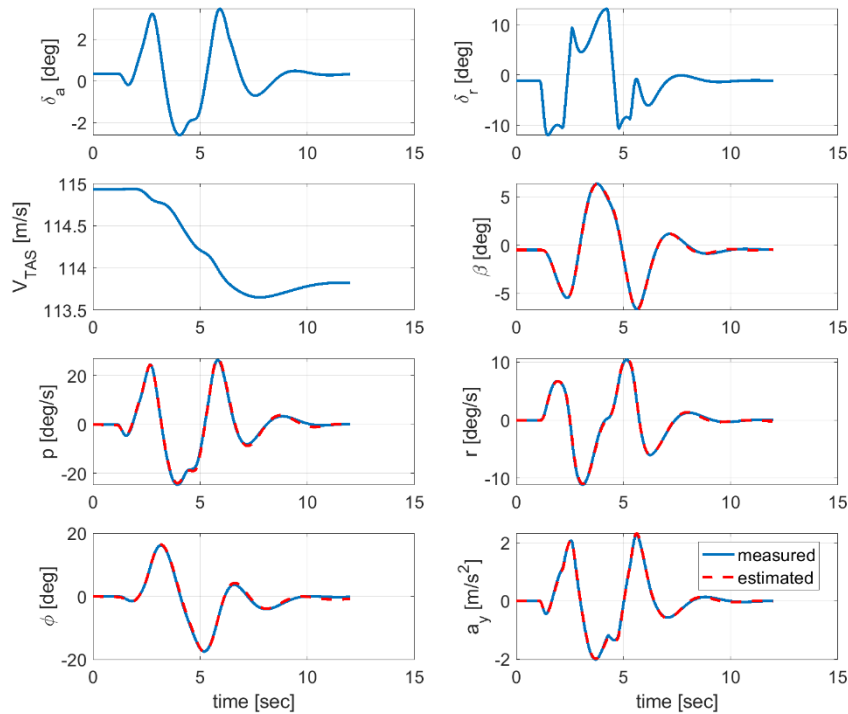


Figure 5.50 Dutch-Roll Dynamics – at $h = 10000$ ft, $CM = 0.35\bar{c}$ and $Ma = 0.35$

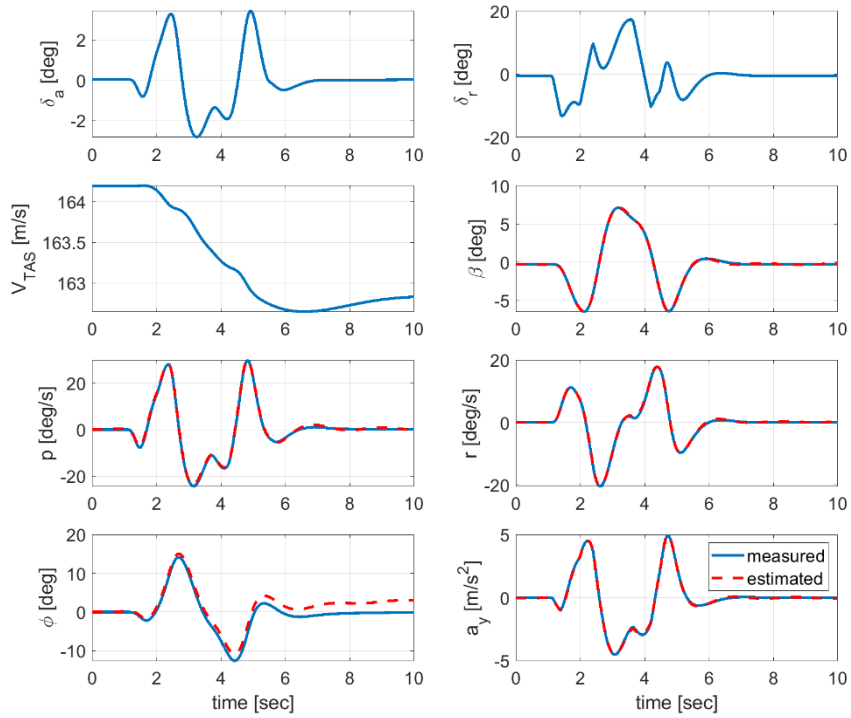


Figure 5.51 Dutch-Roll Dynamics – at $h = 10000$ ft, $CM = 0.35\bar{c}$ and $Ma = 0.50$

5.1.5.1.6 Bank-To-Bank Maneuver

Figure 5.52 and Figure 5.53 show the measured and predicted data comparison of dutch-roll motions at 10000 ft, $CM = 0.35\bar{c}$ and two different speed ($Ma = 0.35$, $Ma=0.50$) flight condition. The predicted model is within the allowable band for the Level-D flight simulator. The small bias (-0.0679 deg) on the aileron deflection in the first maneuver eliminates the error accumulation on the bank angle variable. The first maneuver without any bias term can be seen in Figure 5.54.

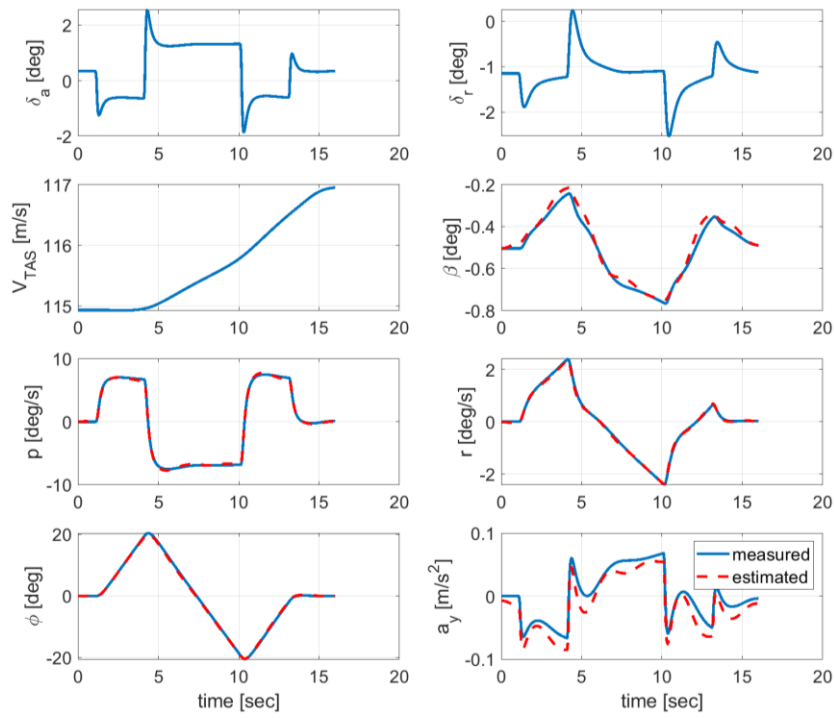


Figure 5.52 Bank-To-Bank Maneuver – at $h = 10000$ ft, $CM = 0.35\bar{c}$ and $Ma = 0.35$

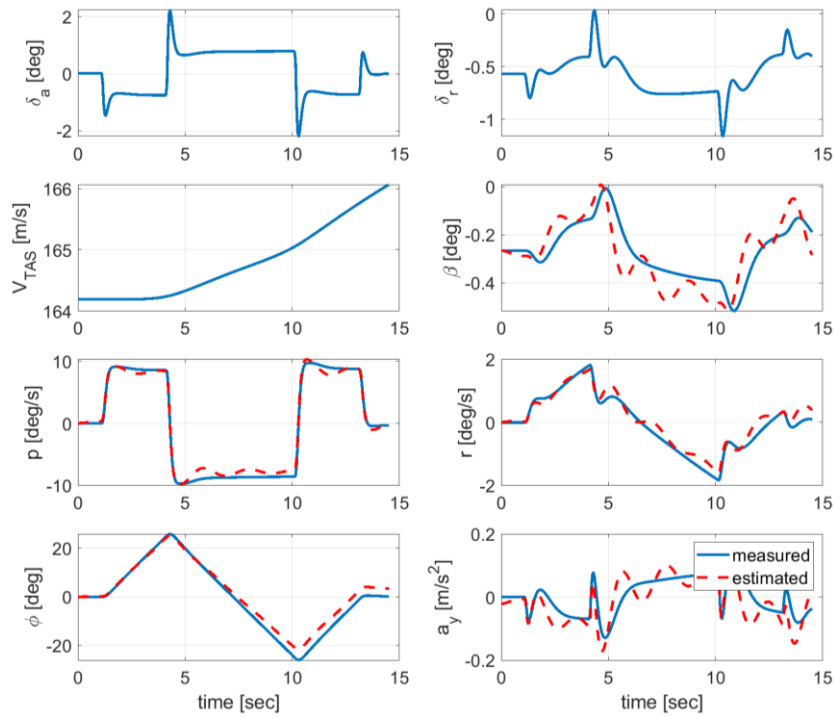


Figure 5.53 Bank-To-Bank Maneuver – at $h = 10000$ ft, $CM = 0.35\bar{c}$ and $Ma = 0.50$

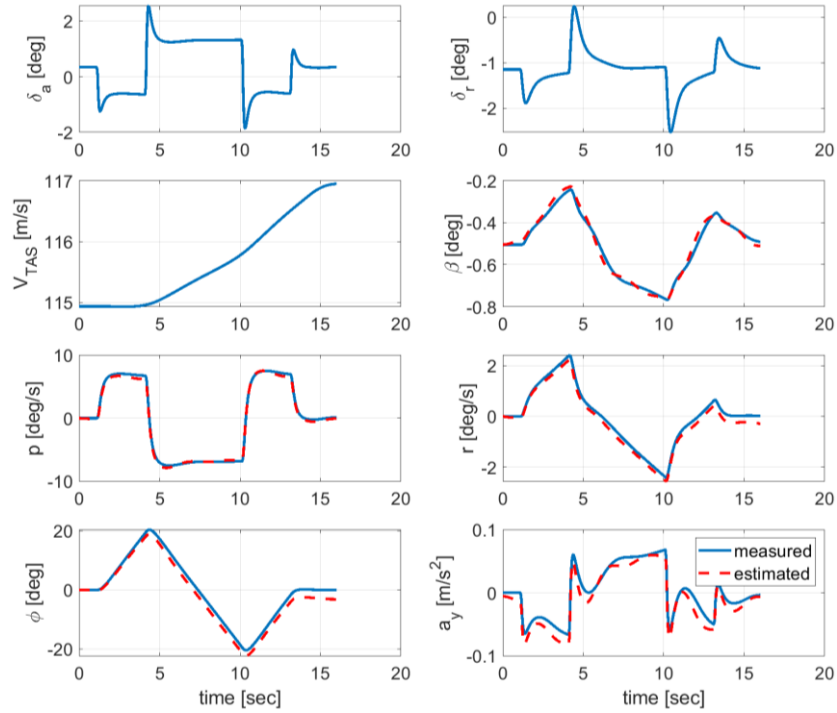


Figure 5.54 Bank-To-Bank Maneuver – at $h = 10000$ ft, $CM = 0.35\bar{c}$ and $Ma = 0.35$ without any bias term on the initial conditions and control deflections

5.1.5.2 Theil's Inequality Coefficient

5.1.5.2.1 Zero Input Initial Condition

The zero input solution is the response of the system to the initial conditions, with the input set to zero. The trimmed values of some states are disturbed and predicted model and aircraft responses are compared.

Figure 5.55 and Figure 5.56 show the measured and predicted data comparison of longitudinal motions at 10000 ft, $CM = 0.30\bar{c}$ and two different speed ($Ma = 0.35$, $Ma=0.50$) flight condition (FC) for 10 m/s disturbance in z-axis linear velocity component. The model adequacy is quite apparent from the figures.

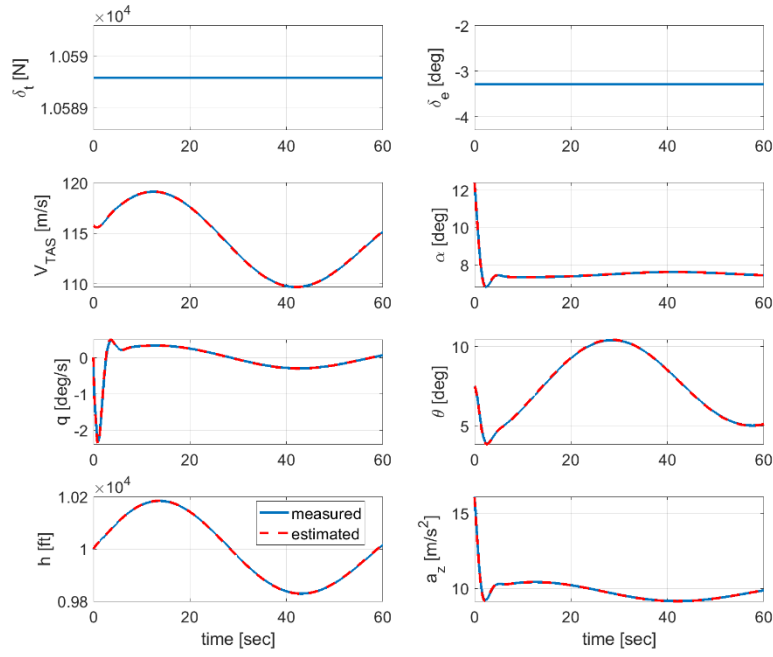


Figure 5.55 Longitudinal Dynamics – at $h = 10000$ ft, $CM = 0.30\bar{c}$ and $Ma = 0.35$

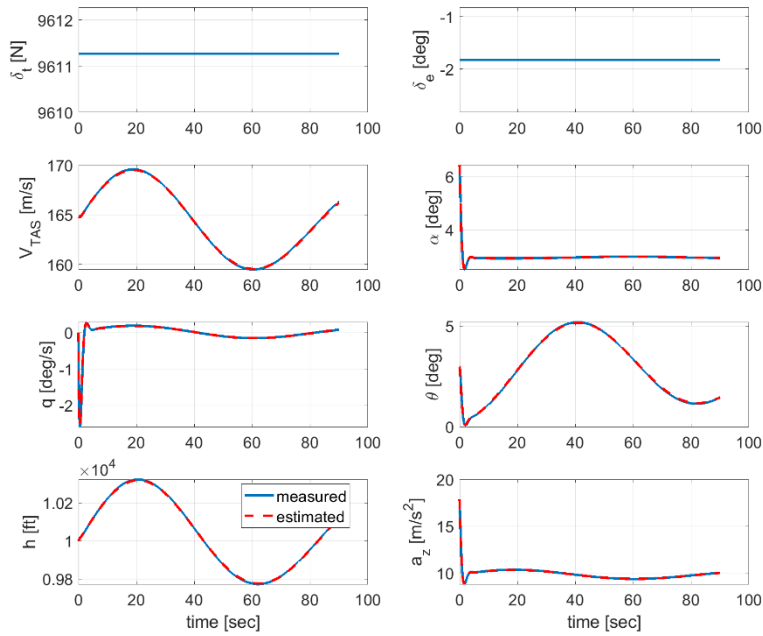


Figure 5.56 Longitudinal Dynamics – at $h = 10000$ ft, $CM = 0.30\bar{c}$ and $Ma = 0.50$

Theil's inequality coefficient for each of the longitudinal variables are given in Table 5.34. TIC values for each longitudinal output variable are below the maximum acceptable values (in the range of 0.25 to 0.30) for both cases.

Table 5.34 Theil's Inequality Coefficient (TIC) for Longitudinal Motion

Output Variable	TIC (Flight Condition 1)	TIC (Flight Condition 2)
V_{TAS}	1.599e-04	1.474e-04
α	6.951e-04	0.0013
q	0.0143	0.0131
θ	0.0017	0.0039
h	6.497e-05	1.300e-04
a_z	5.316e-04	5.764e-04

Figure 5.57 and Figure 5.58 show the measured and predicted data comparison of lateral/directional motions at 10000 ft, $CM = 0.30\bar{c}$ and two different speed ($Ma = 0.35$, $Ma=0.50$) flight condition for 10 m/s disturbance in y-axis linear velocity component. The model adequacy is quite apparent from the figures.

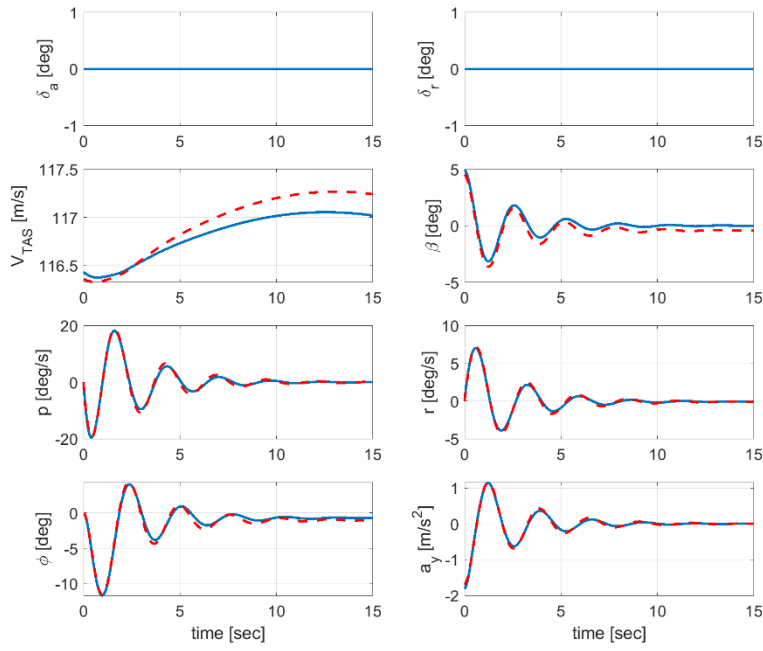


Figure 5.57 Lat/Dir Dynamics – at $h = 10000$ ft, $CM = 0.30\bar{c}$ and $Ma = 0.35$

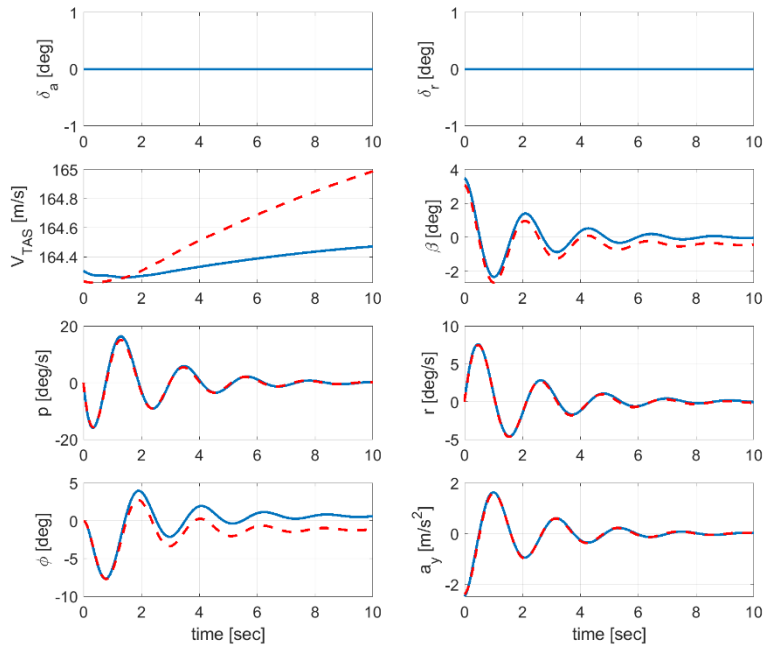


Figure 5.58 Lat/Dir Dynamics – at $h = 10000$ ft, $CM = 0.30\bar{c}$ and $Ma = 0.50$

Theil's inequality coefficient for each of the lateral variables are given in Table 5.35. TIC values for each lateral output variable except the bank angle are below the maximum acceptable values (in the range of 0.25 to 0.30) for both cases.

Table 5.35 Theil's Inequality Coefficient (TIC) for Lateral/Directional Motion

Output Variable	TIC (Flight Condition 1)	TIC (Flight Condition 2)
V_{TAS}	6.384e-04	8.808e-04
β	0.1884	0.2237
p	0.0514	0.0416
r	0.0479	0.0039
ϕ	0.0569	0.3234
a_y	0.0465	0.0273

5.1.5.2.2 Noise Driven Behavior

The band-limited white noise with 0.01 noise power has been introduced to control deflection inputs in the predicted model and TIC values are compared.

Figure 5.59 and Figure 5.60 show the measured and predicted data comparison of longitudinal motions at 10000 ft, $CM = 0.30\bar{c}$ and two different speed ($Ma = 0.35$, $Ma=0.50$) flight condition with a band-limited white noise (0.01 noise power) in elevator deflection. The model adequacy is quite apparent from the figures.

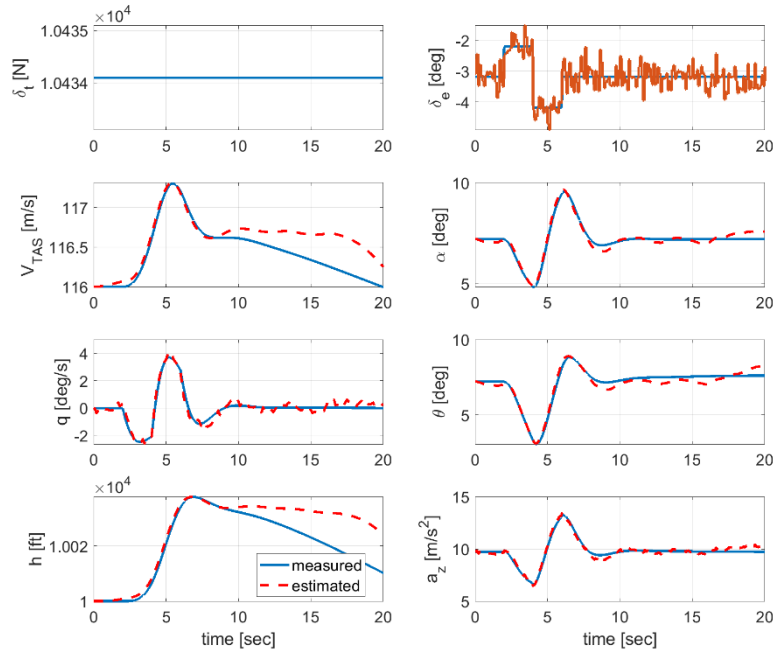


Figure 5.59 Short Period Dynamics – at $h = 10000$ ft, $CM = 0.30\bar{c}$ and $Ma = 0.35$

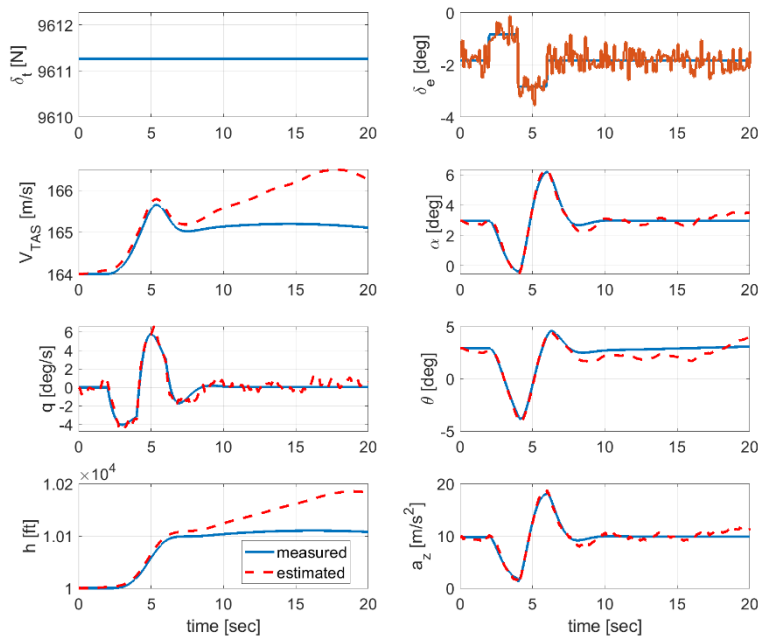


Figure 5.60 Short Period Dynamics – at $h = 10000$ ft, $CM = 0.30\bar{c}$ and $Ma = 0.50$

Theil's inequality coefficient for each of the longitudinal variables are given in Table 5.36 with and without noise on elevator deflections. TIC values for each longitudinal output variable are below the maximum acceptable values (in the range of 0.25 to 0.30) for both cases. When noise is introduced, the TIC values are increased as expected.

Table 5.36 Theil's Inequality Coefficient (TIC) for Longitudinal Motion

Output Variable	TIC (Flight Condition 1)		TIC (Flight Condition 2)	
	Without Noise	With Noise	Without Noise	With Noise
V_{TAS}	2.1182e-04	9.8528e-04	4.9693e-04	0.0022
α	0.0021	0.0117	0.0040	0.0388
q	0.0169	0.1148	0.0090	0.1341
θ	0.0036	0.0198	0.0173	0.1049
h	8.1878e-05	3.7086e-04	4.9072e-04	0.0020
a_z	0.0018	0.0315	0.0034	0.0315

5.1.5.2.3 Combination of Short-Period, Dutch-Roll, and Bank-to-Bank Maneuvers

So far, only one mode of aircraft motion such as short period, phugoid, etc. has been triggered. Now we will excite each motion successively and show the performance of the predicted model with respect to TIC values.

Figure 5.61 and Figure 5.62 show the measured and predicted data comparison of combined longitudinal, lateral and directional motions at 10000 ft, $CM = 0.30\bar{c}$ and two different speed ($Ma = 0.35$, $Ma=0.50$) flight condition. The model adequacy is quite apparent from the figures.

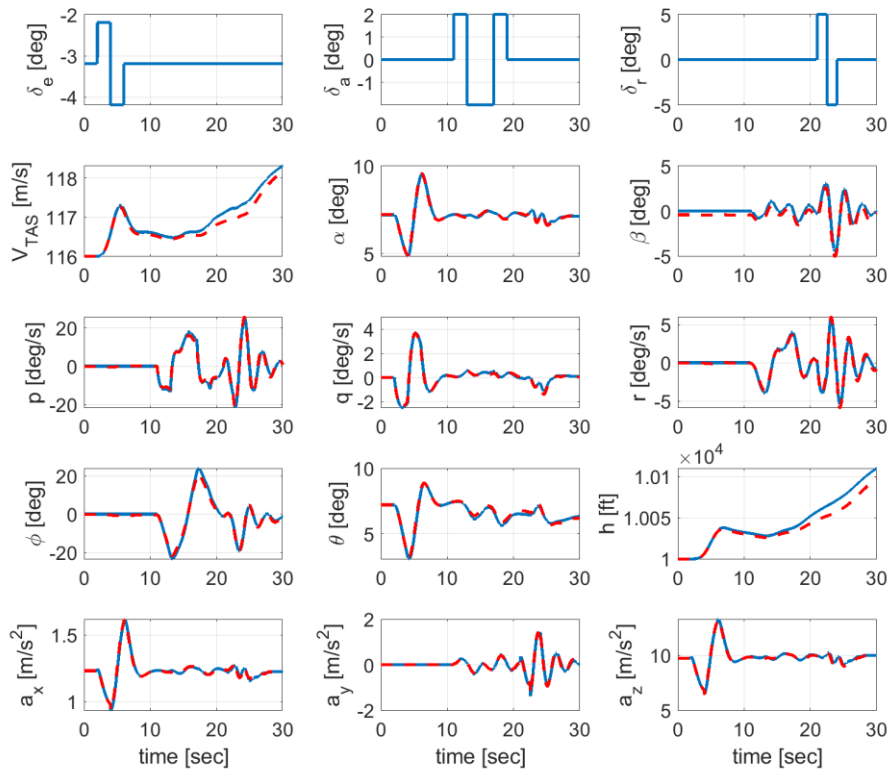


Figure 5.61 Combined Maneuvers – at $h = 10000$ ft, $CM = 0.30\bar{c}$ and $Ma = 0.35$

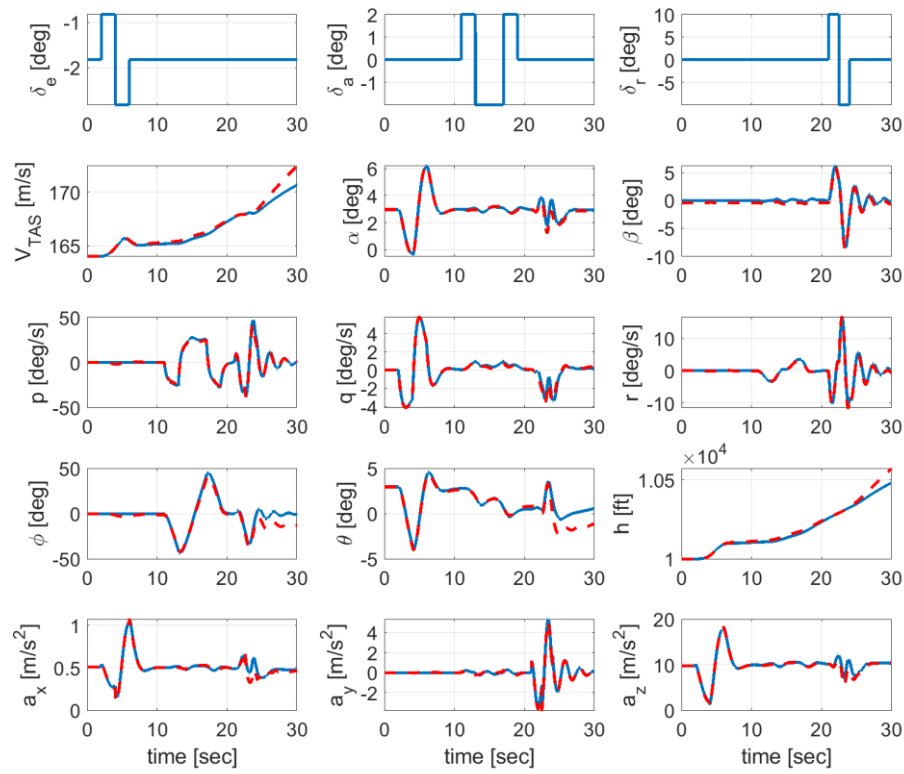


Figure 5.62 Combined Maneuvers – at $h = 10000$ ft, $CM = 0.30\bar{c}$ and $Ma = 0.50$

Theil's inequality coefficient for each of the longitudinal and lateral/directional variables are given in Table 5.37. TIC values for each longitudinal output variable are below the maximum acceptable values (in the range of 0.25 to 0.30) for both cases. It is observed that TIC values for longitudinal variables are less than ones for lateral/directional variables so we can conclude that longitudinal parameters are better estimated.

Table 5.37 Theil's Inequality Coefficient (TIC) for Combined Maneuvers

Output Variable	TIC (Flight Condition 1)	TIC (Flight Condition 2)
V_{TAS}	6.0987e-04	0.0015
α	0.0034	0.0308
β	0.1932	0.1202
p	0.0496	0.0531
q	0.0379	0.0549
r	0.0503	0.0590
ϕ	0.0543	0.1697
θ	0.0110	0.1829
h	3.8531e-04	0.0012
a_x	0.0033	0.0335
a_y	0.0479	0.0431
a_z	0.0040	0.0231

5.1.5.2.4 Proof-of-Match Maneuvers with respect to Strong Control Deflection Inputs

In proof-of-match maneuvers, the control deflections have been excited to stay in the linear region. Now the performance of the predicted model has been shown with respect to strong control deflection inputs. In these maneuvers, models are shown to be accurate for high excursions around the trim point.

Figure 5.63 and Figure 5.64 show the measured and predicted data comparison of short-period motions at 10000 ft, $CM = 0.30\bar{c}$ and two different speed ($Ma = 0.35$, $Ma=0.50$) flight condition. The model adequacy is quite apparent from the figures.

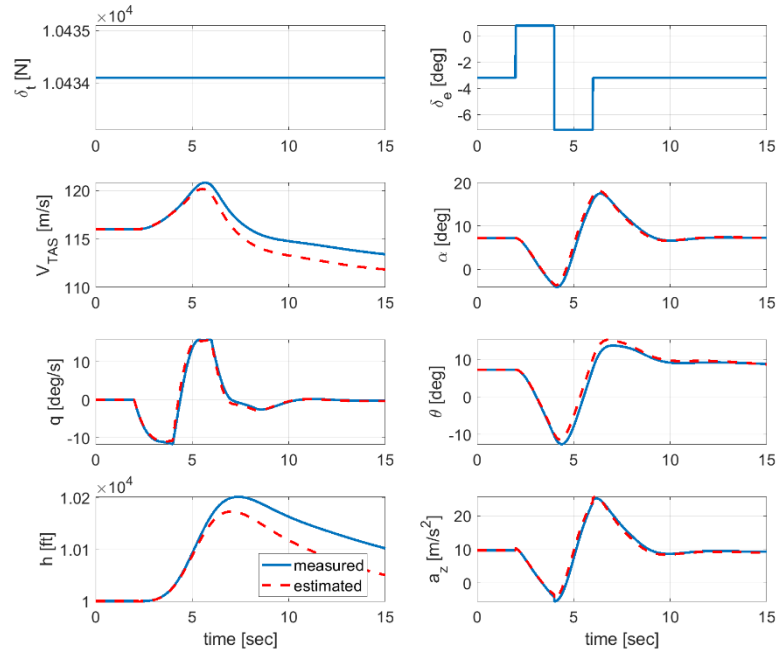


Figure 5.63 Short Period Dynamics – at $h = 10000$ ft, $CM = 0.30\bar{c}$ and $Ma = 0.35$

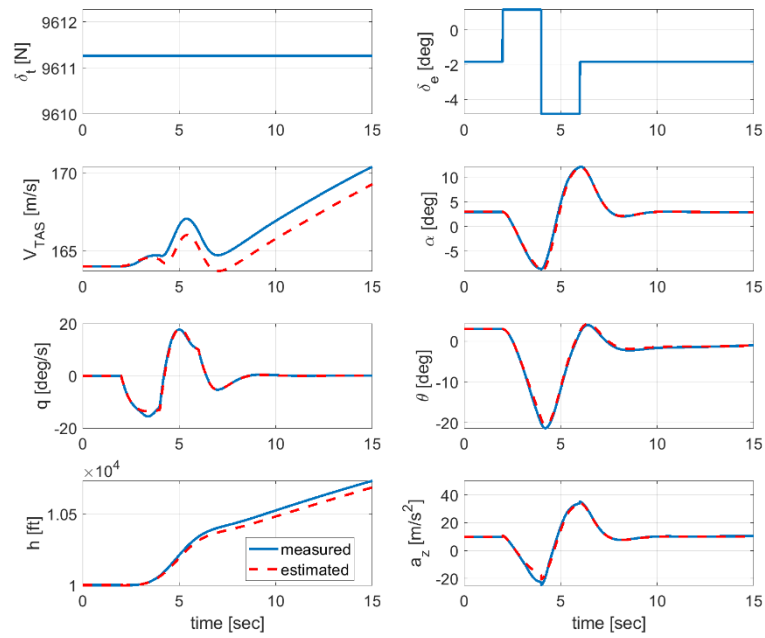


Figure 5.64 Short Period Dynamics – at $h = 10000$ ft, $CM = 0.30\bar{c}$ and $Ma = 0.50$

Figure 5.65 and Figure 5.66 show the measured and predicted data comparison of dutch-roll motions at 10000 ft, $CM = 0.30\bar{c}$ and two different speed ($Ma = 0.35$, $Ma=0.50$) flight condition. The model adequacy is quite apparent from the figures.

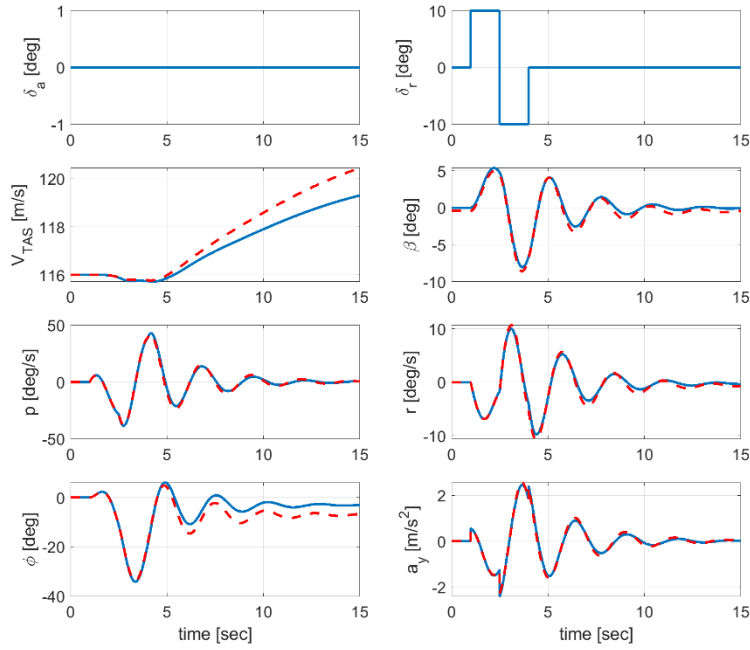


Figure 5.65 Dutch-Roll Dynamics – at $h = 10000$ ft, $CM = 0.30\bar{c}$ and $Ma = 0.35$

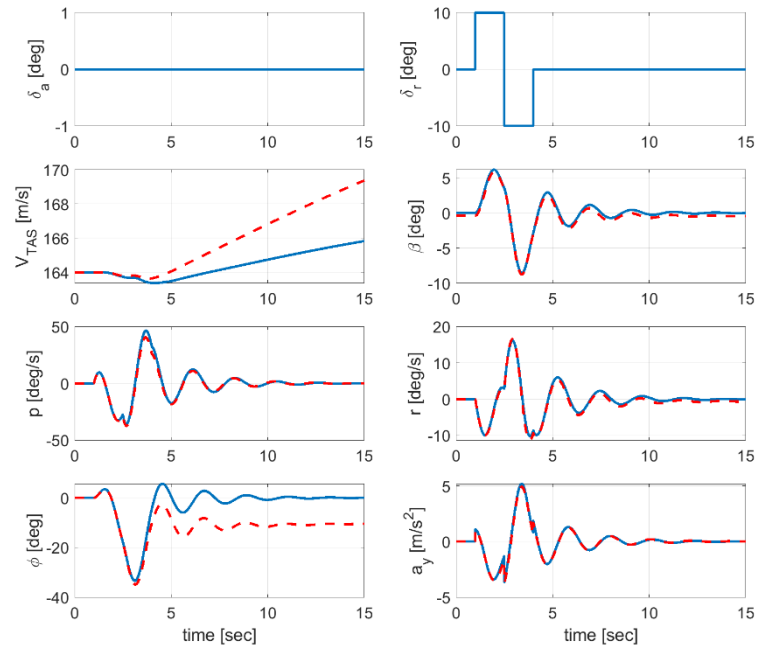


Figure 5.66 Dutch-Roll Dynamics – at $h = 10000$ ft, $CM = 0.30\bar{c}$ and $Ma = 0.50$

Figure 5.67 and Figure 5.68 show the measured and predicted data comparison of bank-to-bank motions at 10000 ft, $CM = 0.30\bar{c}$ and two different speed ($Ma = 0.35$, $Ma=0.50$) flight condition. The model adequacy is quite apparent from the figures.

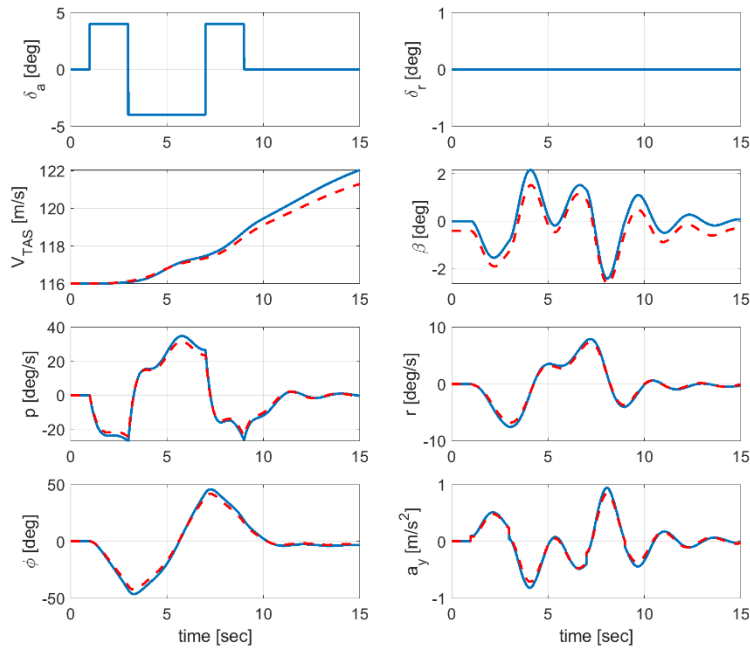


Figure 5.67 Bank-To-Bank Dynamics – at $h = 10000$ ft, $CM = 0.30\bar{c}$ and $Ma = 0.35$

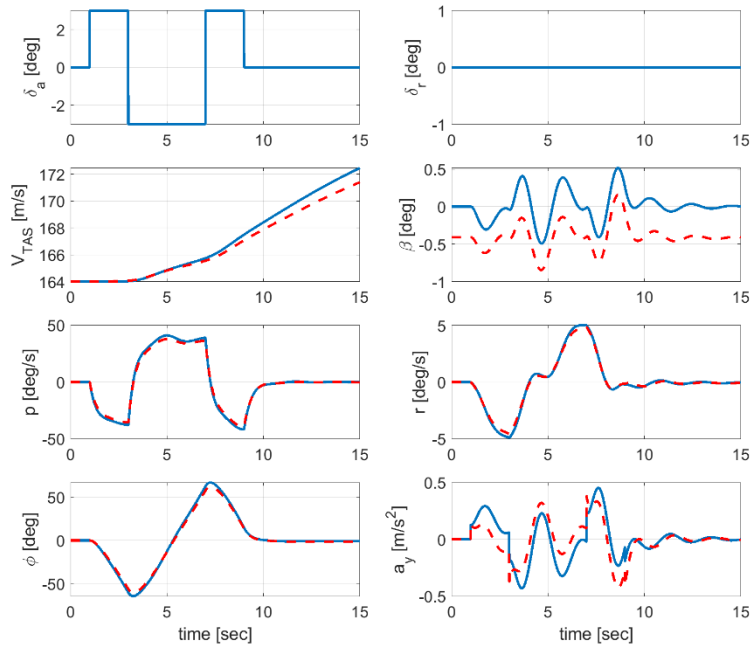


Figure 5.68 Bank-To-Bank Dynamics – at $h = 10000$ ft, $CM = 0.30\bar{c}$ and $Ma = 0.50$

5.1.5.3 Range of Model Applicability in Frequency Domain

Frequency response validation of the predicted models are presented in this section. The frequency response of pitch-rate to elevator input (q/δ_e), roll-rate to aileron input (p/δ_a), and yaw-rate to rudder input (r/δ_r) at different trim settings will be investigated. Frequency sweeps are performed for each control deflection inputs. The difference between the frequency responses of the nonlinear model and the predicted model are also presented with the allowable frequency response error bounds. If the error function is within these allowable error bounds, it indicates that the predicted model is a sufficient representation of the real aircraft. Example of frequency sweeps for longitudinal dynamics are given in Figure 5.69.

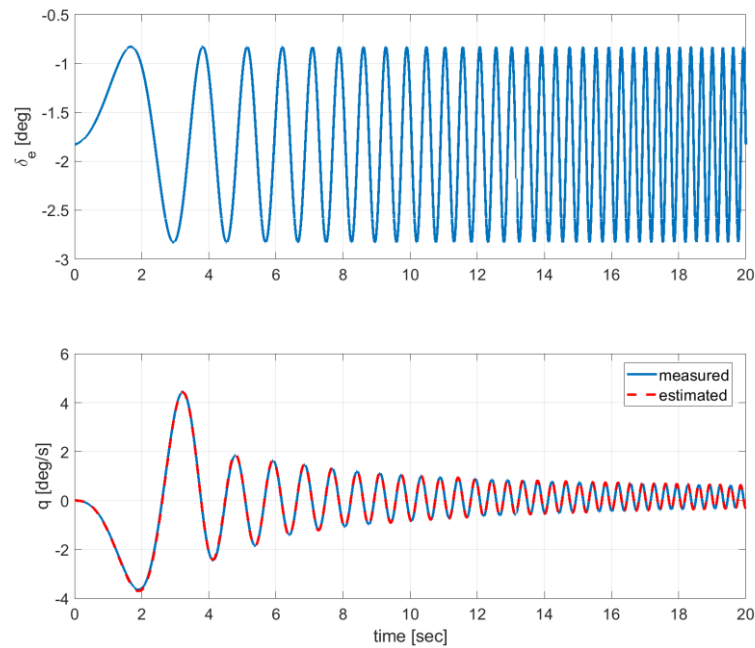


Figure 5.69 Example of a frequency sweep on longitudinal axis.

Frequency response validation of the predicted models for longitudinal dynamics (q/δ_e) at two different trim conditions are presented in Figure 5.70 and Figure 5.71. We can conclude that the predicted model on longitudinal dynamics is quite accurate.

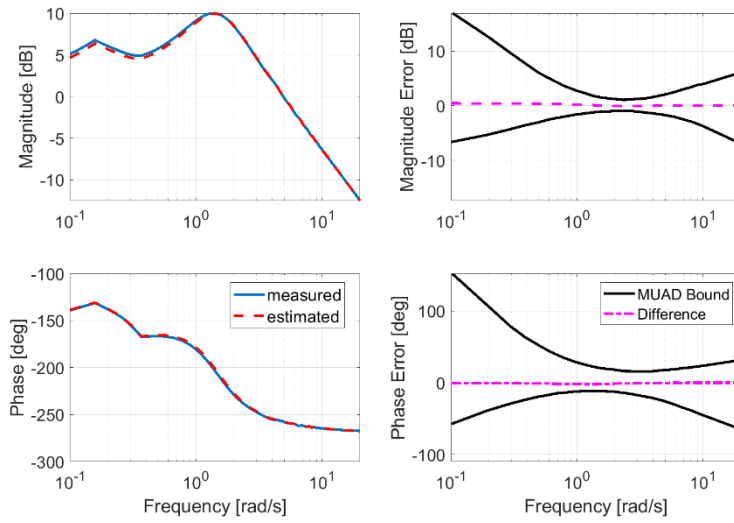


Figure 5.70 Frequency Response Validation of q/δ_e – at $h = 10000$ ft, $CM = 0.30\bar{c}$ and $Ma = 0.35$

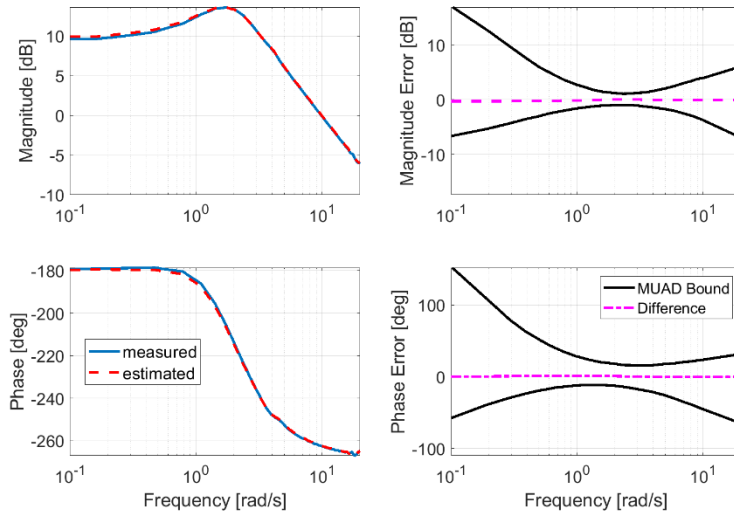


Figure 5.71 Frequency Response Validation of q/δ_e – at $h = 10000$ ft, $CM = 0.30\bar{c}$ and $Ma = 0.50$

Frequency response validation of the predicted models for lateral/directional dynamics (p/δ_a) and (r/δ_r) at two different trim conditions are presented from Figure 5.72 to Figure 5.75. As seen in the figures, differences remain in the MUAD Bounds, so that predicted model is quite accurate.

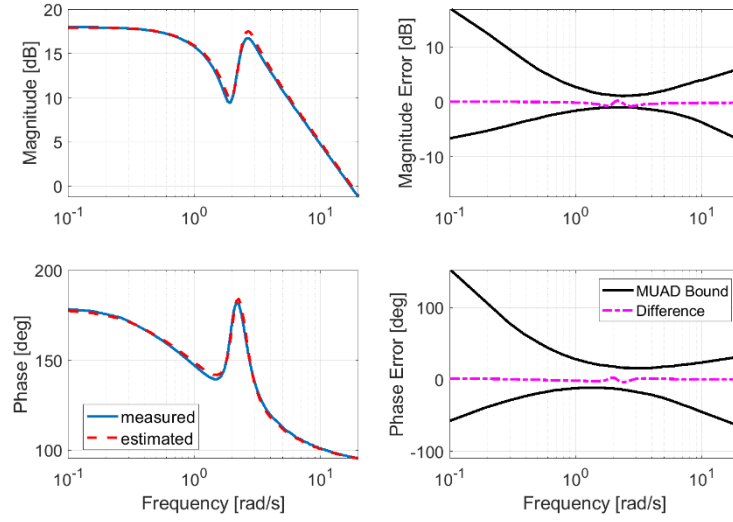


Figure 5.72 Frequency Response Validation of p/δ_a – at $h = 10000$ ft, $CM = 0.30\bar{c}$ and $Ma = 0.35$

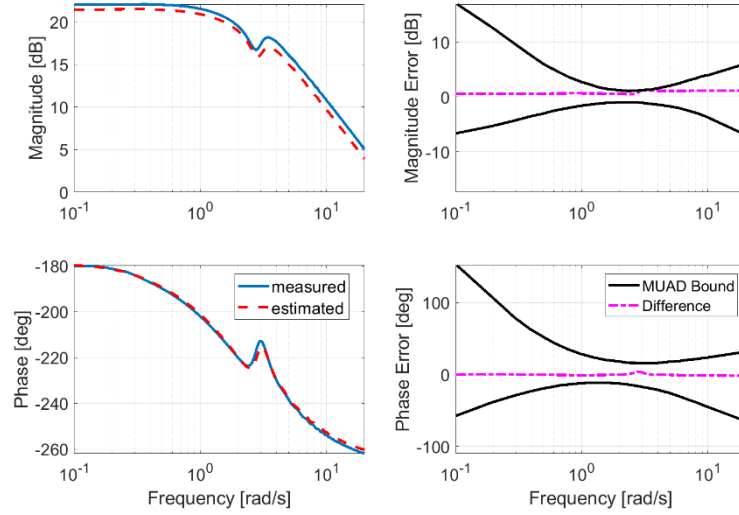


Figure 5.73 Frequency Response Validation of p/δ_a – at $h = 10000$ ft, $CM = 0.30\bar{c}$ and $Ma = 0.50$

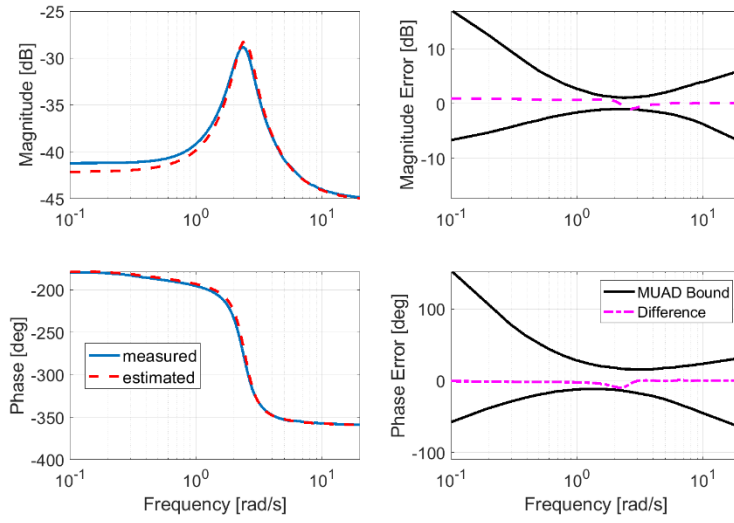


Figure 5.74 Frequency Response Validation of r/δ_r – at $h = 10000$ ft, $CM = 0.30\bar{c}$ and $Ma = 0.35$

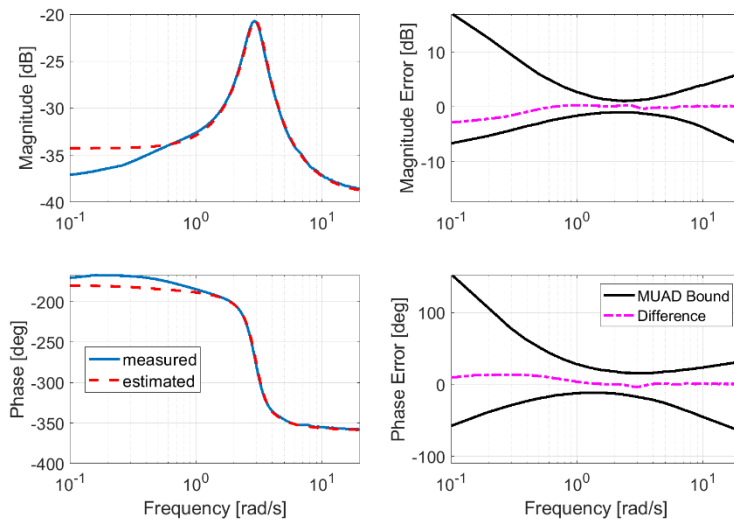


Figure 5.75 Frequency Response Validation of r/δ_r – at $h = 10000$ ft, $CM = 0.30\bar{c}$ and $Ma = 0.50$

5.1.5.4 Comparison of Estimation Results with respect to Wind Tunnel Data

Figure 5.76, Figure 5.77, and Figure 5.78 show the comparison of estimated parameters with the true ones (wind tunnel database) for longitudinal aerodynamic

coefficients, a luxury that is usually out of reach in real life. There is quite good fit between wind tunnel database and predicted model as seen in the figures.

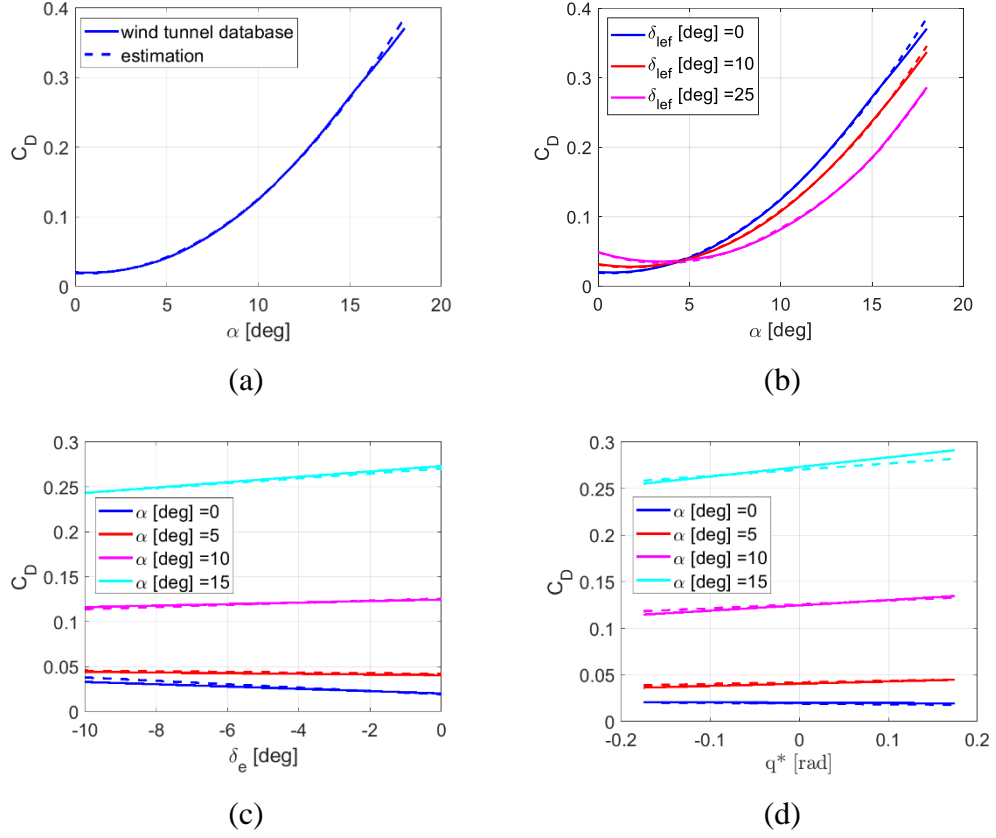
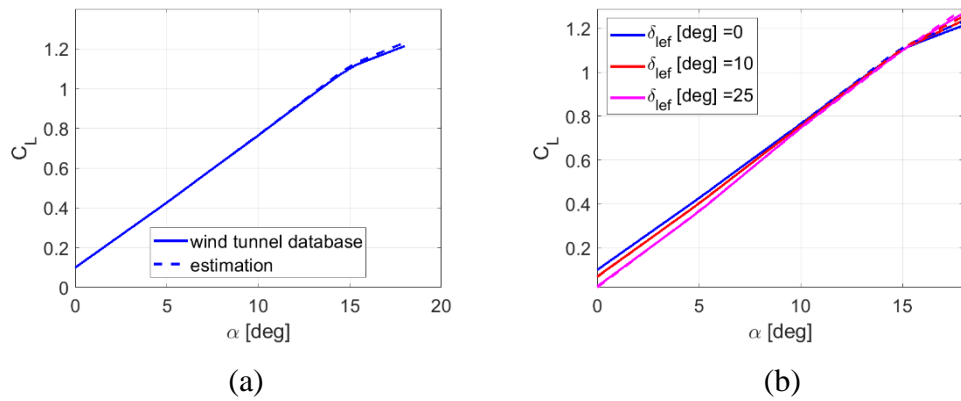
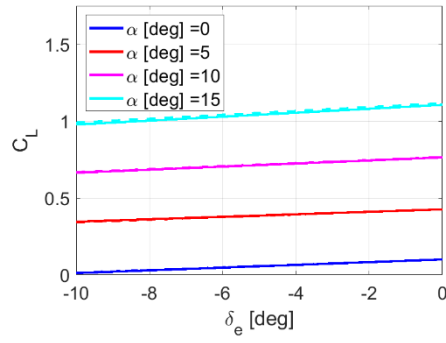
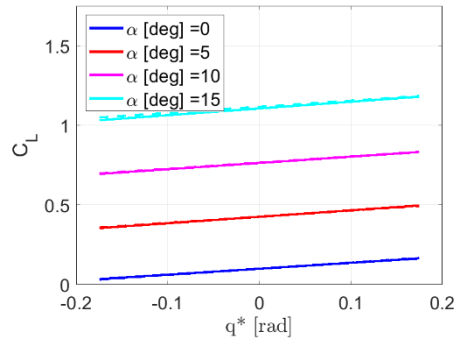


Figure 5.76 Estimation Quality of Drag Coefficient



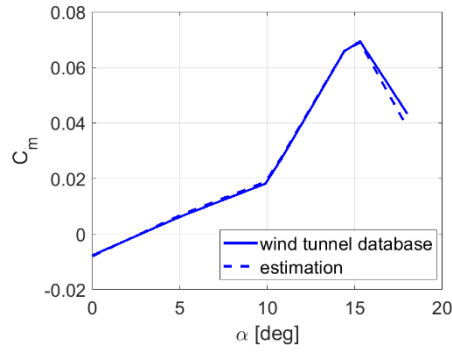


(c)

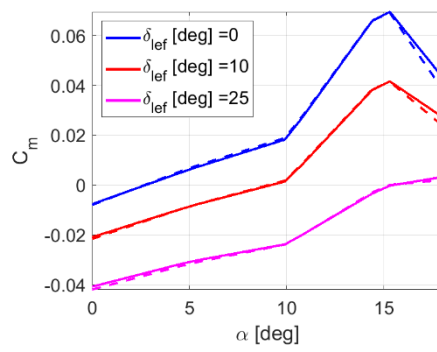


(d)

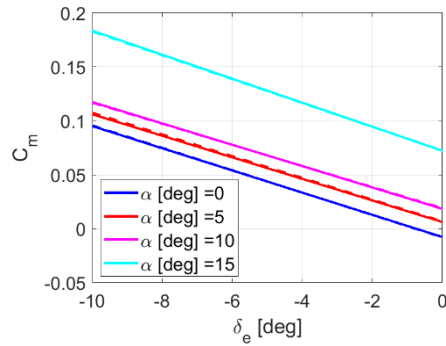
Figure 5.77 Estimation Quality of Lift coefficient



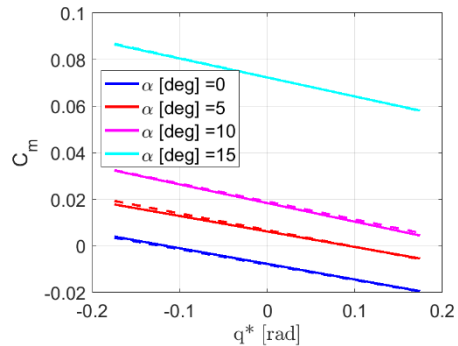
(a)



(b)



(c)



(d)

Figure 5.78 Estimation Quality of Pitch Moment Coefficient

5.2 Case 2: Non-Availability of Engine Database from Manufacturer

In the first case, the engine-related forces and moment are obtained from the engine deck and directly feeded back to the 6-DOF equations of motion model to isolate the aerodynamic model. But in this case, the engine and aerodynamic database are not available. To find an appropriate aerodynamic model, an approximate engine model is to be constructed first. The equations in section 4.4, thrust calculation from steady-state flight tests, are used to do so. After the approximate engine model is constructed, the methodology in Section 5.1 is repeated.

5.2.1 Calculating Thrust from Steady State Flights

Many flight tests were made for different flight conditions expressed in Mach numbers ($M = 0.2$ to $M = 0.6$), altitudes ($h = 0\text{ft}$ to $h = 40000\text{ft}$), and different flight path angles ($\gamma = -5^\circ$ to $\gamma = 5^\circ$). Now we can compare the results for different flight conditions.

Firstly, we compare the estimated results from Eqs. (4.84) and (4.92) with the actual results for level flight.

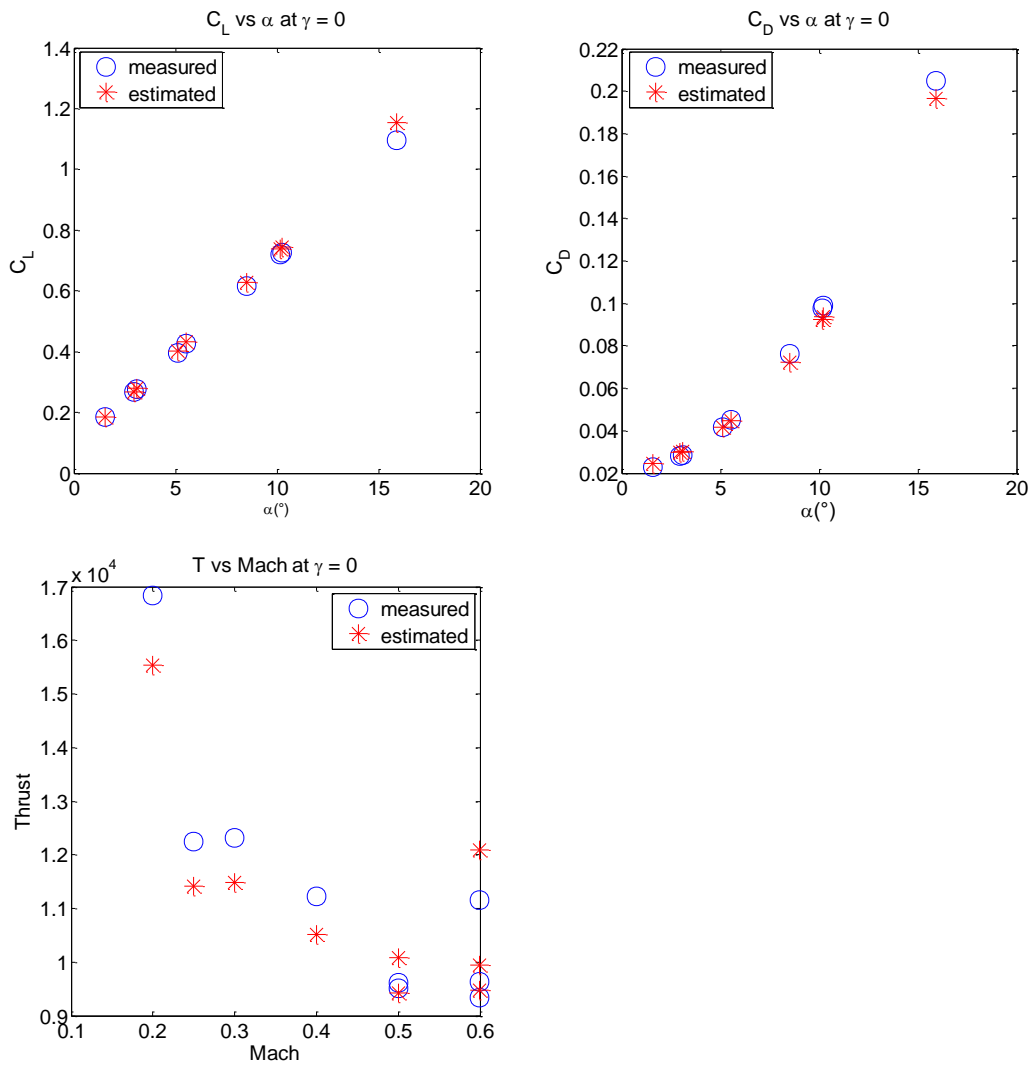


Figure 5.79 Measured and Constructed Thrust, Lift Coefficient, and Drag Coefficient in Steady Level Flight

Secondly, we compare the estimated results from Eqs. (4.84) and (4.92) with the actual results for climbing flight.

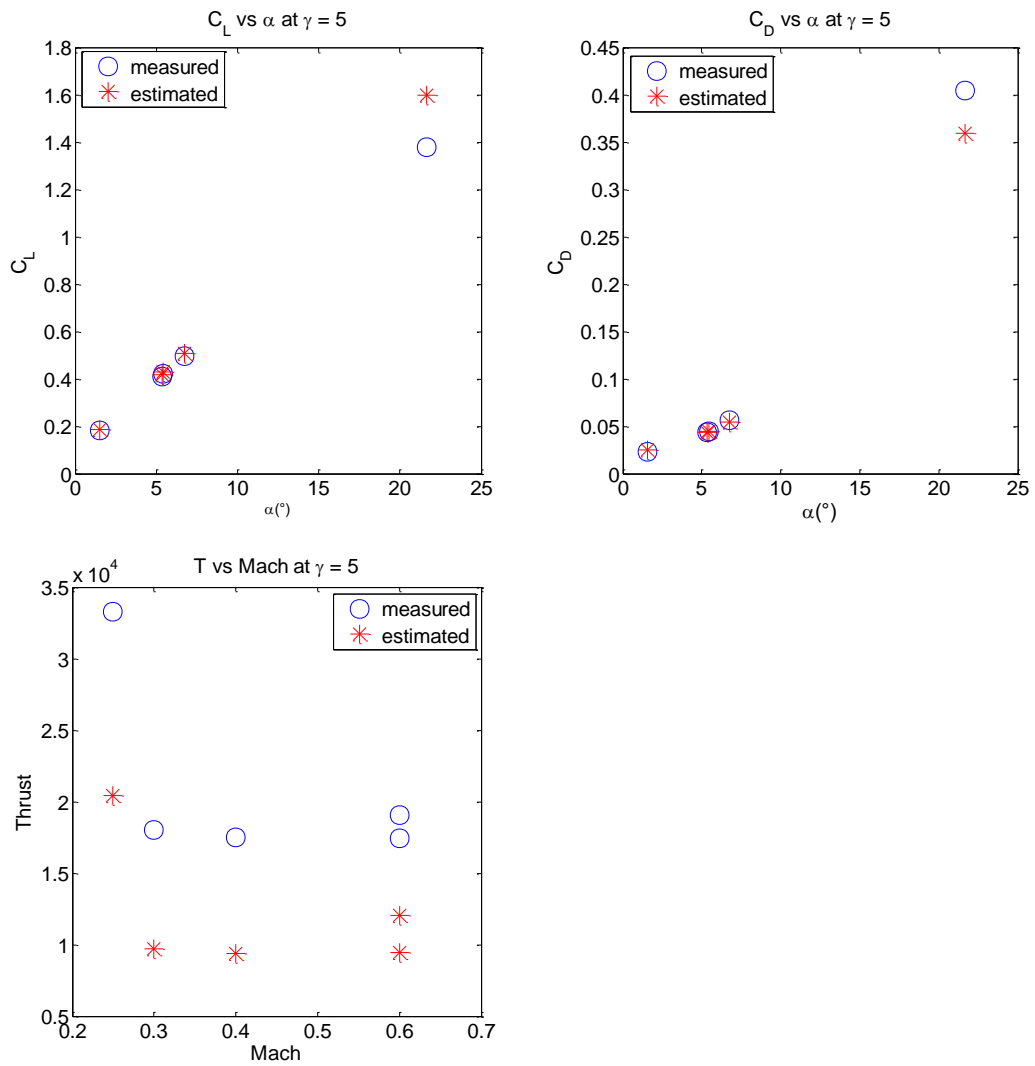


Figure 5.80 Measured and Constructed Thrust, Lift Coefficient, and Drag Coefficient in Steady Climb Flight

We can conclude from the figures that the results are promising. The lift coefficient trend is almost the same, and values are so close to each other for the angle of attack values up to 20 deg, which is in our flight scope. The drag coefficient trend is ok, but values are slightly different for high angle of attack values as expected since Eq. (5.7) is just an approximation for the linear region. So, we can use constructed thrust values in place of actual thrust values as initial points in our future work.

5.2.2 Turbofan Engine Thrust Model

Now, go back to Section 2.2.2.3, Simplified Turbofan Thrust Model. Using the results obtained in 5.2.1 and using the Eqs. (2.58), (2.59), and (2.60), we get the following equation:

$$\tilde{T}(h, M, \delta_{TLA}) = \frac{T(h, M, \delta_{TLA})}{T_0 \times \frac{\rho(h)}{\rho_0} \left[1 + \frac{(\gamma - 1)}{2} M^2 \right]^{\frac{1}{\gamma - 1}}} = \sum_{i=0}^m \sum_{j=0}^n \tilde{T}_{ij}(h) M^i \delta_{TLA}^j \quad (5.8)$$

To decide which m and n values make the best fit, we compare the Mean Square Error using K-Fold Cross Validation for different m and n values. For $m = 3$ and $n = 2$, we get the overall best result. In Table 1, the mean squared error with respect to different altitudes is shown.

Table 5.38 Mean Squared Error Values with respect to Different Altitudes

Altitude [ft]	Mean Square Error
0	5.2788e-04
5000	6.8464e-04
10000	1.2531e-06
20000	1.0063e-05
30000	1.9749e-05

At $h = 0$ ft, the constructed and estimated nondimensional thrust coefficient comparison is shown below.

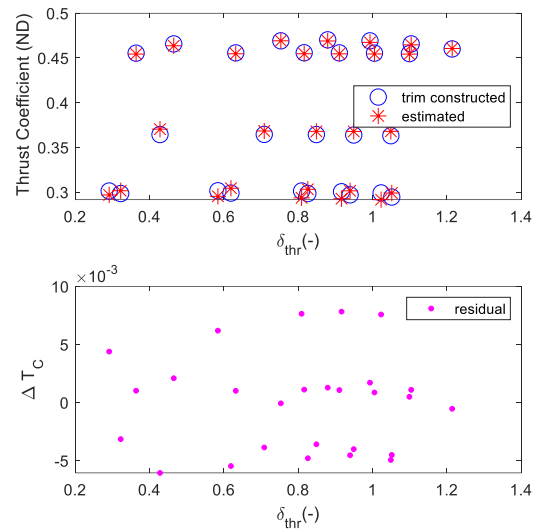


Figure 5.81 Measured and Constructed Thrust Coefficient at $h = 0$ ft

At $h = 5000$ ft, the constructed and estimated nondimensional thrust coefficient comparison is shown below.

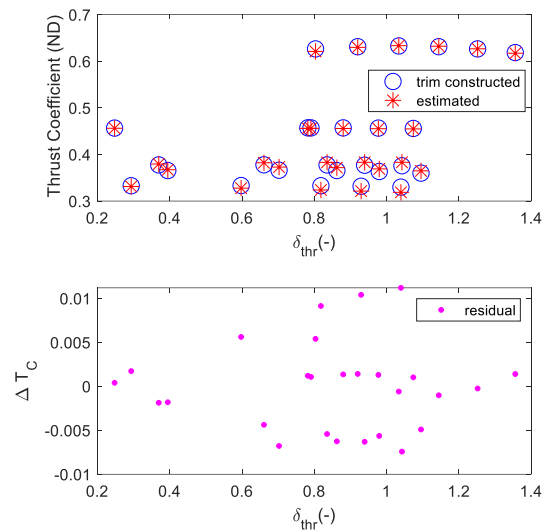


Figure 5.82 Measured and Constructed Thrust Coefficient at $h = 5000$ ft

At $h = 10000$ ft, the constructed and estimated nondimensional thrust coefficient comparison is shown below.

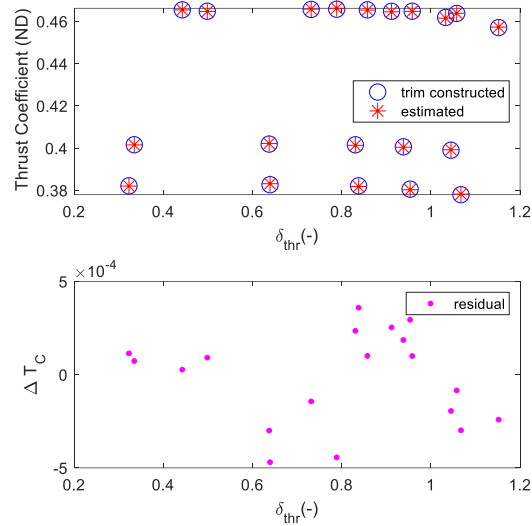


Figure 5.83 Measured and Constructed Thrust Coefficient at $h = 10000$ ft

At $h = 20000$ ft, the constructed and estimated nondimensional thrust coefficient comparison is shown below.

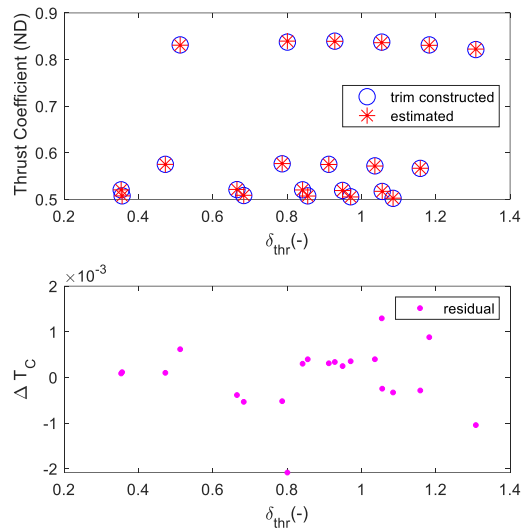


Figure 5.84 Measured and Constructed Thrust Coefficient at $h = 20000$ ft

At $h = 30000$ ft, the constructed and estimated nondimensional thrust coefficient comparison is shown below.

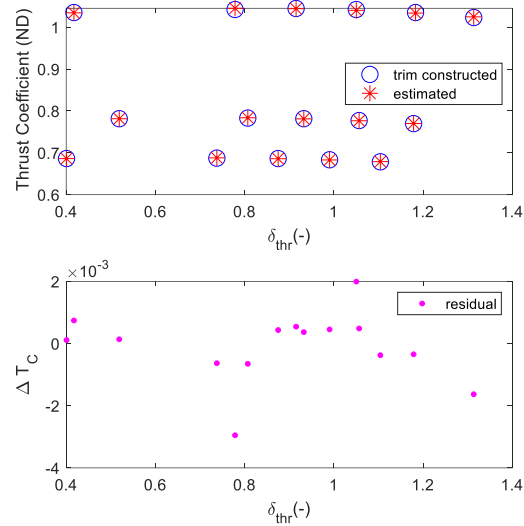


Figure 5.85 Measured and Constructed Thrust Coefficient at $h = 30000$ ft

The estimated results are compatible with the constructed results from trim values. Estimated thrust values are replaced with actual thrust values, and aerodynamic coefficients are re estimated and compared with the new aerodynamic force and moment coefficient results as future work.

5.2.3 Iterative Equation Error Method

After developing the engine thrust model, the next step is to use EEM to obtain the reasonable starting point for longitudinal aerodynamic coefficients. In EEM, a suitable model has been postulated. Then Iterative-EEM is employed.

The convergence of the cost function for the iterative equation error method can be seen below.

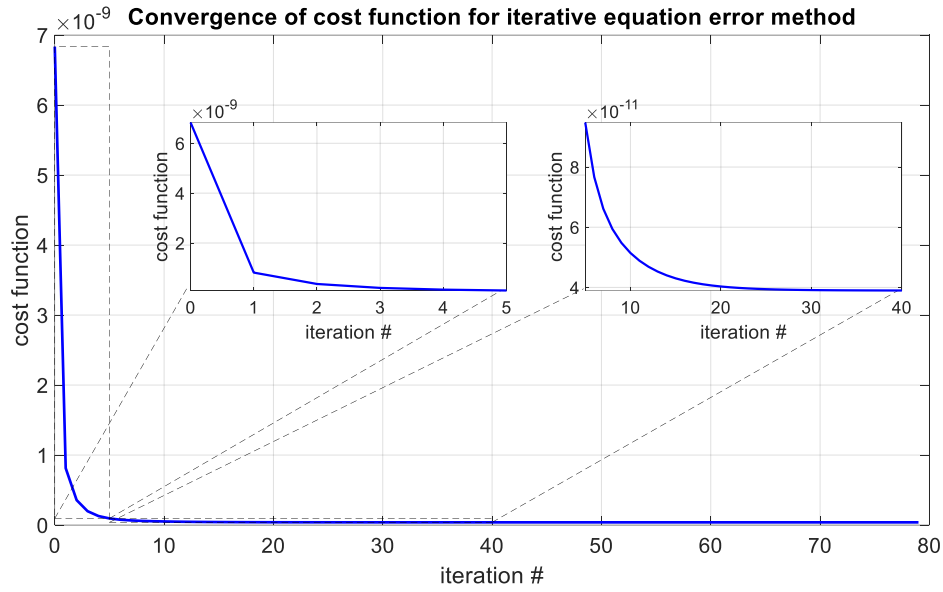


Figure 5.86 Convergence of Cost Function for Iterative Equation Error Method

As it is seen in Figure 5.86, in the first 5 iterations cost function decreases dramatically, and the cost function converges to a minimal value after the 40th iteration. Hence, 40 iteration is enough to get good results.

Table 5.39 and Table 5.40 gives the parameter estimates and their errors. The estimation error is calculated as $\delta = \|\theta_k - \theta_{actual}\| / \|\theta_{actual}\|$

Table 5.39 Drag Coefficient Parameter Estimates and Errors

k	C_{D0}	$C_{D\alpha}$	$C_{D\alpha^2}$	$C_{D\alpha^3}$	$C_{D\delta_e}$	$C_{D\delta_e\alpha}$	$C_{D\delta_e\alpha^2}$
1	0.0206	0.057	2.458	0.027	-0.010	-0.675	5.277
2	0.0206	0.049	2.581	0.168	-0.038	-0.373	4.673
3	0.0201	0.032	3.180	-0.764	-0.053	0.218	1.957
4	0.0200	0.009	3.558	-1.086	-0.059	0.353	1.315
5	0.0200	-0.011	3.780	-1.074	-0.060	0.347	1.370
10	0.0202	-0.061	4.173	-0.675	-0.061	0.320	1.702
15	0.0202	-0.074	4.237	-0.531	-0.062	0.332	1.780
20	0.0202	-0.079	4.250	-0.466	-0.063	0.343	1.818
30	0.0202	-0.083	4.256	-0.413	-0.063	0.353	1.849
40	0.0202	-0.085	4.256	-0.395	-0.064	0.357	1.859
50	0.0202	-0.085	4.254	-0.389	-0.064	0.357	1.863
80	0.0202	-0.086	4.258	-0.383	-0.064	0.357	1.868
Actual	0.0209	-0.1411	4.311	-0.273	-0.057	0.205	2.442

Table 5.40 Drag Coefficient Parameter Estimates and Estimation Error – Continued

k	C_{D_q}	$C_{D_{q\alpha}}$	$C_{D_{\delta_{lef}}}$	$C_{D_{\delta_{lef}\alpha}}$	$C_{D_{\delta_{lef}\alpha_{10}}}$	$C_{D_{\delta_{lef}\alpha_{15}}}$	$\delta(\%)$
1	0.534	22.497	-0.088	0.357	-0.337	0.700	74.242
2	0.564	21.120	-0.080	0.259	-0.368	0.674	62.844
3	0.122	18.320	-0.057	-0.097	-0.243	0.635	32.398
4	-0.030	16.393	-0.037	-0.353	-0.159	0.625	34.181
5	-0.097	15.841	-0.020	-0.530	-0.121	0.627	30.293
10	-0.205	17.114	0.022	-0.897	-0.114	0.620	17.260
15	-0.267	18.354	0.033	-0.969	-0.134	0.625	14.387
20	-0.309	19.142	0.038	-0.989	-0.147	0.631	13.246
30	-0.348	19.870	0.042	-1.002	-0.159	0.637	12.432
40	-0.360	20.107	0.043	-1.005	-0.163	0.639	12.191
50	-0.364	20.184	0.044	-1.005	-0.164	0.640	12.097
80	-0.366	20.217	0.044	-1.002	-0.164	0.639	11.987
Actual	-0.234	19.579	0.0833	-1.067	-0.146	0.636	

Figure 5.87 shows the variation of estimated parameters versus iteration number. The parameters showing variation larger than 50% from the converged solution were dropped from the assumed model. And the converged solution is very close to that obtained with the actual thrust value.

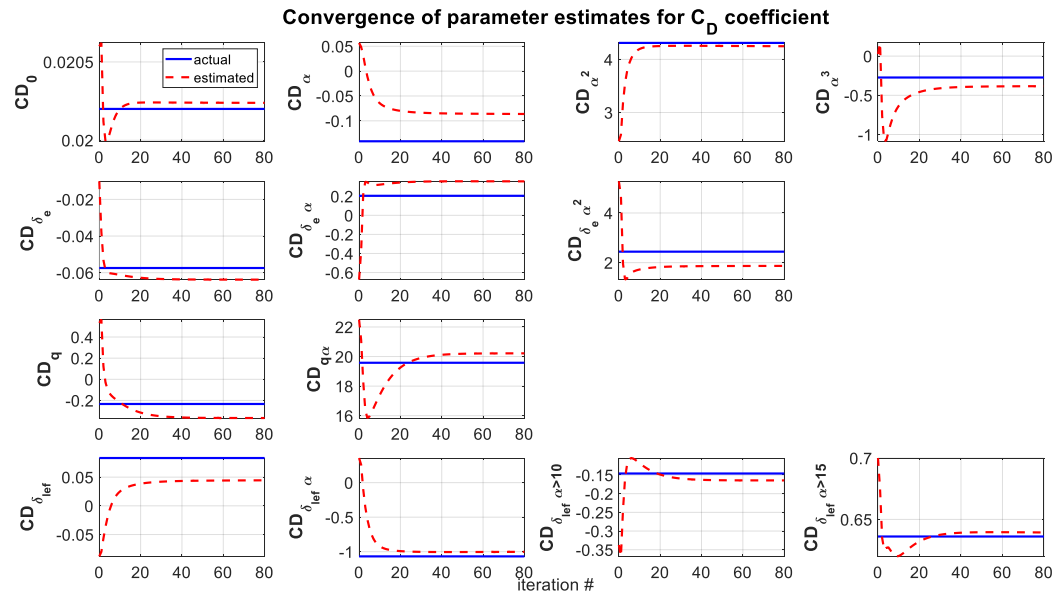


Figure 5.87 Converge of Parameter Estimates for the Drag Coefficient

Table 5.41 and Table 5.42 give the parameter estimates and their errors for lift coefficient. The estimation error is calculated as $\delta = \|\Theta_k - \Theta_{actual}\|/\|\Theta_{actual}\|$.

Table 5.41 Lift Coefficient Parameter Estimates and Errors

k	C_{L_0}	C_{L_α}	$C_{L_{\alpha_5^1}}$	$C_{L_{\alpha_{10}^1}}$	$C_{L_{\alpha_{15}^1}}$	$C_{L_{\delta_e}}$	$C_{L_{\delta_e\alpha}}$	$C_{L_{\delta_e\alpha^2}}$
1	0.0992	3.747	0.175	0.114	-1.834	0.477	-0.084	3.788
2	0.0998	3.740	0.162	0.145	-1.984	0.505	-0.706	6.144
3	0.0998	3.737	0.156	0.137	-1.982	0.508	-0.804	6.615
4	0.0999	3.736	0.152	0.135	-1.981	0.509	-0.833	6.750
5	0.0999	3.735	0.151	0.136	-1.976	0.510	-0.838	6.758
10	0.0999	3.735	0.149	0.140	-1.953	0.510	-0.844	6.722
15	0.0999	3.736	0.149	0.139	-1.942	0.510	-0.843	6.687
20	0.0999	3.736	0.149	0.139	-1.936	0.510	-0.840	6.660
30	0.0999	3.736	0.149	0.138	-1.932	0.510	-0.838	6.635
40	0.0999	3.736	0.149	0.137	-1.931	0.510	-0.837	6.627
50	0.0999	3.736	0.149	0.137	-1.931	0.510	-0.836	6.624
80	0.0999	3.737	0.149	0.137	-1.931	0.510	-0.835	6.620
Actual	0.0995	3.737	0.156	0.135	-1.907	0.489	-0.612	4.808

Table 5.42 Lift Coefficient Parameter Estimates and Errors

k	C_{L_q}	$C_{L_{q\alpha}}$	$C_{L_{\delta_{lef}}}$	$C_{L_{\delta_{lef}\alpha}}$	$C_{L_{\delta_{lef}\alpha_5^1}}$	$C_{L_{\delta_{lef}\alpha_{10}^1}}$	$C_{L_{\delta_{lef}\alpha_{15}^1}}$	$C_{L_{\delta_{lef}q\alpha}}$	$\delta(\%)$
1	28.742	28.348	-0.175	0.511	0.345	-0.804	3.150	-74.932	23.474
2	28.985	21.385	-0.178	0.507	0.430	-0.862	3.620	-54.764	12.770
3	29.016	21.424	-0.178	0.508	0.473	-0.860	3.625	-52.506	12.316
4	29.043	21.258	-0.178	0.508	0.494	-0.870	3.624	-51.168	11.905
5	29.064	21.087	-0.178	0.508	0.504	-0.882	3.609	-50.866	10.577
10	29.110	20.619	-0.178	0.508	0.515	-0.903	3.550	-51.594	10.412
15	29.115	20.640	-0.178	0.507	0.516	-0.902	3.519	-52.577	9.521
20	29.114	20.736	-0.178	0.506	0.516	-0.899	3.501	-53.345	8.487
30	29.112	20.852	-0.178	0.505	0.516	-0.895	3.489	-54.101	8.134
40	29.110	20.899	-0.178	0.505	0.516	-0.894	3.486	-54.359	8.004
50	29.109	20.921	-0.178	0.505	0.516	-0.893	3.485	-54.452	7.892
80	29.107	20.954	-0.178	0.505	0.516	-0.893	3.485	-54.528	7.812
Actual	29.136	22.597	-0.178	0.511	0.454	-0.912	3.361	-59.489	

Figure 5.88 shows the variation of estimated parameters for lift coefficient versus iteration number. No parameter in the assumed postulate showed variation larger than 50% from the converged solution. As expected, the converged solution is very close to that obtained with the actual thrust value

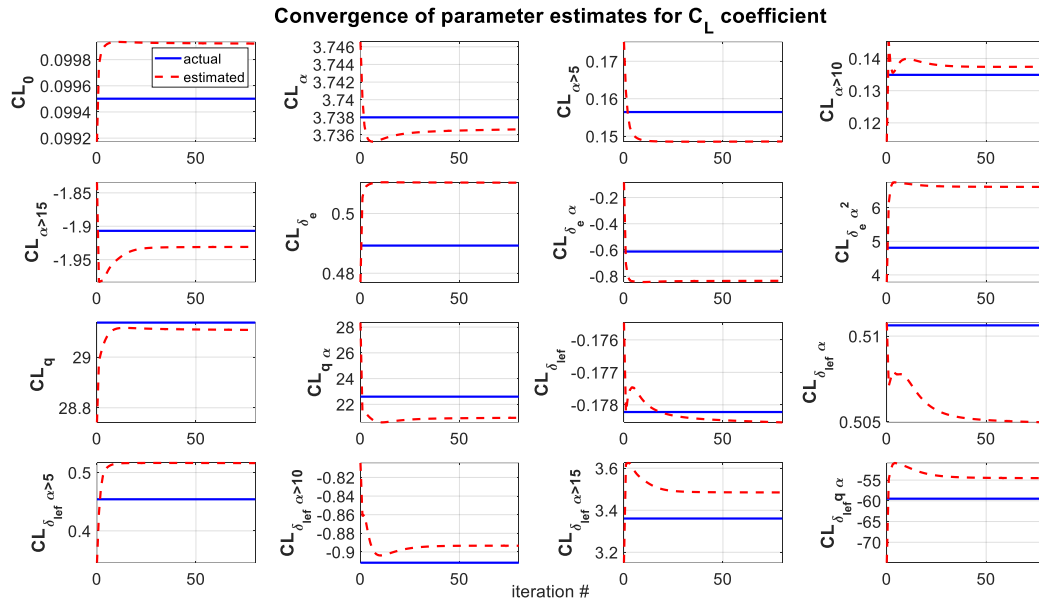


Figure 5.88 Converge of Parameter Estimates for Lift Coefficient

Figure 5.89, Figure 5.90, and Figure 5.91 show the comparison of estimated parameters using iterative -eem and eem methods with the true ones (wind tunnel database), a luxury that is usually out of reach in real life. The iterative eem yields inferior results (far from the actual value), but the results become much closer with increasing iteration numbers. The difference in Figure 5.90.b can be explained such that the leading-edge flap is scheduled with the angle of attack, where a high angle of attack corresponds to a high leading-edge flap. So, when the leading edge flap is zero, the corresponding angle of attack is between -5 and 5 degrees. But when the leading-edge flap increases, it corresponds to a high angle of attack values (more than 10 degrees).

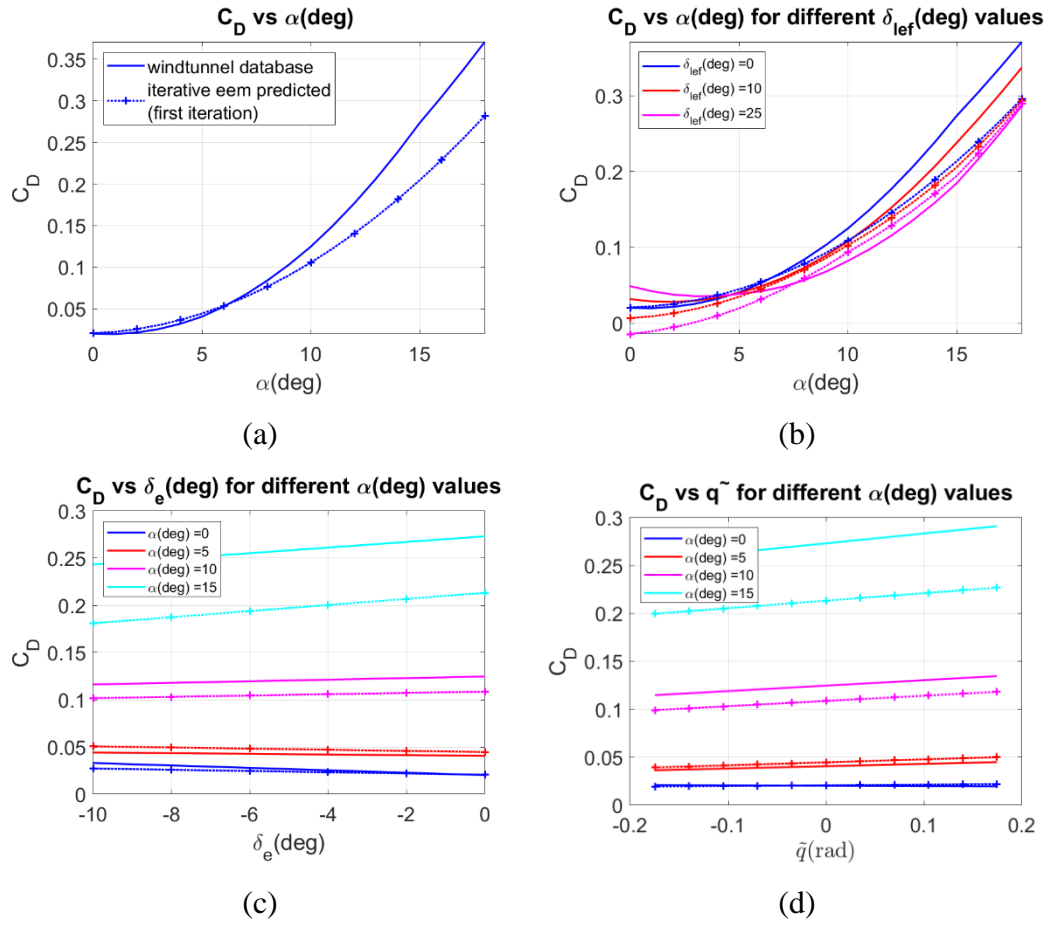
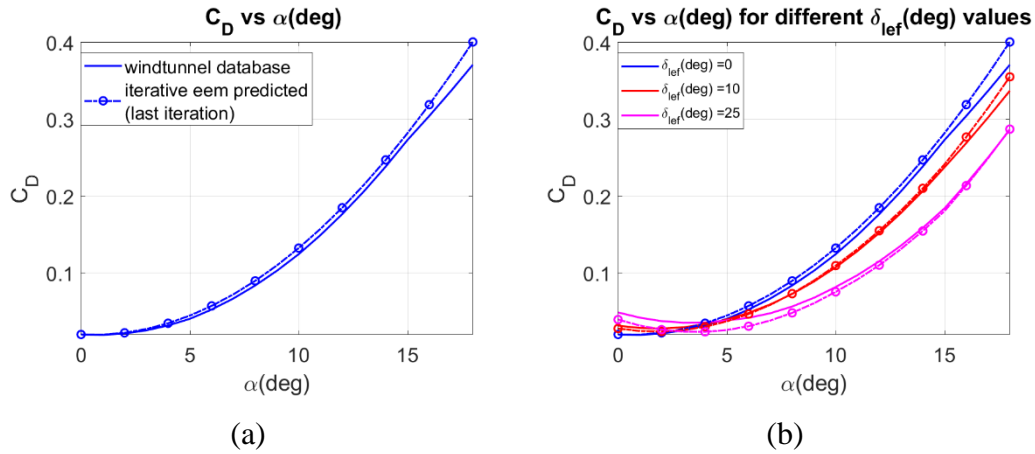
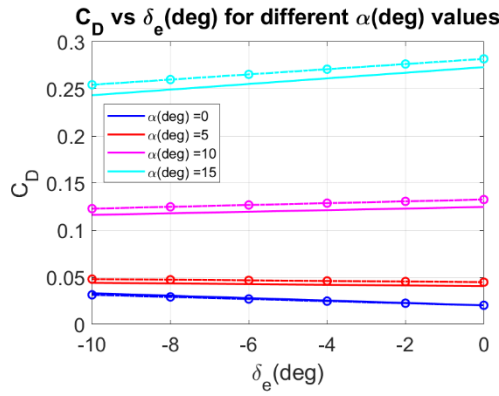
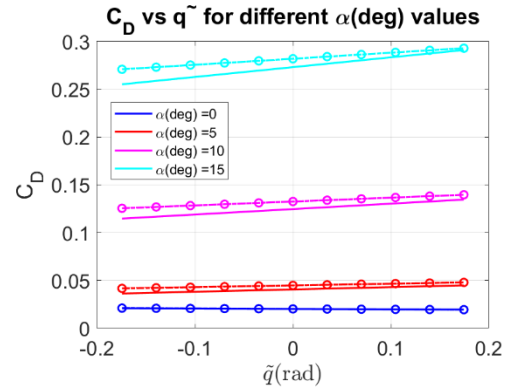


Figure 5.89 Estimation Quality of Drag Coefficient Where Wind Tunnel Data is Compared with Iterative EEM Method (First Iteration)



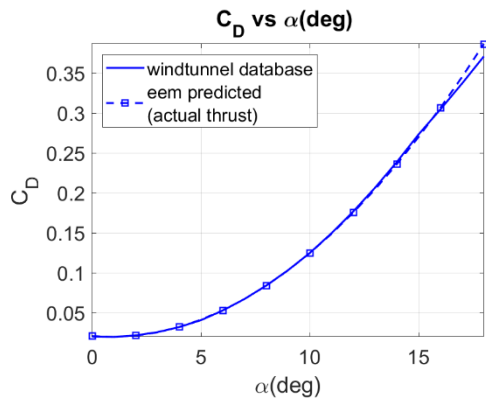


(c)

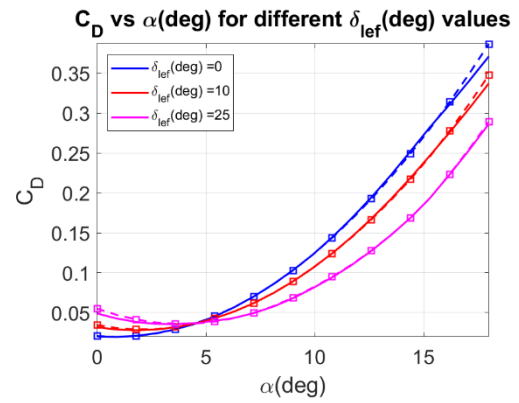


(d)

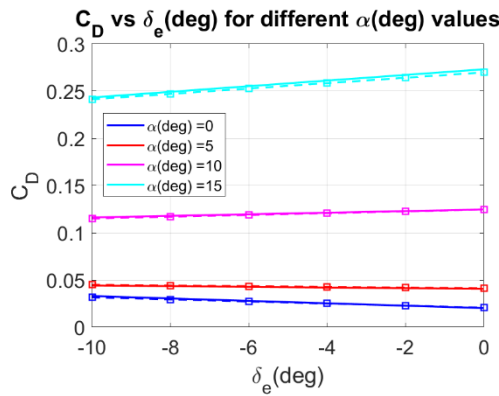
Figure 5.90 Estimation Quality of Drag Coefficient Where Wind Tunnel Data is Compared with Iterative EEM Method (Last Iteration)



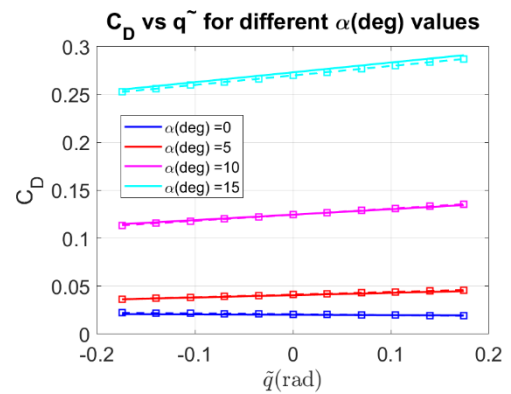
(a)



(b)



(c)



(d)

Figure 5.91 Estimation Quality of Drag Coefficient Where Wind Tunnel Data is Compared with EEM Method (Actual Thrust)

Figure 5.92, Figure 5.93, and Figure 5.94 show the comparison of estimated parameters of lift coefficient using iterative -eem and eem methods with the true ones (wind tunnel database). The lift coefficient is generally easier to estimate because it shows a more linear trend than the drag coefficient. Moreover, the lift coefficient is less correlated with engine thrust; that is why we expect a good agreement between estimates and actual values.

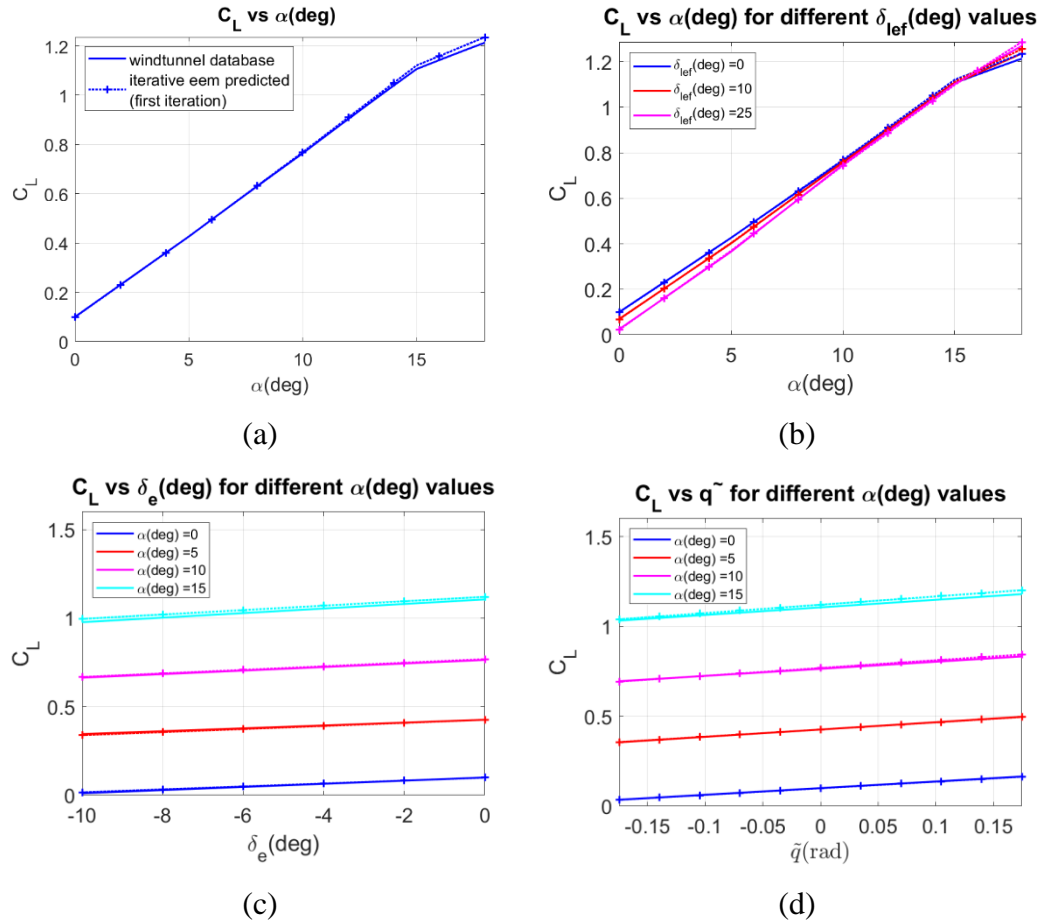


Figure 5.92 Estimation Quality of Lift Coefficient Where Wind Tunnel Data is Compared with Iterative EEM Method (First Iteration)

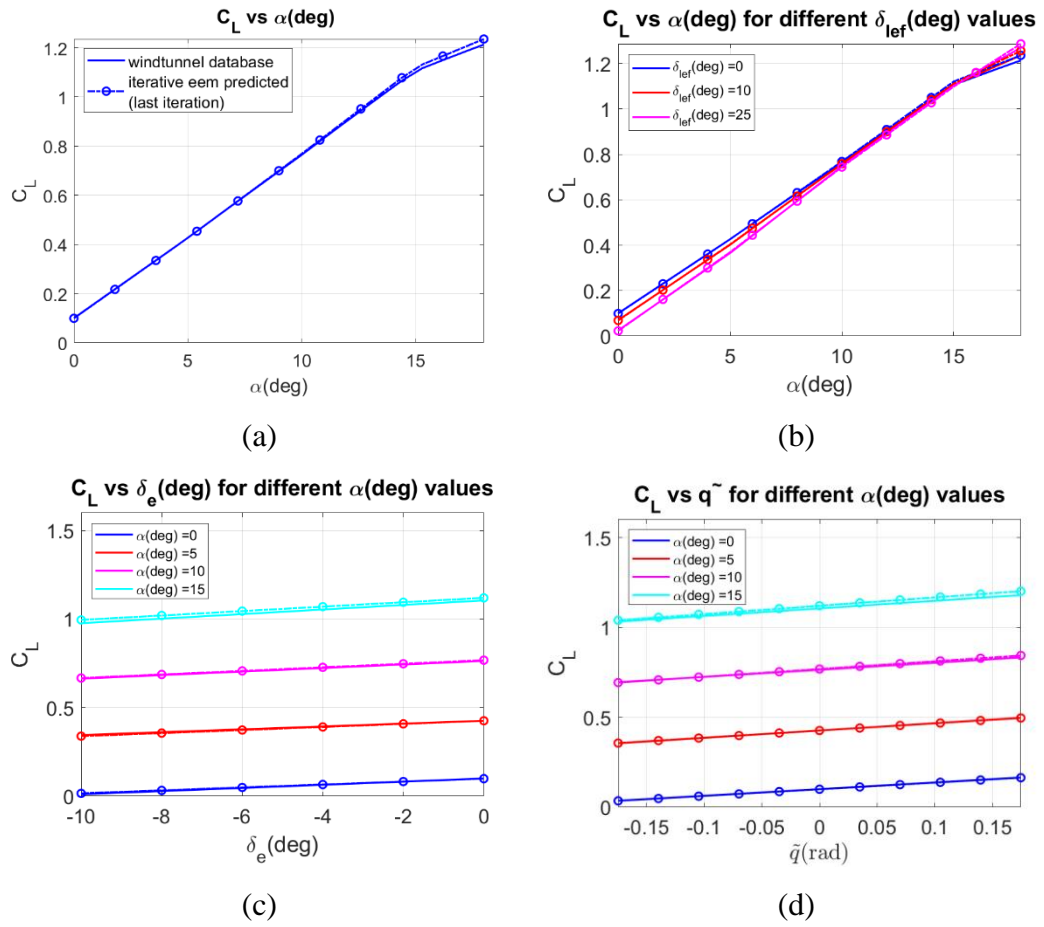
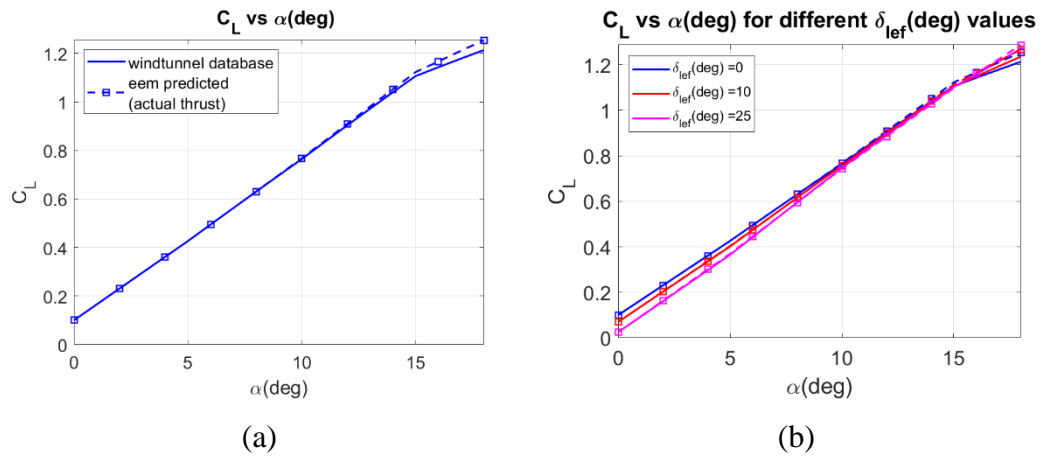
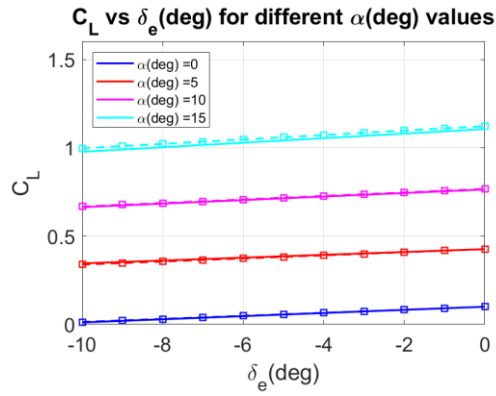
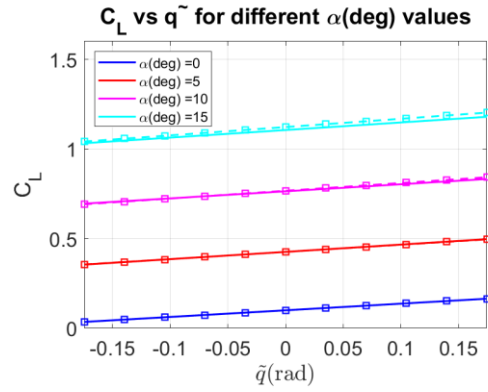


Figure 5.93 Estimation Quality of Lift Coefficient Where Wind Tunnel Data is Compared with Iterative Eem Method (Last Iteration)





(c)



(d)

Figure 5.94 Estimation Quality of Lift Coefficient Where Wind Tunnel Data is Compared with EEM Method (Actual Thrust)

Iterative data processing is the sequential processing of an entire group of data, and the database remains the same, and only some estimated variable is modified at each iterative step. Simulation results indicate that the proposed algorithms are practical, and the iterative EEM algorithm can produce satisfactory estimation accuracy. The parameter separation technique introduced in this study can be applied to identify large-scale systems by reducing the number of parameters to be identified, thereby greatly simplifying the identification procedure.

CHAPTER 6

CONCLUSION

6.1 Iterative Equation Error Estimation Approach

So far, thrust forces and moments are obtained from ground tests and directly feeded back to aircraft models to calculate the aerodynamic forces and moments in the equation error method and calculate the states and outputs in the output error method. A simplified turbofan engine model was developed for this case. Firstly, initial estimate values for some parameters related to the engine are given first, and aerodynamic coefficients are estimated. And then, the estimated aerodynamic coefficients are kept fixed, and these time engine parameters are tuned. This procedure is done while the engine parameters and aerodynamic force, and moment coefficients converge to some fixed values.

The while loop is stopped when the difference between old aerodynamic force and moment coefficients and engine-related parameters and new aerodynamic force and moment coefficients and engine-related parameters goes to below some predefined value.

6.2 Feature Selection Using Correlation-Based Binary Particle Swarm Optimization Approach

The correlation-based particle swarm optimization is used as a feature selection method. The algorithm starts by generating a set of candidate model terms, based on a set of base regressor and a maximum term order. And then, pairwise correlation among the model terms is compared and some terms are removed. And finally, binary Particle Swarm Optimization is utilized to generate the best subset of the remaining terms.

The BPSO is an efficient algorithm to solve feature selection problems. However, specific components, referred to as hyperparameters, are not autonomously updated in the feature selection process. The hyperparameters of the binary PSO approach are the transfer function scheme, inertia weight updating strategy, and the value of acceleration coefficients. The setting for these hyperparameters have a significant impact on the performance of BPSO, and there are no universal default values that perform well for different problems and data sets. The fundamental issue in designing a BPSO is determining the best configuration of the hyperparameters. To determine the best configuration hyperparameters, 160 configurations are tested over 30 times and their mean fitness are compared. It is observed that choice of acceleration scheme does not affect the result, and different choices are seen to give essentially the same performance. The normalized fitness sum of Acceleration Scheme 1 is slightly better than the second one so it can be used for further studies. The most dominant hyperparameter affecting the binary PSO performance is the choice of transfer function. S1 transfer function is superior to other. Among inertia weight schemes, the most influential ones are 4th, 7th and 9th inertia weight strategies which are Constant Inertia Weight, Linear Increasing Inertia Weight, and Random Inertia Weight. After the analysis, 160 total configuration reduced to 3 total configuration.

REFERENCES

- [1] R. V. Jategaonkar, Flight Vehicle System Identification: A-Time Domain Methodology, Reston, VA: American Institute of Astronautics and Aeronautics, Inc., 2015.
- [2] E. A. Morelli and V. Klein, Aircraft System Identification: Theory and Practices, Reston, VA: AIAA, 2006.
- [3] D. Allerton, Principles of Flight Simulation, West Sussex, UK: A John Wiley and Sons Inc., 2009.
- [4] B. Peerlings, "A review of aerodynamic flow models, solution methods and solvers and their applicability to aircraft conceptual design," Master's Thesis, Delft University of Technology, Delft, 2018.
- [5] M. Tyan, M. Kim, V. Pham, C. Choi, L. Nguyen and J. W. Lee, "Development of Advanced Aerodynamic Data Fusion Techniques for Flight Simulation Database Construction," in *AIAA Aviation Forum*, Atlanta, GA, 2018.
- [6] Q. Liu, P. Zhang, W. Xiao and J. D. Diao, "Correction Methods of Aerodynamic Force and Moment Coefficients Based on the Identification Data," in *Chinese Control Conference*, Guangzhou, China, 2019.
- [7] M. R. Malik and D. M. Bushnell, "Role of Computational Fluid Dynamics and Wind Tunnels in Aeronautics R&D," Nasa Technical Paper 217062, Hampton, VA, 2012.
- [8] C. Cavalcanti and M. Papini, "Preliminary Model Matching of the EMBRAER 170 Jet," *Journal of Aircraft*, vol. 41, no. 4, pp. 703-710, 2004.
- [9] S. A. Haser, "Time Domain System Identification for an UAV Using Flight Test Data," in *Ankara International Aerospace Conference*, Ankara, 2013.

- [10] S. Avcioglu, A. T. Kutay and K. Leblebicioglu, "Implementation of Physical Subspace Identification on a Realistic Helicopter," in *AIAA SciTech Forum*, San Diego, CA, 2019.
- [11] P. G. Hamel and R. V. Jategaonkar, "Evolution of Flight Vehicle System Identification," *Journal of Aircraft*, vol. 33, no. 1, pp. 9-28, January-February 1996.
- [12] R. V. Jategaonkar and W. Mönnich, "Identification of DO-328 Aerodynamic Database for a Level D Flight Simulator," in *AIAA Modeling and Simulation Technologies Conference*, New Orleans, LA, 1997.
- [13] M. Millidere, U. Cakin and T. Yigit, "Generating Aerodynamic Database from Closed Loop Simulated Flight Data," in *European Conference for Aeronautics and Space Sciences*, Madrid, Spain, 2019.
- [14] M. B. Tischler and R. K. Remple, *Aircraft and Rotorcraft System Identification: Engineering Methods with Flight Test Examples*, 2 ed., Reston, VA: AIAA, 2012.
- [15] E. A. Morelli and J. A. Grauer, "Practical Aspects of Frequency-Domain Approaches for Aircraft System Identification," *Journal of Aircraft*, vol. 57, no. 2, 2020.
- [16] E. A. Morelli and J. Cooper, "Frequency-Domain Method for Automated Simulation Updates Based on Flight Data," *Journal of Aircraft*, vol. 52, no. 6, 2015.
- [17] J. W. Thurgood and D. F. Hunsaker, "Sensitivity and Estimation of Flying-Wing Aerodynamic, Propulsion, and Inertial Parameters Using Simulation," in *AIAA SciTech Forum*, Virtual Event, 2021.

- [18] L. Ljung and K. Glover, "Frequency Domain Versus Time Domain Methods in System Identification," *Automatica the Journal of IFAC*, vol. 17, no. 1, pp. 71-86, 1981.
- [19] M. Millidere, F. Akgül and K. Leblebicioğlu, "F16 Savaş Uçağının Boylamsal Aerodinamik Veritabanının Tanımlanması ve Doğrulanması," in *Ulusal Havacılık ve Uzay Konferansı*, Virtual Conference, 2021.
- [20] R. Monstein, P. Capone, M. Dettling and M. Vrdoljak, "Determination of Model Structure from Flight Test with Generalized Additive Models," *Journal of Aircraft*, vol. 56, no. 4, 2019.
- [21] J. B. van Ingen, C. C. de Visser and D. M. Pool, "Stall Model Identification of a Cessna Citation II from Flight Test Data Using Orthogonal Model Structure Selection," in *AIAA SciTech Forum*, Virtual Event, 2021.
- [22] A. C. Paris and M. Bonner, "Nonlinear Model Development from Flight-Test Data for F/A-18E Super Hornet," *Journal of Aircraft*, vol. 41, no. 4, pp. 692-702, 2004.
- [23] J. A. Grauer and E. A. Morelli, "Generic Global Aerodynamic Model for Aircraft," *Journal of Aircraft*, 2015.
- [24] M. Millidere, H. B. Kurt, H. Ballı and Ö. Uğur, "Kalman Based Neural Network Model Analysis with Resampling Methods for Longitudinal Aerodynamic Coefficient Estimation," in *AIAA Aviation Forum*, Virtual Conference, 2020.
- [25] K. Kirkpatrick, J. May and J. Valasek, "Aircraft System Identification Using Artificial Neural Networks," in *AIAA Aerospace Sciences Meeting including the New Horizons Forum and Aerospace Exposition*, Grapevine, TX, 2013.

- [26] G. Ghazi, M. Bosne, Q. Sammartano and R. M. Botez, "Cessna Citation X Stall Characteristics Identification from Flight Data using Neural Networks," in *AIAA Atmospheric Flight Mechanics Conference*, Grapevine, TX, 2017.
- [27] J. Harris, F. Arthurs, J. V. Henrickson and J. Valasek, "Aircraft System Identification using Artificial Neural Networks with Flight Test Data," in *International Conference on Unmanned Aircraft Systems*, Arlington, VA, 2016.
- [28] B. M. Simmons, H. G. McClelland and C. A. Woolsey, "Nonlinear Model Identification Methodology for Small, Fixed-Wing, Unmanned Aircraft," *Journal of Aircraft*, vol. 56, no. 3, 2019.
- [29] E. Ozger, "Introducing a Combined Equation/Output Error Approach in Parameter Estimation," in *AIAA Aerospace Sciences Meeting*, Orlando, FL, 2010.
- [30] A. Kornienko, "System Identification Approach for Determining Flight Dynamical Characteristics of an Airship from Flight Data," Ph.D. Dissertation, Stuttgart University, Stuttgart, 2006.
- [31] R. V. Jategaonkar and F. Thielecke, "An Integrated Software Tool for Nonlinear Parameter Estimation," *Aerospace Science and Technology*, vol. 6, no. 8, pp. 565-578, 2002.
- [32] G. James, D. Witten, T. Hastie and R. Tibshirani, *Introduction to Statistical Learning with Applications in R*, Springer, 2013.
- [33] T. Hastie, R. Tibshirani and J. Friedman, *The Elements of Statistical Learning-Data Mining, Inference, and Prediction*, Springer, 2009.

- [34] B. Stevens, F. Lewis and E. Johnson, Aircraft Control and Simulation Dynamics, Controls Design and Autonomous Systems, Wiley-Blackwell, 2015.
- [35] P. H. Zipfel, Modeling and Simulation of Aerospace Vehicle Dynamics, American Institute of Aeronautics and Astronautics (AIAA), 2014.
- [36] M. V. Cook, Flight Dynamics Principles: A Linear Systems Approach to Aircraft Stability and Control, Butterworth-Heinemann, 2012.
- [37] D. Allerton, Principles of Flight Simulation, American Institute of Aeronautics and Astronautics (AIAA), 2009.
- [38] B. Etkin and L. D. Reid, Dynamics of Flight: Stability and Control, John Wiley & Sons, 1995.
- [39] R. F. Stengel, Flight Dynamics, Princeton University Press, 2004.
- [40] J. R. Raol and J. Singh, Flight Mechanics Modeling and Analysis, CRC Press, 2008.
- [41] D. K. Schmidt, Modern Flight Dynamics, McGraw-Hill Education, 2011.
- [42] M. Millidere, U. Karaman, S. Uslu, C. Kasnakoglu and T. Çimen, "Newton Raphson Methods in Aircraft Trim: A Comparative Study," in *AIAA Aviation Forum*, Virtual Event, 2020.
- [43] M. Millidere, U. Karaman, H. Ballı and T. Çimen, "Further Investigations on Newton-Raphson Methods in Aircraft Trim," in *AIAA SciTech Forum*, Virtual Event, 2021.
- [44] T. Çimen, "A Generic Approach to Missile Autopilot Design using State-Dependent Nonlinear Control," in *The International Federation of Automatic Control*, Milano, Italy, 2011.

- [45] M. Millidere, U. Karaman, S. Uslu, C. Kasnakoglu and T. Çimen, "Newton Raphson Methods in Aircraft Trim: A Comparative Study," in *AIAA Aviation Forum*, Reno, NV, 2020.
- [46] L. Nguyen, M. Ogburn, W. P. Gilbert, K. S. Kibler, P. W. Brown and P. L. Deal, "Simulator Study of Stall/PostStall Characteristics of a Fighter Airplane with Relaxed Longitudinal Static Stability," NASA Technical Paper 1538, Hampton, VA, 1979.
- [47] F. R. Garza and E. A. Morelli, "Collection of Nonlinear Aircraft Simulations in MATLAB," NASA Technical Memorandum 212145, 2003.
- [48] B. L. Stevens, F. L. Lewis and E. N. Johnson, *Aircraft Control and Simulation: Dynamics, Controls Design, and Autonomous Systems*, 3 ed., John Wiley & Sons, Inc, 2015.
- [49] H. B. Kurt, M. Millidere and E. Sezer, "Aerodynamic Database Simulation Implementation Based On Neural Network and Neural Network Parameter Selection Using Genetic Algorithms," in *European Conference for Aeronautics and Space Sciences*, Madrid, 2019.
- [50] G. Ghazi and R. M. Botez, "Development of a High-Fidelity Simulation Model Identification for a Research Environment," in *SAE AeroTech Congress&Exhibition*, Seattle, WA, 2015.
- [51] R. Yadav, Y. Kapadi and A. Pashilkar, "Aero-thermodynamic model for digital simulation of turbofan engine," in *ASME Turbofan Expo 2005: Power for Land, Sea and Air*, Reno, NV, 2005.
- [52] R. A. Roberts and S. M. Eastbourn, "Modeling Techniques for a Computational Efficient Dynamic Turbofan Engine Model," *International Journal of Aerospace Engineering*, 2014.

- [53] R. May, J. Csank, T. Lavelle, J. Litt and T.-H. Guo, "A High-Fidelity Simulation of a Generic Commercial Aircraft Engine and Controller," in *AIAA/ASME/SAE/ASEE Joint Propulsion Conference & Exhibit*, Nashville, TN, 2010.
- [54] G. Ghazi, R. M. Botez and J. M. Achigui, "Cessna Citation X Engine Model Identification from Flight Tests," *SAE International Journal of Aerospace*, vol. 8, no. 2, pp. 203-213, 2015.
- [55] J. D. Mattingly, W. H. Heiser and D. H. Daley, *Aircraft Engine Design*, Reston, VA: AIAA, 1987.
- [56] L. F. Rodriguez and R. M. Botez, "Generic New Modeling Technique for Turbofan Engine Thrust," *Journal of Propulsion and Power*, vol. 29, pp. 1492-1495, 2013.
- [57] B. E. Saleh, "Modeling and Simulation of A Double Spool Turbofan Engine Using SIMULINK," Master's Thesis, Zazazig University, Zazazig, 2017.
- [58] D. Unsal, "Estimation of Deterministic and Stochastic IMU Error Parameters," METU, Ankara, 2012.
- [59] T. Bayoglu, "AERODYNAMIC PARAMETER ESTIMATION OF A SUPERSONIC MISSILE WITH RAPID SPEED VARIATION BY USING KALMAN FILTERING," METU, Ankara, 2016.
- [60] J. R. Raol and J. Singh, *Flight Mechanics Modeling and Analysis*, CRC Press, 2008.
- [61] J. Nocedal and S. J. Wright, *Numerical Optimization*, 2 ed., Newyork, NY: Springer, 2006.

- [62] J. A. Mulder, Q. P. Chu, J. K. Sridhar, J. H. Breeman and M. Laban, "Non-linear aircraft flight path reconstruction review and new advances," *Progress in Aerospace Sciences*, vol. 35, no. 7, pp. 673-726, 1999.
- [63] R. V. Jategaonkar, R. Behr, W. Gockel and C. Zorn, "Data Analysis of Phoenix RLV Demonstrator Flight Test," in *AIAA Atmospheric Flight Mechanics Conference and Exhibit*, San Francisco, CA, 2005.
- [64] N. Khadeeja, J. Singh and Basappa, "Drag assessment of a high performance aircraft using system identification techniques," in *IEEE Indian Control Conference*, Hyderabad, India, 2016.
- [65] R. V. Jategaonkar and F. Thielecke, "Aircraft Parameter Estimation - A Tool for Development of Aerodynamic Databases," *Indian Academy of Sciences*, vol. 25, pp. 119-135, 2000.
- [66] R. C. Aster, B. Borchers ve C. H. Thurber, *Parameter Estimation and Inverse Problems*, Burlington, MA: Elsevier Academic Press, 2005.
- [67] R. V. Jategaonkar, D. Fischenberg and W. v. Gruenhagen, "Aerodynamic Modeling and System Identification from Flight Data-Recent Applications at DLR," *Journal of Aircraft*, vol. 41, no. 4, 2004.
- [68] R. V. Jategaonkar and F. Thielecke, "Evaluation of Parameter Estimation Methods for Unstable Aircraft," *Journal of Aircraft*, vol. 31, no. 3, 1994.
- [69] B. P. Barnhart, E. G. Dickes, D. R. Gingras and T. P. Ratvasky, "Simulation Model Development for Icing Effects Flight Training," in *SAT International General Aviation Technology Conference and Exhibition*, Wichita, Kansas, 2002.
- [70] J. Grauer, "Aerodynamic Parameter Estimation Using Reconstructed Turbulence Measurements," *Journal of Aircraft*, 2021.

- [71] S. Mirjalili, *Evolutionary Algorithms and Neural Networks*, Springer International Publishing, 2019.
- [72] D. Wang, D. Tan and L. Liu, "Particle Swarm Optimization Algorithm: An Overview," *Soft Computing*, vol. 22, pp. 387-408, 2017.
- [73] T. Jiang, J. Li and K. Huang, "Longitudinal Parameter Identification of a Small Unmanned Aerial Vehicle Based On Modified Particle Swarm Optimization," *Chinese Journal of Aeronautics*, 2015.
- [74] J. Guan, W. Yi, S. Chang and X. Li, "Aerodynamic Parameter Estimation of a Symmetric Projectile Using Adaptive Chaotic Mutation Particle Swarm Optimization," *Mathematical Problems in Engineering*, 2016.
- [75] B. A. Garro and R. A. Vázquez, "Designing Artificial Neural Networks Using Particle Swarm Optimization Algorithms," *Computational Intelligence and Neuroscience*, 2015.
- [76] H. Wang, R. Ke, J. Li, Y. An, K. Wang and L. Yu, "A correlation-based binary particle swarm optimization method for feature selection in human activity recognition," *International Journal of Distributed Sensor Networks*, vol. 14, no. 4, 2018.
- [77] F. Koumi, M. Aldasht and H. Tamimi, "Efficient Feature Selection using Particle Swarm Optimization: A hybrid filters-wrapper Approach," in *10th International Conference on Information and Communication Systems (ICICS)*, Irbid, Jordan, 2019.
- [78] M. Mafarja, R. Jarrar, S. Ahmad and A. A. Abusnaina, "Feature Selection Using Binary Particle Swarm Optimization with Time Varying Inertia Weight Strategies," in *International Conference on Future Networks and Distributed Systems (ICFNDS)*, Amman / Jordan, 2018.

- [79] J. Too, A. R. Abdullah and N. M. Saad, "A New Co-Evolution Binary Particle Swarm Optimization with Multiple Inertia Weight Strategy for Feature Selection," *Informatics*, vol. 6, no. 21, 2019.
- [80] S. Mirjalili and A. Lewis, "S-shaped versus V-shaped transfer functions for binary Particle Swarm Optimization," *Swarm and Evolutionary Computation*, vol. 9, pp. 1-14, 2013.
- [81] A. R. Garcia, R. Vos and C. C. de Visser, "Aerodynamic Model Identification of the Flying V from Wind Tunnel Data," in *AIAA Aviation Forum*, Virtual Event, 2020.
- [82] P. Umapathy, C. Venkateshaiah and M. S. Arumugam, "Particle Swarm Optimization with Various Inertia Weight Variants for Optimal Flow Solution," *Discrete Dynamics in Nature and Society*, 2010.
- [83] J. Liu, Y. Mei and X. Li, "An Analysis of the Inertia Weight Parameter for Binary Particle Swarm Optimization," *IEEE Transactions on Evolutionary Computation*, 2015.
- [84] J. C. Bansal, P. K. Singh, M. Saraswat, A. Verma, S. S. Jadon and A. Abraham, "Inertia Weight strategies in Particle Swarm Optimization," in *Third World Congress on Nature and Biologically Inspired Computing*, Salamanca, Spain, 2011.
- [85] J. Wisnowski, J. Simpson, D. Montgomery and G. Runger, "Resampling Methods for Variable Selection in Robust Regression," *Journal of Computational Statistics and Data Analysis*, vol. 43, no. 3, pp. 341-355, 2003.
- [86] "Aeroplane Flight Simulator Evaluation Handbook," Royal Aeronautical Society, London, 2005.

- [87] R. T. Galloway, "Validation and Evaluation - Part 1," Binghamton Univeristy
The Annual Flight & Ground Vehicle Simulation Course, New York, NY,
2011.
- [88] "14 CFR FAR Part 60, Requirements for the Evaluation, Qualification, and
Maintenance of Flight Simulation Training Devices," Federal Aviation
Administration, Washington, DC, 2008.
- [89] D. Raymer, Aircraft Design: A Conceptual Approach, 6 ed., Reston, VA:
American Institute of Astronautics and Aeronautics, 2018.

CURRICULUM VITAE

PERSONAL INFORMATION

Surname, Name: Millidere, Murat
Nationality: Turkish (TC)
Date and Place of Birth: 3 July 1985, Ankara
Marital Status: Single
Phone: +90 530 131 86 15
email: muratmillidere@gmail.com

EDUCATION

Degree	Institution	Year of Graduation
BS	METU Aerospace Engineering	2010
BS	METU Physics	2008
High School	Keçiören Lisesi, Ankara	2002

WORK EXPERIENCE

Year	Place	Enrollment
2016-2021	TUSAŞ	Modelling and Simulation Engineer
2012-2016	HAVELSAN	System Engineer
2011-2012	Leal Engineering	Team Lead
2008-2010	Hampton University Nuclear Fusion Center	Research Assistant
2005 July	TUSAŞ	Intern Eng. Student

FOREIGN LANGUAGES

Advanced English, Beginner German

PUBLICATIONS

1. Millidere M., Gömeç F., Kurt B., and Akgül F. "Multi-fidelity Aerodynamic Dataset Generation of a Fighter Aircraft with Deep Neural-Genetic Network", in AIAA Aviation Conference, Virtual Event (2021)

2. Kurt B., Millidere M., Gomec F., and Uğur Ö. "Multi-fidelity Aerodynamic Dataset Generation of a Fighter Aircraft", in AIAA SciTech Conference, Virtual Event (2021)
3. Millidere M., Akgül F., and Leblebicioğlu K. " F16 Savaş Uçağının Boylamsal Aerodinamik Veritabanının Tanımlanması ve Doğrulanması", in Ulusal Havacılık ve Uzay Konferansı, Virtual Event (2020)
4. Millidere M., Karaman U., Uslu S., Kasnakoğlu C., and Çimen T. "Newton Raphson Methods in Aircraft Trim", in AIAA Virtual Conference, Virtual Event (2021)
5. Millidere M., Çakın U., and Yiğit T. "Generating Aerodynamic Database from Closed Loop Simulated Flight Data" in European Conference for Aeronautics and Space Sciences, Madrid, Spain (2019)

Bowling, Flight Simulations, Movies, Travelling